

University of Southampton Research Repository ePrints Soton

Copyright © and Moral Rights for this thesis are retained by the author and/or other copyright owners. A copy can be downloaded for personal non-commercial research or study, without prior permission or charge. This thesis cannot be reproduced or quoted extensively from without first obtaining permission in writing from the copyright holder/s. The content must not be changed in any way or sold commercially in any format or medium without the formal permission of the copyright holders.

When referring to this work, full bibliographic details including the author, title, awarding institution and date of the thesis must be given e.g.

AUTHOR (year of submission) "Full thesis title", University of Southampton, name of the University School or Department, PhD Thesis, pagination

UNIVERSITY OF SOUTHAMPTON
FACULTY OF NATURAL AND ENVIRONMENTAL SCIENCES
CHEMISTRY

Solvothermal Synthesis of Porous Beryllate Containing Materials

By

Benjamin Tarrant Robert Littlefield

Thesis for the Degree of Doctor of Philosophy

January 2013

ABSTRACT

Solvothermal Synthesis of Porous Beryllate Containing Materials

By Benjamin Tarrant Robert Littlefield

Natural and synthetic zeolites have been the focus for extensive research owing to their many applications and huge potential number of new topologies. The work presented here represents the first major study into the formation of zeotypical materials incorporating BeO_4 and T^{5+}O_4 ($\text{T}^{5+} = \text{As}$ or P) tetrahedra and a large number of new structures have been produced. These novel materials have been synthesised *via* hydrothermal procedures and characterised *via* Single Crystal X-ray Diffraction, supported by Powder X-ray Diffraction, Thermogravimetric Analysis, Magic Angle Spinning Nuclear Magnetic Resonance and Electron Dispersive Spectroscopy.

The beryllarsenates produced encompass the entire range of dimensionality, from cluster structures such as $\text{Na}_{3.5}[\text{AsO}_4(\text{BeF}_3)(\text{BeF}_2)] \cdot 0.4\text{H}_2\text{O}$ to the novel three dimensional framework $[\text{H-bis}(2\text{-ethylhexyl})\text{amine}, \text{NH}_4]_4[(\text{AsO}_4)_3(\text{AsO}_3\text{OH})\text{Be}_3(\text{BeOH})]$ and include analogues of known zeolite topologies; MER, AFI and WEI. Four completely novel fully connected three-dimensional zeolitic topologies are also reported with one already being assigned the Framework Type code of BOZ. These new topologies represent the most structurally complicated zeolites known and are remarkable in their high calculated internal pore volume.

The beryllarsenates are supported by parallel research into the beryllphosphates which has produced unusual new structures of low dimensionality such as the one dimensional chain $\text{Na}_2[(\text{BeO}_2\text{OH})(\text{PO}_2)] \cdot \text{H}_2\text{O}$ as well as structural analogues of the beryllarsenate structures including $[\text{H-pyridine}][(\text{BeO}_4)_2\text{BeO}_3(\text{OH}_2)\text{P}_3(\text{OH})]$ which exhibits the AFI topology. These structures could potentially be used in catalysis, ion exchange and due to their low framework density, gas storage.

A short investigation into other beryllate chemistry is also presented which includes the novel two dimensional structures $\text{Na}[\text{BeGeO}_3(\text{OH})]$ and $\text{Ba}[\text{BeGeO}_3(\text{OH})]$ which significantly contribute to the sparse field of beryllgermanates. This section also contains the first structural characterisation of $\text{Sr}[\text{Be}(\text{OH})_4]$, a vital species in beryllium solution chemistry.

Contents

Chapter 1	Introduction	Page
1.1	General introduction	1
1.2	Zeolites	3
1.3	Formation and Synthesis of Zeolites	7
1.4	Applications	11
1.5	Modifications to Synthetic Procedure	14
1.6	Zeotypes	17
1.7	Beryllium	20
1.8	Scope of work	25
1.9	References	26
Chapter 2	Characterisation and Experimental methods	Page
2.1	Synthesis methods	31
2.1.1	Solvothermal synthesis	32
2.1.2	Toxicity of beryllium	33
2.2	Characterisation methods	34
2.2.1	Diffraction of X-rays	34
2.2.2	Generation of X-rays	38
2.2.3	Single Crystal X-ray Diffraction	38
2.2.4	Single Crystal X-ray Diffraction instrumentation	41
2.2.5	Powder X-ray Diffraction instrumentation	42
2.2.6	Variable Temperature Powder X-ray Diffraction	43
2.2.7	Powder X-ray data treatment	43
2.2.8	Neutron Diffraction	45
2.2.9	Electron Microscopy	46
2.2.10	Scanning Electron Microscopy instrumentation	48
2.2.11	Thermogravimetric Analysis	48
2.2.12	Magic Angle Spinning Nuclear Magnetic Resonance	48
2.3	Computational	50
2.3.1	Bond Valance Calculations	50
2.3.2	Totopol	51
2.4	References	52

Chapter 3	Arsenates	Page
3.1	$\text{Na}_{3.5}[\text{AsO}_4(\text{BeF}_3)(\text{BeF}_2)] \cdot 0.4\text{H}_2\text{O}$	66
3.2	$\text{AsO}_3(\text{OH})\text{Be}(\text{C}_3\text{H}_4\text{N}_2)$	71
3.3	$\text{Na}_2[\text{AsO}_4\text{Be}(\text{OH})] \cdot \text{H}_2\text{O}$	75
3.4	$[\{\text{H-pyridine}\}_{0.5}][\text{As}_2(\text{As}_{0.25}\text{Be}_{0.75})_2\text{O}_7(\text{OH})_2] \cdot (\text{H}_2\text{O})_{0.65}$	79
3.5	$\text{Sr}[\text{AsO}_4\text{Be}(\text{OH})] \cdot (\text{H}_2\text{O})_{0.0685}$	84
3.6	$\text{AsO}_4\text{Be}(\text{OH}_2)(\text{Be}(\text{OH})(\text{OH}_2))$	88
3.7	$\text{AsO}_3(\text{OH})\text{Be}$	93
3.8a	$[\text{NH}_4]_2[(\text{AsO}_4)_2\text{Be}_2] \cdot 2\text{H}_2\text{O}$	97
3.8b	$[\text{H}_2\text{-diaminoethane}]_{0.5}[\text{AsO}_4\text{Be}]$	105
3.9	$[(\text{H}_2\text{-diaminopropane})_{1.5}][(\text{AsO}_4)_2(\text{AsO}_3\text{OH})_2(\text{AsO}_2\text{OH})_2\text{Be}_4] \cdot \text{H}_2\text{O}$	108
3.10	$\text{AsO}_4\text{Be}(\text{BeOH}_2)_2$	114
3.11	$[(\text{H-pyridine})_2][(\text{AsO}_4)_2(\text{AsO}_3\text{OH})\text{Be}_2(\text{BeOH}_2)]$	118
3.12a	$[\text{H-bis}(2\text{-ethylhexyl)amine}, \text{NH}_4]_4[(\text{AsO}_4)_3(\text{AsO}_3\text{OH})\text{Be}_3(\text{BeOH})]$	124
3.12b	$\text{Rb}_3[(\text{AsO}_4)_3(\text{AsO}_3\text{OH})\text{Be}_3(\text{BeOH}_2)] \cdot \text{H}_2\text{O}$	129
3.13	$\text{Rb}_2[(\text{AsO}_4)_2\text{Be}_2(\text{Be}(\text{OH})_2)] \cdot 2\text{H}_2\text{O}$	133
3.14	$\text{Na}[\text{AsO}_4\text{Be}]$	140
3.15	$[\text{NH}_4]_2[(\text{AsO}_4)_2\text{Be}_2(\text{Be}(\text{OH})_2)]$	143
3.16	$[\text{C}_2\text{H}_5\text{NH}_2, \text{H}_2\text{O}]_x[\text{Be}_{66.7}\text{As}_{25.3}(\text{O})_{80.5}(\text{OH})_{103.5}]$	148
3.17	$[\text{R}^+]_{1.5}[\text{As}_{6.17}\text{Be}_{13.83}\text{O}_{\sim 20}\text{OH}_{\sim 20}] \cdot n\text{H}_2\text{O}$	153
3.18	$[\text{C}_2\text{H}_5\text{NH}_2][\text{Be}_{42.7}\text{As}_{17.3}(\text{O})_{\sim 55}(\text{OH})_{\sim 65}]$	157
3.19	Trends encountered in the berylloarsenate frameworks	160
3.20	Conclusions for the berylloarsenate frameworks	165
3.21	References	169

Chapter 4	Phosphates	Page
4.1	$\text{Na}_2[(\text{BeO}_2\text{OH})(\text{PO}_2)] \cdot 0.5\text{H}_2\text{O}$	175
4.2	$\{\text{BeO}_2(\text{OH})(\text{OH}_2)\}\{\text{BeO}_2\text{OH}_2\}\text{P}$	179
4.3	$[(\text{H-pyridine})_4][\text{Be}_6(\text{PO}_3\text{OH})_8]$	183
4.4	$[\text{H-pyridine}][(\text{BeO}_4)_2\text{BeO}_3(\text{OH}_2)\text{P}_3(\text{OH})]$	187
4.5	$[\text{H-dimethylamine}][\text{BeO}_4(\text{BeO}_2\text{OH})(\text{BeO}_2\text{OH}_2)\text{P}_2]$	193
4.6	$[(\text{BeO}_4)_2\text{BeO}_2(\text{BeO}_2(\text{OH}_2)_2)(\text{BeO}_2\text{OH}_2)(\text{BeOH}_2\text{BeO}_2)\text{P}_4]$	197
4.7	$[\text{BeO}_3(\text{Be}_{0.5}\text{O}_2)(\text{Be}_{0.5}\text{O}(\text{OH}_2))_2(\text{Be}_{0.5}\text{O})\text{P}_2]$	200
4.8	$[\text{C}_2\text{H}_5\text{NH}_2, \text{H}_2\text{O}]_x[\text{Be}_{\sim 0.78}\text{P}_{\sim 0.22}(\text{O}, \text{OH})_2]$	203
4.9	Trends encountered in the beryllophosphate frameworks	206

4.10	Conclusions for the beryllophosphate frameworks	208
4.11	References	210

Chapter 5	Other beryllate chemistry	Page
5.1	Na[BeGeO ₃ (OH)]	219
5.2	Ba[BeGeO ₃ (OH)]	223
5.3	Sr[Be(OH) ₄] ²⁻	229
5.4	[Co ^{II}] _{0.11} [(AsO ₄ (H) _{0.66}) ₂ Be ₂ (BeOH ₂) _{0.33}]•2H ₂ O	233
5.5	Conclusions for the other beryllates	238
5.6	References	240

Chapter 6	Conclusions	Page
6.1	Overall conclusions	242

Appendix 1	Hydrogenous materials	Page
A.1	Thomsonite	247
A.2	Cavansite	250
A.3	Conclusions	252
A.4	References	253

List of commonly used Abbreviations

IZA – International Zeolite Association

SBU – Secondary Building Unit

CBU – Composite Building Unit

SDA – Structure Directing Agent

OSDA – Organic Structure Directing Agent

PXD – Powder X-ray Diffraction

SXD – Single Crystal X-ray Diffraction

TGA – Thermogravimetric Analysis

VTPXD – Variable Temperature Powder X-ray Diffraction

DECLARATION OF AUTHORSHIP

I, Benjamin Tarrant Robert Littlefield, declare that the thesis entitled:

Solvothermal Synthesis of Porous Beryllate Containing Materials

and the work presented in the thesis are both my own and have been generated by me as a result of my own original research. I confirm that:

- This work was done wholly or mainly while in candidature for a research degree at this University
- Where any part of this thesis has previously been submitted for a degree or any other qualification at this University or any other institution, this has been clearly stated
- Where I have consulted the published work of others, this is always clearly attributed
- Where I have quoted from the work of others, the source is always given. With the exception of such quotations, this thesis is entirely my own work
- I have acknowledged all main sources of help
- Where the thesis is based on work done myself jointly with others, I have made clear exactly what was done by others and what I have contributed myself
- Parts of this work have been published as:

B. T. R. Littlefield, M. T. Weller, *Chem. Commun.*, **2011**, 47, 4769 – 4771, **DOI:**
10.1039/C1CC00118C

B. T. R. Littlefield, C. Hinde, M. T. Weller, *Dalton Trans.*, **2011**, 40, 782 – 284, **DOI:**
10.1039/C0DT00843E

B. T. R. Littlefield, M. T. Weller, *Nat. Commun.*, **2012**, 3, **DOI:** 10.1038/ncomms2129

Signed:

Date:

ACKNOWLEDGEMENTS

To be frank I am surprised I managed to get this far and the only reason I have is because of the many fantastically supporting people I have been lucky enough to encounter on my travels. Firstly I am indebted to my supervisor Prof. Mark Weller, whose guidance, advice and patience has been invaluable. This work would not exist without his enthusiasm and stoic attitude to when I struggled with yet another basic concept. A huge thanks go to the 'Weller group' for that matter, to the old crowd for making me feel welcome; Valeska for constant assistance, advice and impromptu snow-ball fights, Jenny for her guidance and help – a font of all knowledge where beryllium is concerned, Charlie for being the wise older brother and Jess, Kate, Eleni and Rosa for all the much needed laughs. Of course thanks go to the new wave as well of team Weller; Ed, Adam and Kevin.

Extra special thanks go to Dr. Robert Raja, a source of much needed support and motivation whenever I was feeling defeated and to Dr. Mark Light for giving up so much of his time to help with my last minute crystallographic issues.

Thanks and acknowledgment to the contribution of my three rather excellent project students; Chris, Natalie and Harriet, who kept me on my toes with overseeing them as well as the banter (and for winning the project prize for the Weller group!).

A huge thanks to Dr. David Read for his understanding and support while writing my thesis, and to Dr. Paul Duckmanton for his advice and rather amazing short notice proof reading skills. Also thank you to Prof. Gill Reid for her continued support and guidance, a constant throughout my degree and postgraduate study.

A special thank you to my family and friends who over the past four years have been repeatedly let down, stood up and, from their point of view, forgotten, yet still stand by me and support me. One person in particular needs to be thanked, and that is Beccy who has put up with more than anyone and repeated reminders of 'The thesis comes first', I honestly could not have done it without you and your support, understanding and patience, thank you.

Chapter 1

Introduction

1.1: General Introduction

The systematic design of materials at their atomic or molecular level is the fundamental principle behind nanometre (nm) scale research. By controlling the size (typically 1 – 100 nm) ^[1] and the formation of building blocks, the very properties of the assembled nanostructures can be altered. Nanometre scale research generally has two main directions: the first being the investigation and utilisation of the properties of particles at the nm scale known collectively as nanoscience. The second is the formation and manipulation of structures and systems which control shape and size at the nm scale, which in turn is known as nanotechnology.^[2]

In some materials this control of the building blocks can lead to the formation of nanoporous architecture within their structure, either being open to the surface of the material or isolated from the outside, in the form of closed pores. These pores can occur in varying morphologies from simple spheroids to the truncated cuboctahedral seen in zeolite A ^[2] [Fig. 1] and even more complicated shapes. Materials with pore sizes relevant to the nm scale are defined as micropores (pores smaller than 2 nm in diameter), mesopores (pores between 2 to 50 nm in diameter) and macropores (pores with a diameter greater than 50 nm). All of these come under the term nanoporous, a subset of porous materials containing pores of diameters between 1 and 100 nm. Where these pores are classed as ‘open’, channels are often formed leading to nanoporous materials which display properties of interest to materials science, such as; high internal surface area, fluid permeability and molecular sieving effects.

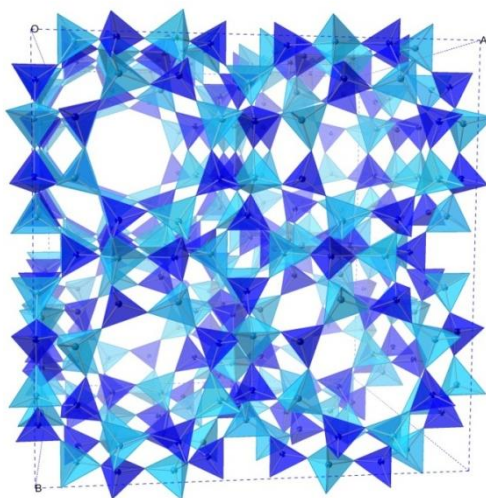


Figure 1: Zeolite A viewed along c. Extra-framework species have been removed for clarity. Light blue and dark blue tetrahedra are Al and Si centred respectively.

The varying pore sizes, porosity (ratio of volume of pores vs total volume of material) and composition of nanoporous materials determine their properties and therefore potential applications. For example, nanoporous activated carbon has a high internal surface area, is microporous, highly thermally/chemically stable and has a long expected lifetime. These properties allow activated carbon to have potential application as hydrogen storage media with recent examples displaying an adsorption capacity at 77 K/ 1 bar being 3% by weight of hydrogen.^[3]

Other applications of nanoporous materials include: The use of activated carbons, zeolites and silica gels for adsorption of SO₂, NO_x, CO₂ and volatile organic compounds from exhaust gases. N₂/CH₄ separation by the zeolite clinoptilolite for improving natural gas. Storage of both H₂ and CH₄ by carbon variants for use in vehicular fuel cells. Nanoporous metal oxides being used as gas sensors, due to their large surface area and high sensitivity to slight changes in environmental factors.^[2]

One of the most important classes of nanoporous materials are the 3D framework structured aluminosilicates, which arise from the facile substitution of Al³⁺ into three dimensional *tecto*-silicates exhibiting tetrahedral coordination. These materials generally have high internal surface areas, high thermal/chemical stability, and long expected lifetimes as well as being cheap to source/produce. This combination of properties makes them extremely versatile and able to be utilised in a large number of applications. The aluminosilicates are divided into three major mineral groups; feldspars, feldspathoids and zeolites.^[4] The research presented in this thesis is concerned with synthetic variants of the latter of the mineral groups, the zeolites.

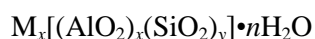
1.2: Zeolites

Zeolites were first discovered to be different from the other tectosilicates when in 1756 the Swedish mineralogist Baron Axel Cronstedt heated the mineral stilbite in a blowpipe flame, where it exhibited intumescence.^[5] This revealed its hydrated nature, and it is from this that Cronstedt created the word ‘zeolite’ from the greek *zeo* (to simmer) and *lithos* (stone).

It was 140 years later in 1896 when Friedel observed that various organic solvents could be occluded on the addition of dehydrated zeolite. This observation led to the conclusion that zeolites had a framework structure with well-defined pores and cavities running through them.^[6] Their open structures, which can reversibly incorporate a multitude of different organic and inorganic species, distinguish zeolites from other aluminosilicate materials. The properties of the framework are intimately related to their compositional and topological features, which leads to their extensive range of applications, from cation exchangers for water softening to being one of the major catalysts used by the petrochemical industry.^[7] These applications have driven the discovery of approximately 56 naturally occurring zeolites, and after the pioneering research by Barrer, Milton and Breck more than 150 synthetic structures have been developed.^[2]

Structure

The most common structure of zeolitic materials is of the primary building units $[\text{SiO}_4]^{4-}$ and $[\text{AlO}_4]^{5-}$ tetrahedra connected by corner sharing, forming oxygen bridges. These building units can also be referred to as ‘T – sites’ or T atoms, where the T represents the central atoms and tetrahedra. The addition of Al^{3+} in the place of Si^{4+} creates an electrostatic imbalance requiring the presence of a positive ion to balance the overall charge of the structure; a three dimensional framework structure composed entirely of SiO_4 would be electronically neutral. This leads to zeolites having a general stoichiometry of:



Where the cation M of varying valence, usually an alkali or alkaline earth metal, balances the negative charge on the framework and H_2O is found inside the structure. Zeolite A has a Si/Al ratio of 1:1, which is the minimum allowed for a zeolite to obey Löwensteins rule of Al-O-Al bond avoidance^[9] which forbid the presence of an Al-O-Al linkage under normal hydrothermal conditions. The ratio however has no upper limit with siliceous zeolites such as ZSM-5 having a Si/Al ratio of twenty to infinity.^[2] The Si/Al ratio is important structurally since it is the amount of Al^{3+} present which

determines the amount of charge balancing cations present in the structure. In the framework, these cations are usually hydrated, therefore a highly siliceous zeolite framework will be hydrophobic and have an affinity for hydrocarbons rather than water. The presence of cations, such as Na^+ in zeolite A reduces the size of the cavities to any guest molecules, this effect can be altered by the exchange of the cation for one of a different valency, made possible by the cations weak interaction with the framework. In the case of zeolite A, the univalent Na^+ can be exchanged for divalent Ca^{2+} , which not only has a smaller ionic radius than Na^+ , but also effectively halves the amount of cations presence in the cavities, therefore freeing up more space for molecule sequestration. This exchange of cations is known as ion exchange.

The angle Al-O-Si is extremely flexible, varying between 120° - 180° , which combined with the tetrahedra having the ability to share just two to all four of its vertices leads to the formation of various secondary building units (SBUs). SBUs are needed to classify and describe the topologies and come in a variety of different two and three dimensional shapes [Fig. 2] and are often described in shorthand, for example a four-membered ring will be referred to as a ‘4R’ and a twelve-membered ring is referred to as a ‘12R’.

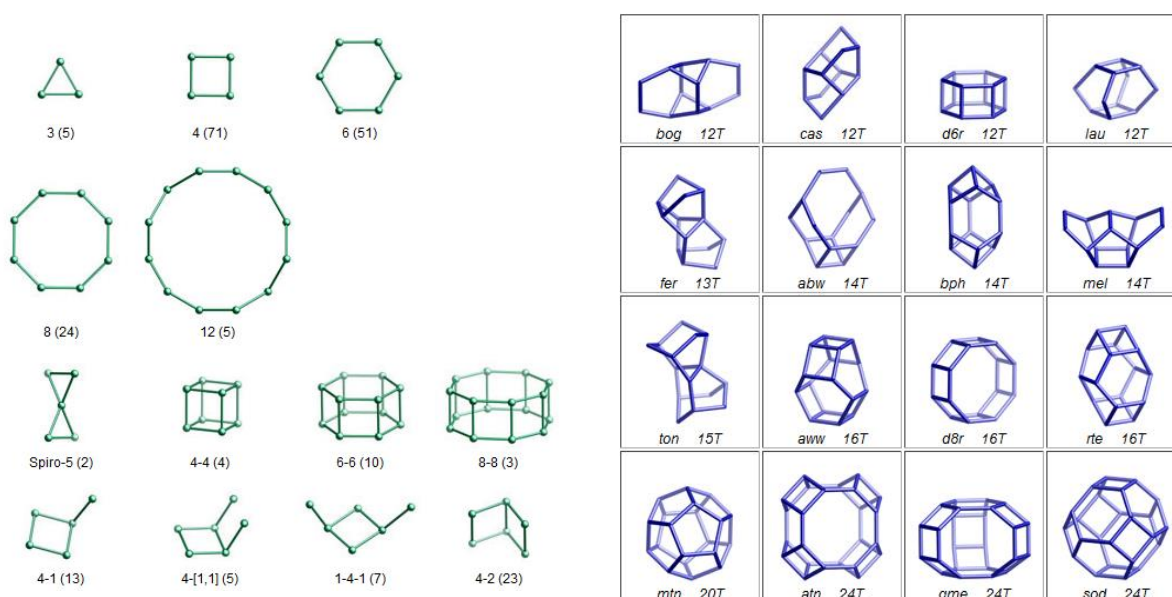


Figure 2: Selection of some of the secondary building units (left) and composite building units (right) present in zeolite-type frameworks ^[10]

The SBUs can be further connected to form another class of structural units identified as composite building units (CBUs) [Fig. 2], which are combinations of SBUs and often are found as cages or chains. CBUs are generally named after the structure they first occurred in, for example the spiro-5 ring is called *lov* since it is found in the mineral lovdarite's structure. The multiple ways in which the SBU/CBUs can be connected allows for potentially millions of different frameworks. Each individual framework that has been synthesised is assigned a unique three letter code, approved by the International Zeolite Association Structure Commission. Different topologies can be made of the same SBU/CBUs for example β – cages are present in both synthetic zeolite Linde type A (LTA) and faujasite (FAU) framework types; it is how the cages are connected which leads to different frameworks.

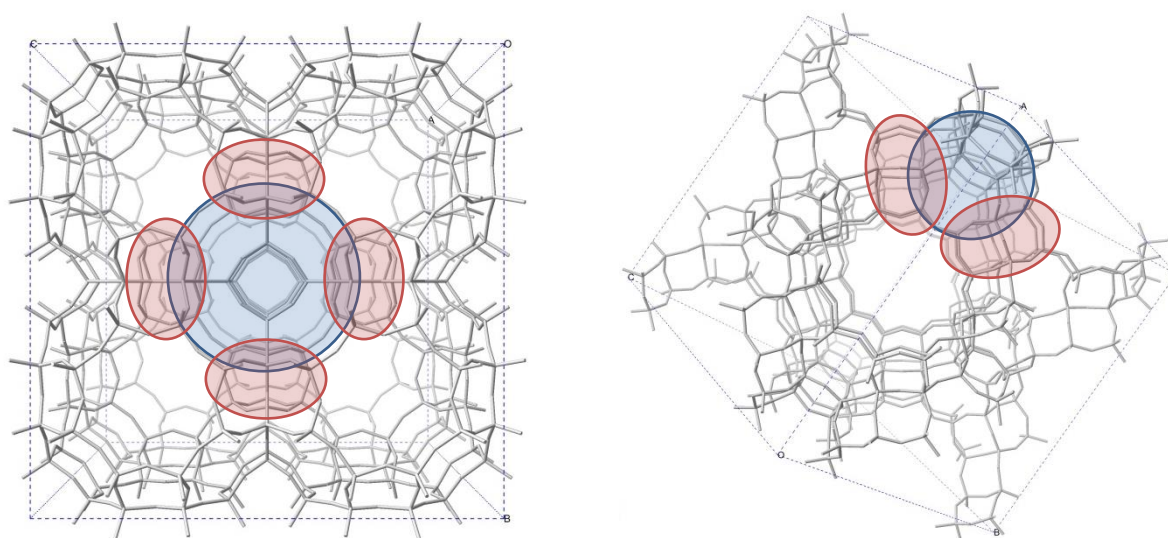


Figure 3: Skeletal representations of zeolite A (left) and faujasite (right) with the sodalite β cage highlighted in blue and the two versions of connectivity in red.

LTA is made up of a space filling combination of sodalite β -cages in a primitive array connected by anion bridging between 4Rs. This framework structure forms channels which run parallel to the three crystallographic axes and intersect in large, charge balancing cation containing cavities [Fig. 3 left]. The β -cages in FAU are connected through the 6Rs however, leading to its very different structure [Fig 3 right].

The sodalite β -cage in LTA can only admit molecules into its structure with diameters less than 2.6 Å such as water, due to the S4R being the window into the cage's cavity. This size selectivity is common to most zeolites and is one of their fundamental properties, with window sizes varying between 2.6 to 10.2 Å.^[11] Zeolites have a large surface area within the cavities in their structures and therefore high sorption capacities for molecules that are small enough to pass through the window into the cavities. This internal surface can be affected by the cation present as previously mentioned.

Like all crystalline materials these structural components combine to form a larger, repeating unit cell. Due to the variety of possible combinations of SBU, Si/Al ratio and cations present, zeolites adopt a multitude of space groups and lattice parameters. For example, zeolite P which adopts the ‘crank shaft’ gismondine (GIS) structure [Fig. 4], is tetragonal crystallographic space group $I4_1/amd$ with cell parameters of $a = 9.801 \text{ \AA}$ and $c = 10.158 \text{ \AA}$.^[12] This is in contrast to zeolite A, which is cubic with space group Fm-3c and a cell parameter of $a = 24.61 \text{ \AA}$. In its dehydrated Na- form however, the unit cell contracts to a rhombohedral framework in the space group Pm-3m, with a cell lattice parameter of 12.3 \AA ^[13,14] showing the level of variety present in the zeolite class of materials.

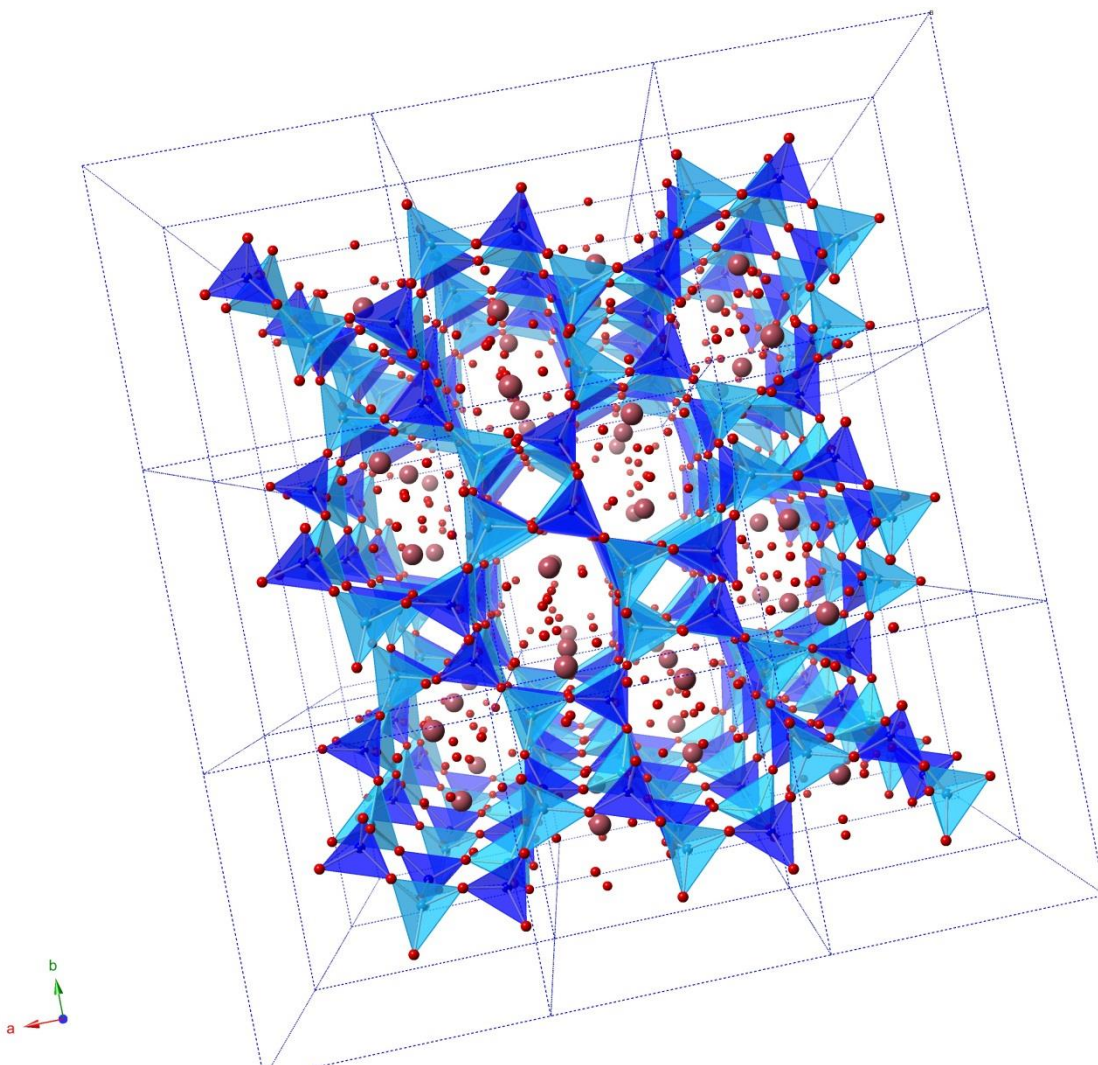


Figure 4: GIS-type topology viewed along c , with calcium and H_2O extra-framework positions. Light and dark blue tetrahedra are Al and Si respectively, pink and red spheres are Ca and O respectively.

1.3: Formation and synthesis of zeolites

Natural Formation

The first identified zeolite was discovered by Axel Fredrik Cronstedt within a ‘vug’ inside basalt, a rock of volcanic origin. The classic geological environment for zeolite formation is within these small basaltic cavities, where over a relatively short geological time period coupled with high temperatures/pressures and a high concentration of mineral-rich solutions, aesthetically pleasing aggregations of often needle-like zeolite crystals can form. Deposits of this form exist naturally all over the world.

Zeolite deposits are known to originate from many other geological environments as well, such as the John Day formation in Oregon, USA,^[7] where zeolites are formed by burial of volcanic tuff under subsequent layers of geological strata. As the depth of burial increases, a positive geothermal gradient alongside a negative hydration gradient determines the zeolites formed, with more porous, hydrated zeolites such as clinoptilolite and mordenite, being discovered above less porous (e.g. analcime, heulandite and laumontite). Another common environment for zeolite formation is the hydrothermal action on volcanic ash by geysers in such locations as Yellowstone Park, USA and in Iceland. In these locations the zeolite formed depends primarily on the temperature gradient, with clinoptilolite forming in the cooler zones, and chabazite forming in deeper/hotter environments.

Artificial Synthesis

The artificial synthesis of zeolites is inspired by the geological processes which are so effective at producing the huge scope of naturally occurring zeolites. Initially the preparation of zeolites focused on emulating these natural processes and preparing already well-known materials. The first laboratory preparation of a zeolite can be traced back to the claimed synthesis of levynite by St Claire Deville in 1862.^[15]

The origins of the modern day synthesis of artificial zeolites are due to the pioneering work of Richard Barrer and Robert Milton in the late 1940s. Barrer investigated the conversion of sodium silicates and aluminates under hydrothermal conditions in the presence of strong salt solutions at temperatures ranging between 170 – 270 °C, the products of which were zeolites P and Q – isostructural variants which represented the first synthetic zeolites unknown as natural materials at the time.^[16] Milton led the way in using more reactive starting materials, allowing for reactions to take

place under milder conditions which eventually led to the formation of synthetic zeolite Linde type A^[17] (named after the Linde Division of the Union Carbide Corporation, Tonawanda, New York of which Milton was a member). These initial findings catalysed an explosion in artificial zeolites structure research, with over 14 unique structures with no known natural analogues being synthesised before 1953.^[18] Since then the rate of new structures being produced has continued unabated, the majority of them sharing hydrothermal synthesis as a common denominator. Hydrothermal synthesis is usually conducted within a sealed autoclave, where pressure is generated on heating, allowing starting materials to dissolve which wouldn't normally be soluble at room temperature.

The hydrothermal synthesis of a zeolite can be summarised into six main steps: Firstly the reactants are combined into a gel, usually they are in the form of amorphous silica and alumina sources with a cation source and in a high pH medium. This gel is then 'aged' which can aid the formation of large crystals of product. The reaction mixture is then heated in an autoclave. For a period of time after heating, known as an induction period, the reactants remain amorphous. Crystalline zeolite material begins to form in detectable quantities. Over time, the majority of amorphous material is converted into crystalline zeolitic material. Finally the product is then recovered by filtration, washing and drying.

In the case of aluminosilicate zeolite formation, the starting materials are usually in the form of oxides, containing both Al-O and Si-O bonds. Since the crystalline zeolite product (Al-O-Si linkages) contains bond types similar to the reactants, no great enthalpy change occurs and the formation is generally kinetically controlled.^[18]

The mechanism behind the hydrothermal synthesis of zeolites has been the subject of intense debate with several *in situ* systematic studies since the work of Barrer, and generally the accepted view is a combination of the most prominent theories. It would be impossible to detail every hypothesis in the scope of this thesis, but the history of the hydrothermal synthesis of zeolites is comprehensively reviewed by Cundy and Cox.^[18] Instead this thesis will detail the major theories and the currently accepted mechanism of zeolite formation.

It was Barrer who first suggested that the crystallisation of zeolites began with the condensation polymerisation of polyhedral secondary building units, from which the overall zeolite structure formed.^[19] The work of Flanigen and Breck^[20] envisaged similar precursor units, however they theorised that the amorphous aluminosilicate gel was broken down into its constituent tetrahedral monomers by the action of the hydroxide ion. These monomers were then envisaged to nucleate around the cation and form the ordered structure of the zeolite. Angell and Flank^[21] demonstrated that

this mechanism involved the formation of an amorphous aluminosilicate intermediate followed by the subsequent dissolution of these species, with solution transport from the gel to the site of nucleation.

The currently accepted mechanism of aluminosilicate formation is detailed in Fig. 1.5 and can be summarised in the following steps:

- a. *Primary amorphous phase*: refers to the visible amorphous gel often observed on mixing the reactants. It represents the initial product and is commonly colloidal aluminosilicate/precipitated alumina and silica at a non-equilibrium^[18].
 - I. The hydroxide ion converts the reactants and primary products into mobile and reactive species, usually in the form of silicate monomers.
 - II. Induction period: Is the time required for the reaction system to first start to develop crystalline product or precursor.
- b. *Secondary amorphous phase*: During this stage the OH⁻ mediated forming and breaking of tetrahedral monomer T-O-T bonds establish equilibrium between the colloidal gel silicates and aluminosilicates, which in turn lead to localised ordering but no long range organisation.
- c. Nucleation: Where a critical volume of the phase is well ordered enough to form a growth centre from which the crystal lattice can propagate. This stage can undergo subsequent redissolution and reprecipitation depending on reaction conditions. This stage of accumulation is generally controlled by the presence of the cation providing structural organisation^[20].
- d. Crystal growth: Zeolite crystals then grow slowly from the site of nucleation. This step is often classed as the rate determining step, and its speed is controlled by the necessity for the formation of a semi-covalent three dimensional polymer of TO₂.

The mechanisms presented represent an initial starting point for understanding zeolite synthesis, however, there are such a large number of variations in chemical reaction, solubility and equilibria in the gel alone that rationalising the entire process or determining zeolite precursors is very challenging.

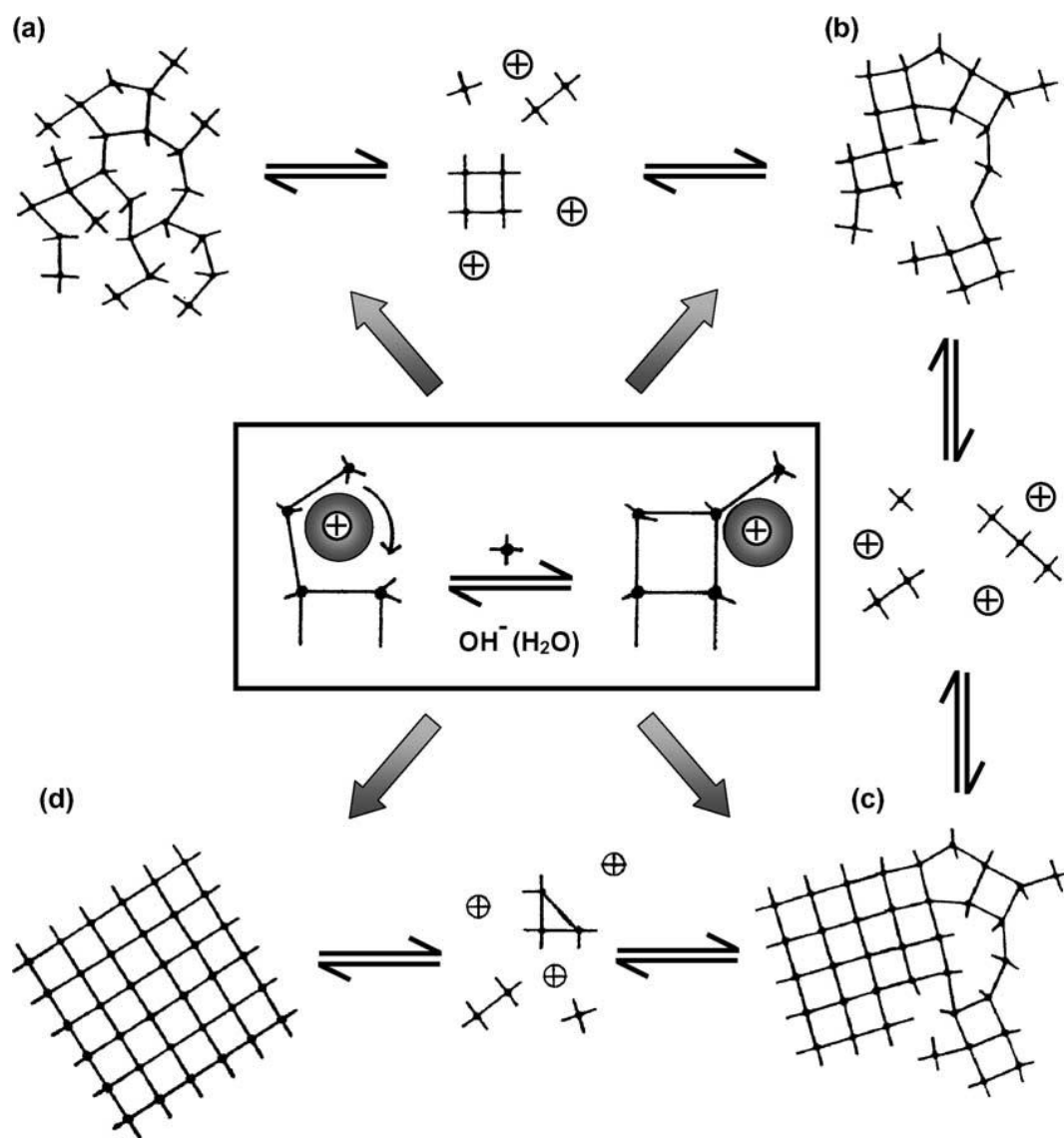


Figure 5: Summary of mechanism for hydrothermal synthesis of zeolites. (a) A domain of amorphous material equilibrates with solution species to form areas of local order (b). (c) The equilibration process leads to a site of periodic ordering i.e. a site of nucleation. From the site of nucleation the crystal grows and amorphous areas dissolve. The insert describes the cations acting as coordination centres for the framework to be constructed around ^[18].

1.4: Applications

The particular structure zeolites possess gives rise to many useful applications, some of which are intrinsic and are shared by most structures, others require further modification as described later (section 1.6). One such intrinsic property is the ability of the zeolite to exchange its M^{n+} charge balancing cations for ones in a surrounding solution. This is possible due to the interaction between the framework and the cation being only a weak electrostatic interaction easily overcome by. For example, the Na^+ form of zeolite A readily exchanges its Na^+ for Ca^{2+} , effectively trapping the divalent atom within its structure. Due to this, zeolite A has been used extensively as a water softener. This process is reversible, the Ca^{2+} form of the zeolite can easily be regenerated by exposing it to a solution containing excess NaCl. This double decomposition is shared with many other materials, such as clays. In clays however, the exchange occurs in inter-lamellar space, whereas zeolites, due to their pore structure are shape selective, thus only certain sized cations can be successfully exchanged, ones with atomic radii larger than the pores cannot be trapped. The ion exchange ability of zeolites hasn't just been used for water softeners; clinoptilolite and zeolite A can also sequester radioactive Cs^+ and Sr^{2+} into their structures. This ability has been used to remove the radioactive ions from nuclear power plant waste, as well as aiding the clean-up operations after the Chernobyl and Three Mile Island incidents. ^[2]

The zeolites open nature and high internal surface area allow the adsorption of large amounts of small molecules. Their affinity for compounds such as water is controlled by the composition of the framework; zeolites containing high amounts of Al within their structure are good at adsorbing polar molecules and thus are hydrophilic. The high Al containing zeolites are used extensively for drying gases and liquids. Highly siliceous zeolites on the other hand are hydrophobic and readily adsorb non-polar and weakly polar molecules. The geometry of the pores also has a large impact on the molecules adsorbed, which can be further fine-tuned by exchange of the cations, as mentioned earlier. In this way, partly Ca^{2+} exchanged zeolite A can be used to separate branched and cyclic hydrocarbons from non-branched alkanes. The alkanes can pass through the structure, whereas the more sterically bulky cyclic molecules cannot.

Zeolites can also be modified to act as both Brønsted and Lewis acids. They can be converted to their Brønsted acid form through the action of ammonium ions and then converted to their Lewis acid form through dehydration [Fig. 6]. The zeolite then can catalyse dehydrations and rearrangements, acting as a strong acid. ^[11]

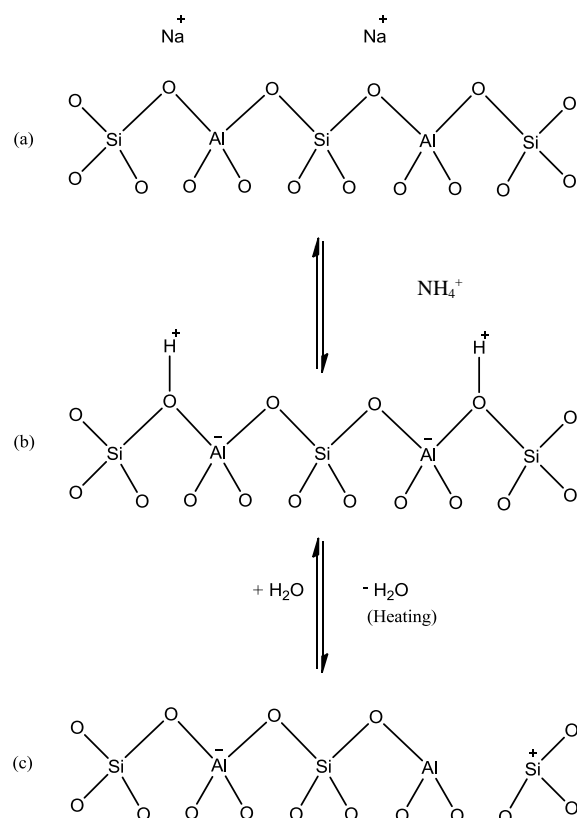


Figure 6:: Brønsted (b) and Lewis (c) site generation in zeolites

Zeolites can also have their cations exchanged with either lanthanide ions or transition metal ions. In the case of the lanthanide exchanged zeolites, the trivalent cation balances the charge on three separate framework Al, causing an electrostatic charge gradient within the cavities. This can polarize or even ionize C-H bonds,^[2] and is a process used extensively in catalytic cracking. The structure itself also has an effect on the catalytic ability of a zeolite, leading to three types of shape-selective catalysis.^[2,11,22]

The first is reactant shape-selective catalysis, where only molecules of the intended size can enter the zeolites structure and react at the catalytic sites, an example of which is the dehydration of butan-1-ol and butan-2-ol over calcium exchanged zeolite A. Linear butan-1-ol passes through the channels and is readily dehydrated, however, butan-2-ol is too sterically hindered to pass through the small apertures of Ca-LTA and so is not reacted. Zeolites can also be shape selective for the products of reactions, which is especially useful where a reaction occurring at the zeolitic catalytic site may have multiple, sterically different, products. An excellent example of product shape selective catalysis is the production of xylene by methanol based alkylation of toluene. The extra methyl group can attach at any position on the aromatic ring, leading to a mixture of *ortho*, *meta* and *para* xylene, however, if the reaction is carried out with ZSM-5, the *ortho* and *meta* xylenes are sterically hindered and diffuse 1000 times slower through ZSM-5's three-dimensional channel system than *para*-xylene.

^[2] Transition state shape-selective catalysis is similar, however rather than multiple products, multiple

transition states lead to different products and it is through selectively promoting the formation of one of those transition states that the desired product can be produced. One example of transition state shape selective catalysis is the transalkylation of dialkylbenzenes, which involves the transfer of alkyl groups. When the reaction progresses it has a diphenylbenzene transition state which can collapse into either the 1,2,4-isomer or the 1,3,5-isomer along with the monoalkylbenzene. The use of mordenite as a catalyst can selectively produce the 1,2,4-isomer as the 1,3,5-isomer is too sterically bulky to fit in the zeolites pores.

Potential future applications include chiral catalysis and hydrogen storage. For chiral catalysis there are two main approaches being researched; either chiral organometallic complexes can be supported within the zeolites' framework, or the structure itself can be enantiomerically pure ^[23]. The occlusion of gases in zeolites is well known, however, it has only been the last decade that their use as sorbents for hydrogen storage has been investigated. In recent studies hydrogen molecules are forced into cavities under high pressure and low temperature and have resulted in determining the maximum hydrogen storage of up to 2.07 wt% ^[24] for zeolite Na-LEV which is closing in on the E.U. target of 6 wt%.

1.5: Modifications to Synthetic Procedure

Structure directing agents

The ultimate goal in the synthesis of zeolite and related structures is the ability to produce corner sharing tetrahedral frameworks with topographies that can be tailored to fit specific applications. To do this, modifications to the synthetic mechanism detailed in section 1.3 are often used. One such modification is the addition of a structure directing agent (SDA).

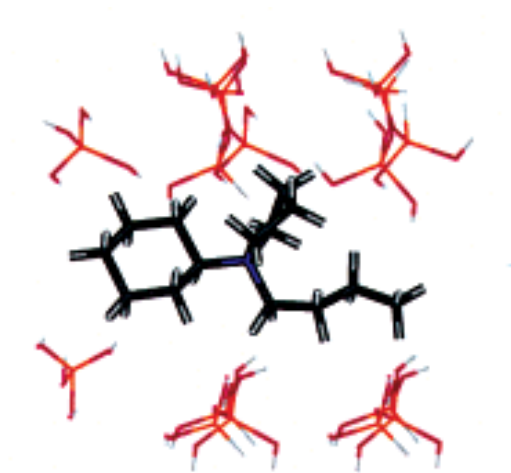


Figure 7: Silicate oligomers surrounding a SDA where they can aggregate which form part of an overall structure^[25]

Organic molecules are often used as structure directing agents, the role of which is described as a template effect^[26] (these are known as organic structure directing agents: OSDAs), alluding to the correlation between the shape of the SDAs and the topography of the product.^[27] The template effect involves the participation of the SDA in the organization of the inorganic tetrahedral units into a particular topology, where they can act as a site of nucleation^[22,25] and provide the building blocks for further crystallisation [Fig. 7]. In ZSM-5 for example there is a clear correlation between the shape of the SDA cation, usually tetrapropylammonium, and the resulting framework.^[28] However, there are some frameworks which can successfully be synthesised using a diverse number of SDAs, this has led to SDAs being classified into three types:^[29] Firstly ‘true templates’, where the template directs the geometry of the frameworks internal structure to match that of the template. The second type are the ‘structure directing agents’ which direct the synthesis to a certain product but do not necessarily have matching internal structure to the template. Finally ‘space fillers’ stabilise the internal structure of the zeolite, but have no structure directing role.

The organic SDA's structure directing ability is optimized by its van der Waals interaction with the TO_4 host framework, therefore a structure is most stable when the shape of the SDA is a close match for the microporous voids.^[32] The structure can be further stabilised through intermolecular hydrogen bonding between electronegative donor atoms on the SDA and acceptor atoms present on the framework. The reverse can also occur when the framework has a high degree of hydroxyl termination. Appropriate criteria of pH control^[33] and hydrophobicity/hydrophilicity of the SDA must also be met through a C/N^+ ratio between 11 and 16,^[32] which can be controlled by the use of specific quaternary ammonium salts and amines.^[25] Literature shows that the steric bulk of the SDA has a direct impact on the host framework, examples being long chain amines and polyamines favouring zeolites having 1-dimensional channels, whereas amines with multiple long branched side chains will stabilise 3-dimensional channel systems.^[30,33] Cyclic amines including hexamethylenamine and 1,4-diazabicyclo[2.2.2]octane are known to yield larger pore sized frameworks such as ZSM-12^[34] and MCM-35^[35].

Organic SDAs are not the only factors influencing the structure of zeolite frameworks. Important variables such as pH, temperature, water content and the presence of alkali-metal cations in the synthesis gel all have a significant impact^[22,32], in some cases having their own structure directing effect, independent of the organic SDA.^[32] As discussed earlier, most zeolite syntheses are carried out under basic conditions to facilitate the solvation of the Al species,^[31] and this is achieved through the presence of alkali-metal cations in the synthesis gel.^[32] The amount of alkali-metal present in the system has a dramatic effect on the crystallisation of a zeolite. A study on zeolite MTW in the presence and absence of alkali metal cations found the addition of sodium cations to the reaction mixture reduced the crystallisation time from 84 days to 7 days.^[35] Higher concentrations of alkali-metal cations have been found to increase the likelihood of layered silicate structures.^[36] Leading to the conclusion that although alkali-metal cations are required throughout the evolution of zeolite crystallisation, excessive amounts will override the structure directing effects of the organic molecules.^[33]

A further chemical variable affecting zeolite synthesis is the presence of a mineralising agent, which can be essential for some structures such as the ITQ-n^[37,38] family. The mineralising agent is a chemical species that increases the solubility of the silicate and aluminate sources. The most common mineralising agent is OH^- , usually in the form of an alkali-metal hydroxides or quaternary ammonium hydroxides. The hydroxyl anion directs the formation of soluble silicate and aluminate anions $[\text{Si}(\text{OH})_{4-n}\text{O}_n]^{n-}$, $[\text{Al}(\text{OH})_4]^-$. Where the OH^- source is alkali-metal hydroxide, the pH of the system is generally greater than 12 and the large amount of cations present facilitates the formation of zeolites with high numbers of aluminium atoms in the framework to charge balance these cations.^[39] If an organic source of OH^- is used then the synthesis is directed towards a more siliceous product since the

sterically bulky organic molecules fill the zeolite void volume, allowing less positive charge in the final solid and so reducing the need for a highly negative framework. The high temperatures and pH classically employed for reactions employing OH^- as a mineraliser obtain high starting material solubility, however, the organic SDAs can suffer thermal degradation. In situations where a lower pH is desirable fluoride anions can be used instead. This is known as the ‘fluoride route’ whereby HF or another suitable fluoride source is added as a nucleation repressing agent ^[40] instead of, or in addition to, the usually present hydroxide solution. It is theorised that the addition of fluoride ions results in the formation of silicon and/or other heteroatom complex fluorides in the solution. Which in turn are hydrolysed more slowly than the original species therefore causing a situation of low supersaturation of so called ‘nutrients’ for crystal growth. Under these conditions nucleation is limited in favour for crystal growth, thus a small quantity of large crystals with a low concentration of connectivity defects are formed. ^[41] An example of such a method is the synthesis of Fe-ZSM-5 zeolite in the presence of various inorganic fluoride salts. ^[42] It was found that although CsF was the most efficient salt for the introduction of Fe^{3+} into the structure, the largest crystals were grown using NaF. It is also acknowledged that besides the several other synthesis parameters, such as the organic template, the amount of alkali-earth metal available and the dilution of the reaction mixture the F^- ion can play a SDA role ^[41].

1.6: Zeotypes

Isomorphic heteroatom substitution at the Si and/or Al sites is another effective way that the zeolite framework can be modified, with elements such as B,^[43] Ga,^[44] Zn,^[45] Cu,^[46] Ti,^[47] P,^[48] Ge^[49] and Zr^[50] being incorporated into the structure.^[11,32] When such modification has occurred, the structure is no longer defined as a zeolite and is instead known as a zeotype. Initially substitutions were aimed at changing the functionality of existing structures, i.e. by replacing trivalent Al positions with divalent Be, leading to an increased negative charge on the framework which can be compensated by the addition of extra cations such as Ca²⁺, Zn²⁺ and Fe²⁺.^[51] Certain heteroatoms however, can influence the synthesis to produce new structural types, a prime example being the isomorphic, isoelectric substitution of Si for Ge.

Aluminophosphates

The aluminophosphates (AlPOs) represent the first, and potentially the most important family of zeotypes and were discovered in 1982.^[52] Since then over 200 open framework aluminophosphates have been characterised.^[53] Through ordered substitution of Al/P for 2Si they can be considered as being derived from pure siliceous zeolites and have a framework composition of AlPO₄. AlPOs show strict adherence to Löwenstein's rule of Al – O – Al linkage avoidance and so structurally differ from zeolites by not being able to exhibit odd numbered rings within their frameworks. Chemically AlPOs have a higher degree of ionic character than zeolites and so can be considered as phosphate ions linked by metal cations to produce an overall neutral framework. The chemical similarities and differences between AlPOs and traditional aluminosilicate zeolites result in the majority of AlPOs being isotypic to zeolite topologies, but also having the potential to produce new topologies unseen in zeolite chemistry: similarly there are some zeolite topologies which are inaccessible to AlPOs. An excellent example is [(C₁₂H₂₈N⁺)(OH⁻)(H₂O)_x][Al₁₂P₁₂O₄₈]- AFI topology or AlPO-5, (Fig. 8).^[54]

AlPO-5 is solvothermally synthesised like a zeolite and exhibits a one-dimensional channel system girdled by a 12R which combined with 6 and 4Rs form a network which is in turn cross-linked via *nsc* (a CBU formed of 6 and 4Rs) type chains. The organic structure directing agent, tripropylammonium hydroxide TPA(OH) is removable by calcination and as such AlPO-5 has applications as absorbents and catalysts. The applications of AlPOs have been the driving force behind their progress with examples including the one step production of niacin^[55] and the hydrogenation of carbon monoxide in the Fischer-Tropsch synthesis.^[56]

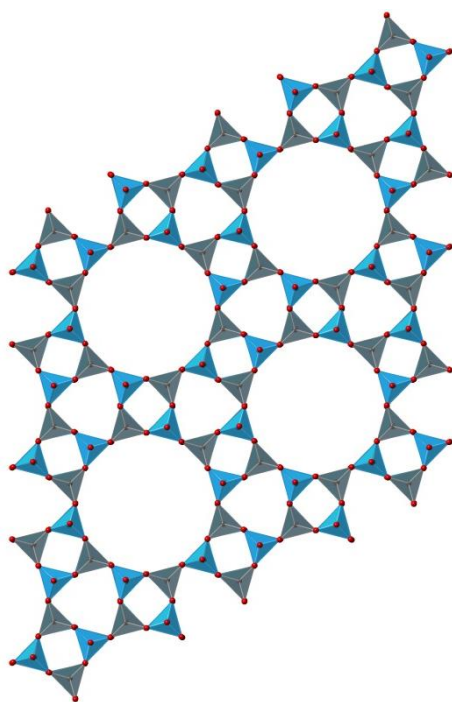


Figure 8: AlPO-5 viewed along *c*, blue and grey tetrahedra are Al/P centred respectively. Red spheres represent O atoms.

Research into non-aluminosilicate frameworks was quickly extended to microporous phosphates and arsenates and produced several gallophosphates,^[57] vanadium phosphates,^[58-61] zinc/beryllophosphates,^[62, 63, 64] and zinc/berylloarsenates. On examination of known arsenates and phosphates with four co-ordinated zeolites topologies, a key pattern becomes apparent. In the T^{+2}/T^{+5} systems such as zincarsenates and zincophosphates both phosphate and arsenate versions of the structure can be made in the presence of alkali metal cations. This does not hold true for the T^{+3}/T^{+5} systems where diverse $AlPO_4$ structures are known^[65] to very few arsenates.^[66] Incorporation of arsenic into three-dimensional microporous structures is interesting as the larger size of the As^{+5} ion (0.335 Å) compared to the P^{+5} (0.170 Å) could create strain in the structure, leading to different bond angles and distances, promoting the formation of new structures.^[67] The size of the As^{+5} ion is also very similar to that of Ge^{+4} and so from a geometric perspective would be expected to form similar structures, however chemically its properties are closer to that of phosphorus. Common starting materials for arsenate or phosphate materials are arsenic acid (H_3AsO_4) and phosphoric acid (H_3PO_4) where phosphoric acid is the stronger acid ($pK_a = 2.148$ compared with H_3AsO_4 , $pK_a = 2.248$) which can impact the reaction mixture pH.

Germanates

Being isoelectronic, silicon and germanium generally present similar properties and reactivity, for example their isostructural Si/Ge-O₂ quartz forms^[19] and elemental bond distances.^[32] In germanate frameworks however, germanium has been known to coordinate up to six times whereas Si based zeotypes are exclusively tetracoordinated. Also, the Ge-O distance is 1.74Å compared to a Si-O distance of 1.60Å^[49] which stabilises certain zeolite topologies and building units such as double four rings (D4R).^[68] This leads to germanium being a key candidate for isomorphous heteroatom substitution of silicon in zeolites due to the potential for the formation of new topologies.

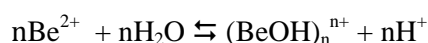
Several known zeolite structures have been produced with Ge substituted Si sites, such as Ge-ZSM-5,^[49] analcime (ANA),^[69] natrolite (NAT),^[70] cancrinite (CAN),^[71] gismondine (GIS),^[70] faujasite (FAU)^[70] and rho (RHO).^[70] The first novel porous silicogermanate was synthesised in 1991^[72] through an aqueous medium with an amine as a SDA, however, this framework proved to be unstable when calcined. Following this a multitude of novel germanium containing structures have been synthesised including the ASU-n (Arizona State University-n) family^[73] which contains four, five and six coordinate Ge atoms as well as frameworks containing all-tetrahedral Ge. Another important silicogermanate family is represented by the ITQ-n^[37,38] series, which presents new topologies which cannot be obtained by germanium-free mixtures owing to their reliance on the smaller angles of the Ge-O-Ge in comparison to the Si-O-Si angle. In contrast, work on beryllium germanates is extremely sparse perhaps owing to the hazards in using beryllium, as such only one structural study has been reported so far and that is the formation of sodalite with a framework composition of BeGeO₄^[74].

1.7: Beryllium

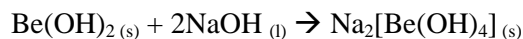
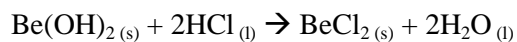
Beryllium is a group two element and as such has an electronic structure of $1s^2 2s^2$ and so its most common oxidation state is $2+$.^[75] In its elemental form, it has a close-packed hexagonal structure and forms a protective oxide layer as seen in aluminium which is an indication of the close chemical similarities of these two elements. The comparative chemistry of Be^{2+} and Al^{3+} is due to their similar charge to radius ratios (z/r), 6.45 and 6.00 respectively, leading to the ionic character (albeit with considerable covalent character) of simple beryllium compounds and substantial polarity of $\text{Be} - \text{X}$ bonds.^[76] Beryllium can accept two extra pairs of electrons to form four sp^3 hybridised covalent (with substantial ionic character) bonds and form a wide range of compounds. Beryllium also shares chemical similarities to zinc, with several naturally occurring materials such as willemite, Zn_2SiO_4 and phenacite, Be_2SiO_4 in existence. This is due to the very similar 1st and 2nd ionisation potentials exhibited by these elements (Be: 1st: 9.320, 2nd: 18.21. Zn: 1st: 9.311, 2nd: 17.89).^[76] Beryllium differs to zinc in its maximum co-ordination number is limited to 6, due to the small size of beryllium and inaccessibility of the 3d orbitals.

Divalent Be is a fairly rare element in the Earth's crust and is found in 110 naturally occurring inorganic compounds in certain locations around the world.^[77] Of these a few fall into the zeolite structure group including: nabasite $\text{Na}_8[\text{Be}_4\text{Si}_{16}\text{O}_{40}] \cdot (\text{H}_2\text{O})_{16}$,^[78] chiavennite $\text{CaMn}(\text{Be}_2\text{Si}_5\text{O}_{13})(\text{OH}_2) \cdot 2(\text{H}_2\text{O})$,^[79] lovdarite $(\text{Na}, \text{K}, \text{Ca})_4(\text{BeAl})_2\text{Si}_6\text{O}_{16} \cdot 4\text{H}_2\text{O}$ ^[80] and roggianite $\text{Ca}_2\text{Be}(\text{OH})_2\text{Al}_2\text{Si}_4\text{O}_{13} \cdot 2.5\text{H}_2\text{O}$.^[81] Divalent beryllium is ideal for isomorphous heteroatom substitution into zeolitic frameworks since its size (0.27 \AA) is comparable to Si^{4+} (0.26 \AA) and many of its compounds involve tetrahedral coordination to oxo-anions.^[82] Substitution of trivalent aluminium by divalent beryllium leads to an overall increase in negative framework charge, which, in turns needs to be balanced with an increased number of cations. This can affect the frameworks ability to ion exchange and also provide higher numbers of Brønsted acid sites for catalysis in the form of increased framework hydroxyl groups. Incorporation of beryllium into reactions can also influence the types of structural features formed, with an increased occurrence of three membered rings which are thought to promote the formation of low density, highly porous structures.^[83]

Beryllium is ideal for incorporation into solvothermal synthesis. Its high z/r polarises surrounding water molecules and the repulsion of the water protons is so great that they are transferred to other water molecules, leaving an OH^- ion bonded to the Be^{2+} ion. This process increases with pH.



In reactions involving beryllium, the source of beryllium is commonly Be(OH)₂ which is a remarkably versatile compound exhibiting amphoterism, where it can react as both acid and base



As such Be(OH)₂ is readily soluble in both acidic and alkali media, with a tendency to form OH bridged polymeric intermediates in acidic conditions, the degree of polymerisation decreases with increasing pH finishing at the Be(OH)₄²⁻ anion in strongly basic solutions. ^[84]

Beryllosilicates

As previously mentioned, beryllium is an ideal candidate for the formation of low density unusual zeolitic structures; it represents the only divalent element present in the framework structure of naturally occurring zeolite-type structures such as [Ca²⁺₄(H₂O)₁₆][Be₁₂P₈O₃₂(OH)₈] which exhibits the WEI ^[85] topology and [K⁺₄Na⁺₁₂(H₂O)₁₈][Be₈Si₂₈O₇₂] – LOV. ^[86] Research into beryllosilicates has historically been very limited with synthetic routes to LOV, ^[87] GIS ^[88] and the novel topologies OSO and OBW ^[89] representing the extent in this field pre-2010. Recently the work of Armstrong and Weller has extended this field, with synthetic routes to the beryllosilicate analogues of GIS, ANA, PHI, MER and NAB, as well as the production of two new topologies; [K_(~14)(N(C₂H₅)₄)_(~2)]₁₆[Si₃₂Be₈O₈₀]•4H₂O (LSJ-10) and K₄[Si₁₂Be₂O₂₈]•5H₂O (LSJ-39).^[90] All the structures reported were formed via hydrothermal synthesis under mild conditions (160 – 220 °C). LSJ-10 exhibits structural features known to be favoured by beryllium incorporation and is formed of networks of 4 and 8Rs cross-linked by spiro-5 rings. The structure is stabilised by extra-framework TEA⁺ and K⁺ cations which interact with the structure through hydrogen bonding and coordination respectively.

Beryllophosphates

After the discovery of the rich structural diversity displayed by the aluminophosphates, investigations into other MPO_4 based structures have been extensive, as mentioned in section 1.6. The beryllophosphates are no exception, despite the potential toxicity barrier. Due to the similarity of ionic radii ($\text{Be}^{2+} = 0.27 \text{ \AA}$ and $\text{P}^{5+} = 0.17 \text{ \AA}$, $\text{Si}^{4+} = 0.26 \text{ \AA}$) and a preference for tetrahedral coordination to anionic species such as O^{2-} the beryllophosphate system is ideal for producing isotypic structures to those usually found as aluminosilicates. A number of fully connected and interrupted three-dimensional structures have been synthesised, many of which exhibit known zeolitic topologies; ABW,^[91,92,93] ANA,^[94] BPH,^[95,96] CAN,^[97] EDI,^[98] CHA,^[99] FAU,^[100,101] GIS,^[93] GME,^[93] LOS,^[102] MER,^[103] RHO,^[104] SOD,^[105,106] and WEI.^[107] The beryllophosphate analogue of MER is archetypal of these structures and of the ease in which aluminosilicate frameworks can be modified by using isomorphous heteroatom substitution to produce topologically similar but chemically different frameworks. BeP-MER was synthesised under mild hydrothermal conditions and crystallises associated with BeP-ABW. The structure of BeP-MER is presented in Fig. 9 and exhibits the characteristic merlinoite topological features of double 8Rs, double crankshaft chains of 4Rs and networks of 4 and 8Rs. The extra-framework voids are occupied by both H_2O and NH_4^+ which stabilise the framework through hydrogen bonding ($\text{O}-(\text{H})-\text{O}$ 2.845 \AA).^[103]

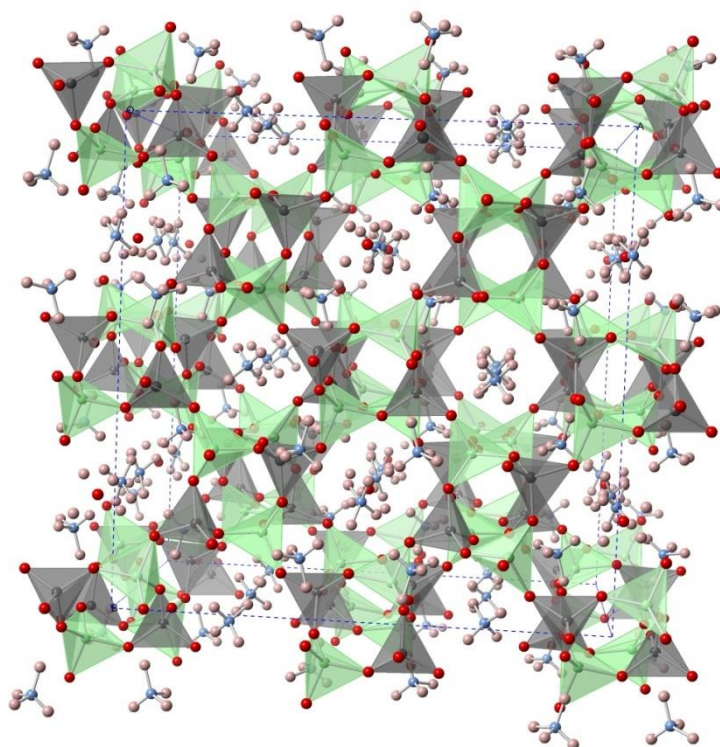


Figure 9: Beryllophosphate analogue of MER type zeolite topology viewed along *c*. Green and grey tetrahedra are Be and P centred respectively, pink, red and blue spheres represent hydrogen, oxygen and nitrogen respectively.

The framework potential of the beryllophosphate system is not just limited to analogues of known zeolites however, through the use of nitrogen-rich organic structure directing agents, novel interrupted frameworks of varying dimensionality have been hydrothermally synthesised. These include the interrupted three-dimensional structure $[\text{H}_3\text{N}(\text{CH}_2)_3\text{NH}_3]\text{Be}_3(\text{HPO}_4)_4$,^[103] and the first examples of beryllophosphates of low dimensionality; The two-dimensional layer structures $[\text{C}_5\text{H}_{14}\text{N}_2]_2[\text{Be}_3(\text{HPO}_4)_5] \bullet \text{H}_2\text{O}$ and $[\text{C}_6\text{H}_{18}\text{N}_2]_{0.5} \cdot [\text{Be}_2(\text{PO}_4)(\text{HPO}_4)\text{OH}] \bullet 0.5\text{H}_2\text{O}$.^[109] These structures all exhibit hydroxyl termination of the P-centred tetrahedra which has leads to their interruption and subsequently their new topologies. The synthesis of these structures emphasise that through the use of OSDAs there is scope for the discovery of new materials in the beryllophosphate system where traditionally the majority of structures are analogues of known aluminosilicates.

Berylloarsenates

There exists very little research into the formation of zeolitic frameworks formed of BeO_4 and AsO_4 primary building units. This is unusual as arsenic is chemically and geometrically similar to phosphorus and germanium and would be expected to form isotopic structures to any beryllophosphates produced. The majority of research carried out was in the 1990s by the Stucky group and only produced low dimensionality phases and analogues of aluminosilicate zeolites; the one-dimensional chain $\text{Be}_2\text{AsO}_4\text{OH} \cdot 4\text{H}_2\text{O}$ which is formed of 3 and 4Rs stabilised by hydrogen bonding.^[109] $\text{Be}(\text{HAsO}_4) \cdot \text{H}_2\text{O}$ exhibits a two-dimensional layered structure^[110] and analogues of the zeolites ABW,^[111] RHO,^[112] SOD,^[111] and UCSB-7.^[113] $\text{Li}_{24}\text{Be}_{24}\text{As}_{24}\text{O}_{96} \cdot 40\text{H}_2\text{O}$ (RHO) were formed under mild sol-gel methods (70 °C) investigated by powder X-ray diffraction and found to exhibit the RHO topology (Fig. 10).

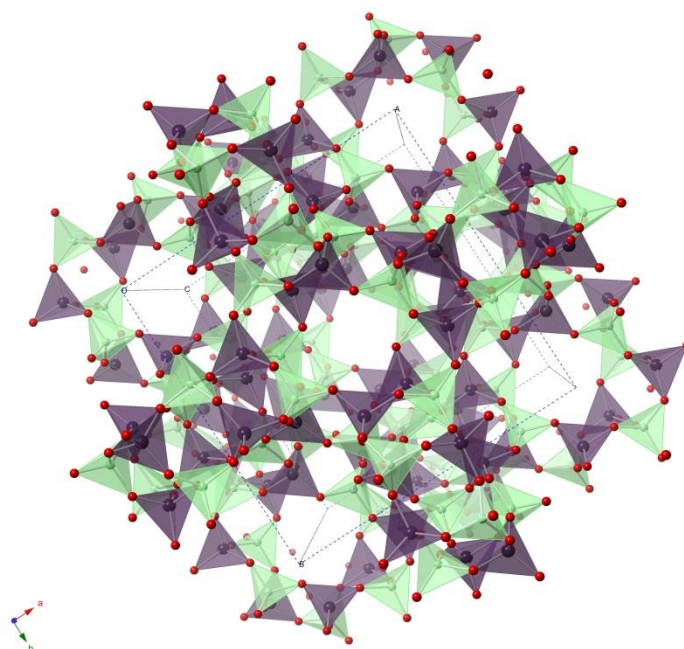


Figure 10: Berylloarsenate analogue of RHO type zeolite topology viewed along *c*. Green and purple tetrahedra are Be and As centred respectively, red spheres represent oxygen. Extra-framework species have been removed for clarity.

The very mild synthetic conditions are something common to the berylloarsenates and are likely due to the increased solubility of the framework elements.^[112] BeAs-RHO is structurally the same as AlSi-RHO, being formed of 8, 6 and 4Rs which in turn connect to produce D8R and *lta* type cages which leads to a three-dimensional channel system. The only differences are a contraction in the structure (BeAs-RHO: unit cell volume 2742.82 Å³, AlSi-RHO: 3320.62 Å³) and elliptical distortion of the rings character which is due to the longer T – O distance and subsequently shorter O – T – O angles.

1.8: Scope of work

The objective of this research is to produce and characterise new zeolite inspired framework materials, with a specific aim of producing new, low density zeolitic topologies based on the 3R secondary building unit. This is achieved by investigating the framework forming potential of a variety of tetrahedral species based on beryllium, phosphorus, arsenic and germanium. The primary method for achieving this objective is the utilisation of a wide variety of organic structure directing agents and other structure influencing factors to produce a comprehensive study into this field and extend the range of structures present in these under-researched areas.

Chapters 3 – 5 present and discuss an extensive range of novel beryllium containing structures of various dimensionalities and structural differences produced in this research, including four entirely new zeolitic topologies. A variety of techniques were employed in the synthesis and characterisation of these materials and they are outlined in chapter 2.

1.9: References

- (1) G. Q. Lu, X. S. Zhao, *Nanoporous Materials: Science and Engineering*, **2004**
- (2) L. E. Smart, E. A. Moore, *Solid State Chemistry, an Introduction*, 3rd edition, **2005**
- (3) L. Zubizarreta, A. Arenillas, J. J. Pis, *International Journal of Hydrogen Energy*, **2009**, 34, 4575 – 4581
- (4) W. L. Brown, *Feldspars and Feldspathoids, Structures, Properties and Occurrences*, **1984**
- (5) A. F. Cronstedt, *Akad. Handl. Stockholm*, **1756**, 18, 120-130
- (6) G. Friedel, *Bull. Soc. Franc. Mineral. Cristallogr.*, **1896**, 19, 94-118
- (7) A. Dyer, *An Introduction to Zeolite molecular Sieves*, **1988**
- (9) W. Loewenstein, *Am. Mineral*, **1954**, 39, 92
- (10) <http://www.iza-structure.org/> (accessed 02/09/12)
- (11) M. T. Weller, *Inorganic Materials Chemistry*, **1994**
- (12) U. Hakanson, L. Falth, *Acta. Crystallogr.*, **1990**, 46, 1363
- (13) T. B. Reed, D. W. Breck, *J. Am. Chem. Soc.*, **1956**, 78, 5972
- (14) L. A. Bursill, E. A. Lodge, J. M. Thomas, A. K. Cheetham, *J. Phys. Chem.*, **1981**, 85, 2409
- (15) H. De St Clarie Deville, *Compt. Rend. Seances Acad. Sci.*, **1862**, 54, 324
- (16) R. M. Barrer, L. Hinds, E. A. White, *J. Chem. Soc.* **1953**, 1466
- (17) R. M. Milton, *US patent 2,882,243*, **1959**
- (18) C. S. Cundy, P. A. Cox, *Micro. and Meso. Mat.*, **2005**, 82, 1 – 78
- (19) R. M. Barrer, J. W. Baynham, F. W. Bultitude, W. M. Meier, *J. Chem. Soc.* **1959**, 195
- (20) E. M. Flanigen, D. W. Breck, *137th Meeting of the ACS, Division of Inorganic Chemistry, Cleveland, OH, April 1960, Abstracts*, 33
- (21) C. L. Angell, W. H. Flank, *Molecular sieves II, ACS sym. Ser.*, **1977**, 40, 194
- (22) H. Bekkum, E. M. Flanigen, J. C. Jansen, *Introduction to zeolite science and practice*, 1st edition, **1991**
- (23) S. I. Zones, M. E. Davis, *Current opinion in Solid State and Materials Science*, **1996**, 1, 107-117
- (24) J. Dong, X. Wang, H. Xu, Q. Zhao, J. Li, *Int. Jnl. Hydrogen Energy*, **2007**, 32, 4998-5004
- (25) G. Sastre, S. Leiva, M. J. Sabater, I. Gimenez, F. Rey, S. Valencia, A. Corma, *J. Phys. Chem. B*, **2003**, 107, 5432-5440
- (26) L. Gomez-Hortiguera, J. Perez-Pariente, F. Cora, C. Richard, A. Catlow, T. Blasco, *J. Phys. Chem. B*, **2005**, 109, 21539-21548
- (27) R. E. Boyett, A. P. Stevens, M. G. Ford, P. A. Cox, *Zeolites*, **1994**, 17, 508
- (28) G. D. Price, J. J. Pluth, J. V. Smith, J. M. Bennett, R. L. Patton, *J. Am. Chem. Soc.*, **1982**, 104, 5971
- (29) M. E. Davis, R. F. Lobo, *Chem. Mater.*, **1992**, 4, 756
- (30) M. Kim, M. Jung, H. Rhee, *Korean J. of Chem. Eng.*, **1995**, 12(4), 410-415
- (31) L. D. Rollmann, J. L. Schlenker, C. L. Kennedy, G. J. Kennedy, D. J. Doren, *J. Phys. Chem. B*, **2000**, 104, 721-726
- (32) G. Sastre, *Phys. Chem. Chem. Phys.*, **2007**, 9, 1052-1058
- (33) R. F. Lobo, S. I. Zones, M. E. Davis, *J. of Inclusion Phenomena and Molecular recognition in Chemistry*, **1995**, 21, 47-78
- (34) M. K. Rubin, *U.S. Patent 5,021,141*, **1991**
- (35) M. K. Rubin, *U.S. Patent 4,981,663*, **1991**
- (36) S. I. Zones, *Microporous Mater*, **1994**, 2, 281
- (37) L. A. Villaescusa, P. A. Barret, M. A. Cambor, *Angew. Chem. Int. Ed. Engl.*, **1999**, 38 (13-14), 1997

- ⁽³⁸⁾ P. Caullet, J. L. Paillaud, A. Simon-Masseron, M. Soulard, J. Patarin, *C. R. Chimie*, **2005**, 8, 245-266
- ⁽³⁹⁾ M. Moliner, *Basic principles of zeolite synthesis*, Zeolites and Ordered Porous Solids: Fundamentals and Applications, Laimprenta CG, **2011**
- ⁽⁴⁰⁾ Z. A. D. Lethbridge, J. J. Williams, R. I. Walton, K. E. Evans, C. W. Smith, *Micro. Meso. Mat.*, **2005**, 79, 339-352
- ⁽⁴¹⁾ S. Qiu, W. Pang, R. Xu, H. Chon, Y. S. Uh (eds), *Progress in Zeolite and Microporous Materials, Proceedings of the 11th IZC, Seoul, Korea*, **1996**, *Studies Surf. Sci. Catal.*, **1997**, 105, 301
- ⁽⁴²⁾ F. Testa, L. Pasqua, F. Crea, R. Aiello, K. Lazar, P. Fejes, P. Lentz, J. B. Nagy, *Micro. Meso. Mat.*, **2003**, 57, 57-72
- ⁽⁴³⁾ G. Coudurier, A. Auroux, J. C. Vedrine, R. D. Farlee, L. Abrams, R. D. Shannon, *Journal of Catalysis*, **1987**, 108(1), 1-14
- ⁽⁴⁴⁾ Y. A. Malinovskii, M. S. Dadashov, E. A. Genkina, *Soviet Physics – Cryst.*, **1991**, 36(3), 313-6
- ⁽⁴⁵⁾ M. A. Cambor, R. F. Lobo, H. Koller, M. E. Davis, *Chemistry of Materials*, **1994**, 6(11), 2193-2199
- ⁽⁴⁶⁾ M. L. de Oliveria, C. M. Silva, R. Moreno-Tost, T. L. Farias, A. Jimenez-Lopez, E. Rodriguez-Castellon, *Applied Catalysis B-environmental*, **2009**, 88, 420-429
- ⁽⁴⁷⁾ V. S. Komarov, L. P. Shirinskaya, N. P. Bokhan, *Zhurnal Fizicheskoi Khimi*, **1976**, 50, 2464-2468
- ⁽⁴⁸⁾ M. L. S. Correa, M. Wallau, U. Schuchardt, *Quimica Nova*, **1996**, 19, 43-50
- ⁽⁴⁹⁾ H. Kosslick, V. A. Tuan, R. Fricke, C. Peuker, W. Pilz, W. Storek, *J. Phys. Chem.*, **1993**, 97, 5678-5684
- ⁽⁵⁰⁾ G. R. Wang, X. Q. Wang, X. S. Wang, S. X. Yu, *Zeolites and Microporous crystals*, **1994**, 83, 67-74
- ⁽⁵¹⁾ J. A. Armstrong, M. T. Weller, *Dalton Trans.*, **2006**, 2998 – 3005
- ⁽⁵²⁾ S. T. Wilson, B. Lok, C. C. Messina, T. R. Cannan, E. M. Flanigen, *J. Am. Chem. Soc.*, **1982**, 104, 1146 – 1147
- ⁽⁵³⁾ J. Yu, R. Xu, *Chem. Soc. Rev.*, **2006**, 35, 593 – 604
- ⁽⁵⁴⁾ J. M. Bennett, J. P. Cohen, E. M. Flanigen, J. J. Pluth, J. V. Smith, *ACS Sym. Ser.*, **1983**, 218, 109 – 118
- ⁽⁵⁵⁾ R. Raja, J. M. Thomas, M. Greenhill-Hooper, S. V. Ley, F. A. Almeida Paz, *Chem. Eur. J.*, **2008**, 14, 2340 – 2348
- ⁽⁵⁶⁾ M. Luisa Cuberio, C. M. López, A. Colmenares, L. Teixeira, M. R. Goldwasser, M. J. Pérez-Zurita, F. Machado, F. González-Jiménez, *Applied Catalysis A*, **1998**, 167, 183 – 193
- ⁽⁵⁷⁾ R. C. L. Mooney-Slater, *Acta. Crystallogr.*, **1966**, 20, 526-534
- ⁽⁵⁸⁾ S. Boudin, A. Guesdon, A. Leclaire, M.-M. Borel, *International Journal of Inorganic Materials*, **2000**, 2, 561-579
- ⁽⁵⁹⁾ Y. Zhou, P. Ming, J. Liu, *Inorg. Chem. Commun.*, **2009**, doi:10.1016/j.inoche.2009.09.028
- ⁽⁶⁰⁾ X. Jing, L. Zhang, S. Gong, G. Li, M. Bi, Q. Huo, Y. Liu, *Micro. Meso. Mat.*, **2008**, 116, 101-107
- ⁽⁶¹⁾ R. Chiang, N. Chuang, *Journal of Solid State Chemistry.*, **2005**, 178, 3040-3045
- ⁽⁶²⁾ X. Bu, T. E. Gier, G. D. Stucky, *Micro. Meso. Mat.*, **1998**, 26, 61-66
- ⁽⁶³⁾ H. Zhang, M. Chen, Z. Shi, X. Bu, Y. Zhou, X. Xu, D. Zhao, *Chem. Mater.*, **2001**, 13, 2042-2048
- ⁽⁶⁴⁾ A. A. Ayi, A. Choudhury, S. Natarajan, S. Neeraj, C. N. R. Rao, *J. Mater. Chem.*, **2001**, 11, 1181-1191
- ⁽⁶⁵⁾ W. M. Meier, D. H. Olson, C. Baerlocher, *Atlas of Zeolite Structure Types*; Elsevier: Amsterdam, 1996
- ⁽⁶⁶⁾ P. Feng, T. Zhang, X. Bu, *J. Am. Chem. Soc.*, **2001**, 123, 86-8-8609

- (67) V. K. Rao, S. Natarajan, *Inorg. Chem. Commun.* **2010**, 13, 163-166
- (68) G. Sastre, A. Pulido, R. Castaeda, A. Corma, *J. Phys. Chem.*, **2004**, 108, 8830-8835
- (69) X. Bu, P. Feng, T. E. Gier, D. Zhao, G. D. Stucky, *J. Am. Chem. Soc.*, **1998**, 120, 13389 – 13397
- (70) G. M. Johnson, A. Tripathi, J. B. Parise, *Chem. Mat.*, **1999**, 11, 10-12
- (71) E. I. Belokoneva, T. G. Uvarova, L. N. Dem'yanets, *Kristallografiya*, **1986**, 31, 874-878
- (72) J. Cheng, R. Xu, *J. Chem. Soc. Chem. Commun.*, **1991**, 1, 483
- (73) H. Li, O. M. Yaghi, *J. Am. Chem. Soc.*, **1998**, 120, 10569
- (74) S. E. Dunn, M. T. Weller, B. D. Rainford, D. T. Adroja, *Inorg. Chem.*, **1997**, 36, 5278-5283
- (75) A. Shayesteh, K. Tereszchuk, P. F. Bernath, R. Colin, *J. Chem. Phys.*, **2003**, 118(3), 1158 – 1161
- (76) D. A. Everest, *The Chemistry of Beryllium*, Elsevier, **1964**
- (77) E. S. Grew, P. H. Ribbe, *Beryllium; Mineralogy, Petrology and Geochemistry*, **2002**
- (78) O. V. Petersen, G. Giester, F. Brandstatter and G. Niedermayr, *Can. Mineral.*, **2002**, 40(1), 173.
- (79) V. Tazzoli, M. C. Domeneghetti, F. Mazzi, E. Cannillo, *Eur. Jnl. of Mineralogy*, **1995**, 7, 1339-1344
- (80) S. Merlino, *Eur. Jnl. of Mineralogy*, **1990**, 2, 809-817
- (81) E. Galli, *International Conference on Zeolites: Proceedings 1980*, **1980**, 205-215
- (82) P. Feng, X. Bu, G. D. Stucky, *Angew. Chem. Int. Ed. Engl.*, **1995**, 34, 1745
- (83) Bu, X.; Gier, T. E.; Stucky, G. D. *Microporous Mesoporous Mater.* **1998**, 26, 61.
- (84) B. T. R. Littlefield, C. Hinde, M. T. Weller, *Dalton Trans.* **2010**, 39, 1 - 3
- (85) F. Walter, *Eur. J. Mineral.*, **1992**, 4, 1275-1283
- (86) Merlino, S. *Eur. J. Miner.* **1990**, 2, 809.
- (87) Grosse-Kunstleve, R.W. Zeolite Structure Determination from Powder Data: Computer-based Incorporation of Crystal Chemical Information. Ph.D. Thesis, Swiss Federal Institute of Technology: Zurich, 1996; p90.
- (88) Ueda, S.; Koizumi, M. *Nature* **1972**, 238, 139.
- (89) Cheetham, T.; Fjellvåg, H.; Gier, T. E.; Kongshaug, K. O.; Lillerud, K. P.; Stucky, G. D. *Stud. Surf. Sci. Catal.* **2001**, 135, 788.
- (90) J. A. Armstrong, M. T. Weller, *J. Am. Chem. Soc.*, **2010**, 132, 15679 - 15686
- (91) Robl, C.; Gobner, V. *J. Chem. Soc., Dalton Trans.* **1993**, 1911.
- (92) Gier, T. E.; Stucky, G. D. *Nature* **1991**, 349, 508.
- (93) Zhang, H.; Chen, M. *Chem. Mater.* **2001**, 13, 2042.
- (94) Zhang, H.; Chen, Z. *Microporous Mesoporous Mater.* **2003**, 57, 309.
- (95) Harvey, G.; Baerlocher, C. H.; Wroblewski, T. *Z. Kristallogr.* **1992**, 201, 113.
- (96) Harvey, G. *Z. Kristallogr.* **1988**, 182, 123.
- (97) Peacor, D. R.; Rouse, R. C.; Ahn, J. H. *Am. Mineral.* **1987**, 72, 816.
- (98) Harvey, G.; Meier, W. M. In *Zeolites: Facts, Figures, Future*: Jacobs, P. A., van Santen, R. A., Eds.; Elsevier: Amsterdam, 1989; p 411.
- (99) Zhang, H.; Weng, L.; Zhou, Y.; Chen, Z.; Sun, J.; Zhao, D. *J. Mater.*

Chem. **2002**, *12*, 658.

⁽¹⁰⁰⁾ Harrison, W. T. A.; Gier, T. E.; Moran, K. L.; Nicol, J. M.; Eckert, H.; Stucky, G. D. *Chem. Mater.* **1991**, *3*, 27.

⁽¹⁰¹⁾ Gier, T. E.; Stucky, G. D. *Zeolites* **1992**, *12*, 770.

⁽¹⁰²⁾ Harrison, W. T. A.; Gier, T. E.; Stucky, G. D. *Zeolites* **1993**, *13*, 242.

⁽¹⁰³⁾ Harrison, W. T. A. *Acta Crystallogr.* **2001**, *C57*, 891.

⁽¹⁰⁴⁾ Harvey, G.; Meier, W. M. *Stud. Surf. Sci. Catal.* **1989**, *49*, 411.

⁽¹⁰⁵⁾ Harrison, W. T. A.; Gier, T. E.; Stucky, G. D. *Acta Crystallogr.* **1994**, *C50*, 471.

⁽¹⁰⁶⁾ Gier, T. E.; Harrison, W. T. A.; Stucky, G. D. *Angew. Chem., Int. Ed. Engl.* **1991**, *30*, 1169.

⁽¹⁰⁷⁾ Walter, F. *Eur. J. Mineral.* **1992**, *4*, 1275.

⁽¹⁰⁸⁾ M. Guo, J. Yu, J. Li, Y. Li, R. Xu, *Inorg. Chem.*, **2006**, *45*, 3281 – 3286

⁽¹⁰⁹⁾ W. T. A. Harrison, T. M. Nenoff, T. E. Gier, G. D. Stucky, *Inorg. Chem.*, **1993**, *32*, 2437 – 2441

⁽¹¹⁰⁾ T. E. Gier, X. Bu, G. D. Stucky, W. T. A. Harrison, *J. Solid State Chem.*, **1999**, *146*, 394 – 398

⁽¹¹¹⁾ T. E. Gier, G. D. Stucky, *Nature*, **1991**, *349*, 508

⁽¹¹²⁾ T. Gier, W. T. A. Harrison, G. D. Stucky, *Angew. Chem. Int. Ed. Engl.* **1991**, *30*, 1169

⁽¹¹³⁾ T. E. Gier, X. Bu, P. Feng, G. D. Stucky, *Nature*, **1998**, *395*, 154 - 157

Chapter 2

Characterisation and Experimental methods

Work reported in this thesis describes the preparation and characterisation of potentially new zeotype materials, primarily produced by solvothermal synthesis. Each reaction undertaken has its reagents individually calculated and added in a specific sequence, usually: beryllium source, solvent, other T atom source, metal hydroxide/organic template and finally any mineraliser. Once all the reagents are added they usually form a 'sol' (see section 2.1 for sol-gel methods) before being aged. The 'gel' is then reacted solvothermally (section 2.1.1) for a period of time ranging between 12 h. – 20 days at temperatures between 100 – 220 °C. The solid product is then filtered, washed with deionised water and a suitable organic solvent (to dissolve any left-over organic template) and dried in a convection oven for 12 h. at 70 °C.

The product is inspected under a polarising optical microscope for crystals of suitable size and quality for analysis by single crystal X-ray diffraction (SXD, section 2.2.3). If a dataset of sufficient quality is produced and it appears novel, then the identity is elucidated by mathematical means. If no large crystals are forthcoming the sample is studied by powder X-ray diffraction (PXD, section 2.2.5) in an attempt to identify the phases present from comparison with databases.

Several further characterisation techniques have been used to further support the conclusions from X-ray diffraction. These include;

- Powder neutron diffraction (PND, section 2.2.8) has been carried out on some of the structures presented here to aid in hydrogen position elucidation or in one case observe the *in situ* dehydration of a mineral.
- Scanning Electron Microscopy and Energy Dispersive X-ray Analysis (SEM, EDAX, section 2.2.9), which provides information on the morphology and atomic composition respectively.
- Thermogravimetric analysis (TGA, section 2.2.10) provides valuable information on the thermal stability and extra framework species within structures.
- Magic Angle Spinning Nuclear Magnetic Resonance (MASNMR, section 2.2.11) has been carried out on structures to confirm beryllium environments.
- Bond valence calculations (section 2.3.1) have been used to assist the solution of structures and confirm the structural formulae presented.

2.1: Synthesis methods

There are a variety of different preparative methods available to the inorganic chemist in the development of new materials. These include ceramic or solid state methods, sol-gel methods and solvothermal synthesis. The chief method of preparation utilised in this research is solvothermal synthesis which is discussed in detail in section 2.1.1, however a brief overview of the solid state and sol gel methods is also provided.

The solid state method was used to prepare non-commercially available starting materials used in synthesis and involved the mixing of stoichiometric amounts of reagents before heating at high temperatures under air or an inert gas flow. The reagents must be a homogeneous mixture of small particles since the absence of solvent confers low mobility, therefore the reaction mixture must be well ground before being transferred to an oven. High temperatures are generally required for the synthesis, in the region of 500 – 2000 °C since the lattice energy of the reagents is typically very high and requires a large amount of thermal energy to overcome it for a reaction to occur. A major disadvantage of this process is its tendency to produce materials of low purity and therefore several cycles of the reaction must be carried out before phase purity is achieved. The products of solid state synthesis are often polycrystalline which limits structural analysis to powder diffraction, making the elucidation of new structures very challenging.

The sol-gel method, although not intentionally utilised within this research, is important as there is several parallels with the initial stages of the solvothermal synthesis method. The sol-gel method involves the preparation of a concentrated solution or colloidal suspension of the reagents used (the sol) which is then matured by low heating or aging to form a homogenous mixture (the gel). The gel is then calcined to form the final, polymeric solid product.

In this research before the reagents were transferred to the reaction vessel for solvothermal synthesis, they were first mixed into a concentrated solution/colloidal suspension depending on their solubility in the solvent. The mixture would then be gently stirred while being aged for approximately one hour to ensure homogeneity before progressing to the next stage of the reaction. This aids the reactivity of the mixture and the phase purity of the final product.

2.1.1 Solvothermal synthesis

All of the new materials produced in this research were formed using solvothermal techniques, which is the process of adding reagents and an appropriate solvent to a reaction vessel which is heated to around the boiling point of the solution. The reaction vessel is sealed and as such the expansion of the solvent generates pressure within the vessel. Generally the vessel is constructed of high-pressurewithstanding stainless steel, and has a chemically inert liner to the reagents used, such as gold, platinum or Teflon®. All reactions detailed within this research were carried out in 23 mL capacity Parr Teflon-lined steel general purpose autoclaves which have a maximum operating temperature of 523 K and can withstand autogeneous pressures of 8000 kPa. Specialist equipment is available that operates at higher temperatures and pressures; however these extreme conditions were not required in this research.

The autoclave is heated in a convection oven and as the vapour pressure increases this leads to an increase of pressure, which in the case of water causes it to remain liquid above its boiling point. When water is super-heated it exhibits greatly increased solvation ability, this combined with a drop in density has dramatic effects on reagents normally insoluble in water. Generally when the solvent used is either water or an aqueous solution it is known as hydrothermal synthesis and is the most commonly encountered form of solvothermal synthesis. If the reagents are still insoluble in super-heated water alkali or metal salts can be added to form water soluble complexes with the starting materials. Other solvents such as ethanol, pyridine and DMF are also routinely used, however, it is important to calculate the potential pressure build up from expansion or evolved gases to ensure the reaction remains within operational limits.

Solvothermal synthesis offers several advantages over classical inorganic techniques. Since all the reagents are in solution, there is increased mobility and thus reactivity at low temperatures in comparison to the solid state where high temperatures are required to enable ion mobility. Solvothermally produced materials tend to crystallise as large crystals (0.01 – 1 mm), suitable for single crystal analysis, whereas solid state reactions produce often mixed phases of polycrystalline material, making structure elucidation more challenging. Of particular relevance to this research is the ability of solvothermal synthesis to form metastable kinetic products, such as microporous materials, instead of the thermodynamic products favoured by the solid state. Another system which benefits from solvothermal synthesis is the study of metal oxides where they encounter solubility issues in water at atmospheric pressure but dissolve in super-heated water.

The major disadvantage of solvothermal synthesis is its closed ‘black box’ nature, many factors can influence the synthesis: Time, temperature, pH, state/concentration/quantity of starting

materials, type/amount of solvent (and, therefore, pressure), cooling time, temperature gradient within the vessel, addition of mineraliser and homogeneity of the starting mixture all might play significant roles in the synthesis. Since it is very difficult to observe *in situ* the reaction mechanisms, the role each factor plays can only be theorised upon. Small changes in conditions can lead to different products therefore solvothermal experiments rely on an iterative process.

2.1.2 Toxicity of beryllium

Beryllium in its common powdered hydroxide and oxide form can easily be airborne, due to their low densities, through disturbance and subsequently be inhaled. This inhalation of beryllium is the known cause of two pulmonary syndromes, acute chemical pneumonitis and chronic beryllium disease. ^[1] The current occupational exposure limit $0.2 \mu\text{g}/\text{m}^3$ ^[2] and therefore, several preventative measures must be undertaken to minimise exposure: all measuring out of the starting material ($\text{Be}(\text{OH})_2$) was undertaken inside a glove box, where the material is transferred to a closed Teflon liner. The rest of the reagents were then added to the Teflon liner within a fume hood, whilst always wearing a dust mask. For the majority of the reaction the reagents are within a sealed autoclave, and so chance of exposure was limited. Final products were envisaged to be less easily airborne as in solution or trapped within a framework, however, precautions such as wearing of dust mask and use of fume hoods was continued. Samples are stored in labelled sample vials, clearly describing their composition, all waste is stored pending professional disposal.

2.2: Characterisation methods

2.2.1 Diffraction of X-rays (theory)

Crystalline solids consist of repeating arrays of unit cells with interatomic spacing of around 1 Å. They generally fall into one of fourteen possible Bravais lattices, summarised in Table 1.

Table 1: The 14 Bravais lattices and relative associated dimensions and crystal systems

Unit cell dimensions	Crystal system	Bravais lattice centring
$a=b=c, \alpha=\beta=\gamma$	Cubic	P, I, F
$a=b \neq c, \alpha=\beta=\gamma=90^\circ$	Tetragonal	P, I
$a \neq b \neq c, \alpha=\beta=\gamma=90^\circ$	Orthorhombic	P, C, I, F
$a \neq b \neq c, \alpha=\gamma=90^\circ \beta \neq 90^\circ$	Monoclinic	P, C
$a \neq b \neq c, \alpha \neq \beta \neq \gamma \neq 90^\circ$	Triclinic	P
$a=b \neq c, \alpha=\beta=90^\circ \gamma=120^\circ$	Hexagonal	P
$a=b=c, \alpha=\beta=\gamma \neq 90^\circ$	Trigonal/Rhombohedral	P

This regular arrangement of atoms allows crystals to act as three dimensional diffraction gratings. Diffraction patterns can be produced from both single crystals of sufficient quality and polycrystalline ‘powder’ samples. However, for diffraction to take place, the incoming electromagnetic radiation needs to be of a suitable wavelength. The $K_{\alpha 1}$ X-ray emission from a Cu target has a wavelength of 1.5406 Å, since this is comparable to the interatomic distances in many crystalline compounds, constructive and destructive interference between X-rays scattered from these atomic electron densities can arise. This leads to the observation of only constructively interfering X-rays being reflected from the crystal, therefore leading to maxima of intensity. This diffraction can be conveniently explained through Bragg reflection [Fig. 1].

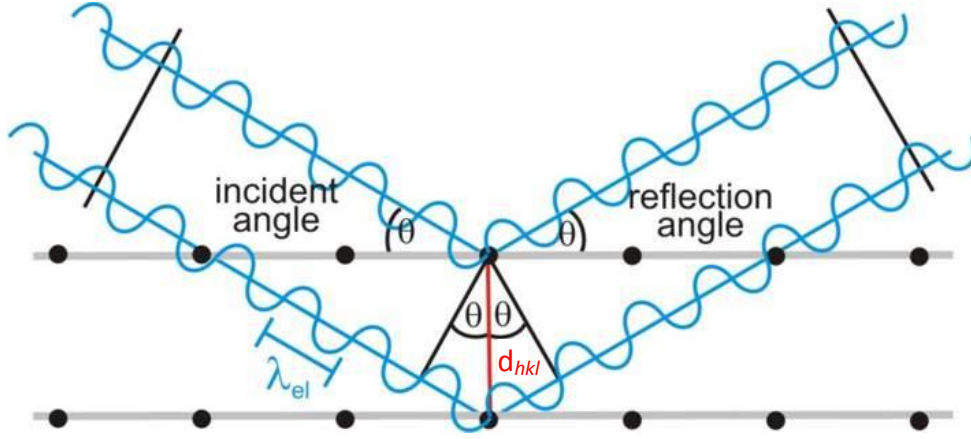


Figure 1: Diffraction of X-rays off lattice planes^[3]

The repeating black spots represent lattice points which sit on planes defined by the Miller indices hkl with an interplanar spacing of d_{hkl} . The notation hkl refers to the reciprocal of the intercept of the plane upon the cell axis. A beam of monochromatic X-rays (λ) of wavelength λ is incident to the crystal planes at an angle θ_{hkl} . For constructive interference to occur, and thus an observable reflected X-ray, the difference in path length must be equal to an integral number, n , of wavelengths. The path difference can be calculated using the equation:

$$\text{difference in path length} = 2d_{hkl}\sin\theta_{hkl} \quad (1)$$

When this is equal to an integer number, n , wavelengths, it gives the Bragg equation:

$$n\lambda = 2d_{hkl}\sin\theta_{hkl} \quad (2)$$

This equation relates the spacing of the crystal planes to the angle at which reflections from these planes are observed (also known as the Bragg angle). When combined with expressions for the d-spacings of the individual crystal systems and indexed Miller indices the relationship between the angle of diffraction and lattice parameter can be elucidated.

For a cubic crystal system the expression for d_{hkl} can be written with respect to lattice parameter (a) and Miller indices (hkl) as:

$$1/d^2 = (h^2 + k^2 + l^2)/a^2 \quad (3)$$

This can be rearranged to give:

$$d = a/\sqrt{(h^2 + k^2 + l^2)} \quad (4)$$

When combined with the Bragg equation and rearranged, this gives:

$$\sin^2\theta = (\lambda^2/4a^2) (h^2 + k^2 + l^2) \quad (5)$$

Which, when combined with indexed hkl values, can be used to calculate the crystal lattice parameter a .

This simple way of looking at crystal structures holds true if you do not consider symmetry, however, the vast majority of crystalline structures have congruent lattice point/atom positions related by symmetry operators. Therefore as well as the fourteen Bravais lattices, there are 32 point groups related to different possible additional translational and rotation symmetries. Each point group is comprised of various operators such as rotations or inversions. The combination of the 32 point groups and 14 Bravais lattices leads to 73 possible symmorphic space groups. Consideration of translations, i.e. replacing mirror planes with glide planes and rotation axes with screw axes, the number of unique space groups jumps to 230.

The space group is defined as ‘a set of geometrical symmetry operations that map a three-dimensional periodic object onto itself’^[4] and is represented by the Hermann-Mauguin notation, for example: $P4_2/nbc$. The P denotes a primitive cell with atoms related by a fourfold sub 2 screw axis along z with a perpendicular diagonal glide plane (n), an axial glide plane b normal to x and an axial glide plane c normal to the $[110]$ plane.

Diffraction should be visible from each lattice plane in the crystal structure, however, the type of Bravais lattice and various symmetry elements within the crystal can cause systematic absences, which become apparent when indexing observed reflections using Miller indices. These absences commonly arise from face or body centring of the lattice, where the scattering from the centred atom is out of phase with the other lattice atoms, causing destructive interference. Various translational symmetry elements can also lead to systematic absences, and by inspection it is possible to characterise the type of Bravais lattice present.

The combination of systematic absences and the ability to elucidate cell measurements from indexed reflection data goes some way towards allowing the solution of a structure. However, to interpret all but the simplest of structures more data is generally required and although it is possible to

solve new structures from only powder diffraction data, issues such as peak overlap can cause complications. To solve a structure from single crystal diffraction dataset is also complicated but the larger range of information available from a standard experiment makes the task more feasible. The exact range of data required from a single crystal is determined by the size and symmetry relationships of the asymmetric unit in relation to the unit cell. Where there is a small asymmetric unit which undergoes several symmetry operations to produce the unit cell, such as in a cubic crystal system, a small range of data needs to be collected. Whereas a low symmetry system such as monoclinic, where the asymmetric unit may be half of the unit cell, would require a much larger range of data before the structure could be solved. This is represented graphically by Ewalds' sphere of reflection (Fig. 2).

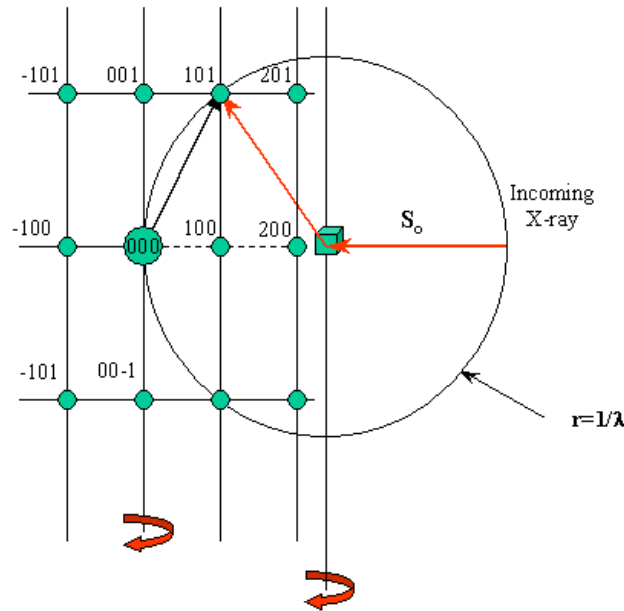


Figure 2: Ewald sphere of diffraction ^[5]

The single crystal is situated in the centre of a sphere of radius $1/\lambda$ (Å), the X-ray beam bisecting the sphere at the horizontal (OI) is attributed the lattice point (000). Diffracted X-rays are observed along a reciprocal lattice parallel to OP where the relationship in equation 7 is observed.

$$OP = r_H^* = 1/d_H = IO \sin\theta = 2 \sin\theta/\lambda \quad (7)$$

Where r_H^* represents the reciprocal lattice vector, the values produced for a^r , b^r and c^r correspond to $1/a$, $1/b$ respectively.

2.2.2 Generation of X-rays

X-rays are generated when a heated metal filament emits electrons which are then accelerated via a high potential difference and strike a water-cooled metal anode. This causes the ejection of an electron from a core orbital of the target anode, which is filled by electron decay from a higher orbital, generating X- radiation. This radiation (X-rays) is emitted in a variety of wavelengths, with a large broad background from the bremsstrahlung radiation, and intense closely-spaced doublet maxima corresponding to the electron transitions. The metal target's identity determines the wavelength of the maxima, with Cu K_α at $\lambda = 1.54 \text{ \AA}$. Generally there are multiple maxima due to the electron decay from, in case of Cu, the 2p or 3p levels, K_α and K_β respectively. The unwanted maxima can either be removed by use of a metal filter close in atomic number to the X-ray source, which has a high absorption coefficient, or by use of a single crystal monochromator, which takes advantage of Bragg's law [Eqn. 2] to provide X-rays of a single wavelength.

2.2.3 Single crystal X-ray diffraction (SXD)

SXD is an extremely powerful technique for solving crystal structures. If the crystal being measured is of sufficient quality with atoms with high enough electron density, the position and intensity of the hkl reflections can be measured accurately, leading to the quick determination of the unit cell dimensions, space group and atomic coordinates and subsequently a structural determination.

Data collection is carried out when the monochromatic X-ray beam scatters off regularly spaced atoms within a crystal to be detected as peaks of intensity, 'spots', by a scintillation counter or charge coupled device [Fig. 3] combined with the angle θ which the peak occurs at. The intensity of the peak is partly dependant on the electron density of an atom, thus the scattering length is proportional to the atomic number.

The intensity observed is a combination of the scattering factor due to the electron density of the atoms and the effect of multiple planes. The electron density itself is related to the diffraction pattern by reverse Fourier transformation shown in the equation below:

$$p(xyz) = 1/V \sum_{hkl} |F(hkl)| \cdot \exp[i\Phi(hkl)] \cdot \exp[-2\pi i(hx + ky + lz)] \quad (8)$$

Where $p(xyz)$ refers to the electron density, $1/V$ allows for the correct units, \sum_{hkl} is the summation of the three dimensional diffraction of the X-ray, $F(hkl)$ is known as the structure factor and denotes the amplitude of the waves, with $\exp[i\Phi(hkl)]$ denoting the phase relative to the incident beam and $\exp[-$

$2\pi i(hx + ky + lz)]$ describing an extra phase shift relative to the origin. However, as it is, the Fourier transform cannot be calculated, since a measured diffraction pattern only provides the amplitude, not the phases. This is known as the ‘phase problem’.

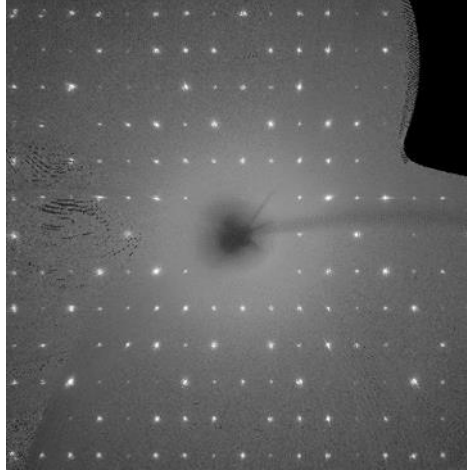


Figure 3: An example of SXD intensity peaks from an area detector

This problem can be solved in the structure analysis by using methods embedded within the WinGX suite of programs ^[6] including XPREP ^[7] and SHELX-97. ^[8] This involves the use of either the Patterson function or direct methods to produce an initial partial structural model before the model can be refined until a good agreement with the predicated diffraction data is achieved. The Patterson function uses vectors (u) to produce a Patterson map, peak intensity is the contribution of both original structure ($p(r_j)$) and product of the vector between atoms $p(r_j+u)$ summed where $p(r_j+u) \neq 0$. Higher weight is attributed to areas of higher electron density, and so the most obvious peaks present in the Patterson map would be those from the heaviest elements present in the structure. The presence of heavier elements simplifies the solution; the peaks due to the vectors between these heavy atoms will be the most obvious, which allows the derivation of positional data. If the atoms located represent a sufficiently high proportion of the structures electron density a working structure factor ($|F_h^c|$) can be produced where it can be assumed that the phase (Φ_h^c) is a good approximation of the true phase. Φ_h^c can then be combined with the experimental amplitude to produce an electron density map, from which the lighter atoms positions can be elucidated and an approximate model produced.

Since the majority of materials produced in this research are formed of elements with similar numbers of electrons, solving by direct methods is therefore more appropriate. Direct methods are a trial and error based iterative process which attempts to derive the structure factor by relating the phase and amplitude of a wave. The structure factor is given by the equation:

$$F_h = \sum_{j=1}^N f_j(|h|) \exp(2\pi i h \cdot r_j) = |F_h| \exp[i\phi_h] \quad (9)$$

Where r_j is the position vector of atom j , which is referred to as the unit cell origin and ϕ_h is the phase of the structure factor corresponding to the diffraction vector, h . The phase of the structure factor depends on the position of the defined unit cell origin. In direct methods the origin is defined via an iterative process based on the symmetry operators from the inputted space group. The phase is then determined by the Sayre equation, the derivation of which relies on two assumptions: Firstly the atoms present in the unit cell are exactly the same, have spherical symmetry and identical isotropic displacement parameters. This is roughly satisfied when atoms present have similar electron density. Secondly a hypothetical structure is considered where the electron density is squared at every point, the positions of maxima will be same as the real structure. The scattering factors are therefore equal and so the structure factor is written as:

$$F_h = f \sum_{j=1}^N \exp(2\pi i h \cdot r_j) \quad (10)$$

Where f is the common scattering factor. The structure factor for the squared structure is defined in the same manner and the relationship between the two allows for the phase to be worked out via the tangent formula and probabilistic means. Once the most plausible phase set is elucidated, it is used to work out an electron density map and from that an approximate model. Once an approximate model has been produced by either Patterson or direct methods, the parameters are then refined by the Least squares method to find all the other atomic positions and to make their positional, occupancy and thermal parameters as close as possible to the experimental result.

By combining the approximate model with the forward Fourier transform equation:

$$F(hkl) = \int_{\text{cell}} p(xyz) \cdot \exp[2\pi i(hx + ky + lz)] dV \quad (11)$$

A comparison between the calculated structure factor (F_c) and the observed structure factor (F_o) can be made. If the model's atoms are in approximately the right positions, the values will be comparable, assessed by the agreement index (R-index) defined as:

$$R = \sum [|F_o| - |F_c|] / \sum |F_o| \quad (12)$$

Which is a measure of the level of agreement between the two structural factors. The refinement is generally assumed to be correct if it has an R-index of around 0.02-0.07.

The agreement index does not take into account the different strengths of reflection and for this reason the 'weighted' R-index is often used:

$$wR2 = [\sum w(F_o^2 - F_c^2)^2 / \sum w(F_o^2)^2]^{1/2} \quad (13)$$

Where w denotes the weight attributed to each reflection. Another method of determining agreement is the goodness of fit (GofF), which is also very relevant to powder diffraction data:

$$\text{GofF} = S = [\sum w(F_o^2 - F_c^2)^2 / n - p]^{1/2} \quad (14)$$

Where n is the number of reflections and p is the total number of parameters refined.

2.2.4 SXD instrumentation

The majority of structural information in this work was collected using a Bruker-Nonius Kappa CCD diffractometer (MoK $_{\alpha}$ radiation, $\lambda = 0.71703 \text{ \AA}$) fitted with an area detector and running at low temperature (120 K) [Fig. 2.4]. The crystal was mounted onto a glass fibre and oriented into the X-ray path using a goniometer. Initially a unit cell was determined by a quick eight image phi/chi scan, then if the crystal is of interest, a full data collection was initiated, the time of which varies depending on the symmetry, size and quality of the crystal.



Figure 4: Image of one of two single crystal diffractometers used in this work, CCD area detector is visible on left, goniometer centre, with cyrostream, microscope and x-ray source from left to right

Datasets collected in the later part of this research instead utilised a Rigaku AFC12 diffractometer (MoK $_{\alpha}$ radiation, $\lambda = 0.71703 \text{ \AA}$) fitted with a Rigaku HG Saturn724+ area detector and running at low temperature (100 K).

2.2.5 Powder X-ray diffraction (PXD) instrumentation

If a single crystal of sufficient quality was not obtained, the sample was ground to avoid preferred orientation of the material and a data set collected over a range of $\sim 5 - 110 2\theta$. The room temperature data in this report were collected using a Siemens D5000 diffractometer, using a Cu anode running at 40 mA and 40 kV. When combined with a Ge crystal primary monochromator provides a fixed wavelength of Cu K $_{\alpha}$ ($\lambda = 1.5406 \text{ \AA}$). The emitted radiation was then collimated by a 2 mm pre-slit before hitting the sample, normally held in flat plate orientation on a plastic or aluminium sample holder. The diffracted X-rays then passed through a 2 mm post sample slit and a 0.2 mm detector slit before being collected by a scintillation detector which was set to rotate at twice the rate of the sample stage, maintaining a fixed $\theta/2\theta$ relationship [Fig. 5]. Sample times varied between quick (~ 45 minute) and ~ 12 hour collections, the former providing enough data to determine crystallinity and phase purity by inspection, the latter providing data for further analysis through Rietveld ^[9] refinement using the GSAS ^[10] suite of programs and the EXPGUI user interface ^[11]. Quick collections could usually be easily identified against the JCPDS database using the DIFFRAC-plus Evaluation package.

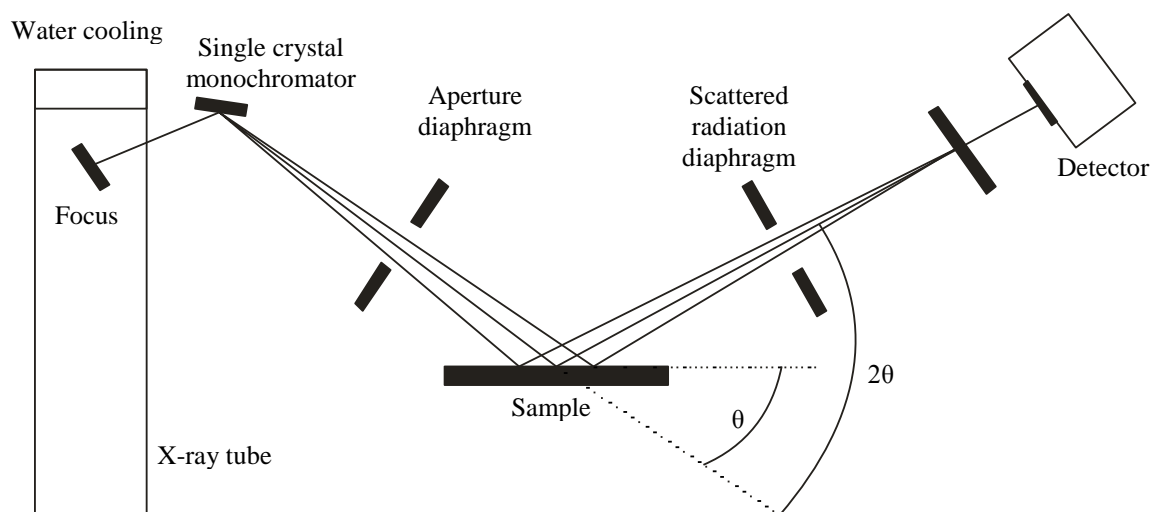


Figure 5: Set up of the D5000 PXD instrument used in this work

2.2.6 Variable Temperature Powder X-ray Diffraction

Samples of sufficient purity were further analysed using a Bruker D8 powder X-ray diffractometer set up with an Anton Parr HTK-1200 high temperature furnace (RT – 1200 °C). The mechanics of this instrument are fundamentally the same as for the D5000, however, the addition of the furnace allows for *in-situ* temperature studies to be carried out, providing useful data on the stability and possible phase changes of materials. To avoid oxidation or damage to the instrument all experiments of this nature are carried out under an inert atmosphere such as flowing nitrogen or argon.

2.2.7 PXD data treatment

Unlike SXD data, PXD data is not usually used for structure determination owing to the high degree of peak overlap, instead it is highly effective for the identification of known phases through characteristic peaks or for the refinement of structures under the influence of temperature or pressure. For an experiment to succeed, data of sufficient quality needs to be coupled with a good trial model, usually in the form of a crystallographic information file. The ultimate goal of the method is to minimise the difference between the collected data and the calculated diffraction pattern of the inputted model. This process is known as Rietveld refinement and for the research described here the majority of processes involved in structure refinement was carried out by the GSAS ^[10] suite of programs.

The Rietveld method is an iterative process involving various stages that eventually lead to a workable model which describes lattice parameters as well as atomic positions and thermal effects. Several preliminary data treatment steps must be carried out first before refinement can commence. Initially a peak search is run, where noise is reduced and artefact peaks are ignored. The diffraction pattern is then indexed, combining observed reflections with their approximate Miller indices. This stage causes the most problems when solving the structure from powder diffraction data alone, since all the data is along the 2 θ axis, peak overlap is common, as well as superfluous peaks from impurities being incorrectly indexed. The Le Bail method is then used for a process called ‘Full pattern decomposition’ which minimises the differences between the observed and calculated profile. The final preliminary step is determination of the space group, which can again be challenging from experimental powder patterns, since it relies on the identification of systematic absences from both symmetry elements and Bravais centring which can be lost by peak overlap.

The mathematical model where the observed intensity at the i th step, y_{io} can be compared with the calculated intensity y_{ic} is then refined by minimizing the residual by a least-squares process:

$$S = \sum w_i \left| y_{io} - y_{ic} \right|^2 \quad (15)$$

Where the weight, w_i is given by:

$$(w_i)^{-1} = \sigma_i^2 = \sigma_{ip}^2 + \sigma_{ib}^2 \quad (16)$$

σ_{ip} is based on counting statistics and represents the standard deviation associated with the peak. σ_{ib} is the standard deviation of the background intensity y_{ib} . The contribution from neighbouring Bragg reflections is given by y_{ic} :

$$y_{ic} = s \sum_k m_k L_k \left| F_k \right|^2 G(\Delta\theta_{ik}) + y_{ib} \quad (17)$$

Where s is a scale factor, m_k is the multiplicity factor for the reflection k , L_k is the Lorentz-polarisation factor, F_k is the structure factor, $\Delta\theta_{ik}$ is formed from $2\theta_i - 2\theta_k$ where $2\theta_k$ is the calculated position or the peak taking into account potential zero shift of the detector. $G(\Delta\theta_{ik})$ is the reflection profile function and its determination represents a major problem in Rietveld analysis. $G(\Delta\theta_{ik})$ represents the peak shape, which can be affected by a variety of physical parameters for example; the radiation source, collimeter arrangements and particle size. This can be solved by varying a combination of peak-shape functions, Gaussian, Lorentzian and pseudo-Voigt, until the calculated and observed are in good agreement. The background intensity is usually defined as:

$$y_{ib} = \sum_n b_n (2\theta_i)^n \quad (18)$$

where b_n is a refinable parameter.

Several parameters must be refined to bring the calculated and observed data sets into coherence, these are: the unit cell lattice parameters, atomic positional and thermal parameters, the zero shift and the parameters defining the reflection profile and background. Coherence is indicated by the previously discussed terms R_p , R_{wp} and GofF.

An example refinement of a powder pattern using GSAS is carried out as follows: Initially the scale factors and background parameters are allowed to vary, followed by the zero point shift and lattice parameters to allow the matching up of diffraction maxima. The intensity of the maxima is further modified by varying the atomic positions of the unit cell contents, which in turn is followed by varying the Lorentzian and Gaussian peak shape parameters to ensure a matching peak shape. Finally

thermal motion is taken into account by the variation of the isotropic temperature factors. Further refinement generally consists of continued variation of the different parameters, not necessarily in the order detailed above. Further modification can be made by constraining bond angles and distances to those likely within the structure to avoid false minima. This process continues until the previously mentioned R-factor is at a reasonable value.

2.2.8 Neutron Diffraction

A fundamental restriction of the use of X-rays is that they are scattered by electron density and while this is not a problem for elements with high atomic numbers, elements such as H and Li are much harder to resolve due to low electron density. Also, the relative size of the electron cloud in comparison to the wavelength of the X-ray means that those scattered from different regions of the electron cloud may not all be in phase and thus cause partial destructive interference.

A beam of thermal or cold neutrons displaying wave-like properties according to the de Broglie relationship, elastically scatter off the nuclei of atoms. The resulting diffraction data provides accurate nuclei to nuclei bond distances, unaffected by electron cloud polarisation or high angle signal drop off. Neutron scattering is also affected by resonance scattering, where the neutron is absorbed by the nucleus then emitted, this varies dependant on atomic number and therefore it is possible to distinguish between isotopes as well as neighbouring elements. Neutrons exhibit spin and as such can be used to study paramagnetic atoms in magnetic experiments, however, for this research neutrons have been solely utilised in structural studies.

For the research presented in this thesis the elucidation of hydrogen positions is required, this is challenging through both single crystal and powder neutron diffraction. To locate hydrogen positions through single crystal neutron diffraction requires the formation of very large single crystals, which is often experimentally challenging. Similarly powder neutron diffraction suffers from high incoherent scattering contribution from hydrogen as well as a low flux which makes extraction of positional data very difficult. Deuteration of materials lowers the incoherent background and is a potential solution to this problem however it is expensive, can be experimentally challenging and argued that does not truly represent the hydrogen environment present within materials.^[12] The method applied to a small amount of structures presented within this thesis has recently been advocated by Mark Weller *et al*^[12] and involves the combination of PND and SXD data to quickly and accurately determine the hydrogen positions within complicated structures. Data collected by these methods were refined in the same fashion as PXD and SXD.

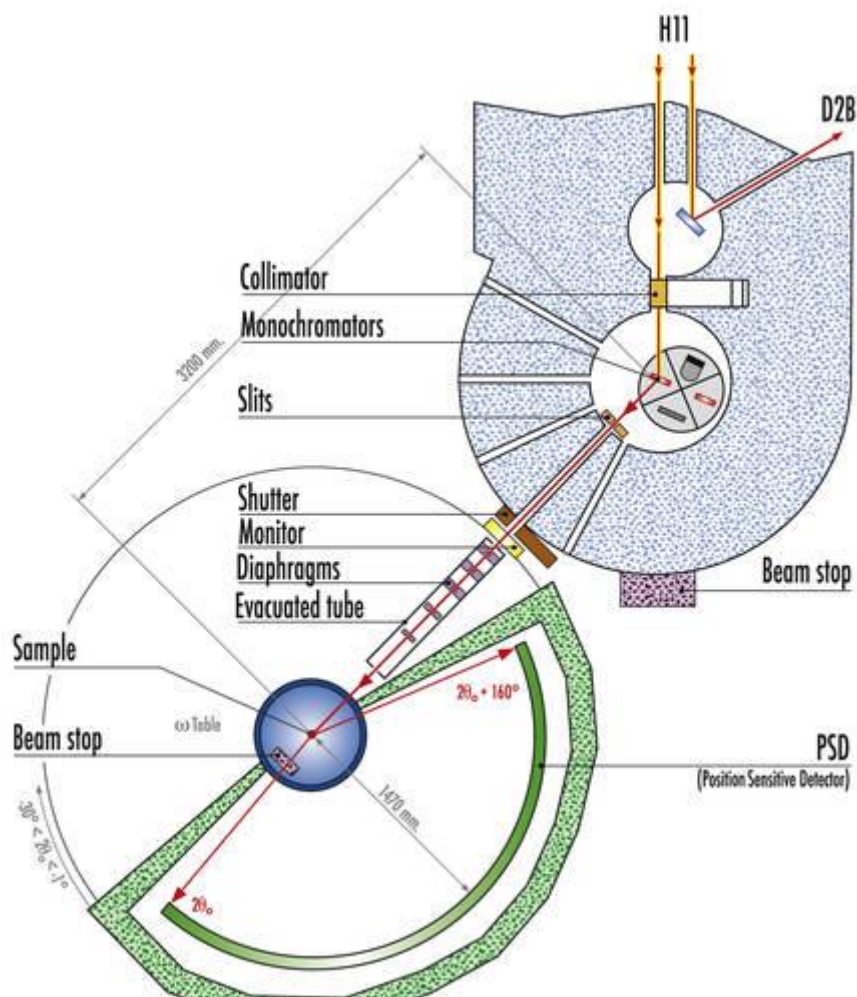


Figure 6: Schematic of the D20 instrument^[13]

The neutron source used was the D20 instrument at the ILL Grenoble. The instrument is a high intensity two-axis diffractometer with variable resolution set up with a Ge (200) monochromator working in transmission to generate neutrons with a wavelength of 1.87 Å. The detector is a large array PSD with a continuous coverage of $153.6^\circ 2\theta$ [Fig. 6].

2.2.9 Electron microscopy

Scanning Electron Microscopy (SEM) was used in this work to provide information on the morphology and crystallite size for materials, as well as Energy Dispersive X-ray Analysis (EDAX) providing information on which elements were present within crystallites.

In a standard SEM, electrons are produced by thermionic emission from a tungsten filament, which are focused by magnetic fields in high vacuum and then bombard the target crystal [Fig. 2.6]. The electron beam interacts with the sample in different ways, leading to the reflection and emission of backscattered electrons, secondary electrons, X-rays and Auger electrons. These fall under two

categories of electron/sample interaction; elastic and inelastic scattering. In elastic scattering, the direction of the primary (generated at the source) electron is changed, but with no change in energy, whereas inelastically scattered electrons lose a detectable amount of energy (> 0.1 eV) upon interaction with the sample, energy loss is usually associated with the generation of X-rays or secondary electrons.

In SEM, secondary electrons are emitted from the surface of the sample and give an image of the surface topography with a range of magnification of down to ~ 3 nm. The features of the image produced can be seen through differences of contrast

In EDAX the incident electron beam gives rise to X-ray emissions, characteristic of the element. The X-rays are then separated by a detector to provide both semi-qualitative and semi-quantitative analysis of the sample. A major disadvantage of this method however, is the emission of X-rays from lighter elements is generally indistinguishable from the background.

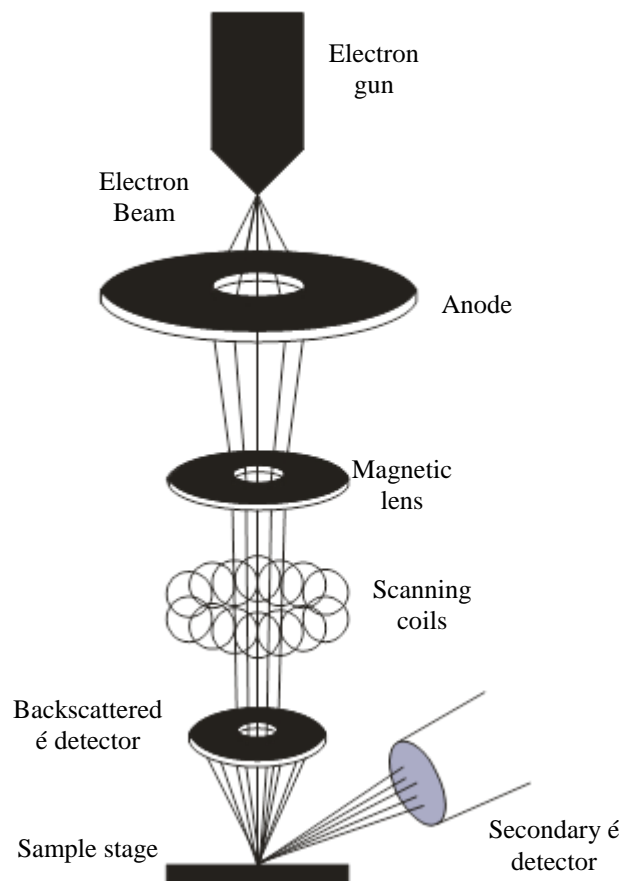


Figure 7: General setup of an SEM

2.2.10 SEM instrumentation

This work used a JSM 5910 scanning electron microscope, with an accelerating voltage of 0.3 to 30 kV, leading to a maximum resolution of 3.0 nm. The detector assembly allows for detection of both secondary and backscattered electrons. The instrument is also fitted with an Oxford Inca 300 detector, allowing EDAX to be performed. Samples for SEM are first mounted on aluminium stubs and carbon coated, before being inserted into the instrument and analysed under vacuum.

2.2.11 Thermogravimetric Analysis

In thermogravimetric analysis (TGA) the mass of a sample is measured as a function of time while its temperature is increased or decreased at a controlled rate. This technique is ideal for the study of structure stability and for observing the removal of volatile extra framework species, such as water or incorporated organics. Any mass loss or gain can be expressed as a percentage of the sample's stoichiometry and therefore can provide information as to the number of volatile molecules. Mass gain can be attributed to oxidation or adsorption of gas. Any dramatic mass loss observed is generally due to sample decomposition.

The instrument used in this research was a Polymer Laboratories STA 1500 Simultaneous Thermogravimetric Analysis System. A standard experiment uses approximately 16 mg of sample which was weighed on the instrument to an accuracy of 0.001 mg. The sample was then heated to the desired temperature at a rate of 10 °C/min and a sampling rate of once every 3 seconds. Target temperatures of up to 650 °C can be reached under air whereas higher temperatures require an inert atmosphere, such as provided by nitrogen.

2.2.12 Magic angle spinning nuclear magnetic resonance

Nuclear magnetic resonance (NMR) spectroscopy is a powerful and widely used technique; it provides valuable information about the shape and symmetry of molecular structures as well as detailed information on the environment of individual atoms within a structure, which can substantially aid full structural solution. However, NMR studies of materials cannot provide more detailed structural information such as lattice parameters and so in this research it has only been used in a supportive role. The use and sensitivity of NMR is dependent on the nuclear magnetic moment of the material to be studied as well as its abundance. Where the number of protons and neutrons in a nucleus are even the spin quantum number (I) is equal to zero and therefore has no NMR absorption. The most commonly studied nuclei that exhibit NMR absorption spectra are those with a spin of $I = \frac{1}{2}$ or a dipolar moment, such as ^1H , ^{13}C and ^{31}P . These have two possible degenerate spin states ($-\frac{1}{2}$ and $\frac{1}{2}$, $2I + 1$) which when subjected to a magnetic field (B_0) separate in energy relative to the strength of the applied field, the energy difference is expressed as equation 19.

$$\Delta E = \hbar \gamma B_o \quad (19)$$

where \hbar = the reduced Planck constant, γ = magnetogyric ratio

The interaction itself is known as the Zeeman interaction where the Zeeman energy is expressed as:

$$E = -\gamma \hbar I \cdot B_o \quad (20)$$

This resonance is then expressed as chemical shift (δ) which is the difference between the resonance frequency of the studied nuclei and an accepted standard, such as tetramethylsilane for ^1H , ^{13}C and ^{29}Si . [Equation 21]

$$\Delta = (\nu - \nu^o / \nu^o) \times 10^6 \quad (21)$$

The common shifts of most isotopes are tabulated and so environments can be identified through observed correlation. Positional and symmetry information can be elucidated since chemical shifts differ for elements in inequivalent positions. Structural assignment is also aided by the occurrence of spin-spin coupling (or J coupling named after the coupling constant J) where the influence of local elements causes resonances to occur as multiplets separated by J . This splitting of peaks is observed for both homonuclear and heteronuclear coupling, however, with homonuclear coupling if the elements are related by symmetry a single resonance peak is seen, as each position is equivalent.

When attempts are made to characterise solid state materials using NMR problems arise, which are due to there being little signal averaging by Brownian motion as observed for materials in solution. As such, in the solid state chemically equivalent materials may have different magnetic environments and anisotropic interactions which lead to resonance peaks having broad Gaussian character potentially losing any coupling information. Spinning the sample at the so called ‘magic angle’ can increase the resolution significantly since the anisotropic interaction contribution to signal broadening contains the term $3\cos^2\theta - 1$, which becomes zero when $\cos\theta = (1/3)^{1/2}$ or $\theta = 54^\circ 44'$.

Quadrupolar interactions also cause significant problems, especially relevant for ^{75}As ($I = 3/2$). The peaks are broader due to a nonspherical electric field, however this effect is also partially reduced by magic angle spinning.

MASNMR was collected by the University of Durham's solid state NMR research service on a Varian VNMRs spectrometer. ^{31}P measurements were referenced to 85 % H_3PO_4 and collected at 161.874 MHz with a spectral width of 100 KHz, acquisition time of 30 ms, 192 repetitions and the sample stage was rotated at 8000 Hz. ^9Be measurements were not referenced (no suitable standards were available) and collected at 56.194 MHz with a spectral width of 500 KHz, acquisition time of 25 ms, 448 repetitions and the sample stage was rotated at 8000 Hz. ^{75}As measurements were not referenced (no suitable standards were available) and collected at 68.785 MHz with a spectral width of 1250 KHz, 2560 repetitions and the sample stage was not rotated.

2.3: Computational

This project has primarily been concerned with experimental results rather than theoretical predications, however, two non-structure solution programs have been used routinely throughout to produce supplementary details for structures produced.

2.3.1 Bond valence method

Bond valence calculations were performed on atoms within the structures presented in this work. They were applied to confirm atomic site occupation and assist in overall structure charge balancing and the prediction of hydrogen atom positions.

The bond valence method links the bond valence to the bond distance and uses correlations between the length and strength of chemical bonds within crystalline substances to provide estimates of either value based on the other. This method does not distinguish between ionic or covalent bonding, instead regards atoms based on their electronegativity. The valence of an atom (V) is the summation of the bond valences interacting with that atom (v_i)

$$V = \sum(v_i) \quad (22)$$

Where v_i can be calculated from observed bond lengths collected from characterisation data, for example for As^{5+} $V = \sim 5$.

$$v_i = \exp[(R_0 - R_i)/b] \quad (23)$$

v_i = the valence of an individual atom i , R_0 = empirical bond valence parameter expressing bond length where i is of valence 1, R_i = observed bond length and b = generally 0.37 Å.^[14] Equation 23 can be rearranged to estimate bond lengths within structures where valencies are known.

Throughout this work files outputted from SHELX were tested via the *softBV 0.96* program^[14] where positions with v.u's (valence units) outside of tolerance limits are highlighted and based on the calculated deficit, decisions on the sites occupation, bonding environment and possible presence of hydrogen atoms can be made.

2.3.2 Use of Totopol

Totopol^[15] is a program directly linked into a database of hypothetical zeolite structures produced by M. D. Foster and M. M. J. Treacy and was used in the scope of this work to test structures produced against the database to confirm new topologies.

The database is produced by taking the asymmetric unit of a unit cell and determining every possible neighbouring asymmetric unit (edge, vertex or face sharing). Tetrahedral atoms are then systematically placed on every possible site, possible interatomic bonds are predicted and investigated leading to a connectivity graph. The next stage is to position the T atoms in the geometric centres of their bonded neighbours and adjust the cell dimensions until reasonable T – T distances and T - T – T angles are achieved. Following this the positions of the T atoms and unit cell parameters are allowed to vary while the bond distances and angles are fixed to 3.05 Å and 109.47 °. If the resultant structure is of a feasible low energy it is further refined with the addition of oxygen before being classed as a potential framework structure. Following this procedure Totopol has produced over 2175685 unique topologies to date.

2.4: References

- ¹ <http://emedicine.medscape.com/article/296759-overview> (accessed 27/08/09)
- ² E. S. Grew, P. H. Ribbe, *Beryllium; Mineralogy, Petrology and Geochemistry*, **2002**
- ³ <http://www.microscopy.ethz.ch/bragg.htm> (accessed 03/08/12)
- ⁴ C. Giacovazzo, H. L. Monaco, G. Artioli, D. Viterbo, G. Ferraris, G. Gilli, G. Zanotti, M. Catti, *Fundamentals of Crystallography*, **2002**, Oxford University press.
- ⁵ <http://www.ruppweb.org/xray/tutorial/ewald.htm> (accessed 03/08/12)
- ⁶ L. J. Farrugia, *J. Appl. Crystallogr.*, **1999**, 32(4), 837-838
- ⁷ XPREP Bruker AXS Inc., Madison, Wisconsin, USA
- ⁸ G. Sheldrick, SHELX-97, Programs for Crystal Structure Analysis (release 97-2), **1997**, University of Gottingen, Gottingen, Germany
- ⁹ H. M. Rietveld, *J. Appl. Cryst.*, **1969**, 2, 65
- ¹⁰ A. C. Larson, R. B. Von Dreele, *General structure Analysis system GSAS*, Los Alamos National Laboratory Report LAUR, **1994**, 86-748
- ¹¹ B. H. Toby, EXPGUI, a graphical interface for GSAS, *J. Appl. Crystallogr.*, **2001**, 34, 210-213
- ¹² M. T. Weller, P. F. Henry, V. P. Ting, C. C. Wilson, *Chem. Commun.*, **2009**, 2973-2989
- ¹³ <https://www.ill.eu/> (accessed 03/08/12)
- ¹⁴ I. D. Brown, *J. Appl. Cryst.* **1996**, 29, 479-480.
- ¹⁵ M. D. Foster, M. M. J. Treacy, A Database of Hypothetical Zeolite Structures:
<http://www.hypotheticalzeolites.net>

Chapter 3

Beryllium frameworks containing arsenic

There has been considerable interest in the formation of arsenic containing frameworks as the larger size of the pentavalent arsenic ion (0.335 Å) compared to pentavalent phosphorus ion (0.17 Å) ^[1] is likely to cause high degrees of distortion and strain on secondary building units within frameworks. The resulting strain is theorised to lead potentially to entirely new structures, or interruption of known structures, both of which could lead to increased functionality or new applications. There are close similarities chemically between phosphorus and arsenic due to periodicity, however, where phosphorus (the aluminophosphates) containing frameworks are very common and have been isolated as analogues of zeolites and entirely new three dimensional open-frameworks, there remains very little research on open-framework arsenates. Especially lacking are examples of open-framework arsenates of divalent metals other than zinc. Through the production and characterisation of multiple new frameworks formed of tetrahedral divalent beryllium and tetrahedral pentavalent arsenic this work aims to provide a comprehensive overview of the chemistry of these materials.

As discussed in Chapter 1, the majority of non-naturally occurring zeolites and zeotypes are produced by emulating geological processes via hydrothermal synthesis. Arsenic containing framework structures are no exception. For example the novel framework $[\text{C}_4\text{N}_3\text{H}_{16}]_2[\text{Zn}_5(\text{AsO}_4)_4(\text{HAsO}_4)_2]$ ^[2] has been prepared under extremely mild mixed solvent solvothermal synthesis conditions at 150 °C for 48 hours. Large colourless crystals were produced exhibiting an interrupted three dimensional framework with no known natural analogue. Formation of zincoarsenate analogues of zeolitic structures such as ABW, ANA, CHA and EDI ^[3] can also be carried out at a similar temperature and time scale, suggesting that simply varying the reaction composition has a massive effect on the structure and the success of the reaction.

Since there are so many parameters to consider, it was decided to investigate the effect of varying the structure directing agent as the primary goal in this research in an attempt to product new materials. As previously discussed, this is a parameter that has gathered much interest in the past 30 years, however literature on the berylloarsenates ^[4, 5] deals mainly with synthesis methods where the structure directing agent is an alkali/alkali earth metal complex such as in $\text{LiBeAsO}_4 \cdot \text{H}_2\text{O}$. ^[5] Apart from RHO ^[6] and ANA, ^[7] very few zeolitic berylloarsenates have been reported, and as such initial reactions emulated the formation of the beryllophosphates GME, ABW ^[8] and GIS ^[9] owing to the similarities in chemistry between arsenic and phosphorus. In particular the synthesis methods applied for the synthesis of the GME zeotype at 180 °C in alkaline media for four days ^[8] was used as the baseline for this research, where the OSDA was the major varied factor but most other major

experimental parameters were also varied: concentration of starting materials, amount and type of solvent, length of reaction, pH, addition of competitive structure directing agents such as group I/II metal hydroxides or 1st row transition metal chlorides, temperature, addition of mineraliser in the formation metal and hydrogen fluorides and the form of the starting material. The approach taken was primarily trial and error with successful synthesis passing through an iterative process to attempt to isolate pure material.

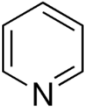
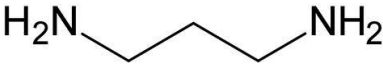

A large selection of organic structure directing agents was investigated and selected based upon their charge balancing ability, size of molecule and whether they had been used in framework synthesis found in the literature. The OSDAs utilised in successful synthesis are summarised along with any structures produced in table 1. It is worth remembering that the OSDA does not just fulfil a templating role; it also affects the pH, the composition of the solvent (where large amounts of OSDA were added) as well as in some cases having a mineralising role by decomposing into further organic species which in turn become the OSDAs present in some structures, facilitating the formation of larger crystals owing to the decomposition being the rate determining step.

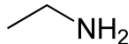
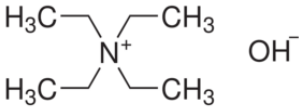
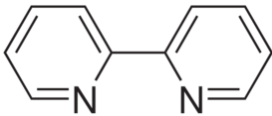
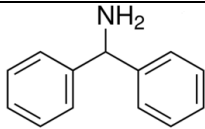
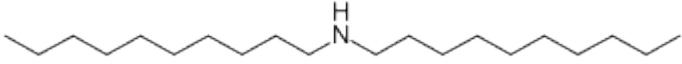
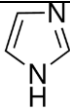
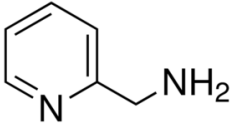
The novel structures discussed within this chapter are the result of extensive fine tuning of reaction conditions, starting from the initial baseline of the beryllophosphate GME. The vast majority of reactions carried out produced known materials, unreacted starting materials, unidentifiable powders or glasses. A typical reaction consisted of the starting materials being transferred into a 23 mL Parr hydrothermal vessel, where they were allowed to ‘age’ while being stirred gently at room temperature; this facilitated the homogeneity of the primary amorphous phase or ‘gel’. The vessel was then transferred to an oven for a specified period of time and at a controlled temperature. The reaction time was based upon early studies carried out in this research where it was found that a reaction time of at least 168 hours was required to produce crystals of sufficient size for SXD. The products are the most kinetically stable material formed after complete dissolution of the ‘gel’ and subsequent nucleation of the product.^[10] On removal of the vessel it was allowed to cool to room temperature naturally over several hours and its contents were then filtered under vacuum. The resulting bulk was then washed with distilled water and ethanol to remove any unreacted organic molecules or water soluble impurities, the products of interest being chemically stable. A reaction was deemed successful when it produced crystals of sufficient quality and quantity to warrant investigation *via* X-ray single crystal diffraction. Further characterisation was carried out utilising EDS, SEM, VTPXD and TGA, however, the vast majority of structures presented here were only produced as minor phases, despite extensive efforts to produce pure phases. Where a product was produced as the major/single phase, further characterisation has been carried out in the form of VTPXD and TGA studies. Whereas the minor phases were investigated *via* PXD and commonly found to contain a mixture of starting materials, secondary amorphous phases and product. The successful reactions carried out are

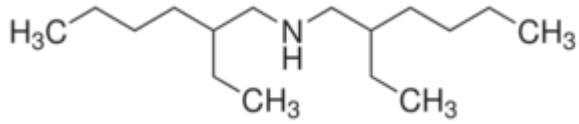
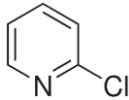
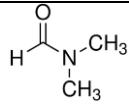
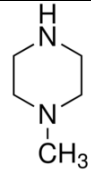
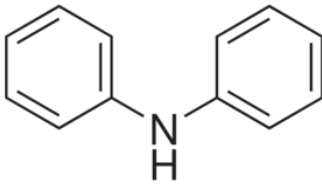
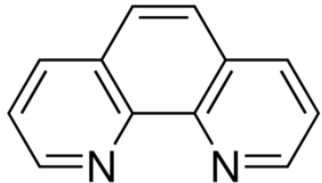
summarised in table 2 along with the materials produced and the relevant section if that material was novel.

EDS and SEM measurements were carried out to show semi-quantitatively the composition and morphology of crystals produced. EDS was of limited use however, as the emissions from beryllium are of too low energy to be able to pass through the detector window on the instrument used. TGA and VTPXD were carried out to investigate the thermal stability of materials produced and confirm the number of volatile extra-framework species present within structures.

Table 1: OSDAs that were involved in successful synthesis

Name of OSDA	Structure ^[11]	Outcome
Pyridine		Formation of the novel structures: $[\{ \text{H-pyridine} \}_{0.5}]$ $[\text{As}_2(\text{As}_{0.25}\text{Be}_{0.75})_2\text{O}_7(\text{OH})_2]$ $\bullet(\text{H}_2\text{O})_{0.65}$ $\text{AsO}_4\text{Be}(\text{OH}_2)(\text{Be}(\text{OH})(\text{OH}_2))$ $[(\text{H-pyridine})_2]$ $[(\text{AsO}_4)_2(\text{AsO}_3\text{OH})\text{Be}_2(\text{BeOH}_2)]$ Rb_3 $[(\text{AsO}_4)_3(\text{AsO}_3\text{OH})\text{Be}_3(\text{BeOH}_2)] \bullet \text{H}_2\text{O}$ $[(\text{AsO}_4)_6\text{Be}_6(\text{BeOH}_2)_2] \bullet 2\text{H}_2\text{O}$
1,3-diaminopropane		Formation of the novel structures: $[\text{H}_2\text{-diaminoethane}][\text{AsO}_4\text{Be}]$ $[(\text{H}_2\text{-diaminopropane})_{1.5}]$ $[(\text{AsO}_4)_2(\text{AsO}_3\text{OH})_2(\text{AsO}_2\text{OH})_2\text{Be}_4]$ $\bullet \text{H}_2\text{O}$ $[\text{NH}_4]_2[(\text{AsO}_4)_2\text{Be}_2(\text{Be}(\text{OH})_2)]$ $[\text{NH}_4]_2[(\text{AsO}_4)_2\text{Be}_2] \bullet 2\text{H}_2\text{O}$ $\text{Na}_3[\text{AsO}_4\text{Be}]$ Formation of the known structures: Bearsite $\text{Be}_2(\text{AsO}_4)(\text{OH}) \bullet 4\text{H}_2\text{O}$ Li - ABW
N-(3-Aminopropyl)-1,3-propanediamine		Formation of novel structures: $\text{Na}_{3.5}[\text{AsO}_4(\text{BeF}_3)(\text{BeF}_2)] \bullet 0.4\text{H}_2\text{O}$ $\text{Na}_2[\text{AsO}_4\text{Be}(\text{OH})] \bullet \text{H}_2\text{O}$ $\text{Rb}_2[(\text{AsO}_4)_2\text{Be}_2(\text{Be}(\text{OH})_2)]$

		$\text{Na}_3[\text{AsO}_4\text{Be}]$ $[\text{NH}_4]_2[(\text{AsO}_4)_2\text{Be}_2(\text{Be}(\text{OH})_2)_2]$ $[\text{NH}_4]_2[(\text{AsO}_4)_2\text{Be}_2] \cdot 2\text{H}_2\text{O}$
Ethylamine		Formation of novel structures: $[\text{R}^+]_{1.5}[\text{As}_{6.17}\text{Be}_{13.83}\text{O}_{\sim 20}\text{OH}_{\sim 20}] \cdot n\text{H}_2\text{O}$ $[\text{C}_2\text{H}_5\text{NH}_2][\text{Be}_{42.7}\text{As}_{17.3}(\text{O})_{\sim 55}(\text{OH})_{\sim 65}]$ $[\text{NH}_4]_2[(\text{AsO}_4)_2\text{Be}_2(\text{Be}(\text{OH})_2)_2]$
Tetraethylammonium hydroxide		Formation of novel structures: $\text{Sr}[\text{AsO}_4\text{Be}(\text{OH})]$
2,2'Bipyridyl		Crystals of unreacted 2,2'bipyridyl Formation of novel structure: $\text{AsO}_4\text{Be}(\text{OH}_2)(\text{Be}(\text{OH})(\text{OH}_2))$
Aminodiphenylmethane		Crystals of unreacted aminodiphenylmethane
Didecylamine		Formation of novel structures: $\text{AsO}_4\text{Be}(\text{BeOH})$ $[\text{NH}_4]_2[(\text{AsO}_4)_2\text{Be}_2] \cdot 2\text{H}_2\text{O}$
Imidazole		Formation of novel structures: $\text{AsO}_3(\text{OH})\text{Be}(\text{C}_3\text{H}_4\text{N}_2)$
2-(aminomethyl)pyridine		Formation of novel structures: $[\text{NH}_4]_2[(\text{AsO}_4)_2\text{Be}_2] \cdot 2\text{H}_2\text{O}$ $[\text{NH}_4]_2[(\text{AsO}_4)_2\text{Be}_2(\text{Be}(\text{OH})_2)_2]$

Bis(2-ethylhexyl)amine		Formation of novel structures: $[\text{H-bis(2-ethylhexyl)amine, NH}_4]_4$ $[(\text{AsO}_4)_3(\text{AsO}_3\text{OH})\text{Be}_3(\text{BeOH})]$ $\text{AsO}_4\text{Be}(\text{OH}_2)(\text{Be}(\text{OH})(\text{OH}_2))$ Formation of known structures: As_2O_3
2-Chloropyridine		Formation of novel structure: $\text{AsO}_4\text{Be}(\text{OH}_2)(\text{Be}(\text{OH})(\text{OH}_2))$
DMF		Formation of novel structure: $\text{AsO}_4\text{Be}(\text{OH}_2)(\text{Be}(\text{OH})(\text{OH}_2))$
1-methylpiperzine		Formation of novel structure: $\text{AsO}_4\text{Be}(\text{OH}_2)(\text{Be}(\text{OH})(\text{OH}_2))$
Diphenylamine		Formation of novel structure: $\text{AsO}_3(\text{OH})\text{Be}$ $\text{Rb}_2[(\text{AsO}_4)_2\text{Be}_2(\text{Be}(\text{OH})_2)]$ Formation of known structures: As_2O_3
1,10-Phenanthroline		Formation of novel structure: $\text{AsO}_4\text{Be}(\text{OH}_2)(\text{Be}(\text{OH})(\text{OH}_2))$

The following OSDAs were also attempted however they produced only unidentifiable mixed phases or glasses: Piperazine, tert-octylamine, allylamine, 1-(2-aminoethyl)-piperazine, Ethylenediamine, Triethylenediamine, 1-(2-aminoethyl)piperazine, Dipentylamine, 2,3-diaminotoluene, N, N-dimethyldodecylamine, trans-1,4-diaminocyclohexane, dibutylamine, diisopropylamine, isobutylamine, 1,5-diamino-2-methylpentane, 2-phenylamine and Hexamethonium chloride.

Table 2: Synthesis conditions for novel beryllioarsenates produced as part of this research

Product	Relevant section	Defining Synthesis (Reaction that produced first solvable single crystals)	Temperature (°C)	Reaction time (Hr)
$\text{Na}_{3.5}[\text{AsO}_4(\text{BeF}_3)(\text{BeF}_2)] \cdot 0.4\text{H}_2\text{O}$	3.1	BL135.9: $\text{Be}(\text{OH})_2$ (0.055 g, 1.28 mmol), HAsF_6 (0.25 mL, 2.17 mmol) and distilled H_2O (1.5 mL) were added to a Teflon® vessel and stirred at room temperature for 30 minutes. NaOH (50 %, 0.27 mL, 5.11 mmol) and N-(3-aminopropyl)-1,3-propanediamine (0.55 mL, 2.7 mmol) were then added and the resulting ‘sol’ allowed to age while gently stirring for one hour before autoclaving.	220	168
$\text{AsO}_3(\text{OH})\text{Be}(\text{C}_3\text{H}_4\text{N}_2)$	3.2	BL124.1: $\text{Be}(\text{OH})_2$ (0.055 g, 1.28 mmol), H_3AsO_4 (0.165 mL, 2.17 mmol), ethanol (1.92 mL) and distilled H_2O (0.75 mL) was added to a Teflon® vessel and stirred at room temperature for 30 minutes. Imidazole (0.366 g, 5.37 mmol) was then added and the resulting ‘sol’ allowed to age while gently stirring for one hour before autoclaving.	160	168
$\text{Na}_2[\text{AsO}_4\text{Be}(\text{OH})] \cdot \text{H}_2\text{O}$	3.3	BL119.1: $\text{Be}(\text{OH})_2$ (0.055 g, 1.28 mmol), H_3AsO_4 (0.165 mL, 2.17 mmol) and distilled H_2O (1.5 mL) were added to a Teflon® vessel and stirred at room temperature for 30 minutes. NaOH (50 %, 0.27 mL, 5.11 mmol) and N-(3-aminopropyl)-1,3-propanediamine (0.55 mL, 2.7 mmol) were then added and the resulting ‘sol’ allowed to age while gently stirring for one hour before autoclaving. Pre-autoclave mixture had a pH of 12.64.	160	168
$[\{\text{H-pyridine}\}_{0.5}] [\text{As}_2(\text{As}_{0.25}\text{Be}_{0.75})_2\text{O}_7(\text{OH})_2] \cdot (\text{H}_2\text{O})_{0.65}$	3.4	BL084.5: $\text{Be}(\text{OH})_2$ (0.11 g, 2.56 mmol), H_3AsO_4 (0.33 mL, 4.34 mmol) and distilled H_2O (3 mL) were added to a Teflon® vessel and stirred at room temperature for 30 minutes. Pyridine (9.78 mL, 0.126 mol) was then added and the resulting ‘sol’ allowed to age while gently stirring for one hour before autoclaving.	160	192

$\text{Sr}[\text{AsO}_4\text{Be}(\text{OH})]$	3.5	BL101.3: $\text{Be}(\text{OH})_2$ (0.0945 g, 2.2 mmol), H_3AsO_4 (0.19 mL, 2.5 mmol) and distilled H_2O (10 mL) were added to a Teflon® vessel and stirred at room temperature for 30 minutes. $\text{Sr}(\text{OH})_2 \cdot 8\text{H}_2\text{O}$ (0.216 g, 8.13×10^{-4} mol) and TEAOH (0.94 mL, 2.5 mmol) were then added and the resulting ‘sol’ allowed to age while gently stirring for one hour before autoclaving.	175	168
$\text{AsO}_4\text{Be}(\text{OH}_2)(\text{Be}(\text{OH})(\text{OH}_2))$	3.6	NS2.1: (first synthesised by Natalie Seaton) $\text{Be}(\text{OH})_2$ (0.11 g, 2.56 mmol), H_3AsO_4 (0.33 mL, 4.34 mmol) and distilled H_2O (3 mL) were added to a Teflon® vessel and stirred at room temperature for 30 minutes. Pyridine (1.4 mL, 0.0173 mol) was then added and the resulting ‘sol’ allowed to age while gently stirring for one hour before autoclaving.	160	168
$\text{AsO}_3(\text{OH})\text{Be}$	3.7	BL124.4: ($\text{Be}(\text{OH})_2$ (0.055 g, 1.28 mmol), H_3AsO_4 (0.165 mL, 2.17 mmol), ethanol (1.92 mL) and distilled H_2O (0.75 mL) were added to a Teflon® vessel and stirred at room temperature for 30 minutes. Diphenylamine (0.091 g, 5.37×10^{-4} mol) was then added and the resulting ‘sol’ allowed to age while gently stirring for one hour before autoclaving.	160	168
$[\text{NH}_4]_2[(\text{AsO}_4)_2\text{Be}_2] \cdot 2\text{H}_2\text{O}$	3.8a	BL116.9: ($\text{Be}(\text{OH})_2$ (0.055 g, 1.28 mmol), H_3AsO_4 (0.165 mL, 2.17 mmol) and distilled H_2O (1.5 mL) were added to a Teflon® vessel and stirred at room temperature for 30 minutes. 2-Aminomethylpyridine (3 mL, 0.029 mol) was then added and the resulting ‘sol’ allowed to age while gently stirring for one hour before autoclaving. Pre-autoclave mixture had a pH of 10.53.	160	192
$[\text{H}_2\text{-diaminoethane}]$ $[\text{AsO}_4\text{Be}]$	3.8b	BL139.1: $\text{Be}(\text{OH})_2$ (0.54 g, 0.0126 mol), H_3AsO_4 (2.1 mL, 0.0276 mol) and distilled H_2O (10 mL) were added to a Teflon® vessel and stirred at room temperature for 30 minutes. $\text{CoCl}_3(\text{H}_2\text{NCH}_2\text{CH}_2\text{NH}_2)_3 \cdot 2\text{H}_2\text{O}$ (1.2 g, 3.15 mmol) and 1,3-diaminopropane (1.126 mL, 0.0152 mol) were then added and the resulting ‘sol’ allowed to age while gently stirring for one hour before	220	168

		autoclaving.		
[(H ₂ -diaminopropane) _{1.5}] [(AsO ₄) ₂ (AsO ₃ OH) ₂ (AsO ₂ OH) ₂ Be ₄] •H ₂ O	3.9	BL084.7: Be(OH) ₂ (0.54 g, 0.0126 mol), H ₃ AsO ₄ (2.1 mL, 0.0276 mol) and distilled H ₂ O (10 mL) were added to a Teflon® vessel and stirred at room temperature for 30 minutes. 1,3-Diaminopropane (1.126 mL, 0.0152 mol) was then added and the resulting ‘sol’ allowed to age while gently stirring for one hour before autoclaving.	160	72
AsO ₄ Be(BeOH)	3.10	BL107.4: Be(OH) ₂ (0.055 g, 1.28 mmol), H ₃ AsO ₄ (0.165 mL, 2.17 mmol) and distilled H ₂ O (1.5 mL) were added to a Teflon® vessel and stirred at room temperature for 30 minutes. Didecylamine (0.187 g, 6.3x10 ⁻⁴ mol) was then added and the resulting ‘sol’ allowed to age while gently stirring for one hour before autoclaving.	160	192
[(H-pyridine) ₂] [(AsO ₄) ₂ (AsO ₃ OH)Be ₂ (BeOH ₂)	3.11	NS2.2: (first synthesised by Natalie Seaton) Be(OH) ₂ (0.11 g, 2.56 mmol), H ₃ AsO ₄ (0.33 mL, 4.34 mmol) and distilled H ₂ O (3 mL) were added to a Teflon® vessel and stirred at room temperature for 30 minutes. Pyridine (2.8 mL, 0.0346 mol) was then added and the resulting ‘sol’ allowed to age while gently stirring for one hour before autoclaving.	160	168
[H-bis(2-ethylhexyl)amine, NH ₄] ₄ [(AsO ₄) ₃ (AsO ₃ OH)Be ₃ (BeOH)]	3.12a	BL115.2: Be(OH) ₂ (0.055 g, 1.28 mmol), H ₃ AsO ₄ (0.165 mL, 2.17 mmol) and distilled H ₂ O (1.5 mL) were added to a Teflon® vessel and stirred at room temperature for 30 minutes. Bis(2-ethylhexyl)amine (1.89 mL, 0.0063 mol) was then added and the resulting ‘sol’ allowed to age while gently stirring for one hour before autoclaving.	160	192
Rb ₃ [(AsO ₄) ₃ (AsO ₃ OH)Be ₃ (BeOH ₂)]•H ₂ O	3.12b	NS19.5: (first synthesised by Natalie Seaton) Be(OH) ₂ (0.055 g, 1.28 mmol), H ₃ AsO ₄ (0.165 mL, 2.17 mmol) and distilled H ₂ O (1.5 mL) were added to a Teflon® vessel and stirred at room temperature for 30 minutes. Pyridine (0.7 mL, 8.65 mmol) and RbF (0.125 g, 1.19 mmol) were then added and the	160	168

		resulting 'sol' allowed to age while gently stirring for one hour before autoclaving. Pre-autoclave mixture had a pH of 6.25.		
$\text{Rb}_2[(\text{AsO}_4)_2\text{Be}_2(\text{Be}(\text{OH})_2)] \bullet 2\text{H}_2\text{O}$	3.13	BL119.3: $\text{Be}(\text{OH})_2$ (0.055 g, 1.28 mmol), H_3AsO_4 (0.165 mL, 2.17 mmol) and distilled H_2O (1.5 mL) were added to a Teflon® vessel and stirred at room temperature for 30 minutes. RbOH (50 %, 0.55 mL, 4.67 mmol) and N-(3-aminopropyl)-1,3-propanediamine (0.55 mL, 2.7 mmol) were then added and the resulting 'sol' allowed to age while gently stirring for one hour before autoclaving. Pre-autoclave mixture had a pH of 12.63.	160	168
$\text{Na}[\text{AsO}_4\text{Be}]$	3.14	BL129.9: $\text{Be}(\text{OH})_2$ (0.055 g, 1.28 mmol), H_3AsO_4 (0.165 mL, 2.17 mmol) and distilled H_2O (1.5 mL) were added to a Teflon® vessel and stirred at room temperature for 30 minutes. NaOH (50 %, 0.27 mL, 5.11 mmol) and N-(3-aminopropyl)-1,3-propanediamine (0.55 mL, 2.7 mmol) were then added and the resulting 'sol' allowed to age while gently stirring for one hour before autoclaving.	220	168
$[\text{NH}_4]_2[(\text{AsO}_4)_2\text{Be}_2(\text{Be}(\text{OH})_2)]$	3.15	BL112.5: $\text{Be}(\text{OH})_2$ (0.055 g, 1.28 mmol), H_3AsO_4 (0.165 mL, 2.17 mmol) and distilled H_2O (5 mL) were added to a Teflon® vessel and stirred at room temperature for 30 minutes. N-(3-aminopropyl)-1,3-propanediamine (4.4 mL, 0.031 mol) was then added and the resulting 'sol' allowed to age while gently stirring for one hour before autoclaving.	160	192
$[\text{C}_2\text{H}_5\text{NH}_2, \text{H}_2\text{O}]_x$ $[\text{Be}_{66.7}\text{As}_{25.3}(\text{O})_{80.5}(\text{OH})_{103.5}]$	3.16	NS12.6: (first synthesised by Natalie Seaton) $\text{Be}(\text{OH})_2$ (0.374 g, 8.7 mmol), H_3AsO_4 (0.33 mL, 4.34 mmol) and distilled H_2O (3 mL) were added to a Teflon® vessel and stirred at room temperature for 30 minutes. Ethylamine (70 % 2.83 mL, 0.0356 mol) was then added and the resulting 'sol' allowed to age while gently stirring for one hour before autoclaving. Pre-autoclave mixture had a pH of 12.32.	160	168

$[\text{R}^+]_{1.5}[\text{As}_{6.17}\text{Be}_{13.83}\text{O}_{\sim 20}\text{OH}_{\sim 20}]\cdot n\text{H}_2\text{O}$	3.17	BL098.12: $\text{Be}(\text{OH})_2$ (0.055 g, 1.28 mmol) and H_3AsO_4 (0.165 mL, 2.17 mmol) were added to a Teflon® vessel and stirred at room temperature for 30 minutes. Ethylamine (70 %, 5 mL, 0.063 mol) was then added and the resulting ‘sol’ allowed to age while gently stirring for one hour before autoclaving.	160	192
$[\text{C}_2\text{H}_5\text{NH}_2][\text{Be}_{42.7}\text{As}_{17.3}(\text{O})_{\sim 55}(\text{OH})_{\sim 65}]$	3.18	BL098.12: $\text{Be}(\text{OH})_2$ (0.055 g, 1.28 mmol) and H_3AsO_4 (0.165 mL, 2.17 mmol) were added to a Teflon® vessel and stirred at room temperature for 30 minutes. Ethylamine (70 %, 5 mL, 0.063 mol) was then added and the resulting ‘sol’ allowed to age while gently stirring for one hour before autoclaving.	160	192

Rationale:

The following attempts to describe only the novel berylloarsenate structures produced as part of this thesis. The structures are divided into individual sections (3.1 – 3.18) and are ordered by ascending levels of dimensionality, zero-dimensional or cluster structures to fully connected three-dimensional zeolitic frameworks. Each structure section includes an introductory paragraph with selected crystallographic parameters, brief overview of the structure, commentary on synthetic conditions and structure solution, specific structural features of note, appreciation of the bonds and any bond valence deviations and any further characterisation data. The structure presentations are followed by a section on trends observed in these materials and a summary section. Further structural details such as crystallographic information files and PXD data can be found in the e-appendices.

The aim of the work depicted in this chapter was focused on the formation of new zeotypical topologies and as such does not discuss the potential applications these structures may have, however a purely speculative commentary is present in the summary section.

3.1: $\text{Na}_{3.5}[\text{AsO}_4(\text{BeF}_3)(\text{BeF}_2)] \cdot 0.4\text{H}_2\text{O}$

The bulk of material produced in this reaction was a mixed powder phase which was a combination of unreacted starting materials and unidentifiable polycrystalline material. Small thin colourless plates were present as a minor phase and a suitable crystal was manually selected for single crystal X-ray diffraction, a summary of the crystal data is presented in Table 3. The unit cell is monoclinic and in the $C 2/c$ space group, which contains multiple zero dimensional clusters made up of three types of tetrahedra: AsO_4 , BeO_2F_2 and BeOF_3 . The tetrahedra are connected via oxygen bridging where BeO_2F_2 and AsO_4 form a four ring aligned with the a/c plane and the trifluoro-beryllium tetrahedra terminates the AsO_4 tetrahedra. The two terminating BeOF_3 tetrahedra present on each cluster are aligned parallel to the b axis and form a pincer shape, as shown in figure 1.

Table 3: Crystallographic information for $\text{Na}_{3.5}[\text{AsO}_4(\text{BeF}_3)(\text{BeF}_2)] \cdot 0.4\text{H}_2\text{O}$

Empirical formula	$\text{Na}_{3.5}[\text{AsO}_4(\text{BeF}_3)(\text{BeF}_2)] \cdot 0.4\text{H}_2\text{O}$
Formula weight	338.8
Appearance	Irregular blocks
Temperature	120 K
Wavelength	0.71073 Å
Crystal system	Monoclinic
Space group	$C 2/c$
a	20.2589(5) Å
b	7.5418(2) Å
c	14.1941(3) Å
β	133.475(2) °
Volume	1573.77 (21) Å ³
Z	8
D_c	2.92 g cm ⁻³
R index	0.0413
Weighted R index	0.1279

Structure solution was carried out by direct methods and the dataset and model converged rapidly. Density was quickly assigned to the As and Na positions, leading to logical assignment of O and Be based on bond lengths and geometry.

The structure contains only two extra-framework species; water and four sodium cation sites. The intended organic structure directing agent present in the synthesis mixture of this structure is not observed and so likely only has a pH controlling role. There is a high concentration of sodium in the reaction mixture, which suggests that the formation of a sodium containing structure was preferred over a structure stabilised by N-(3-aminopropyl)-1,3-propanediamine. The high degree of fluorine termination is due to the use of the hexafluoro arsenate anion as the starting material rather than the more commonly employed arsenic acid. This choice was made to attempt the formation of more complicated fluorine containing structures, with the possibility of fluorine bridging, however all attempts resulted in the formation of zero dimensional $\text{Na}_{3.5}[\text{AsO}_4(\text{BeF}_3)(\text{BeF}_2)] \cdot 0.4\text{H}_2\text{O}$. Interestingly it can be hypothesised that if the fluorine was not present within the structure as a terminating influence the structure would actually be slightly more complicated being formed of 4- and 8Rs which is inferred from the water oxygen position being 2.486 Å from the nearest cluster fluorine, which is representative of a tetrahedral O – (T) – O distance.

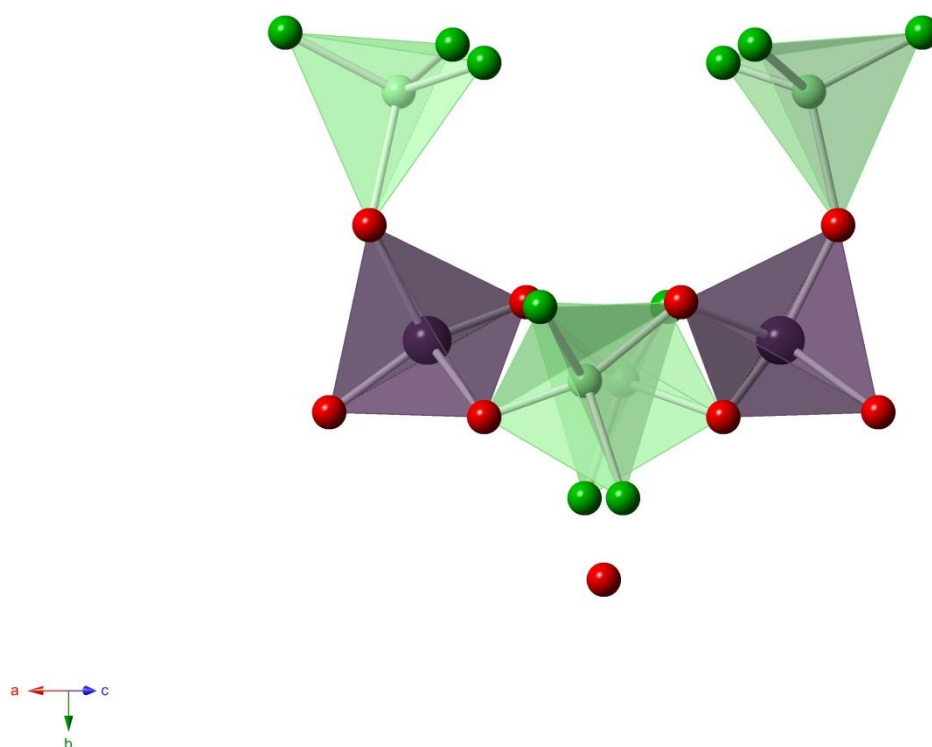


Figure 1: $\text{Na}_{3.5}[\text{AsO}_4(\text{BeF}_3)(\text{BeF}_2)] \cdot 0.4\text{H}_2\text{O}$, green and purple tetrahedra are Be and As centred respectively, red and green spheres are oxygen and fluorine. The high degree of fluorine termination is evident on the two apical Be tetrahedra.

$\text{Na}_{3.5}[\text{AsO}_4(\text{BeF}_3)(\text{BeF}_2)] \cdot 0.4\text{H}_2\text{O}$ has four crystallographically unique sodium sites which charge balance the negative framework and likely acted as the structure directing agent in the formation of the cluster. Each site is hexa-coordinated to two oxygen and four fluorine sites, with three of the sites in an approximate trigonal prismatic geometry and the fourth (Na2) octahedrally coordinated [Fig. 2]. The sodium ions sit within the open 8R ‘pincers’ either above or below the plane of the ring. The water site is 80 % occupied and is likely hydrogen bonded to nearby framework fluorine atoms, however, due to the limitations of X-rays in studying hydrogen positions it has been impossible to prove this through analytical means [Fig 3]. Bond valence calculations confirm the bonding environments suggested and also confirm the likely presence of the hydrogen bonding by showing a BV sum deviation of -1.72 v. u on the water oxygen site and when the BV deviations on the surrounding fluorine sites are considered [Table 4] it can be seen that hydrogen bonding likely occurs between O10 and F5/F4. This hydrogen bonding will help stabilise the clusters overall repeating structure. Selected bond distances and angles are given in Table 5.

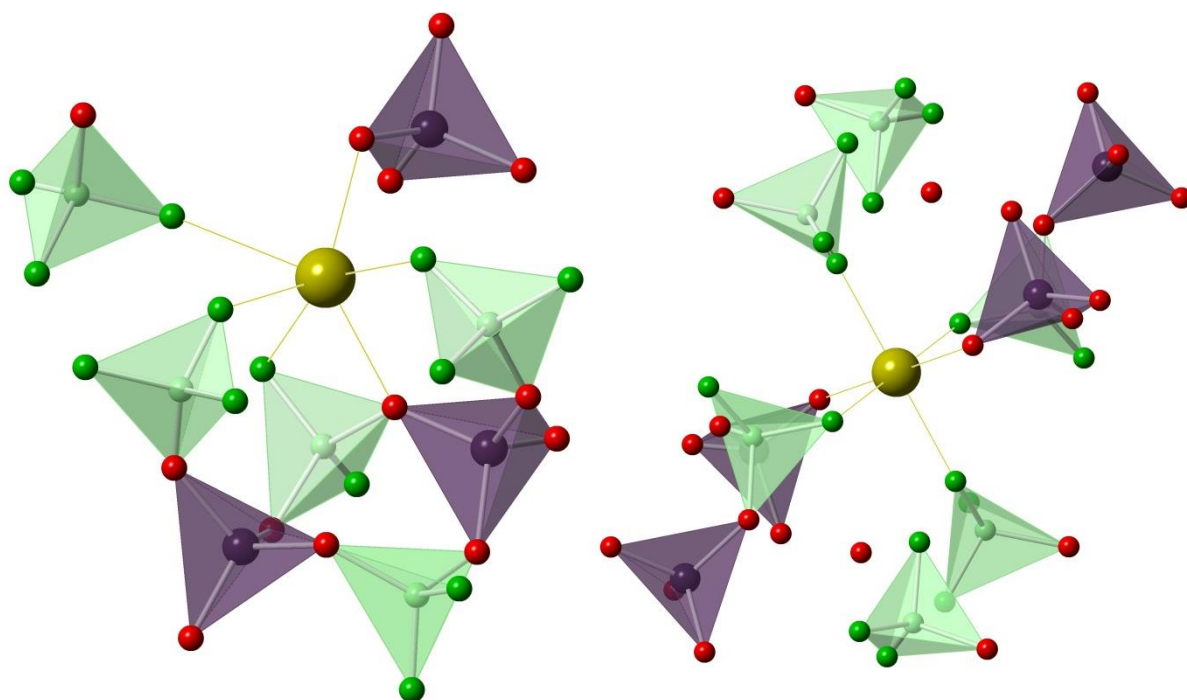


Figure 2: Sodium positions in $\text{Na}_{3.5}[\text{AsO}_4(\text{BeF}_3)(\text{BeF}_2)] \cdot 0.4\text{H}_2\text{O}$. Left is the trigonal prismatic coordinated Na1, Na3 and Na4 sites. Right is the octahedrally coordinated Na2 site. Yellow spheres represent Na atoms, other colouring is as before.

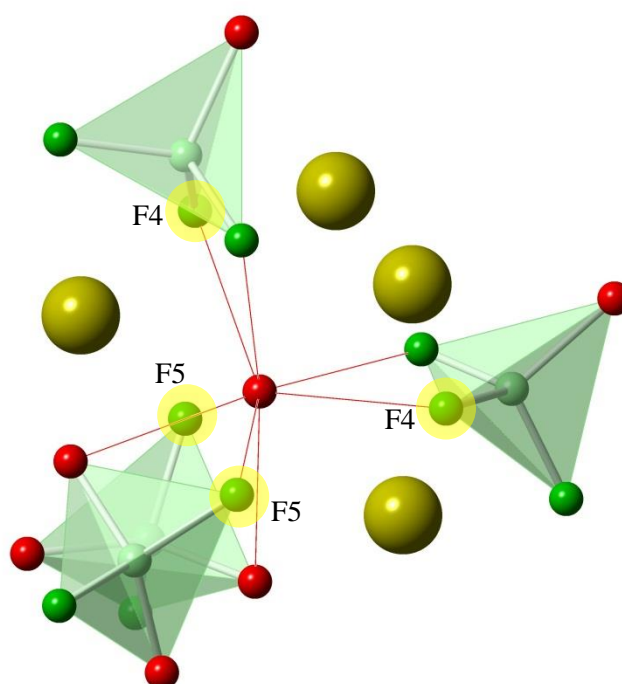


Figure 3: Water oxygen site in $\text{Na}_{3.5}[\text{AsO}_4(\text{BeF}_2)(\text{BeF}_3)] \cdot 0.4\text{H}_2\text{O}$, red bonds represent distances of below 2.7 \AA where likely hydrogen bonding occurs. Fluorine atoms involved in hydrogen bonding are highlighted by yellow circles

Table 4: Table showing bond valence sums for potential hydrogen bonding candidates

Atom (expected BV)	Σ of BV deviation from expected (v.u)
F5 (1.00)	-0.13
F4 (1.00)	-0.14
O10 (2.00)	-1.72

Table 5: Selected bond distances and angles for cluster components

Bond	Bond length (Å)	Bond	Bond angle (°)
Average As-O	1.650(5)	As – O1 – Be2	128.55(3)
Be1 – F6	1.553(6)	As – O4 – Be1	133.60(3)
Be1 – F3	1.573(6)		
Be1 – F4	1.539(6)		
Be1 – O4	1.618(7)		
Be2 – F5	1.548(6)		
Be2 – F1	1.547(6)		
Be2 – O1	1.654(6)		
Be2 – O3	1.616(6)		

Unfortunately due to this structure being formed only as a minor phase in the product mixture it was difficult to carry out any further bulk characterisation techniques. An EDS collection confirmed the presence of arsenic, fluorine, oxygen and sodium, which added to the bond valence calculations confirms the charge balanced formula of $\text{Na}_{3.5}[\text{AsO}_4(\text{BeF}_2)(\text{BeF}_3)] \cdot 0.4\text{H}_2\text{O}$. This structure represents the first zero dimensional and fluorine containing berylloarsenate structure known.

3.2: [AsO₃(OH)Be(C₃H₄N₂)]

Reactions with imidazole were carried out in an attempt to produce the first beryllium containing zeolitic imidazole framework (ZIF) however they were unsuccessful in their objective. Instead only two reactions produced any viable product; in the first case a mixture of beryllioarsenate MER type zeotype (section 3.8a) and [AsO₃(OH)Be(C₃H₄N₂)], the second produced phase pure [AsO₃(OH)Be(C₃H₄N₂)]. A clear hexagonal prismatic crystal was analysed by single crystal X-ray diffraction and the resulting crystallographic parameters listed in Table 6. The structure crystallises in the monoclinic crystal system and the P 2₁/c space group. The structure consists of a one dimensional sinusoidal chain structure (Fig. 4) similar to the structure of Be₂AsO₄OH•4H₂O described in the literature,^[12] however there are a number of notable differences. Firstly, the literature structure is formed of zig-zags of 3- and 4Rs whereas this structure is exclusively formed of 4Rs. Secondly, where Be₂AsO₄OH is formed of arsenic and beryllium centred tetrahedra with a small degree of hydroxyl termination, the beryllium tetrahedra in [AsO₃(OH)Be(C₃H₄N₂)] are terminated by a highly unusual Be – N bond (1.734 (3) Å) linking the imidazole structure directing agent to the chain. This bond distance is consistent with the bond distances observed in the trimer Be₃(NMe₂)₆ for the central tetrahedral beryllium (Be – N: 1.76 Å).^[13] Selected bond distances and angles are presented in Table 7.

The chains of zig-zag 4Rs run parallel to the *a* crystallographic axis, with each four ring made of two crystallographically unique sites, one arsenic and one beryllium-centered tetrahedra which, through oxygen bridges form an alternating infinite chain of Be-O-As-O-Be along *a*. The arsenic site is fully occupied and three of the four oxygens are involved in bridges with the beryllium centres, leaving one hydroxyl termination. The O-As-O angles (average: 109.4 °) are consistent with expected values and the average As-O distance is slightly longer (average: 1.677 Å) due to the hydroxyl group termination. The beryllium environment is similar with the only difference being in the nature of the two different forms of termination. Average O-Be-O angles are slightly distorted at 112.75 ° due to the influence of the Be-N bond, when O-Be-N angles are taken into account the average becomes 109.3 ° which is only slightly lower than that expected for a regular tetrahedra. Beryllium oxygen bond distances are slightly shorter than expected (average: 1.6224 Å), again due to the slight distortion of the tetrahedral character. The chain of 4Rs is arranged so that the apical hydroxyl termination is aligned along the *b* axis and the apical Be-N bond is aligned along the *c* axis. The well resolved imidazole ring is present between unconnected layers of the chains and acts as a structure directing agent, charge balancing species and part of the chain structure itself. The imidazole ring shows no signs of distortion, with the three locatable hydrogen positions being situated on a plane with the ring. The distance and alignment of the hydrogen positions on the imidazole ring suggest that

further structure stabilisation is achieved through hydrogen bonding; this is supported through bond valence calculations.

Table 6: Crystallographic information for [AsO₃(OH)Be(C₃H₄N₂)]

Empirical formula	[AsO ₃ (OH)Be(C ₃ H ₄ N ₂)]
Formula weight	215
Appearance	Colourless hexagonal prism
Temperature	120 K
Wavelength	0.71073 Å
Crystal system	Monoclinic
Space group	P 2 ₁ /c
<i>a</i>	4.999(3) Å
<i>b</i>	7.496(4) Å
<i>c</i>	17.039(10) Å
β	90.171(15) °
Volume	638.5(6) Å ³
<i>Z</i>	4
D _c	2.24 g cm ⁻³
R index	0.0671
Weighted R index	0.1115

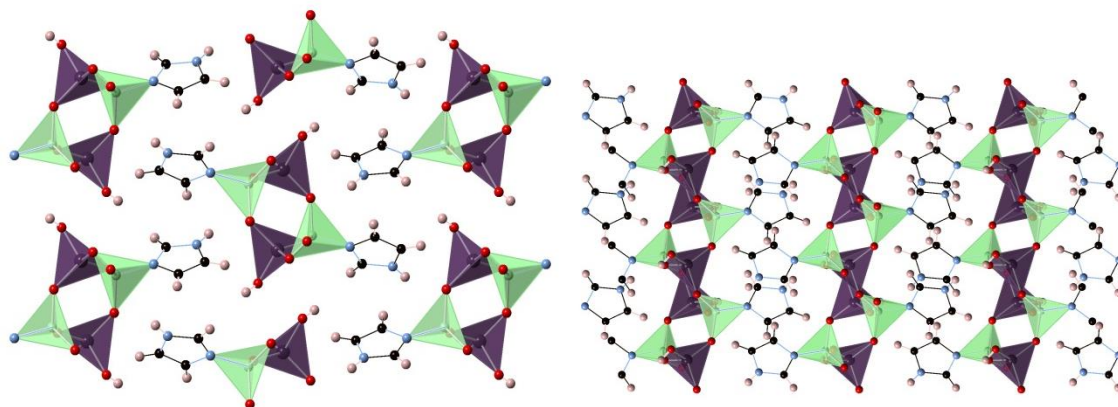


Figure 4a/b: $[\text{AsO}_3(\text{OH})\text{Be}(\text{C}_3\text{H}_4\text{N}_2)]$ viewed along a and b . Green and purple tetrahedra are Be and As respectively. Black, pink, blue and red spheres are C, H, N and O respectively.

Table 7: Selected bond lengths and angles in $[\text{AsO}_3(\text{OH})\text{Be}(\text{C}_3\text{H}_4\text{N}_2)]$

Bond	Bond length (Å)	Bond	Bond angle (°)
Average As – O	1.677(9)	As – O1 – Be	125.36(9)
Average Be – O	1.622(13)	Average N2 – Be – O	105.95(11)
Be1 – N2	1.734(2)	C4-H4---O2	149.57
(C4)H4 --- O2(As1)	2.343(15)		

Although it is not possible to fully resolve with the data collected, it is likely that the unshared oxygen on the arsenic tetrahedra is terminated by a hydrogen atom. This is further supported by bond valence calculations as an unprotonated terminal oxygen has a BV Σ deviation of -0.74 v. u. which would be balanced by the proximity of a proton and the hydrogen bond.

EDS analysis confirmed semi-quantitatively that there was arsenic and oxygen present in the structure and an SEM image is presented in figure 5.

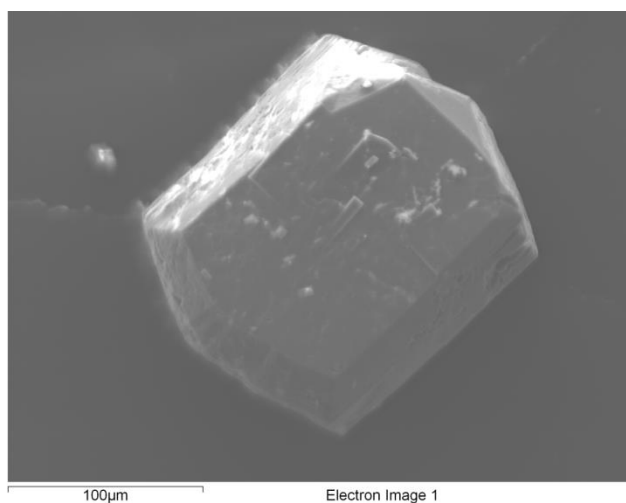


Figure 5: SEM image of a single crystal of $[\text{AsO}_3(\text{OH})\text{Be}(\text{C}_3\text{H}_4\text{N}_2)]$

A TGA investigation was carried out and in combination with VTPXD indicated that $[\text{AsO}_3(\text{OH})\text{Be}(\text{C}_3\text{H}_4\text{N}_2)]$ is thermally stable up to approximately 420 °C [Fig. 6]. Up to 340 °C there is a gradual 6 % reduction in mass related to the loss of surface water. Between 340 °C and 420 °C a steep exothermic loss of mass is observed which corresponds to the removal of propene-1-amine, a decomposition product of imidazole (observed: 24 %, calculated: 24.8 %). Above 420 °C there is a rapid fall in mass followed by a Gaussian tail off which represents the decomposition of the chain structure.

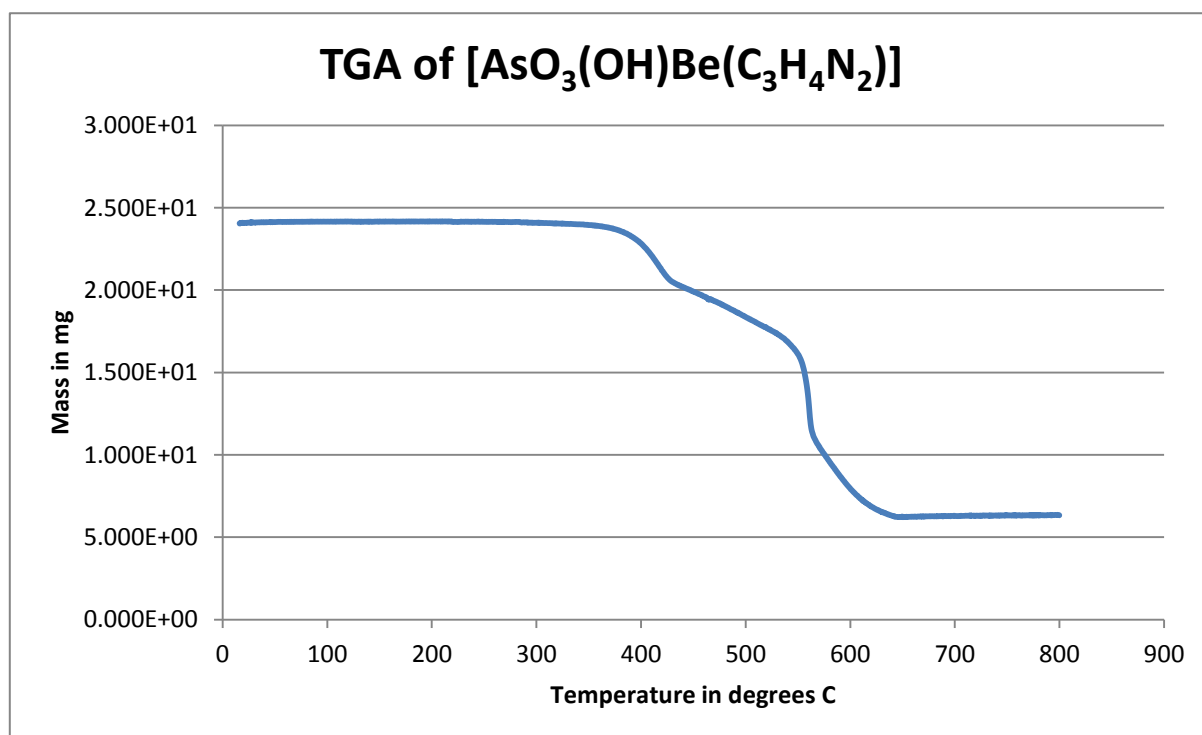


Figure 6: TGA of $[\text{AsO}_3(\text{OH})\text{Be}(\text{C}_3\text{H}_4\text{N}_2)]$

3.3: Na₂[AsO₄Be(OH)]•½ H₂O

A combination of colourless blocks and small colourless needles were produced as a mixed phase in basic conditions in the presence of sodium hydroxide and N-(3-aminopropyl)-1,3-propanediamine. Single crystals of both morphologies were selected for single crystal X-ray diffraction and the blocks were elucidated to being sodium arsenate (NaH₂AsO₄). The needles were found to be a novel one dimensional chain structure of composition Na₂[AsO₄Be(OH)]•1/2H₂O with the crystallographic parameters summarised in table 8. The structure possesses orthorhombic symmetry and is formed of a chain of consecutively bonded beryllium tetrahedra along *c*. Arsenic tetrahedra alternate along either side of the chain in the *a/c* plane to form a sinusoidal chain of 3Rs as shown in figure 7. The arsenic site is fully tetrahedral, sharing two oxygen positions with the beryllium chain and having two terminating oxygen positions. The tetrahedral beryllium sites are linked via a hydroxyl bridge, the hydrogen of which is intrinsically responsible for the structures stability due to it hydrogen bonding between chains. The extra-framework space is occupied by two fully occupied crystallographically unique sodium sites and a 50 % occupied water position.

Table 8: Crystallographic parameters for Na₂[AsO₄Be(OH)]•½H₂O

Empirical formula	Na ₂ [AsO ₄ Be(OH)]•½H ₂ O
Formula weight	218.9
Appearance	Colourless flat needle
Temperature	120 K
Wavelength	0.71073 Å
Crystal system	Orthorhombic
Space group	Aba 2
<i>a</i>	16.9989(10) Å
<i>b</i>	10.5321(6) Å
<i>c</i>	5.5441(3) Å
Volume	992.58(1) Å ³
<i>Z</i>	8
<i>D_c</i>	2.93 g cm ⁻³
R index	0.0366
Weighted R index	0.0844

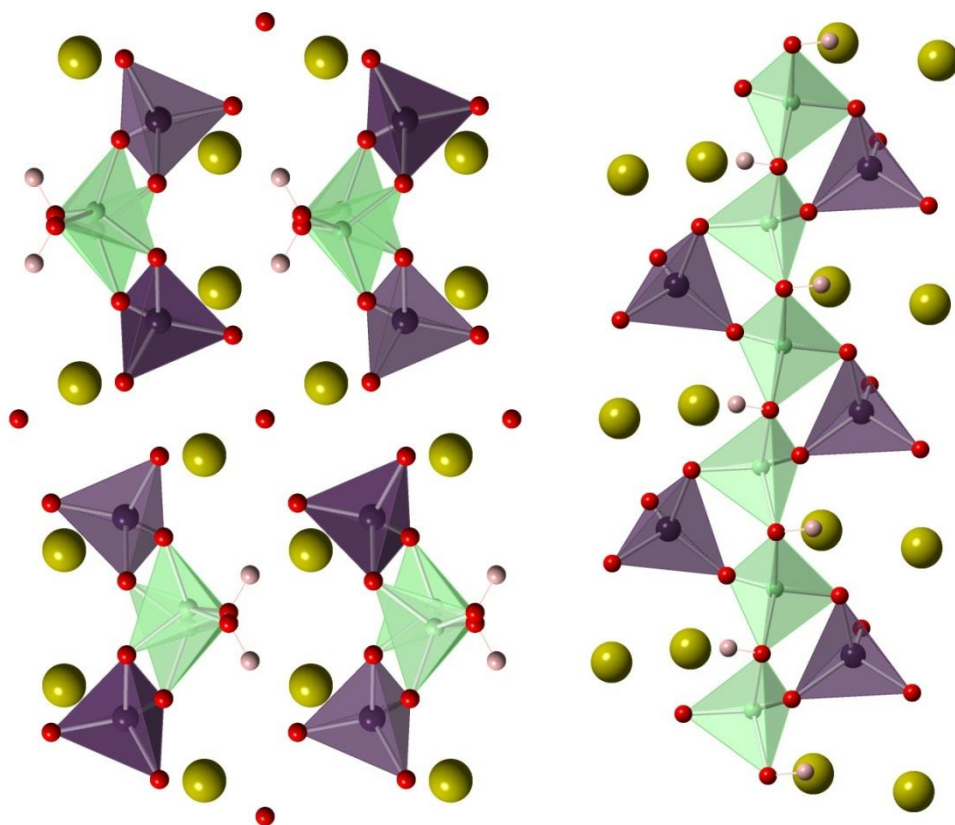


Figure 7a/b: $\text{Na}_2[\text{AsO}_4\text{Be}(\text{OH})]\cdot\frac{1}{2}\text{H}_2\text{O}$ viewed along c and b . The beryllate chain is clearly visible when viewed down b . Green and purple tetrahedral are beryllium and arsenic. Yellow, red and pink spheres are sodium, oxygen and hydrogen respectively.

The hydroxyl character of the bridging group between the two beryllium tetrahedra is inferred from the difference map and confirmed by bond valence calculations since without including hydrogen bonding the oxygen is underbonded with a calculated deviation of -0.79 v.u. Hydroxyl bridging is a common phenomenon in berylloarsenate frameworks and has been encountered in several other structures presented in this thesis, and is due to the oxygen bridging two divalent species requiring a further proton to balance the charge imbalance. In this way many berylloarsenate structures that have been produced in this study can be regarded as having ‘built in’ Brønsted sites rather than requiring the calcining and ammonisation steps classically used to produce Brønsted sites. The acidity of these sites is likely strong and could be confirmed by FTIR if a phase pure sample could be isolated. In this case the hydroxyl group is also responsible for further structure stabilisation *via* strong, short distance hydrogen bonding between columns of chains [Fig 8] the bond distances are presented in table 9 along with other selected lengths and angles.

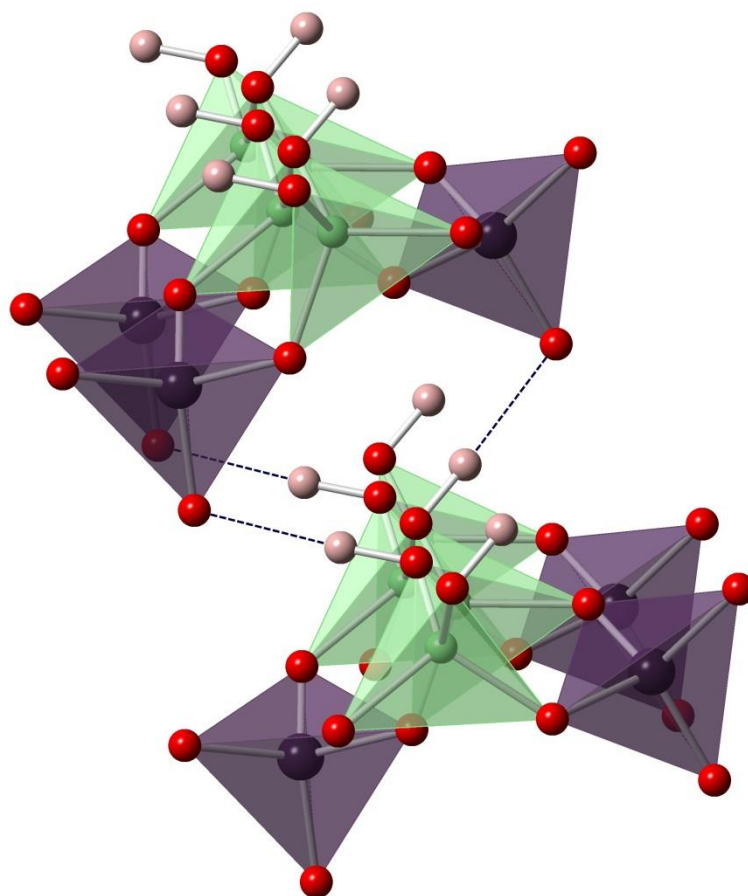


Figure 8:Hydrogen bonding (dashed lines) between chains, note that hydrogen bonding is only present between columns, not rows. Green and purple tetrahedra are Be and As respectively, pink and red spheres are hydrogen and oxygen.

Table 9: Selected bond distances and angles in $\text{Na}_2[\text{AsO}_4\text{Be}(\text{OH})]\cdot\frac{1}{2}\text{H}_2\text{O}$

Bond	Bond length (Å)	Bond	Bond angle (°)
Average As – O	1.689(5)	As – O2 – Be	122.84(4)
Average Be – O	1.643(10)	O5 – H --- O3	171.03(13)
Be – O5H	1.661(1)	Be – O5H – Be	116.43(13)
H – O5	0.938(6)		
(O5)H --- O3	1.841(4)		
Average Na1 – O	2.340(7)		
Average Na2 – O	2.420(6)		

Further structural stabilisation is in the form of the two fully occupied octahedrally coordinated sodium sites, which also play a structure directing as well as charge balancing role. The OSDA present in the synthesis is not observed within the crystal structure and so likely only plays a pH balancing role during the reaction. The only extra-framework species present within this structure is a

50 % occupied water site, due to the low occupancy it is impossible to resolve the hydrogen positions however it is likely that the identity of this site is correct. Further characterisation was carried out in the form of semi-quantitative EDS measurements which confirmed the presence of arsenic and sodium as well as producing a SEM image presented in figure 9.

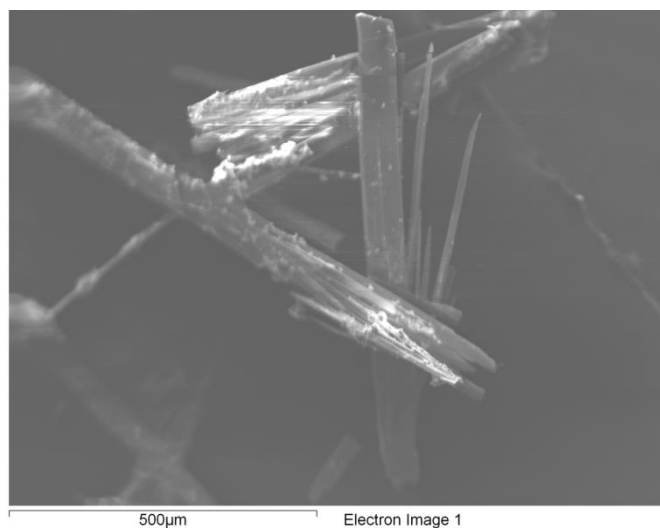


Figure 9: SEM image of $\text{Na}_2[\text{AsO}_4\text{Be}(\text{OH})] \cdot \frac{1}{2}\text{H}_2\text{O}$ clearly showing the plate-like needle morphology

3.4: $[\{\text{H-pyridine}\}_{0.5}][(\text{As}_{0.785}\text{Be}_{0.215})_2(\text{As}_{0.17}\text{Be}_{0.83})_2\text{O}_7(\text{OH})_2]\cdot 0.65\text{H}_2\text{O}$

This material crystallised as large colourless rods, one of which was deemed high enough quality for single crystal X-ray diffraction and the resultant summary of crystallographic parameters is presented in table 13. $[\{\text{H-pyridine}\}_{0.5}][(\text{As}_{0.785}\text{Be}_{0.215})_2(\text{As}_{0.17}\text{Be}_{0.83})_2\text{O}_7(\text{OH})_2]\cdot 0.65\text{H}_2\text{O}^{[12]}$ is a highly disordered one dimensional tetragonal structure which is formed of infinite tubes aligned parallel with the c axis. These tubes are formed of elliptical 8Rs of oxygen bridged tetrahedra which alternate in their orientation between having the point of the ellipses aligned along a or b . The alternation follows a pattern of AABBA where A is aligned along the a axis and *vice versa*. Each 8R in the alternate orientation is connected to the next in sequence so that eight 4Rs are formed, however, the 8Rs in the same orientation are only joined via two 4Rs and form 8R channels through the tubes parallel to b [Fig 10].

All of the tetrahedra are seemingly mixed sites between beryllium and arsenic with two sites averaging 83.7 % beryllium and the other two sites averaging 78.5 % arsenic. Despite this level of disorder the majority of sites are fully bonded and there are only two terminated sites present. Between the tubes are highly disordered pyridine sites which are impossible to fully resolve owing to the several different positions possible, however, it is likely these pyridine rings are protonated and stabilise the overall structure via hydrogen bonding and charge balancing. The only other extra-framework species present are two water sites which combined are 65 % occupied and located within the cages formed by the 4- and 8Rs.

Table 10: Summary of crystallographic data for $[\{\text{H-pyridine}\}_{0.5}][(\text{As}_{0.785}\text{Be}_{0.215})_2(\text{As}_{0.17}\text{Be}_{0.83})_2\text{O}_7(\text{OH})_2]\cdot 0.65\text{H}_2\text{O}$

Empirical formula	$[\{\text{H-pyridine}\}_{0.5}]$ $[(\text{As}_{0.785}\text{Be}_{0.215})_2(\text{As}_{0.17}\text{Be}_{0.83})_2\text{O}_7(\text{OH})_2]\cdot 0.65\text{H}_2\text{O}$
Formula weight	165
Appearance	Colourless large rod
Temperature	120 K
Wavelength	0.71073 Å
Crystal system	Tetragonal
Space group	P 4 ₂ /nbc
a	16.9831(5) Å
c	12.7839(6) Å
Volume	3687.21(2) Å ³

Z	32
D _c	2.38 g cm ⁻³
R index	0.0804
Weighted R index	0.1459

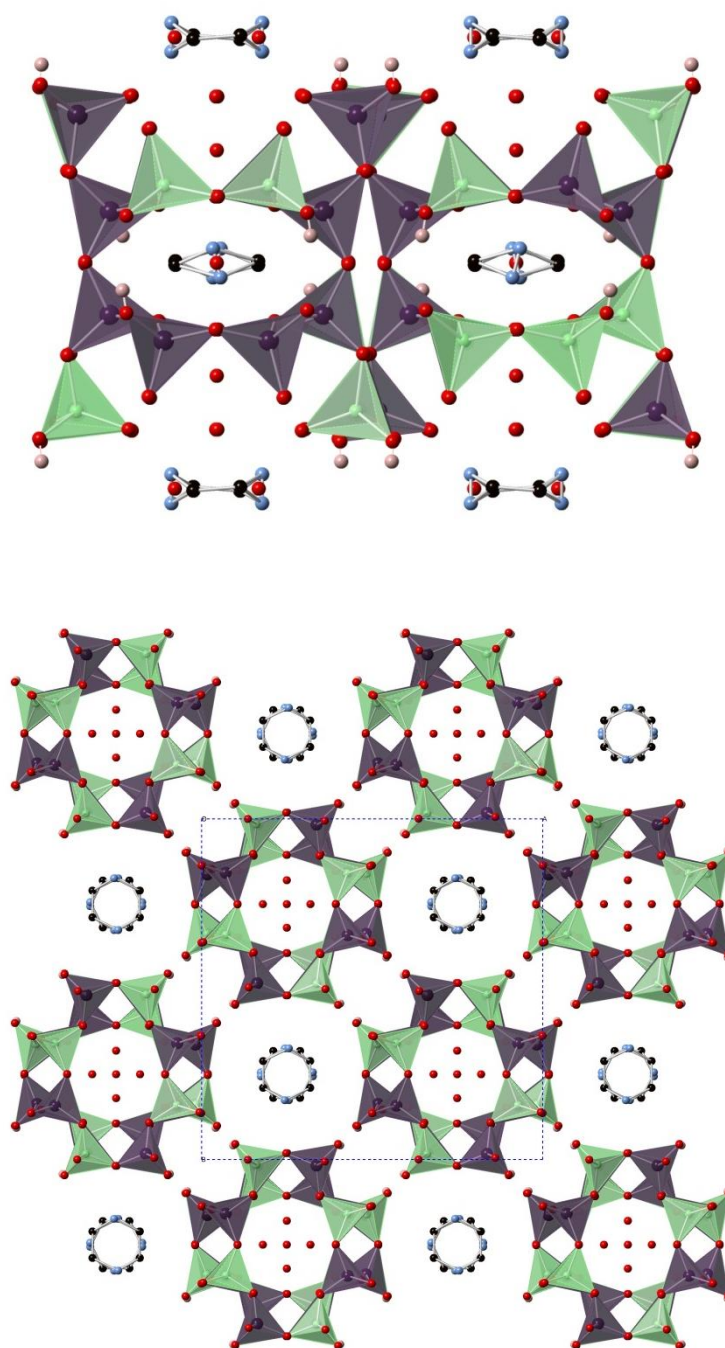


Figure 10a/b: $[(\text{H-pyridine})_{0.5}][(\text{As}_{0.785}\text{Be}_{0.215})_2(\text{As}_{0.17}\text{Be}_{0.83})_2\text{O}_7(\text{OH})_2] \cdot 0.65\text{H}_2\text{O}$ viewed along *b* and *c* respectively. Green and purple tetrahedra are Be and As respectively. Black, pink, blue and red spheres are C, H, N and O respectively.

There are four crystallographically unique T sites present within the structure; each one is jointly occupied by either beryllium or arsenic. As such during refinement each site was allocated as a mixed site and had their thermal and positional parameters constrained together. Two of the sites are predominantly beryllium (83.7 %), supported by a lower average T – O bond distance of 1.634(10) and 1.631(11) Å whereas the other two sites are predominantly arsenic (78.5 %) and this is again reflected in the bond distances, this time with the longer distances of 1.678(9) and 1.679(8) Å. The shared sites As3/Be3 (83.7 % Be) and As1/Be1 (78.5 % As) are both fully connected to other T sites via vertex sharing whereas sites As2/Be2 (78.5 % As) and As4/Be4 (83.7 % Be) both have a single terminating hydroxyl group. Further information on bond distances and angles can be found in Table 11.

Table 11: Selected bond distances and angles

Bond	Bond length (Å)	Bond	Bond angle (°)
Average As1/Be1 – O	1.678(9)	As1/Be1 – O8 – As4/Be4	118.27(5)
Average As2/Be2 – O	1.679(8)	As1/Be1 – O5 – As4/Be4	171.03(6)
Average As3/Be3 – O	1.634(10)	As1/Be1 – O7 – As3/Be3	126.85(5)
Average As4/Be4 – O	1.631(11)	As1/Be1 – O6 – As3/Be3	136.07(5)
		As2/Be2 – O4 – As3/Be3	131.82(6)
		As2/Be2 – O2 – As4/Be4	131.21(5)
		As2/Be2 – O3 – As3/Be3	128.46(6)

The regular 8R is an extremely common and stable secondary building unit in zeolitic frameworks, however the 8Rs encountered within this structure are the first of a trend of distorted secondary building units that occur in berylloarsenates. When compared with the naturally occurring zeolite paulingite [Fig. 11] a major difference in T – O – T angles is observed, for paulingite the average 8R angle is: 145.36 ° whereas for $[\{H\text{-pyridine}\}_{0.5}][(\text{As}_{0.785}\text{Be}_{0.215})_2(\text{As}_{0.17}\text{Be}_{0.83})_2\text{O}_7(\text{OH})_2]\cdot 0.65\text{H}_2\text{O}$ it is 131.89 °. This difference has a huge effect on the overall structure, changing an open aperture into a much narrower elliptical aperture which is likely to stabilise the formation of new structures or modify existing ones.

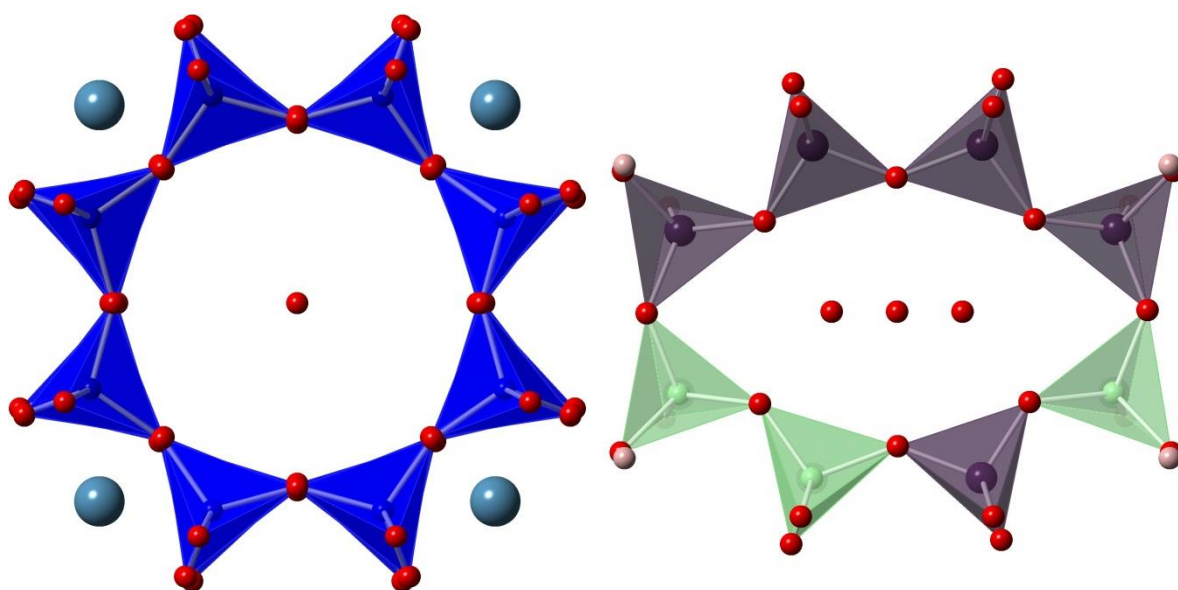


Figure 11a/b: Left is the 8R present in paulingite, right is the 8R present in $[\{H\text{-pyridine}\}_{0.5}][(\text{As}_{0.785}\text{Be}_{0.215})_2(\text{As}_{0.17}\text{Be}_{0.83})_2\text{O}_7(\text{OH})_2] \cdot 0.65\text{H}_2\text{O}$ with an obvious difference in shape. Blue, green and purple tetrahedra are silicon, beryllium and arsenic respectively. Blue, red and pink spheres are calcium, oxygen and hydrogen.

The thermal stability of $[\{H\text{-pyridine}\}_{0.5}][(\text{As}_{0.785}\text{Be}_{0.215})_2(\text{As}_{0.17}\text{Be}_{0.83})_2\text{O}_7(\text{OH})_2] \cdot 0.65\text{H}_2\text{O}$ has also been investigated by TGA measurements [Fig. 12]. No reduction in mass is observed in the TGA until approximately 250 °C where there is a gradual decrease in 13.49 % of mass until approximately 400 °C. This corresponds to the loss of both the pyridine and the extra-framework water (calculated as 14.26 %), which causes the long range ordering of the structure to collapse).

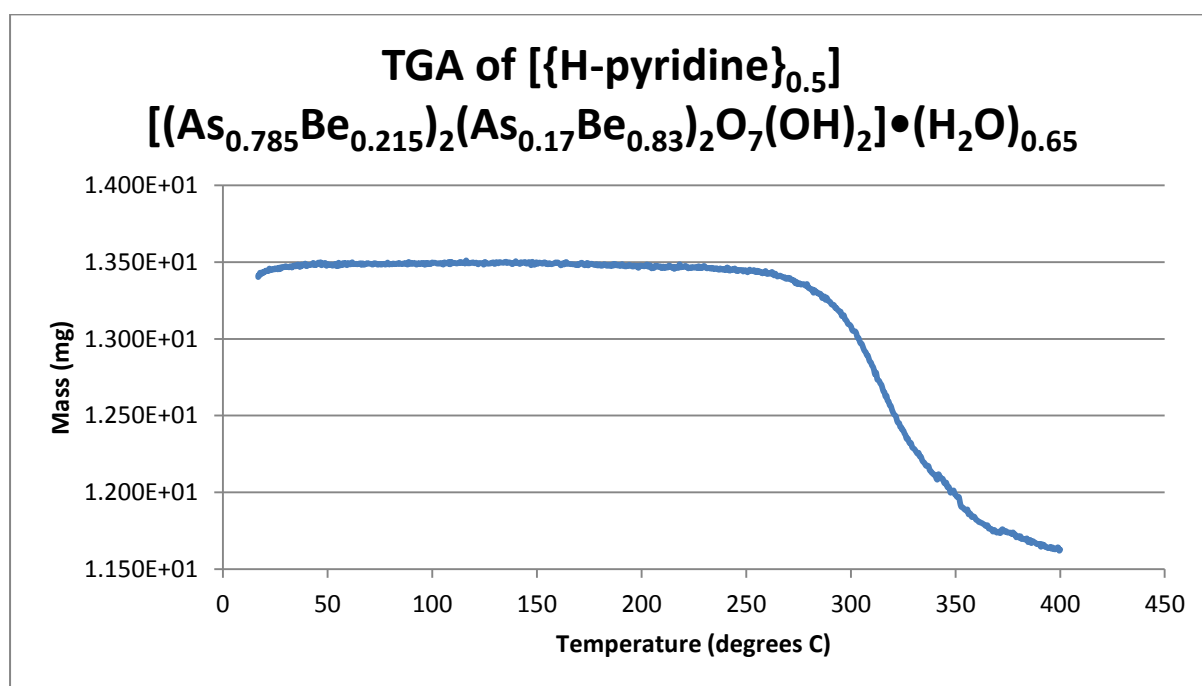


Figure 12: TGA of $[\{H\text{-pyridine}\}_{0.5}][(\text{As}_{0.785}\text{Be}_{0.215})_2(\text{As}_{0.17}\text{Be}_{0.83})_2\text{O}_7(\text{OH})_2] \cdot 0.65\text{H}_2\text{O}$

EDS measurements have confirmed semi-quantitatively (As:O, 33:66) the presence of arsenic and oxygen within the structure and while they were collected a SEM image of the crystalline material was acquired which confirms the large rod-like morphology of $[\{H\text{-pyridine}\}_{0.5}][(\text{As}_{0.785}\text{Be}_{0.215})_2(\text{As}_{0.17}\text{Be}_{0.83})_2\text{O}_7(\text{OH})_2] \cdot 0.65\text{H}_2\text{O}$ (Fig. 13).

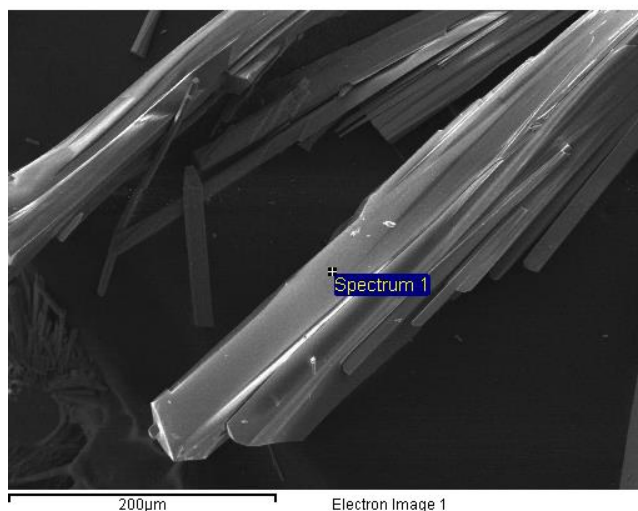


Figure 13: SEM image of $[\{H\text{-pyridine}\}_{0.5}][(\text{As}_{0.785}\text{Be}_{0.215})_2(\text{As}_{0.17}\text{Be}_{0.83})_2\text{O}_7(\text{OH})_2] \cdot 0.65\text{H}_2\text{O}$

3.5: $\text{Sr}[\text{AsO}_4\text{Be}(\text{OH})]\cdot(\text{H}_2\text{O})_{0.0685}$

Colourless rhombohedral crystals of $\text{Sr}[\text{AsO}_4\text{Be}(\text{OH})]\cdot(\text{H}_2\text{O})_{0.0685}$ ^[14] form hydrothermally in the presence of tetraethylammonium hydroxide and strontium hydroxide. The monoclinic network structure has the $\text{P2}_1/\text{c}$ space group and is formed of two crystallographically unique T atom sites, one each fully occupied by arsenic and beryllium. The tetrahedra are oxygen bridged to form an infinite two dimensional lattice of 4- and 8Rs along the b/c plane where each layer is separated by a divalent strontium cation and a single water site. Full crystallographic parameters are given in table 12.

Table 12: Crystallographic parameters for $\text{Sr}[\text{AsO}_4\text{Be}(\text{OH})]\cdot(\text{H}_2\text{O})_{0.0685}$

Empirical formula	$\text{Sr}[\text{AsO}_4\text{Be}(\text{OH})]\cdot(\text{H}_2\text{O})_{0.0685}$
Formula weight	253.6
Appearance	Colourless kite-shaped plate
Temperature	120 K
Wavelength	0.71073 Å
Crystal system	Monoclinic
Space group	$\text{P2}_1/\text{c}$
a	5.0833(2) Å
b	7.9685(3) Å
c	10.2929(4) Å
β	90.638(2) °
Volume	416.90(3) Å ³
Z	4
D_c	2.81 g cm ⁻³
R index	0.0240
Weighted R index	0.0264

The overall structure is comprised of repeated distorted 4R secondary building units which are roughly aligned along the b/c plane. Each corner of the 4Rs are connected to another 4R and this connectivity forms highly distorted elliptical 8R channels running through the network along a (Fig. 14). The degree of distortion on the 8Rs is highly significant since the average T – O – T' angle is 120.68 ° compared to the angle of 145.36 ° encountered in paulingite. The apical point of the beryllium tetrahedra which is orientated perpendicular to the plane of the 4R, is terminated by a hydroxyl group which stabilises the overall structure by strong (O---H: 1.39 Å) hydrogen bonding to the extra-framework water position (Fig. 15). Further structure stabilisation and charge balancing is provided by the 8 coordinate divalent strontium which exhibits square antiprismatic geometry in its

coordination to the framework oxygen and is located in the void between 8Rs in different layers (Fig. 16).

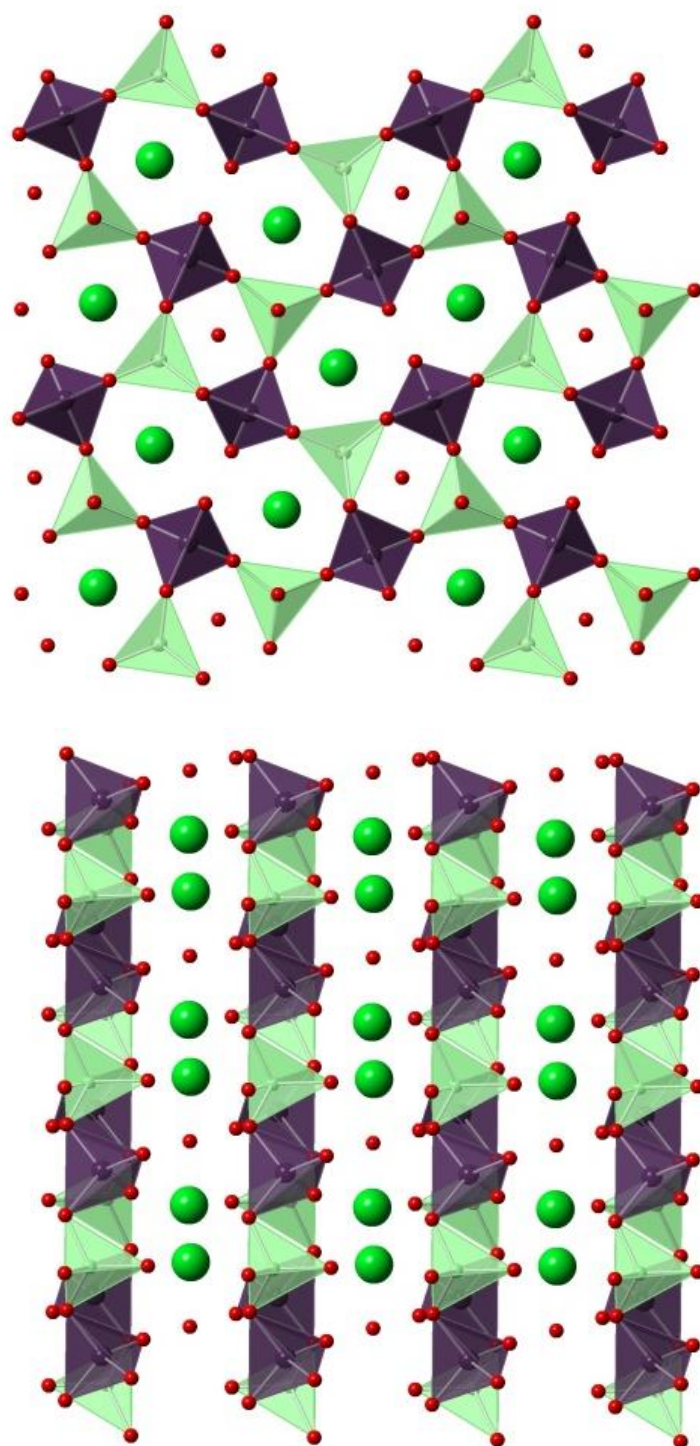


Figure 14: $\text{Sr}[\text{AsO}_3\text{Be}(\text{OH})]\cdot(\text{H}_2\text{O})_{0.0685}$ viewed along a and b , green and purple tetrahedra are Be and As centred respectively. Pink, red and green spheres represent H, O and Sr respectively.

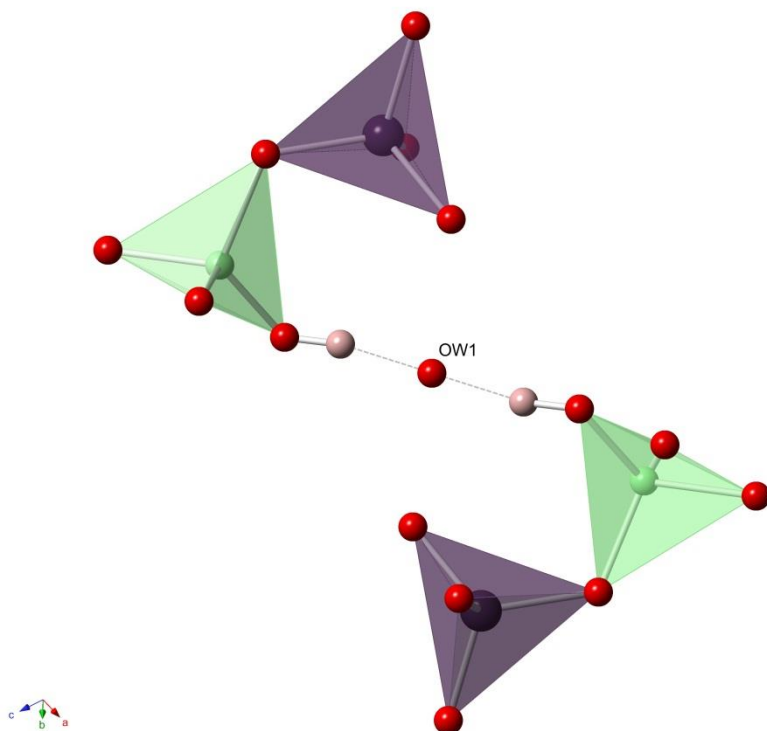


Figure 15: Hydrogen bonding between network and extra-framework water species

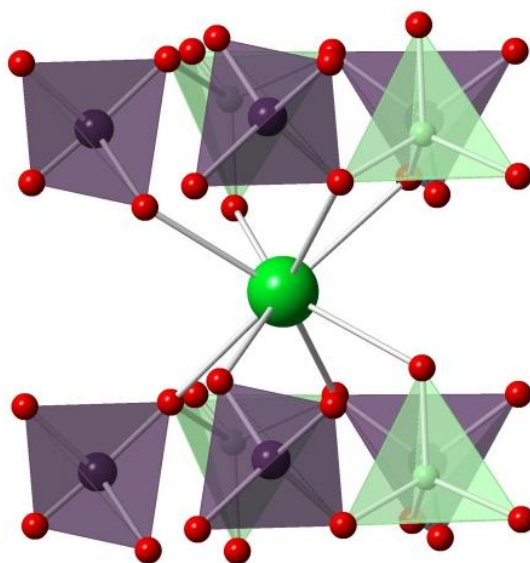


Figure 16: Sr coordination geometry in $\text{Sr}[\text{AsO}_3\text{Be}(\text{OH})]\cdot(\text{H}_2\text{O})_{0.0685}$. Green and purple tetrahedra are Be and As centred respectively. Pink, red and green spheres represent H, O and Sr respectively

The beryllium centred tetrahedra are slightly distorted due to the shortening of the Be – OH bond distance to 1.612(7) Å, this is due to the steric and electrostatic influence of the proximity of the

extra-framework water position. The hydroxyl groups character is confirmed by bond valence calculations where the BV sum deviation is 0.13 v. u. this is due to the short O – H bond distance (0.9426 (10) Å), however it was necessary to constrain this distance to produce reasonable thermal parameters for the hydrogen position. It is possible that the framework hydrogen is actually shared between the extra-framework water position and the framework, however this has proven challenging to resolve using X-ray data. Selected bond distances and angles are presented in table 13.

The presence of the eight coordinate strontium between the networks suggests a structure directing role for this reagent, since the OSDA is not observed in any form it is likely that its role in the synthesis is only pH control. Semi-quantitative EDS measurements were carried out on a spray of crystals which confirmed the presence of arsenic, oxygen and strontium. A SEM image was also acquired (Fig. 17) which shows the morphology and form of crystal growth of $\text{Sr}[\text{AsO}_3\text{Be}(\text{OH})]\cdot(\text{H}_2\text{O})_{0.0685}$.

Table 13: Selected bond distances and angles for $\text{Sr}[\text{AsO}_3\text{Be}(\text{OH})]\cdot(\text{H}_2\text{O})_{0.0685}$

Bond	Bond length (Å)	Bond	Bond angle (°)
Average As – O	1.687(3)	Average O – As – O	109.42(14)
Average Be – O	1.651(7)	Average O – Be – O	109.31(4)
Average Sr – O	2.607(3)		
Be – OH	1.612(7)		

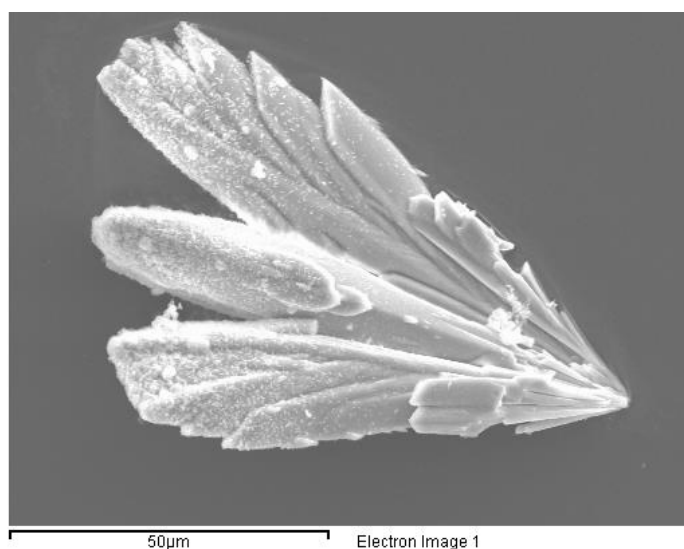


Figure 17: SEM image of $\text{Sr}[\text{AsO}_3\text{Be}(\text{OH})]\cdot(\text{H}_2\text{O})_{0.0685}$ exhibiting growth of kite crystals in a spray formation from a single point of nucleation

3.6: $\text{AsO}_4\text{Be}(\text{OH}_2)\text{Be}(\text{OH})(\text{OH}_2)$

A single irregularly shaped colourless needle crystal of $\text{AsO}_4\text{Be}(\text{OH}_2)\text{Be}(\text{OH})(\text{OH}_2)$ was isolated and analysed via single crystal X-ray diffraction, the resulting two dimensional monoclinic structure exhibits some features which are observed frequently in the more complicated berylloarsenate structures. The layers of $\text{AsO}_4\text{Be}(\text{OH}_2)\text{Be}(\text{OH})(\text{OH}_2)$ are aligned along the b/ac plane and are formed exclusively of the 3-4-3 secondary building unit which is a zig-zag of two 3Rs in the same orientation connected by a 4R. The 3Rs are formed of two beryllium and one arsenic centred tetrahedra and the apical beryllium tetrahedra is oxygen bridged to the 4R of the next 3-4-3 SBU, thus forming the repeating structure (Fig. 18/19). The layers are cross-linked via extensive hydrogen bond interaction between terminating and bridging hydroxyl and water groups. Crystallographic parameters are summarised in table 14.

Table 14: Crystallographic parameters for $\text{AsO}_4\text{Be}(\text{OH}_2)\text{Be}(\text{OH})(\text{OH}_2)$

Empirical formula	$\text{AsO}_4\text{Be}(\text{OH}_2)\text{Be}(\text{OH})(\text{OH}_2)$
Formula weight	209.9
Appearance	Colourless irregular needle
Temperature	120 K
Wavelength	0.71073 Å
Crystal system	Monoclinic
Space group	$P2_1/n$
a	6.4806(2) Å
b	11.0971(4) Å
c	8.4133(2) Å
β	105.881(2) °
Volume	581.96(3) Å ³
Z	4
D_c	2.40 g cm ⁻³
R index	0.0199
Weighted R index	0.0219

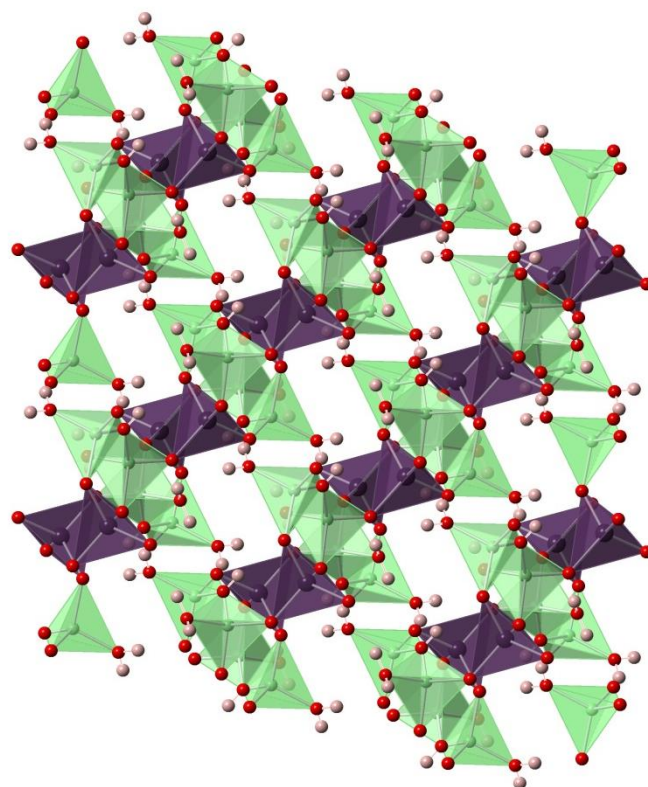
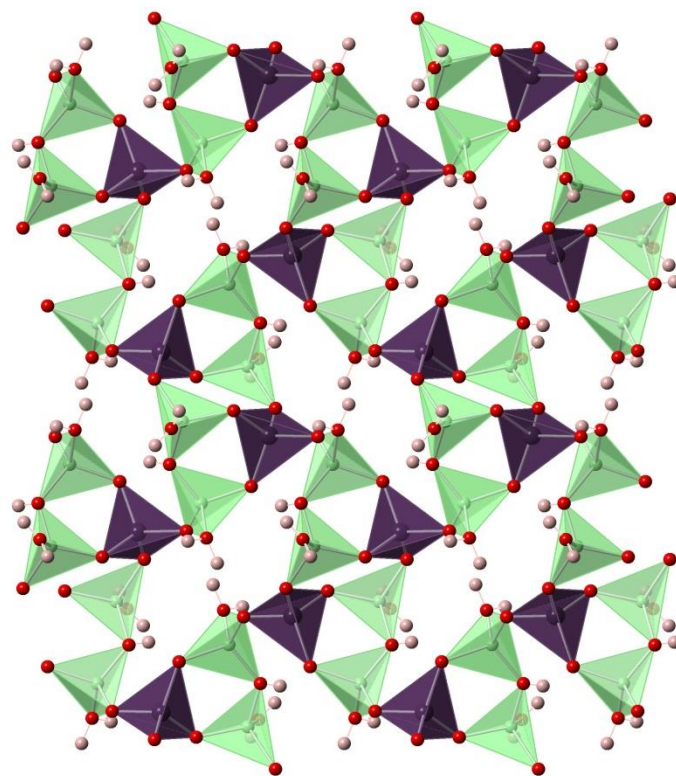


Figure 18a/b: $\text{AsO}_4\text{Be}(\text{OH}_2)\text{Be}(\text{OH})(\text{OH}_2)$ viewed along a and b crystallographic axis. Green and purple tetrahedral are beryllium and arsenic. Red and pink spheres are oxygen and hydrogen.

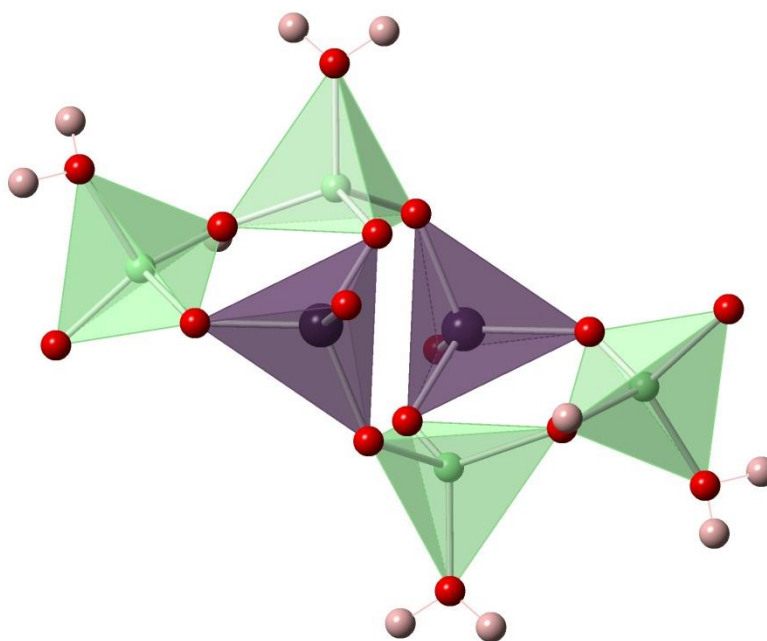


Figure 19: 3-4-3 SBU found in $\text{AsO}_4\text{Be}(\text{OH}_2)\text{Be}(\text{OH})(\text{OH}_2)$. Green and purple tetrahedral are beryllium and arsenic. Red and pink spheres are oxygen and hydrogen.

The connectivity of the 3-4-3 SBU leads to the formation of rhomboid 10R channels running through the network along the a axis. Where most zeolitic T-atom sites are bridged via oxygen, this structure contains a permanently protonated oxygen bridge between the two unique beryllium sites. Although uncommon, this form of bridging has been encountered before in the naturally occurring beryllophosphate zeotype, weinebeneite (WEI).^[15] It can be predicted that if the structure did not contain permanent sites of protonation then the oxygen atoms would charge imbalance due to the proximity to divalent beryllium, leading to a highly negative overall framework charge. This permanent protonation is confirmed by comparison with the bond distances present in WEI and bond valence calculations [Table 15]. Protonation of the framework is also present in the form of water termination of the apical beryllium sites, extensive hydrogen bonding between these sites and the adjoining layer provides structural stabilisation as well as charge balancing. There is no extra-framework species present within the pores, owing to the high degree of steric hindrance that would be encountered, therefore where pyridine is present in the reaction medium, it can be envisaged that it only has a pH controlling role.

Table 15: Selected bond distances, angles and bond valence values for $\text{AsO}_4\text{Be}(\text{OH}_2)\text{Be}(\text{OH})(\text{OH}_2)$

Bond	Bond length (Å)	Bond	Bond angle (°)
Average As – O	1.678(15)	Average O – As – O	109.46(8)
Average Be1 – O	1.633(3)	Average O – Be1 – O	109.33(18)
Average Be2 – O	1.621(3)	Average O – Be2 – O	109.42(19)

Be1 – (OH ₂)	1.678(3)	H2 – O7 – H1	111.88(11)
Be1 – OH	1.595(3)	H4 – O6 – H5	104.80(9)
Be2 – (OH ₂)	1.636(3)		
Be2 – OH	1.604(3)		
Bridging O – H	0.888(2)		
WEI bridging O – H	0.890(2)		
BV-sum deviation of bridging O5	0.05 v.u.		

Aside from the unusual bridging hydroxyl group encountered in this structure, the most interesting feature is the extremely high degree of strong and complex (1.827 – 1.919 (5) Å) inter-network hydrogen bonding [Fig. 20]. This causes a condensed interlayer distance which explains the lack of extra framework species. Each apical water group is hydrogen bonded to both the adjacent layer and to its own layer, further stabilising the network.

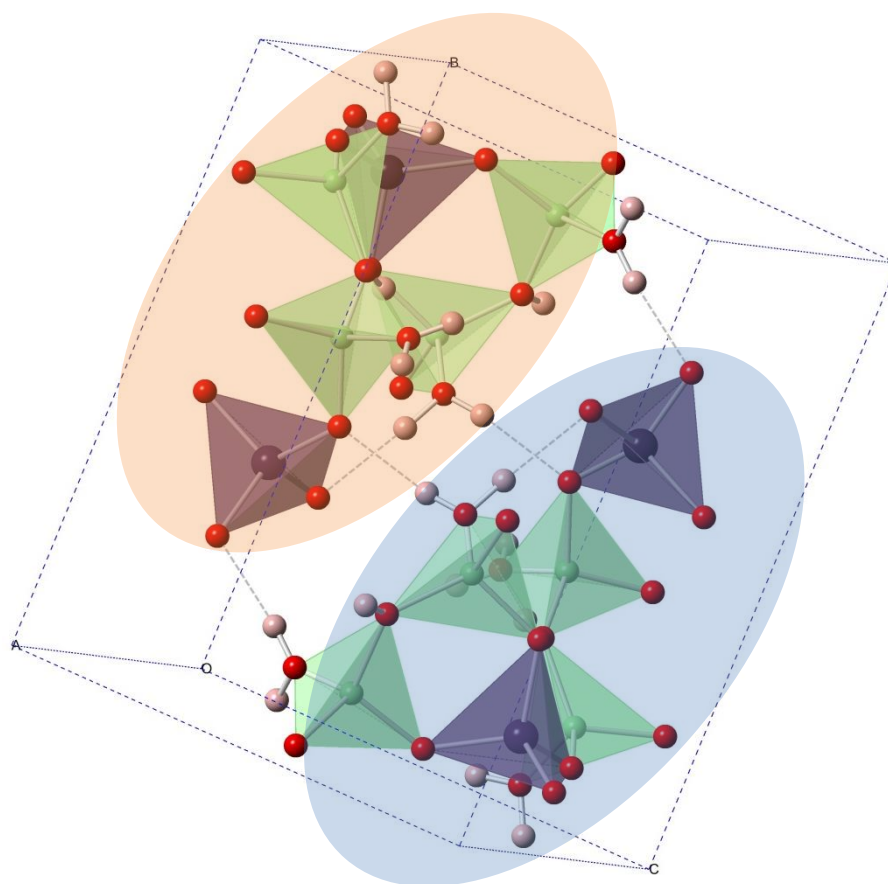


Figure 20: Extent of hydrogen bonding present in $\text{AsO}_4\text{Be}(\text{OH}_2)\text{BeOH}(\text{OH}_2)$, hydrogen bonds are represented as dashed lines, the two different networks present in this image are shaded blue and orange.

Semi-quantitative EDS measurements were carried out on a cluster of crystals which confirmed the presence of arsenic and oxygen. A SEM image was also acquired [Fig. 21] which shows the morphology and form of crystal growth of $\text{AsO}_4\text{Be}(\text{OH})_2\text{BeOH}(\text{OH}_2)$.

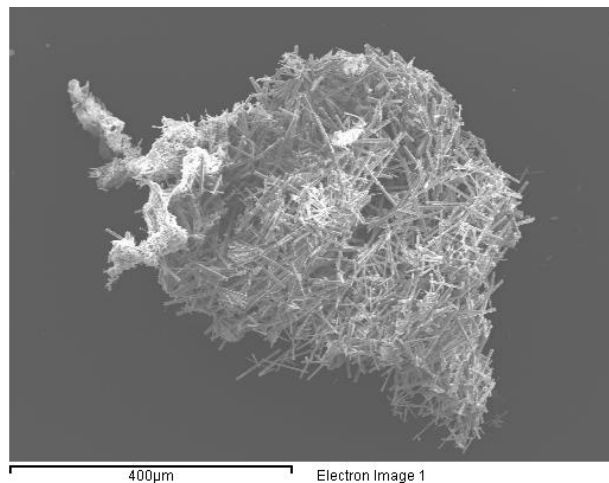


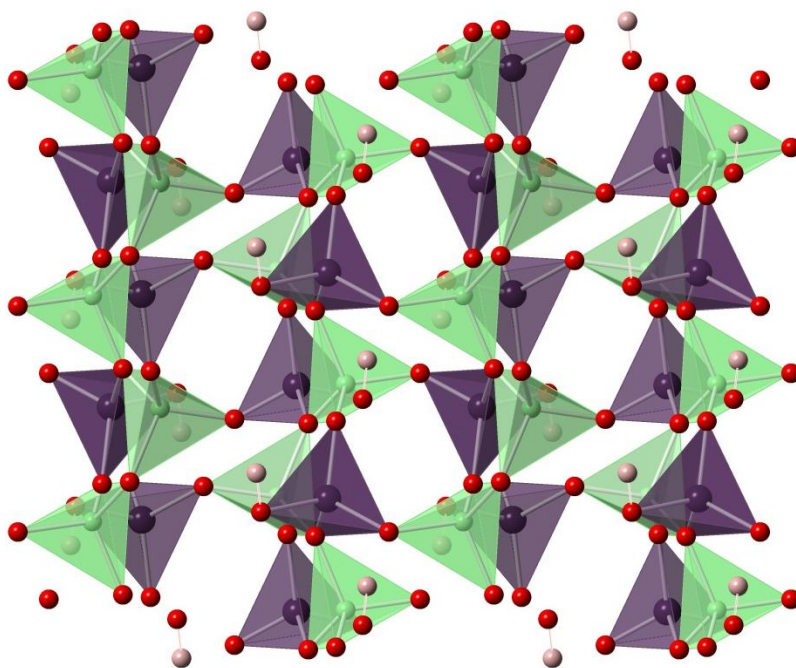
Figure 21: SEM image of $\text{AsO}_4\text{Be}(\text{OH})_2\text{BeOH}(\text{OH}_2)$ exhibiting its needle morphology.

3.7: AsO₃(OH)Be

AsO₃(OH)Be crystallises as a minor phase (AsO₃(OH)Be 10 %, starting material 90 %) exhibiting irregular plate morphology. A suitable crystal was selected and analysed via single crystal X-ray diffraction. The resulting two dimensional framework crystallises in the monoclinic crystal system and P2₁/n space group, its crystallographic parameters are presented in Table 16. This structure is one of the few formed solvothermally in ethanol with only reagent quantities of water present, impacting the mobility of the reagents present owing to their low solubility in organic solvents. The reduced reagent mobility has led to the formation of similar structural features to the previously reported AsO₄Be(OH)₂BeOH(OH₂) (section 3.6) but exhibiting a much more dense overall structure (calc. density of 3.4 gcm⁻³ as opposed to 2.4 gcm⁻³). AsO₃(OH)Be is formed of networks of distorted 4- and 3Rs along the *a/c* plane which are composed of chains of consecutive vertex sharing Be-centred tetrahedra bridged by triply bonded Be-O(As)-Be units to form the 3-4-3 SBU. The layers are then cross-linked by hydrogen bonding from hydroxyl termination on apical As centred tetrahedra [Fig. 22].

Table 16: Crystallographic parameters for AsO₃(OH)Be

Empirical formula	AsO ₃ (OH)Be
Formula weight	148.9
Appearance	Colourless plate
Temperature	120 K
Wavelength	0.71073 Å
Crystal system	Monoclinic
Space group	P2 ₁ /n
<i>a</i>	7.9210(5) Å
<i>b</i>	4.7267(3) Å
<i>c</i>	7.9527(6) Å
β	102.334(4) °
Volume	290.88(3) Å ³
<i>Z</i>	4
D _c	3.40 g cm ⁻³
R index	0.0437
Weighted R index	0.1235



a

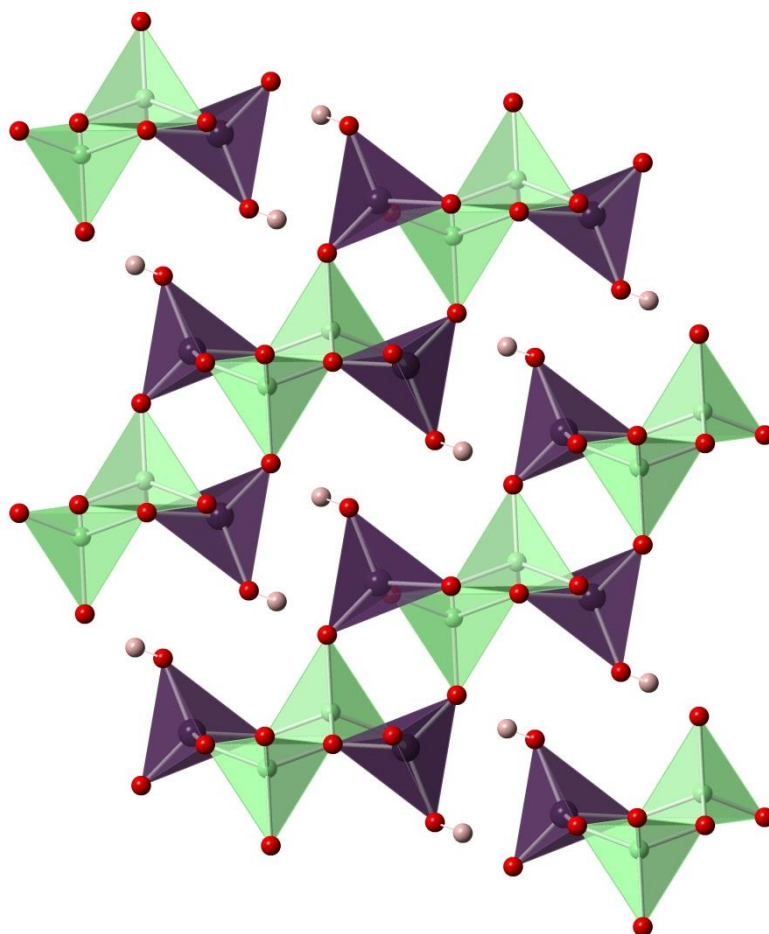


Figure 22a/b: $\text{AsO}_3(\text{OH})\text{Be}$ viewed along *a* and *b*. Green and purple tetrahedral are beryllium and arsenic. Red and pink spheres are oxygen and hydrogen.

There are two unique T atom sites present within $\text{AsO}_3(\text{OH})\text{Be}$. The As tetrahedra share two vertices with single beryllium tetrahedra, one vertex with two beryllium tetrahedra with the final vertex terminated by a hydroxyl group. Subsequently the beryllium environment is fully connected with two vertices shared with arsenic tetrahedra and the remaining two shared with arsenic and symmetry related beryllium tetrahedra. Such connectivity results in a sinusoidal chain of consecutive beryllium tetrahedra running along *b*. Each chain is connected to the next *via* an arsenic tetrahedra, leading to the formation of the 3-4-3 SBU observed in $\text{AsO}_4\text{Be}(\text{OH})_2\text{BeOH}(\text{OH}_2)$. The overall network has a low porosity with the largest ring size being a 4R. The hydroxyl terminating group present on the arsenic centre provides vital charge balancing as well as strong hydrogen bonding ($1.691(15) \text{ \AA}$) between the layers.

The connectivity of $\text{AsO}_3(\text{OH})\text{Be}$ leads to the occurrence of a triply bonded oxygen site (O1, figure 23), confirmed through bond valence calculations (table 20), the resulting steric interaction leads to longer bond lengths between the oxygen and the three (two Be and one As) involved tetrahedral sites. The dense structure and lack of extra-framework species can be attributed to the low solubility of the reagents in the primary solvent used, this provides evidence that by controlling the mobility of the reagents you can influence the density of the product.

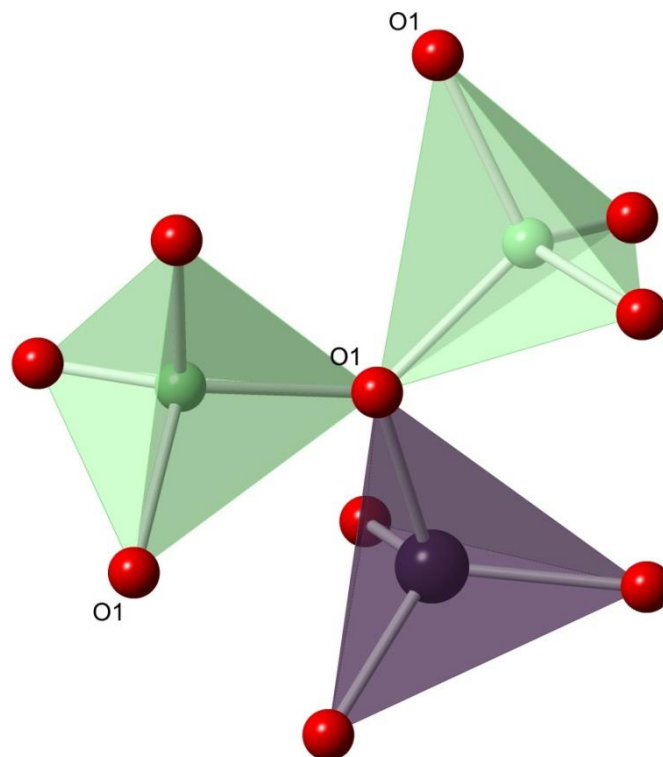


Figure 23: Triply bonded oxygen site in $\text{AsO}_3(\text{OH})\text{Be}$. Green and purple tetrahedral are beryllium and arsenic. Red spheres are oxygen

Table 17: Selected bond distances, angles and bond valence values for $\text{AsO}_3(\text{OH})\text{Be}$

Bond	Bond length (Å)	Bond	Bond angle (°)
Average As – O	1.684(6)	Average O – As – O	109.42(3)
Average Be – O	1.639(13)	Average O – Be – O	109.46(7)
As – OH	1.694(6)		
O1 – Be	1.672(13)		
O1 – Be	1.678(13)		
O1 – As	1.712(6)		
O4 – H	1.003(13)		
BV-sum deviation of triply bonded O1	0.08 v.u.		

Semi-quantitative EDS measurements were carried out on a spray of crystals which confirmed the presence of arsenic and oxygen.

3.8a: $[\text{NH}_4]_2[(\text{AsO}_4)_2\text{Be}_2]\cdot 2\text{H}_2\text{O}$

This phase was the most commonly encountered beryllioarsenate in this study, being formed as a pure phase or co-phase in nine unique experiments. $[\text{NH}_4]_2[(\text{AsO}_4)_2\text{Be}_2]\cdot 2\text{H}_2\text{O}$ crystallises as large (> 1 mm) rhombohedra/octahedra which commonly grow as clusters or have intergrowths of the same phase. A large single crystal was selected and examined *via* single crystal X-ray diffraction and the resulting structure was found to occupy the orthorhombic crystal system in the *Ccca* space group.

$[\text{NH}_4]_2[(\text{AsO}_4)_2\text{Be}_2]\cdot 2\text{H}_2\text{O}$ is a beryllioarsenate analogue of the well-known merlinoite zeolite (MER).^[16] $[\text{NH}_4]_2[(\text{AsO}_4)_2\text{Be}_2]\cdot 2\text{H}_2\text{O}$ is a fully connected three dimensional structure [Fig. 25] formed of slightly twisting double crankshaft chains of 4Rs running parallel with *c*. This is suggested by a *c* length of 9.760 Å (where the repeat distance of a crankshaft chain is between 8.4 – 9.9 Å) and confirmed through visual appreciation of the structure. The connectivity of the double crankshaft chain leads to the formation of elliptical D8R Periodic Building Unit (PBU) which is a distorted equivalent to the channels found in the ACO^[17] framework type. The D8R also connect between *pau* composite building units (CBU) which are formed of 8⁶ and 4¹² Rs. The 8Rs which are part of the *pau* CBU are heavily distorted into elliptical apertures which alternate between having their longest dimension aligned along *a* or *b* leading to constricted 8R channels parallel to *c*. The framework is relatively dense when considered along *a* or *b*, with the largest accessible aperture being from 4Rs. Exchangeable ammonium and two water sites are present as extra-framework space filling species and for charge balancing. Crystallographic parameters can be found in table 18.

Table 18: Crystallographic parameters for $[\text{NH}_4]_2[(\text{AsO}_4)_2\text{Be}_2]\cdot 2\text{H}_2\text{O}$

Empirical formula	$[\text{NH}_4]_2[(\text{AsO}_4)_2\text{Be}_2]\cdot 2\text{H}_2\text{O}$
Formula weight	445.2
Appearance	Large colourless rhombus/octahedra
Temperature	120 K
Wavelength	0.71073 Å
Crystal system	Orthorhombic
Space group	<i>Ccca</i>
<i>a</i>	17.9811(9) Å
<i>b</i>	18.6982(9) Å
<i>c</i>	9.7597(5) Å
Volume	3281.35(3) Å ³
Z	12
D _c	2.70 g cm ⁻³

R index	0.0471
Weighted R index	0.0986

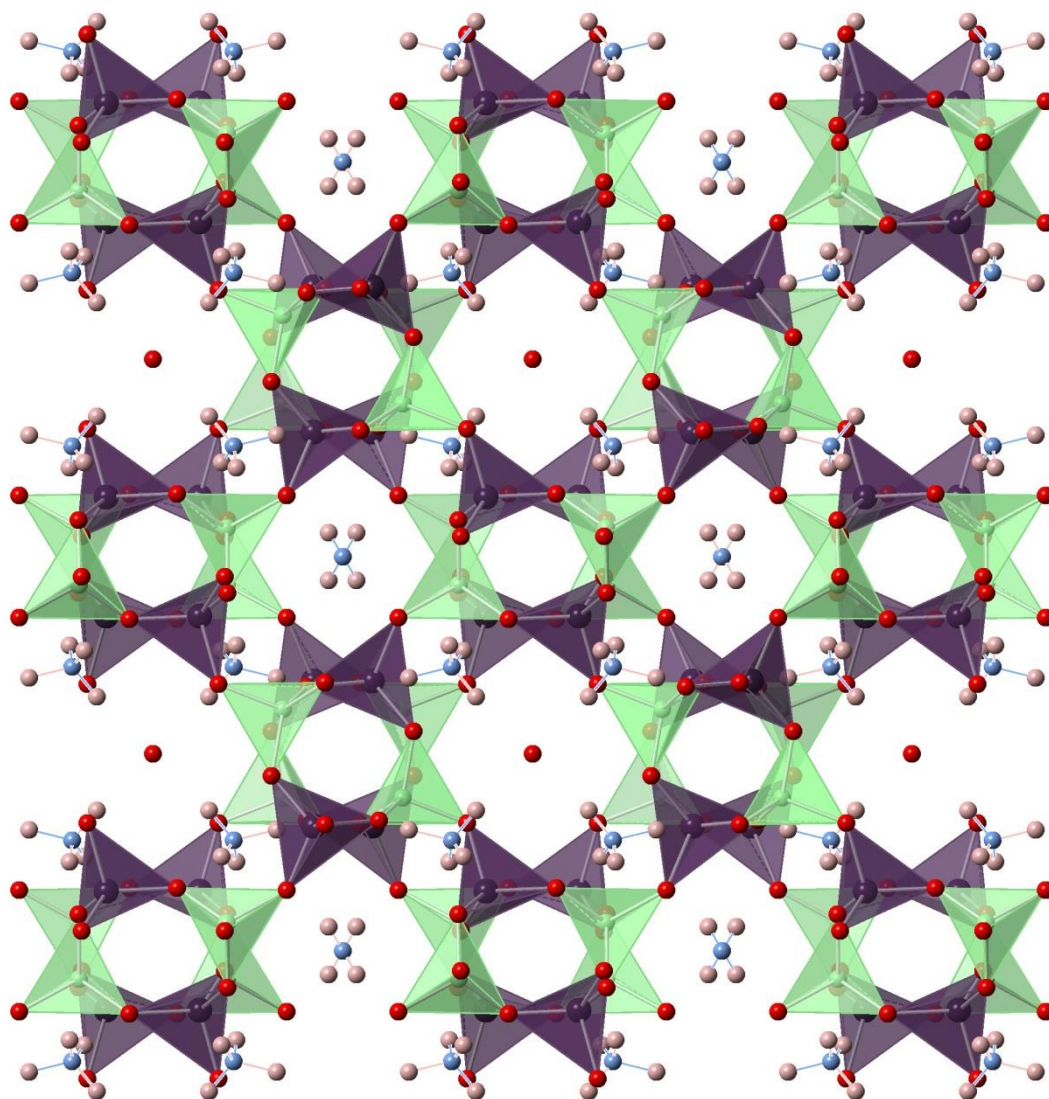


Figure 25: $[\text{NH}_4]_2[(\text{AsO}_4)_2\text{Be}_2] \cdot 2\text{H}_2\text{O}$ viewed along c. Green/purple tetrahedra are Be and As respectively, pink, blue and red spheres are hydrogen, nitrogen and oxygen respectively.

$[\text{NH}_4]_2[(\text{AsO}_4)_2\text{Be}_2]\cdot 2\text{H}_2\text{O}$ is generally formed as a major phase hydrothermally at mild alkaline pHs (10 – 12), at a range of temperatures (433 – 493 K) and lengths of reaction (48 – 168 Hrs). displays a tendency to form around the ammonium decomposition product of more complicated amines, however it can also be formed with other OSDAs present (section 3.8b) suggesting that ammonium provides a structure directing role rather than acting as a ‘true template’. The decomposition step of the amine has a similar effect as the addition of a mineraliser – reducing the availability of reagents leading to larger crystals but reduced sites of nucleation. When reaction mixtures also contain a mineraliser it leads to the formation of large crystals (>1-2 mm), however structural defects become increasingly prevalent.

There are four fully connected unique tetrahedral sites present in the structure of $[\text{NH}_4]_2[(\text{AsO}_4)_2\text{Be}_2]\cdot 2\text{H}_2\text{O}$ with a 1:1 Be:As ratio. Each site is involved in the single 4R which represents the fundamental repeating unit of the overall structure. Solid state ^9Be NMR studies confirm that both beryllium environments are equivalent by exhibiting a singlet [Fig. 26].

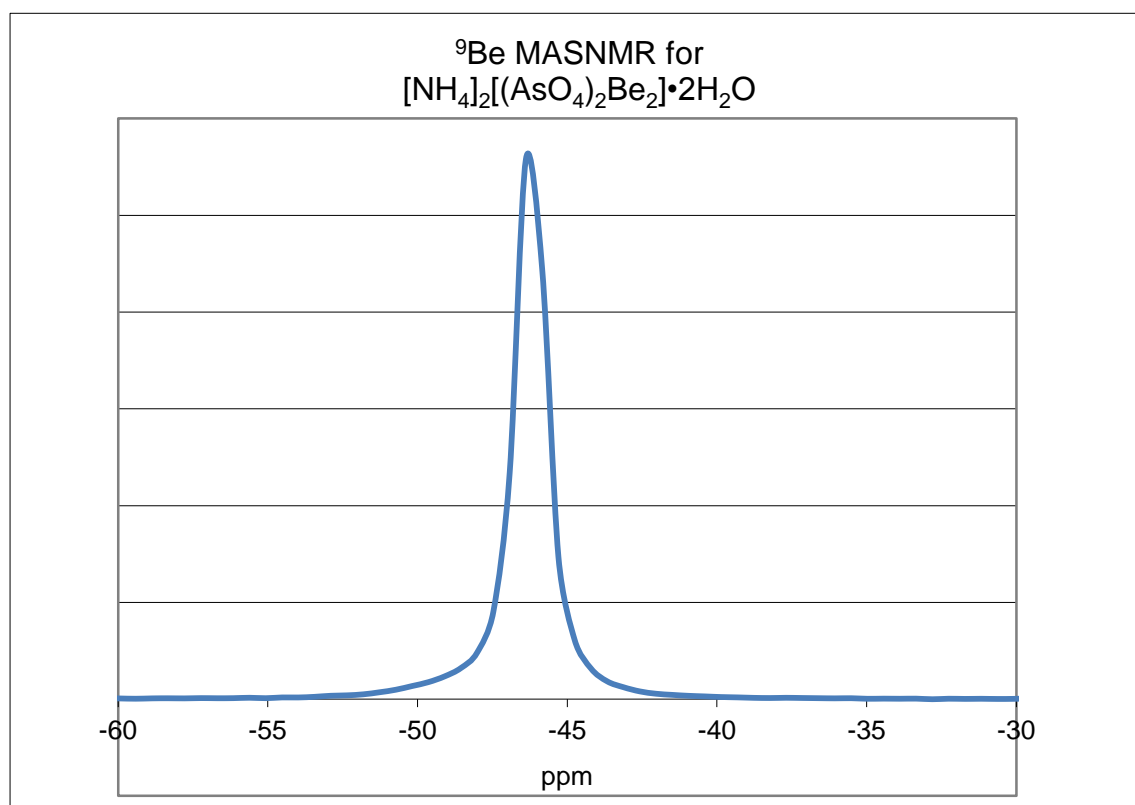


Figure 26: ^9Be NMR of $[\text{NH}_4]_2[(\text{AsO}_4)_2\text{Be}_2]\cdot 2\text{H}_2\text{O}$

The four rings themselves are distorted compared to a silicon containing 4R, due to the increased size of the arsenic atomic radii and the increased difference in bond length between Be – O and As – O. This has ramifications for all berylloarsenate structures but is most apparent when considering the three dimensional structures. The distortion tends to lead to condensed structures as opposed to silicate analogues, which manifests as reduced unit cell volume, increased framework density and lower accessible pore volume. The 4Rs are then connected to form a highly distorted double crankshaft chain (DCC, Fig. 27) which runs parallel with *c*.

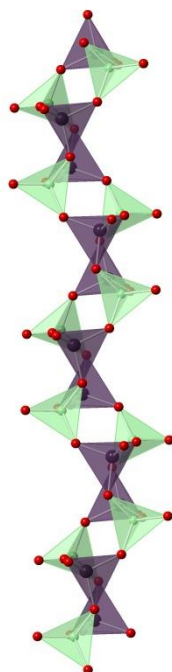


Figure 27a:
DCC as encountered in
 $[\text{NH}_4]_2[(\text{AsO}_4)_2\text{Be}_2] \cdot 2\text{H}_2\text{O}$



Figure 27b:
DCC represented
skeletal

The connectivity between DCCs leads to the formation of the more complicated secondary and composite building units seen in the MER topology: D8Rs and the *pau* cage. Extra-framework water and ammonium are present within the voids formed by the D8R and *pau* cage. The ammonium sites are near the 8R aperture of the *pau* where three of its hydrogen are involved in structure stabilisation *via* weak (2.008 – 2.130 Å) hydrogen bonding with the fourth, apical hydrogen orientated out into the void [Fig. 28]. Connectivity of each site has been confirmed *via* bond valence calculations.

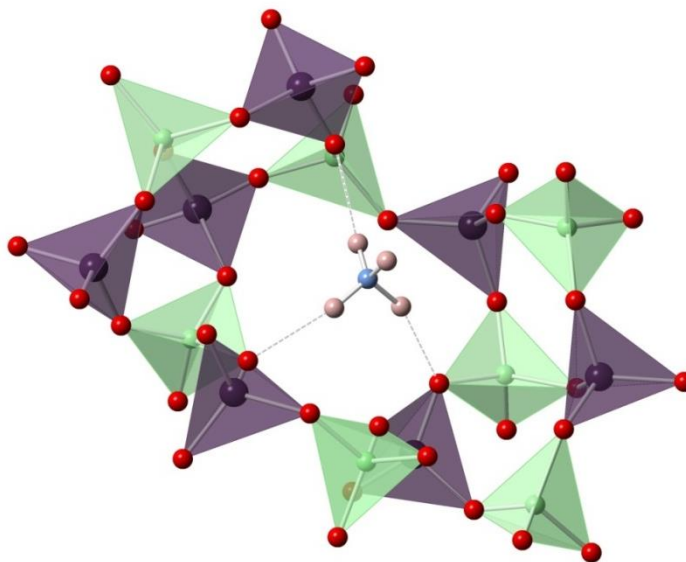


Figure 28: Ammonium environment in $[\text{NH}_4]_2[(\text{AsO}_4)_2\text{Be}_2] \cdot 2\text{H}_2\text{O}$. Green and purple tetrahedral are beryllium and arsenic. Red, blue and pink spheres are oxygen, nitrogen and hydrogen respectively.

On comparison with the aluminosilicate type material ^[16] and the beryllosilicate analogue ^[18] the level of structural distortion is immediately apparent, the distorted 4Rs lead to a much denser overall framework, perhaps best reflected by comparing the framework densities (FD, T atoms/1000 Å³). Aluminosilicate MER has a FD of 16.01, beryllosilicate; 17.08 and the beryllarsenate exhibits a FD of 19.5, significantly higher than either analogue. This is explained through comparison of the 4Rs present in each structure [Fig. 29].

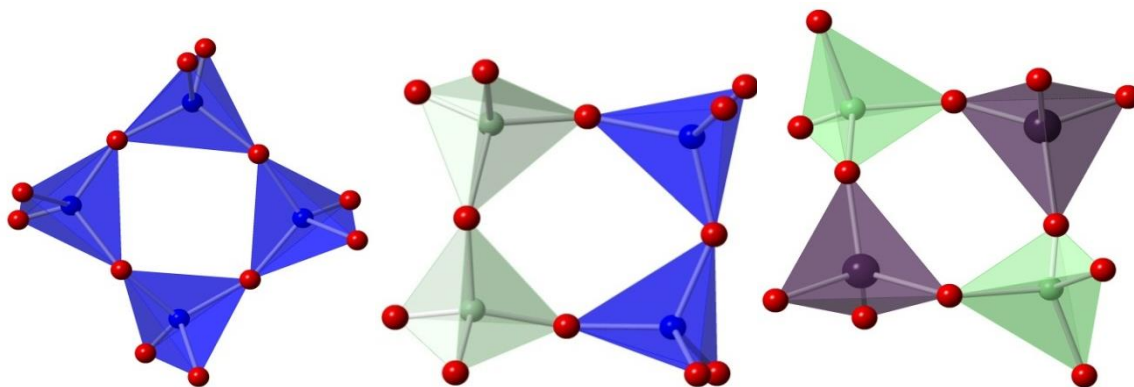


Figure 29: Visual comparison between 4Rs present in the three existing MER analogues. From left to right, aluminosilicate, beryllosilicate and beryllarsenate

In the aluminosilicate MER analogue (henceforth called AlSi-MER) the max deviation for the T – O bond distance is 0.02 Å and the average T – O – T angle is 146.84 °, this is similar to that found in beryllosilicate MER (BeSi-MER) with a max deviation of 0.006 Å and T – O – T angle of 141.80 °. The beryllarsenate MER (BeAs-MER) is substantially different with a deviation of 0.062 Å and T – O – T angle of 130.62 °. This non-regularity in BeAs-MER is due to the larger ionic radii of pentavalent As in comparison with Si and also the greater difference in bond length between As and Be as opposed to Si and Be. Comparison of selected bond angles and lengths can be found in table 19.

Table 19: Comparison between key bond distances and angles for the different MER analogues**AlSi-MER**

Bond	Bond length (Å)	Bond	Bond angle (°)
Average Al – O	1.642	Average O – Al – O	109.46
Average Si – O	1.652	Average O – Si – O	109.46

BeSi-MER

Bond	Bond length (Å)	Bond	Bond angle (°)
Average Be – O	1.615	Average O – Be – O	109.47
Average Si – O	1.616	Average O – Si – O	109.47

BeAs-MER

Bond	Bond length (Å)	Bond	Bond angle (°)
Average Be – O	1.633(9)	Average O – Be – O	109.42(5)
Average As – O	1.677(4)	Average O – As – O	109.42(2)

Since this twists and distorts the fundamental building unit of BeAs-MER, the overall structure and all secondary/composite building units are distorted, with the overall effect being a denser framework as represented by the FD. This is illustrated by visual comparison of the three MER-analogues when viewed along *c* (figure 25 vs figure 30). This is a trend which is observed in all 4R containing beryllioarsenates and therefore forming a beryllioarsenate version of any 4R containing topology is a viable method of selectively controlling the density and pore size, which are vital factors when considering application as molecular sieves or for gas sorption.

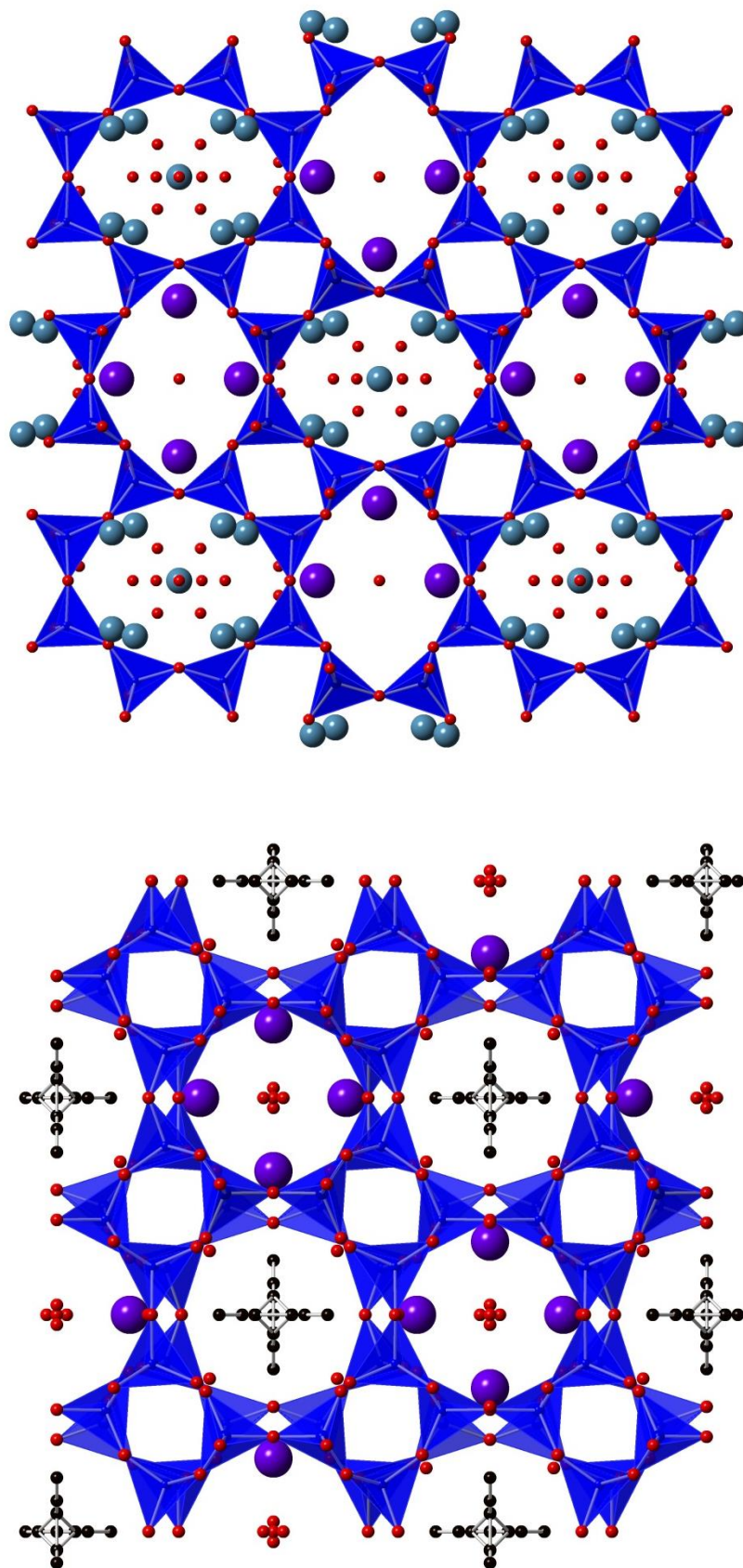


Figure 30: AlSi-MER (top) and BeSi-MER (bottom), when compared to BeAs-MER in figure 25, distortion and condensation of structure is immediately apparent. Blue tetrahedral are silicon. Red, black and purple spheres are oxygen, carbon and calcium respectively

Further characterisation has been carried out on BeAs-MER in the form of VTPXD to determine structure stability and it is found to lose crystallinity at $\sim 250\text{ }^{\circ}\text{C}$ [Fig.31].

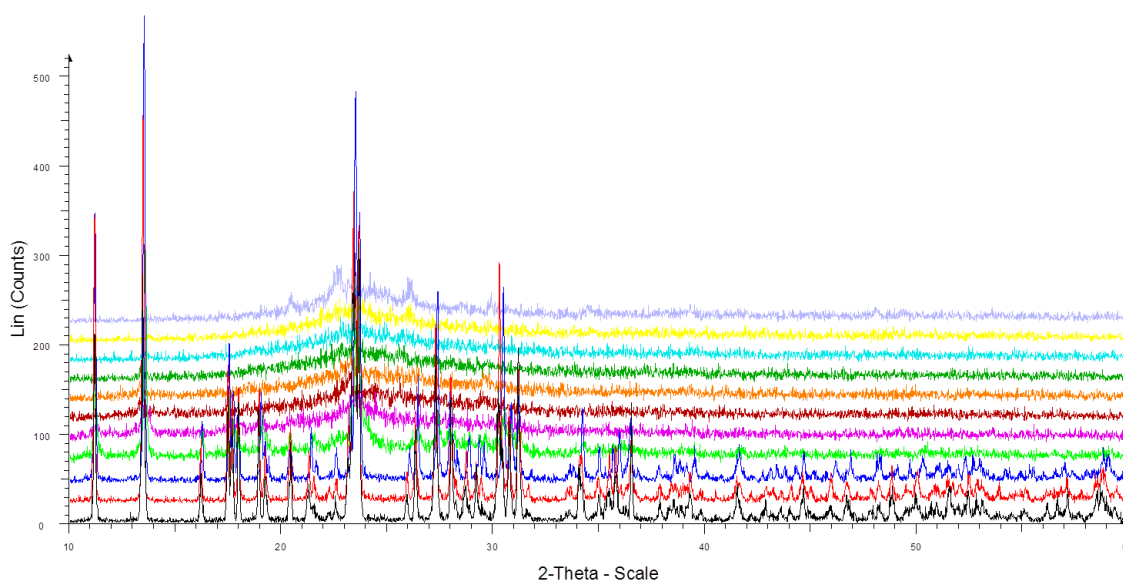


Figure 31: VTPXD of BeAs-MER, carried out between $100\text{ }^{\circ}\text{C}$ and $600\text{ }^{\circ}\text{C}$, with low temperature patterns at the bottom, sampled every $50\text{ }^{\circ}\text{C}$.

Semi-quantitative EDS measurements were carried out on a cluster of crystals which confirmed the presence of arsenic and oxygen. A SEM image was also acquired [Fig. 32] which shows the morphology of crystal growth for BeAs-MER.

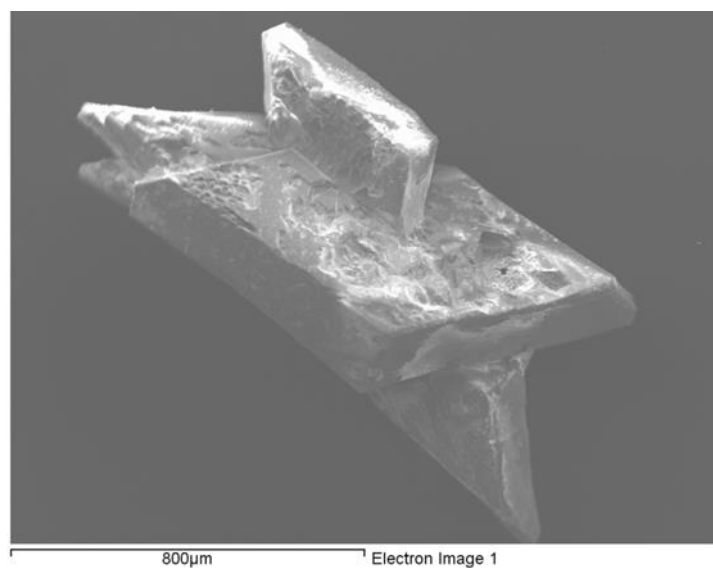


Figure 32: SEM image of BeAs-MER

3.8b: [H₂-diaminoethane]_{0.5}[AsO₄Be]

This phase has only been encountered once as a major phase with [Co^{II}]_{0.11}[(AsO₄(H)_{0.66})₂Be₂(BeOH₂)_{0.33}]•2H₂O (section 5.4) as a minor phase; a large colourless octahedra was selected and analysed *via* single crystal X-ray diffraction. The resulting fully connected three dimensional framework crystallises in the monoclinic crystal system and C2/c space group. This structure is another beryllioarsenate analogue of the zeolite topology MER (as discussed in section 3.8a) as such only brief discussion is provided here. [H₂-diaminoethane]_{0.5}[AsO₄Be] is a fully connected three dimensional structure [Fig. 33] formed of slightly twisting double crankshaft chains of 4Rs running parallel with *c*, this is suggested by a *c* length of 9.83 (5) Å and confirmed through analysis of the structure. The connectivity of the double crankshaft chain leads to the formation of elliptical D8R PBUs. The D8R also connect between *pau* composite building units (CBU) which are formed of 8⁶ and 4¹² Rs. The 8Rs which are part of the *pau* CBU are heavily distorted into elliptical apertures which alternate between having their longest dimension aligned along *a* or *b* leading to constricted 8R channels parallel to *c*, the framework is relatively dense when considered down *a* or *b* with the largest accessible aperture being from 4Rs. Connectivity is confirmed via bond valence calculations. Extra-framework species are heavily disordered and so it is difficult to resolve the actual species, however, their difference to the ammonium present in the MER analogue discussed in section 3.8a is confirmed by the different symmetry and crystallographic parameters [table 20] encountered in [H₂-diaminoethane]_{0.5}[AsO₄Be].

Table 20: Crystallographic parameters for [H₂-diaminoethane]_{0.5}[AsO₄Be]

Empirical formula	[H ₂ -diaminoethane] _{0.5} [AsO ₄ Be]
Formula weight	176.4
Appearance	Large colourless octahedra
Temperature	120 K
Wavelength	0.71073 Å
Crystal system	Monoclinic
Space group	C2/c
<i>a</i>	13.9330(8) Å
<i>b</i>	9.2245(6) Å
<i>c</i>	9.8302(5) Å
<i>β</i>	134.458(2) °
Volume	901.79(25) Å ³
<i>Z</i>	8

D_c	2.61 g cm^{-3}
R index	0.0587
Weighted R index	0.1270

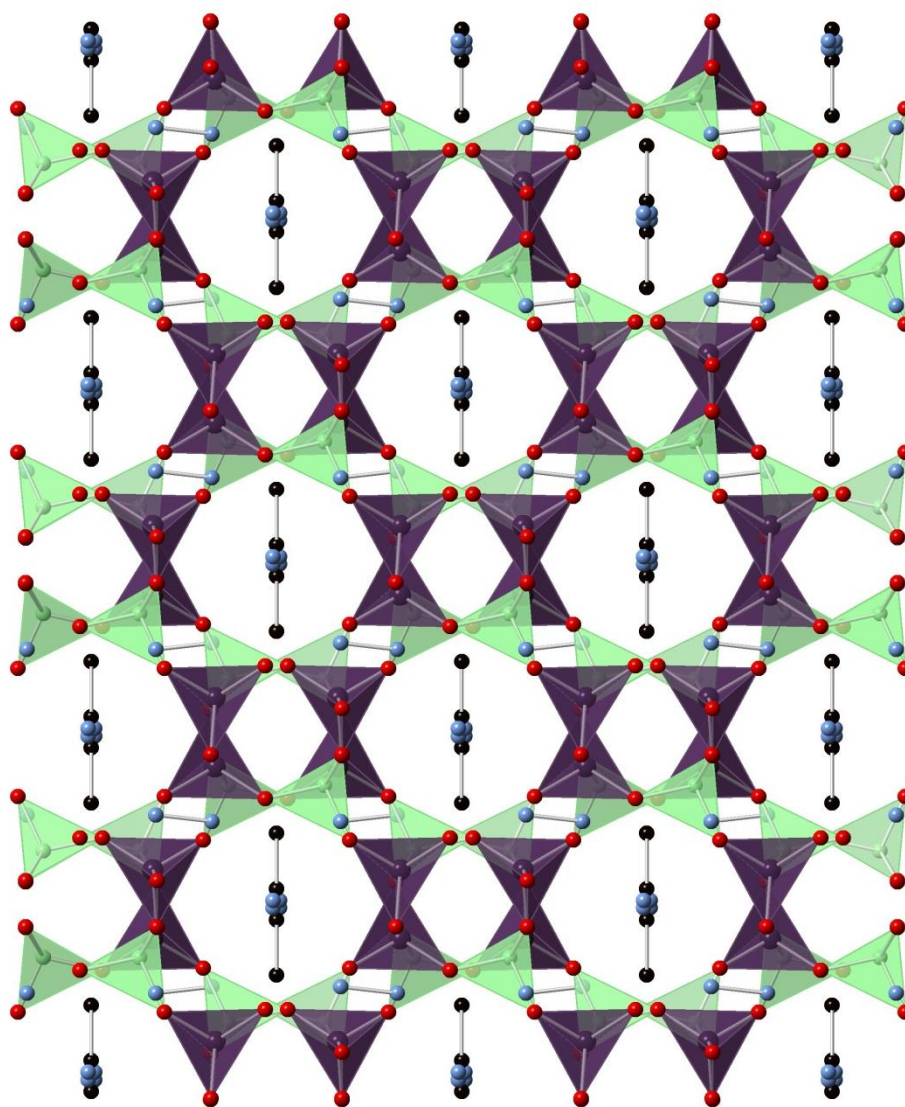


Figure 33: $[\text{H}_2\text{-diaminoethane}]_{0.5}[\text{AsO}_4\text{Be}]$ viewed along c . Green/purple tetrahedra are Be/As respectively, black, blue and red spheres are carbon, nitrogen and oxygen respectively.

On comparison with the crystallographic parameters for the ammonium containing BeAs-MER analogue [table 18] substantial differences are immediately apparent. The b length is roughly halved due to the reduced symmetry in $[\text{H}_2\text{-diaminoethane}]_{0.5}[\text{AsO}_4\text{Be}]$, whereas the c length is slightly increased due to the incorporation of the larger $\text{H}_2\text{-diaminoethane}$ as opposed to ammonium cations. The effect of the incorporated amine also decreases the framework density to 17.7 compared to 19.5 encountered in $[\text{NH}_4]_2[(\text{AsO}_4)_2\text{Be}_2]\cdot 2\text{H}_2\text{O}$. This can only be attributed to the effect of the amine since the bond lengths and angles in the distorted 4R are comparable to values found in $[\text{NH}_4]_2[(\text{AsO}_4)_2\text{Be}_2]\cdot 2\text{H}_2\text{O}$ (table 21).

Table 21: Selected bond distances and angles for $[\text{H}_2\text{-diaminoethane}]_{0.5}[\text{AsO}_4\text{Be}]$

Bond	Bond length (Å)	Bond	Bond angle (°)
Average As – O	1.667(6)	Average O – As – O	109.38(3)
Average Be – O	1.620(12)	Average O – Be – O	109.35(7)
4R T – O bond deviation	0.061	4R average T – O – T	134.95

Semi-quantitative EDS measurements were carried out on a cluster of crystals which confirmed the presence of arsenic and oxygen. A SEM image was also acquired [Fig. 34] which shows the morphology of crystal growth of $[\text{H}_2\text{-diaminoethane}]_{0.5}[\text{AsO}_4\text{Be}]$.

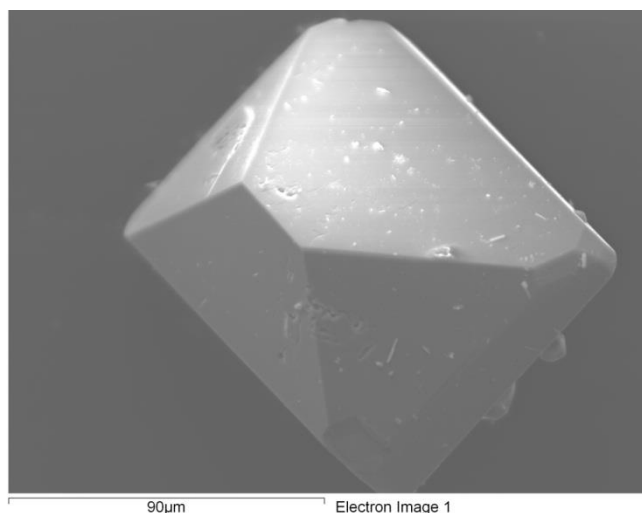


Figure 34: SEM image of $[\text{H}_2\text{-diaminoethane}]_{0.5}[\text{AsO}_4\text{Be}]$

3.9: [(H₂-diaminopropane)_{1.5}][(AsO₄)₂(AsO₃OH)₂(AsO₂(OH)₂)Be₄]•H₂O

A pale blue cluster of plates was shattered and one of the resulting colourless plates was analysed by single crystal X-ray diffraction. The resulting structure was found to occupy the monoclinic crystal system and C2/*c* space group. [(H₂-diaminopropane)_{1.5}][(AsO₄)₂(AsO₃OH)₂(AsO₂(OH)₂)Be₄]•H₂O is an interrupted three dimensional framework which has nucleated around slightly disordered H₂-diaminopropane.^[14] Structure 3.10 forms as a mixed phase (30/30/40 with bulk phase) with the naturally occurring hydrated berylloarsenate bearsite, Be₂(AsO₄)(OH)•4H₂O.^[12] Structure 3.9 is formed of networks of 8- and 12Rs perpendicular to *b* and cross-linked by sinusoidal chains of 4Rs and elliptical 8Rs along *b* [Fig. 36]. The resulting channels contain disordered amine and a single water site. Crystallographic parameters are summarised in Table 22.

Table 22: Crystallographic parameters for [(H₂-diaminopropane)_{1.5}][(AsO₄)₂(AsO₃OH)₂(AsO₂(OH)₂)Be₄]•H₂O

Empirical formula	[(H ₂ -diaminopropane) _{1.5}] [(AsO ₄) ₂ (AsO ₃ OH) ₂ (AsO ₂ (OH) ₂)Be ₄]•H ₂ O
Formula weight	854.94
Appearance	Sprays of terminated plates
Temperature	120 K
Wavelength	0.71073 Å
Crystal system	Monoclinic
Space group	C2/ <i>c</i>
<i>a</i>	25.4169(6) Å
<i>b</i>	9.8928(2) Å
<i>c</i>	18.7178(4) Å
<i>β</i>	92.178(1) °
Volume	4703.08(3) Å ³
<i>Z</i>	8
<i>D</i> _c	2.42 g cm ⁻³
R index	0.0716
Weighted R index	0.1375

[(H₂-diaminopropane)_{1.5}][(AsO₄)₂(AsO₃OH)₂(AsO₂(OH)₂)Be₄]•H₂O has only been formed once in the presence of divalent CoCl₂ and 1,3-diaminopropane suggesting a co-templating effect since this structure does not form in the presence of just one of these compounds. Bearsite^[12] has been shown to form at similar temperatures (150 °C in the literature) and reaction time periods, and so it is likely that bearsite is the most stable product encountered at these conditions. By modifying the reaction with the

addition of SDAs a mixed phase is produced. When the reaction is repeated at double the autoclave time we are presented with a solution, likely formed of monomeric species/unreacted starting material.

The structure has an interrupted 3D framework formed of networks of 8- and 12Rs which are perpendicular to *b* and are cross-linked by sinusoidal chains of 4Rs and 8Rs along *b*. As with the previously discussed BeAs-MER a high degree of distortion is observed in the 4Rs as opposed to aluminosilicates which leads to irregularly shaped pores and channels [Fig 34/36]. When considered from the *a* or *c* directions the structure is relatively dense with the exception of 4Rs and elliptical 8Rs respectively.

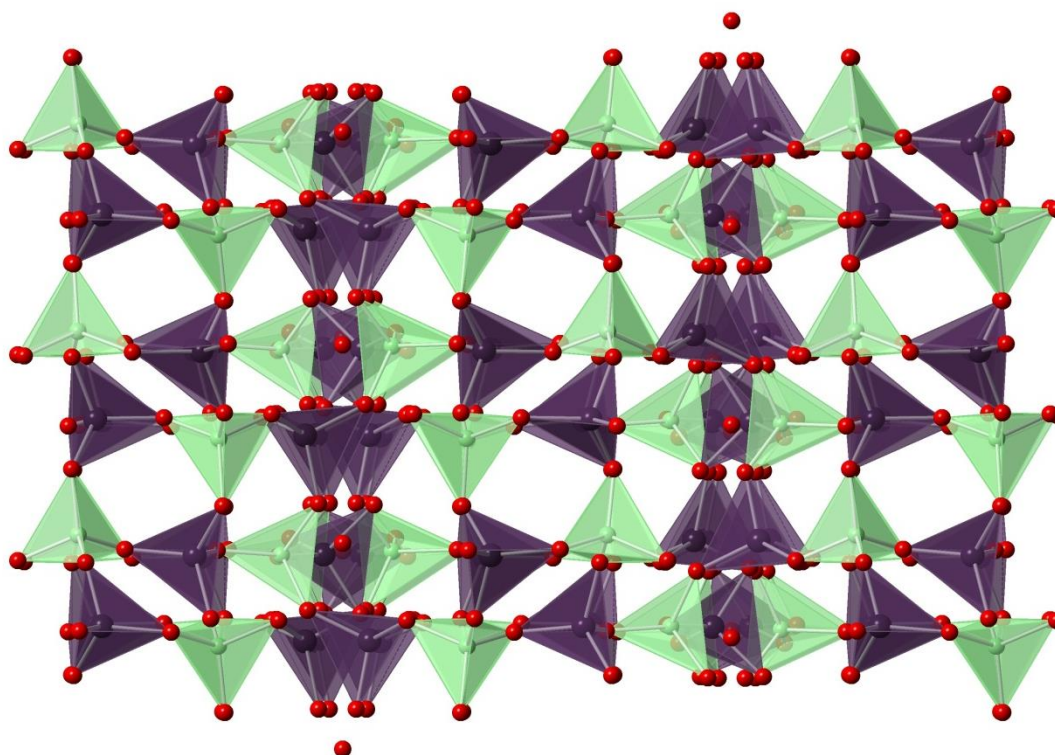


Figure 35: $[(\text{H}_2\text{-diaminopropane})_{1.5}][(\text{AsO}_4)_2(\text{AsO}_3\text{OH})_2(\text{AsO}_2(\text{OH})_2)\text{Be}_4]\cdot\text{H}_2\text{O}$ viewed along *a*. With C/N/H removed for clarity. Green and purple tetrahedra are Be and As centred respectively. Red spheres represent oxygen

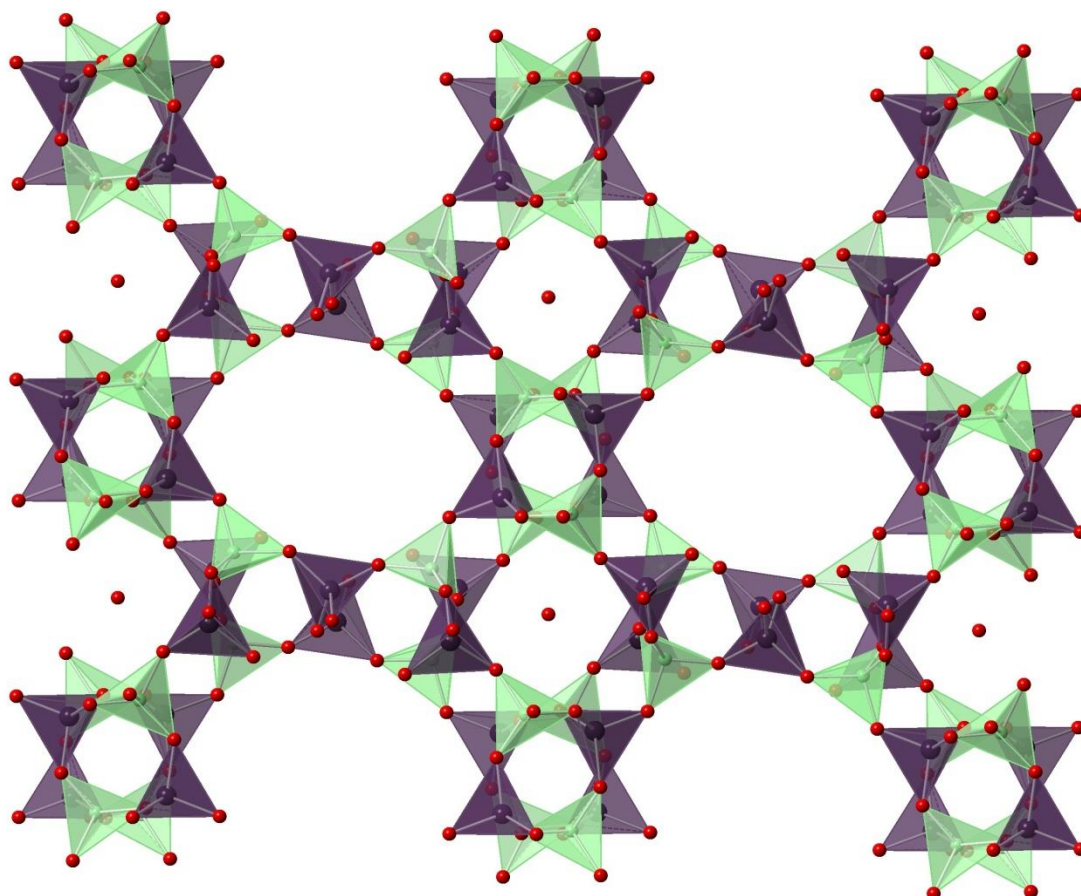


Figure 36: $[(\text{H}_2\text{-diaminopropane})_{1.5}][(\text{AsO}_4)_2(\text{AsO}_3\text{OH})_2(\text{AsO}_2(\text{OH})_2)\text{Be}_4]\cdot\text{H}_2\text{O}$ viewed along b . With C/N/H removed for clarity. Green, purple tetrahedra and red spheres are beryllium, arsenic and oxygen respectively.

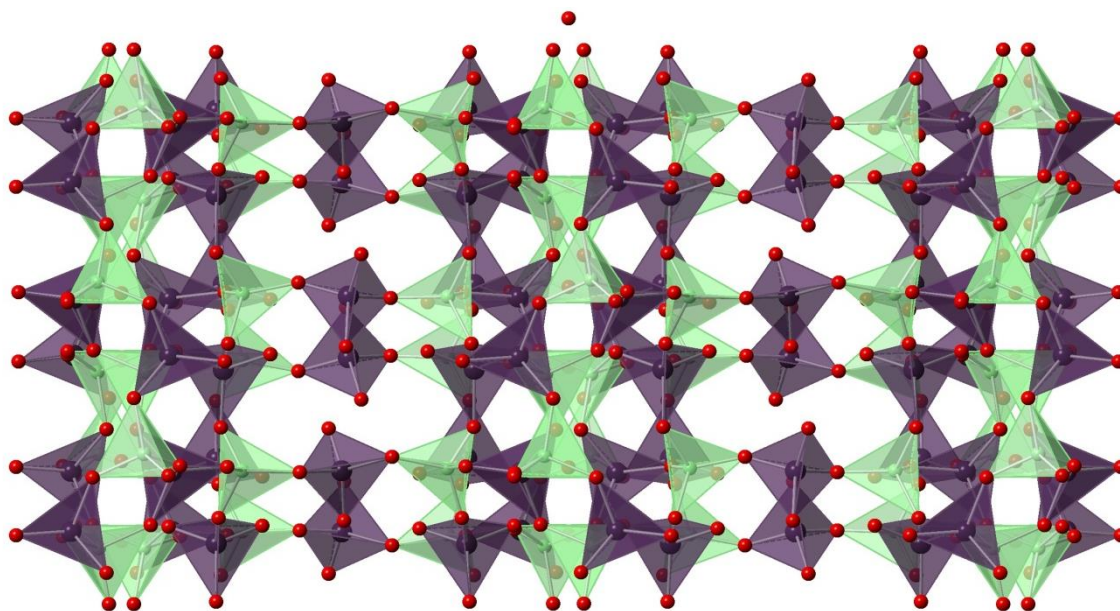


Figure 37: $[(\text{H}_2\text{-diaminopropane})_{1.5}][(\text{AsO}_4)_2(\text{AsO}_3\text{OH})_2(\text{AsO}_2(\text{OH})_2)\text{Be}_4]\cdot\text{H}_2\text{O}$ viewed along c . With C/N/H removed for clarity. Green, purple tetrahedra and red spheres are beryllium, arsenic and oxygen respectively.

Structure 3.10 has 5 crystallographically unique arsenic positions two of which are fully coordinated to four oxygen atoms and are both involved in the four ring SBUs that are the basic building blocks for the overall structure. The third and fourth arsenic positions are singly terminated via hydroxyl groups which is suggested by slightly longer As – OH bond distances compared to As – O (1.717(6) Å as opposed to an average 1.667(6) Å) (Table 23) and bond valence calculations (Table 24). The final As site is doubly terminated with hydroxyl groups, suggested by distortion of the O – As – OH angles (113.89 (6) ° as opposed to the expected 109.5°) and confirmed by bond valence calculations. The beryllium sites are all fully connected. This high degree of framework hydroxide is required to charge balance the overall structure in lieu of the high overall negative charge and the low contribution from the extra framework species. Unfortunately it has been impossible to resolve the hydrogen positions due to the limitations of X-ray techniques therefore hydrogen locations have been inferred from bond valence calculations.

Structure 3.9 has two extra-framework species present in the form of a water site situated within a heavily distorted *lau* cage and two 1,3-diaminopropane positions. The first 1,3-diaminopropane position is well defined and fully occupied [Fig. 38] and sits within the large cages formed between the two 8- and 12R networks.

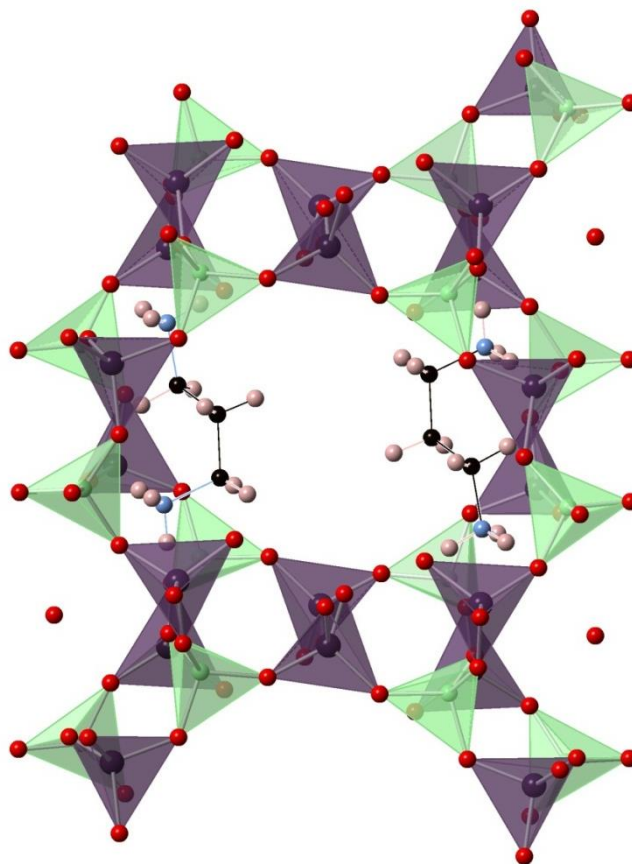


Figure 38: Position of the fully occupied 1,3-diaminopropane site on either side of the main cage. Green, purple tetrahedra red, black, blue and pink spheres are beryllium, arsenic, oxygen, carbon, nitrogen and hydrogen respectively

The second 1,3-diaminopropane position suffers from disorder of the carbon chain with there being two 25 % occupied sites per carbon, alongside singular 50 % occupied nitrogen sites leading to an overall occupation of 50 % resulting in an electrostatic contribution of just +1 to the overall structure's charge. This disordered site is located within the centre of the 12R [Fig. 38]. As well as providing charge balance the protonated 1,3-diaminopropane molecules also stabilise the overall structure through hydrogen bonding between the NH and framework O sites [table 23].

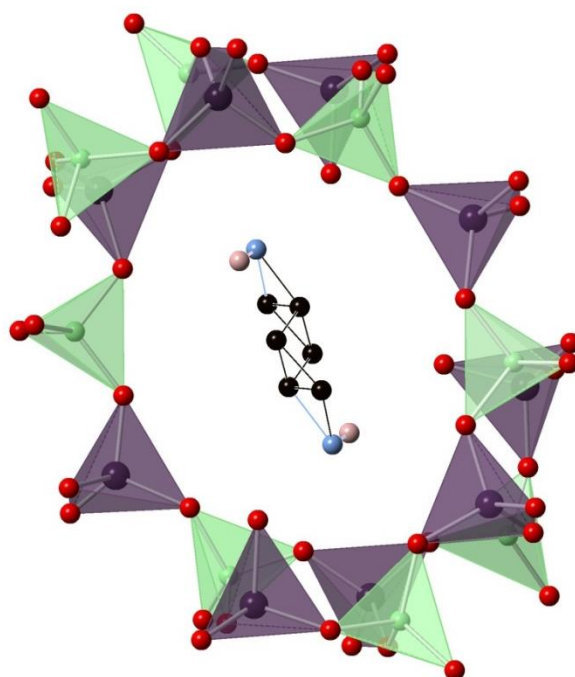


Figure 39: Position of the disordered 1,3-diaminopropane site. Green and purple tetrahedra are beryllium and arsenic. Red, black, blue and pink spheres are oxygen, carbon, nitrogen and hydrogen respectively

Table 23: Selected bond distances and angles for $[(\text{H}_2\text{-diaminopropane})_{1.5}][(\text{AsO}_4)_2(\text{AsO}_3\text{OH})_2(\text{AsO}_2(\text{OH})_2)\text{Be}_4]\cdot\text{H}_2\text{O}$

Bond	Bond length (Å)	Bond	Bond angle (°)
Average As – O ₄	1.681(6)	Average O – As – O	109.46(3)
Average As – O ₃ (OH)	1.679(6)	Average O – Be – O	109.46(8)
Average As – O ₂ (OH) ₂	1.684(6)	(H)O – As – O(H)	102.73(4)
Average Be – O	1.629(12)		
Average As – OH	1.724(6)		
NH – O5 (framework)	1.997(11)		
NH – O6 (framework)	2.144(11)		
N2H – O19(framework)	2.030(11)		
N2H – O8(framework)	2.483(11)		

Table 24: Selected bond valence deviation for sites in $[(\text{H}_2\text{-diaminopropane})_{1.5}][(\text{AsO}_4)_2(\text{AsO}_3\text{OH})_2(\text{AsO}_2(\text{OH})_2)\text{Be}_4]\cdot\text{H}_2\text{O}$

Atom	Σ of BV deviation (v.u)
O1	-0.21
O2	-0.19
O3	-0.22
O4	-0.25
O5	-0.12
O6	-0.18
O7 (-As4)	-0.81
O8	-0.24
O10 (-As3)	-0.78
O12	-0.22
O16 (-As5)	-0.72
O17 (-As5)	-0.87
O19	-0.23

The table above shows the deviation in bond valence on a large number of framework oxygen sites, the sites with notation (-As3/4/5) are actually the hydroxyl terminators and this explains the high degree of deviation encountered. Sites without notation are all fully bonded framework oxygen which are further involved in hydrogen bonding with the extra framework 1,3-diaminopropane.

EDS measurements and an SEM image was taken of one of the crystals [Fig. 40]. EDS confirms the presence of both As and O and the SEM exhibits the morphology previously described.

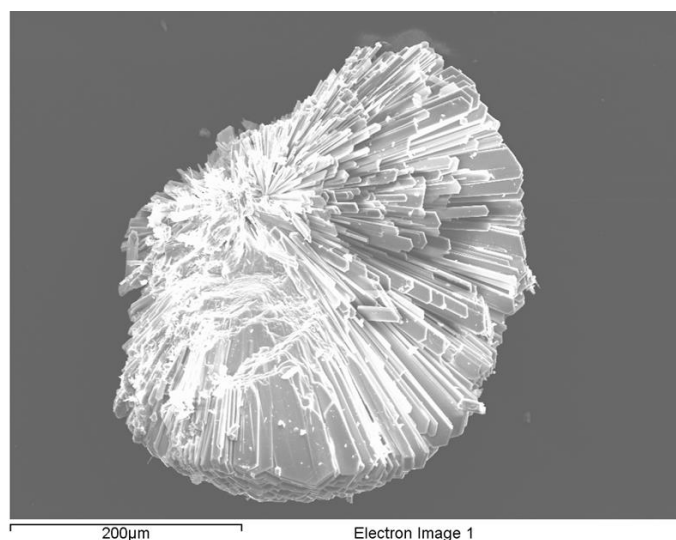


Figure 40: SEM image of $[(\text{H}_2\text{-diaminopropane})_{1.5}][(\text{AsO}_4)_2(\text{AsO}_3\text{OH})_2(\text{AsO}_2(\text{OH})_2)\text{Be}_4]\cdot\text{H}_2\text{O}$

3.10: (AsO₄)₂Be(BeOH₂)₂

A dark red viscous matrix was produced and washed vigorously with EtOH and distilled water which resulted in the collection of a small amount of solid phase (table 2). The solid phase was investigated by visual microscopy and found to be a combination of bulk amorphous powder and large thin colourless plates, these were investigated via single crystal X-ray diffraction. Initially reduced scattering was observed due to the thinness of the plates but eventually a crystal was selected which presented a structure crystallising in the monoclinic crystal system with a space group of C2/c. (AsO₄)₂Be(BeOH₂)₂ is a dense interrupted 3D framework which contains no extra-framework species. ^[14] Its structure consists of a network of distorted 4- and 10Rs perpendicular to *b*, crosslinked by sinusoidal chains of 3Rs parallel to the *b* axis [Fig. 41]. Crystallographic parameters are summarised in Table 25.

Table 25: Crystallographic parameters for (AsO₄)₂Be(BeOH₂)₂

Empirical formula	(AsO ₄) ₂ Be(BeOH ₂) ₂
Formula weight	330
Appearance	Thin colourless plates
Temperature	120 K
Wavelength	0.71073 Å
Crystal system	Monoclinic
Space group	C2/c
<i>a</i>	16.2789(6) Å
<i>b</i>	4.6530(2) Å
<i>c</i>	9.8544(4) Å
<i>β</i>	93.679(2) °
Volume	744.89(1) Å ³
<i>Z</i>	4
<i>D_c</i>	2.03 g cm ⁻³
R index	0.0179
Weighted R index	0.0472

The single As site is fully connected to a sinusoidal chain of consecutive vertex sharing symmetry related beryllium tetrahedra running parallel to the *b* crystallographic axis. Each chain is linked to the next by the As centred tetrahedra orientated in $-a$ and a in relation to the centre of the chain, leading to two of the As vertices forming a 3R and a third connecting to the next Be-chain along *c* via 4Rs. The first As vertex is a triply bonded oxygen site shared between two Be and the As, as seen in

AsO₃(OH)Be (section 3.7) which leads to a lengthening of the As – O bond distance (1.721(17) Å). The final vertex of the As tetrahedra alternates in orientation between $-a$ and a and is connected to the second Be site, forming the network of elliptical 10Rs introduced above. The Be site involved in the beryllium ‘backbone’ is fully connected whereas the second Be site is doubly terminated with hydroxyl group (confirmed by BV calculations) and its symmetry related equivalent. This is reflected by longer than usual bond lengths (Be – OH, 1.661(4) Å) leading to a slightly distorted tetrahedra (selected bond lengths and angles can be found in table 26). The hydroxyl groups are orientated directly into the centre of the 10R sterically hindering any potential extra-framework species and via weak hydrogen bonding (2.112 (4) Å) [Fig. 42], causing the elliptical character of the 10Rs. The lack of incorporation of the OSDA (in this case didecylamine) suggests that the potential template is too bulky and under reaction conditions had no templating decomposition products. It is likely that the didecylamine played a pH controlling role.

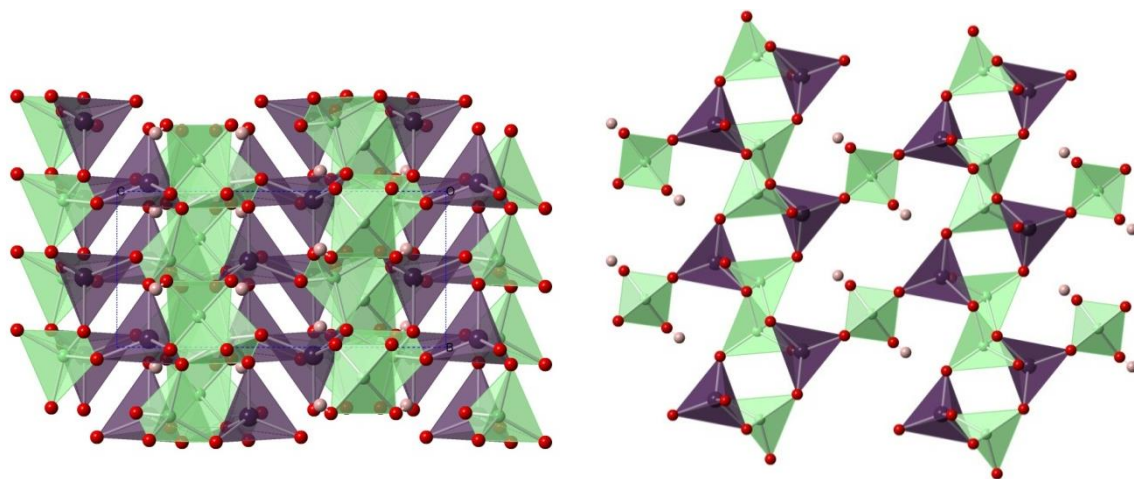


Figure 41a: (AsO₄)₂Be(BeOH₂)₂ viewed along a (left) and b (right). Green and purple tetrahedra are Be and As centred respectively. Pink and red spheres are H and O.

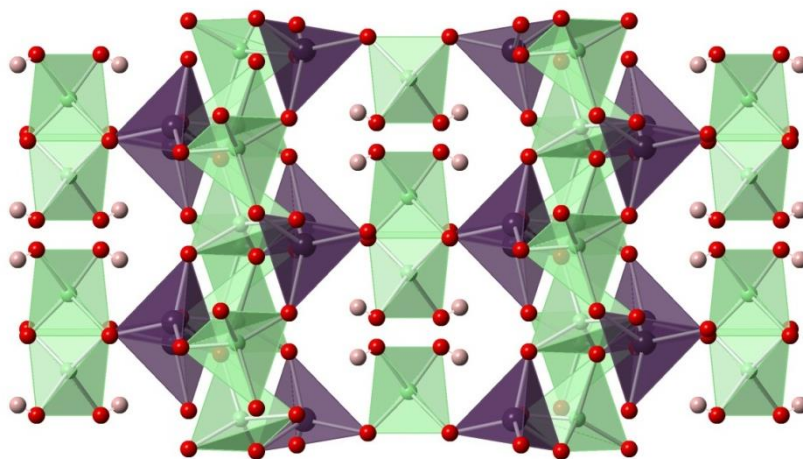


Figure 41b: (AsO₄)₂Be(BeOH₂)₂ viewed along c . Green and purple tetrahedra are beryllium and arsenic respectively. Pink and red spheres are hydrogen and oxygen respectively.

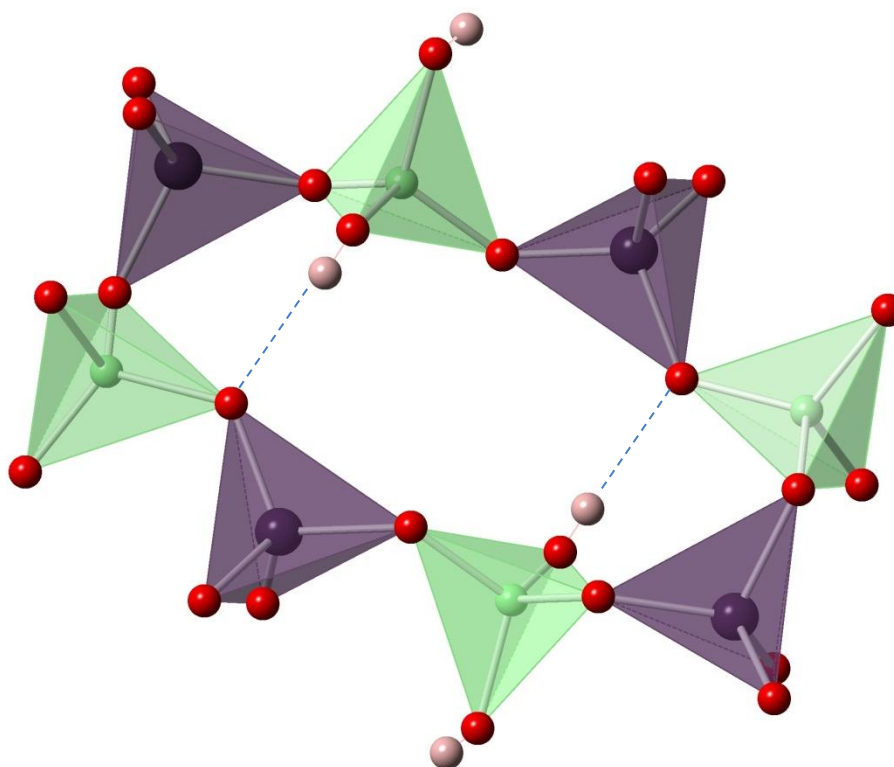


Figure 42: Intra-framework hydrogen bonding encountered in $(\text{AsO}_4)_2\text{Be}(\text{BeOH}_2)_2$

Interestingly the beryllium backbone feature encountered in $(\text{AsO}_4)_2\text{Be}(\text{BeOH}_2)_2$ is also exhibited in the one dimensional structure $\text{Na}_{3.5}[\text{AsO}_4\text{Be}(\text{OH})]\cdot 0.4\text{H}_2\text{O}$ previously discussed (section 3.3), this structure can therefore be viewed as a cross-linked version of that basic chain where there is no extra-framework cation present.

Table 26: Selected bond lengths and angles for $(\text{AsO}_4)_2\text{Be}(\text{BeOH}_2)_2$

Bond	Bond length (Å)	Bond	Bond angle (°)
Average As – O	1.678(16)	Average O – As – O	109.46(9)
Average Be – O	1.631(3)	Average O – Be – O	109.44(2)
Be – OH	1.724(4)		
H---O – As	2.112(4)		

SEM and EDS measurements were carried out, EDS confirms the presence of both As and O and the SEM exhibits the morphology previously described [Fig. 43].

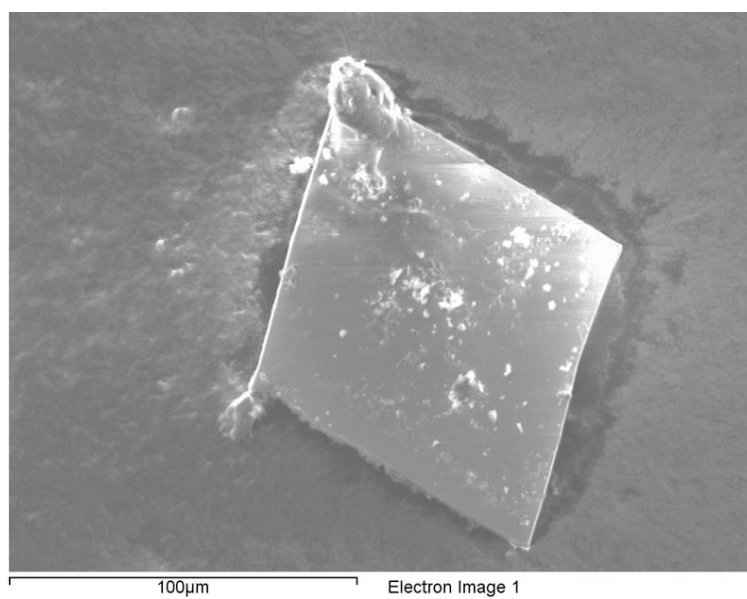


Figure 43: SEM image of $A(sO_4)_2Be(BeOH_2)_2$

3.11: [(H-pyridine)₂][(AsO₄)₂(AsO₃OH)Be₂(BeOH₂)]

The title compound crystallises as part of a mixed phase with AsO₄Be(OH₂)Be(OH)(OH₂) (section 3.6) in approximately 30:30:40 (3.7:3.12:bulk powder phase). A large chunky rod-like crystal was broken off a spray and analysed by single crystal X-ray diffraction. The resulting monoclinic structure has the C2/c space group and is an interrupted three dimensional berylloarsenate framework semi-analogues to the well-known AFI aluminophosphate topology.^[19] Structure 3.11 is loosely formed of a network of 4-, 6- and 12Rs in the *ac* plane cross linked by double sinusoidal chains of 4Rs running parallel to *b* which gives rise to distorted *afi* type CBUs. The topology is templated by well-defined pyridine molecules. Crystallographic parameters are summarised in table 27.

Table 27: Crystallographic parameters for [(H-pyridine)₂][(AsO₄)₂(AsO₃OH)Be₂(BeOH₂)]

Empirical formula	[(H-pyridine) ₂][(AsO ₄) ₂ (AsO ₃ OH)Be ₂ (BeOH ₂)]
Formula weight	542.9
Appearance	Sprays of chunky needles/rods
Temperature	120 K
Wavelength	0.71073 Å
Crystal system	Monoclinic
Space group	C2/c
<i>a</i>	26.2341(6) Å
<i>b</i>	4.9127(1) Å
<i>c</i>	24.6048(5) Å
β	118.718(1) °
Volume	2781.02(17) Å ³
<i>Z</i>	8
D _c	2.59 g cm ⁻³
R index	0.0381
Weighted R index	0.0478

Synthetic studies show that the formation of [(H-pyridine)₂][(AsO₄)₂(AsO₃OH)Be₂(BeOH₂)] is directed by both the presence of pyridine and the arsenic acid concentration. Where reactions were attempted with different templates at the same starting materials ratios, different structures were produced. When the effect of the Be:As ratio was investigated it was found that an increase of Be(OH)₂ with its accompanying increase in pH (pH > 5.95) resulted in the preferential formation of

the other phase encountered (section 3.6) whereas when the amount of H_3AsO_4 was increased ($\text{pH} < 5.95$) the phase $[(\text{H-pyridine})_2][(\text{AsO}_4)_2(\text{AsO}_3\text{OH})\text{Be}_2(\text{BeOH}_2)]$ was formed.

Structurally $[(\text{H-pyridine})_2][(\text{AsO}_4)_2(\text{AsO}_3\text{OH})\text{Be}_2(\text{BeOH}_2)]$ has six crystallographically unique T sites, leading to a framework density of 17.2. The first two As tetrahedra are fully vertex oxygen sharing with neighbouring Be tetrahedra and are both part of the double zig-zag chain of 4Rs running parallel with *b*. These double zig-zags form the main mode of crosslinking between the *ac* networks and form 6Rs leading to distorted *afi* composite building units. The final As centred tetrahedra is hydroxyl terminated (confirmed by bond valence calculations) which disconnects a third of the 4R zig-zags. The three alternating Be centred tetrahedra have analogous character to the As, with two sites being fully coordinated and involved with the connected 4R zig-zags and the third being terminated. This is confirmed by ^9Be MASNMR with a slight shoulder being observed on the main peak representative of the two Be environments [Fig. 44].

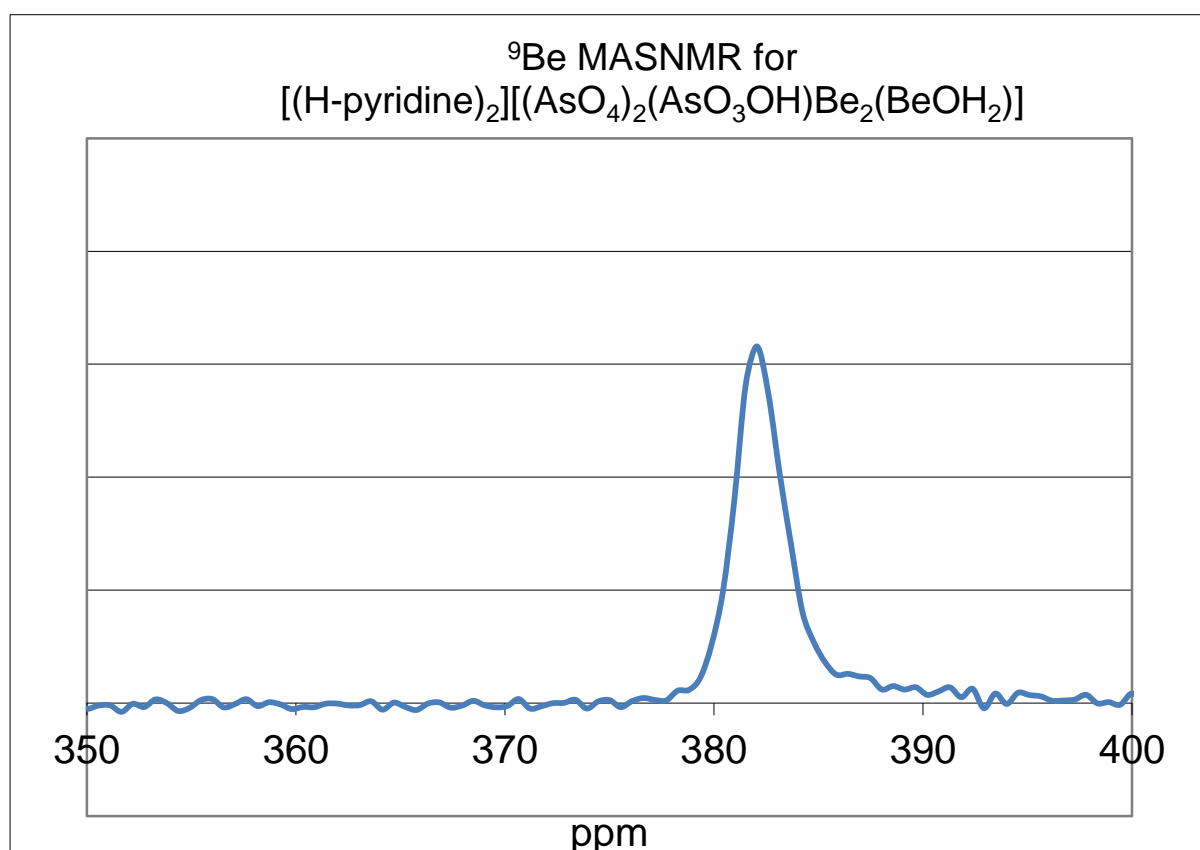


Figure 44: ^9Be MASNMR of $[(\text{H-pyridine})_2][(\text{AsO}_4)_2(\text{AsO}_3\text{OH})\text{Be}_2(\text{BeOH}_2)]$ showing slight shoulder implying two different beryllium environments.

The termination is interesting as it is in the form of water (confirmed by bond valence calculations) rather than the more commonly encountered hydroxyl, this form of termination is unusual in three dimensional structures but seems to be prevalent in the berylloarsenates described here.

The stacks of 4Rs link to produce pillars of strongly distorted 6Rs which in turn link to form the 12Rs where the pyridine rings are sited. The pyridine molecules are protonated and fully ordered forming a strong hydrogen bond (NH---O, 1.80 (3) Å) with an framework oxygen, this suggests the pyridine plays a structure stabilising role as well as structure directing in the formation of [(H-pyridine)₂][(AsO₄)₂(AsO₃OH)Be₂(BeOH₂)].

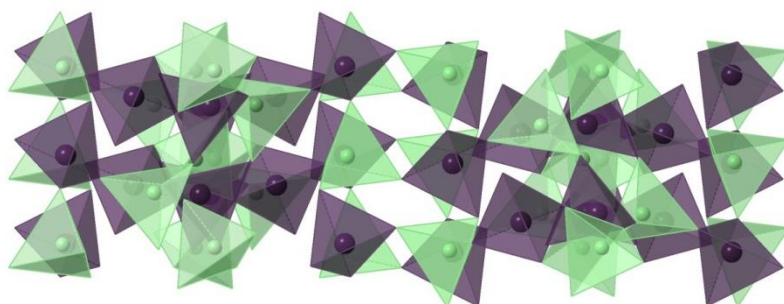


Figure 45: [(H-pyridine)₂][(AsO₄)₂(AsO₃OH)Be₂(BeOH₂)] viewed along *a*. Pyridine template and H atoms removed for clarity – from this direction the structure is dense with no accessible channels. Green and purple tetrahedra represent Be and As.

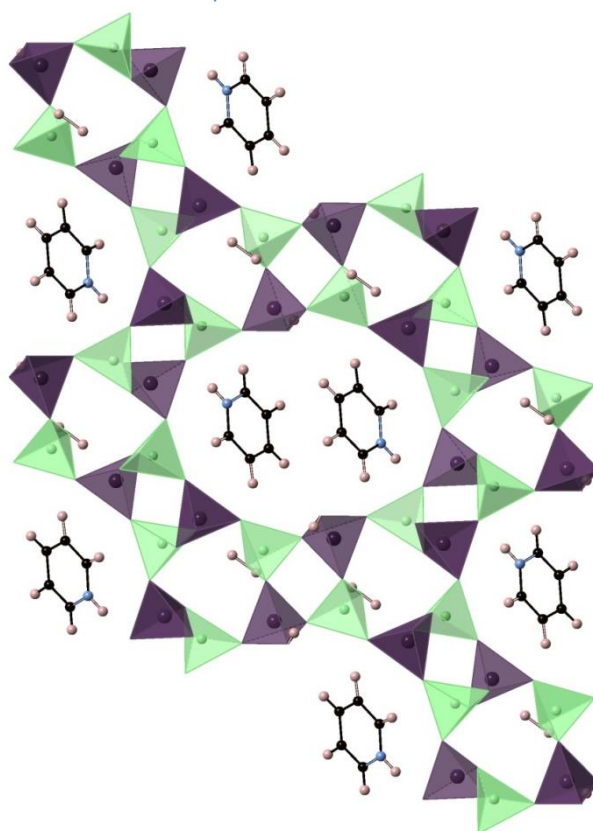


Figure 46: [(H-pyridine)₂][(AsO₄)₂(AsO₃OH)Be₂(BeOH₂)] viewed along *b*.

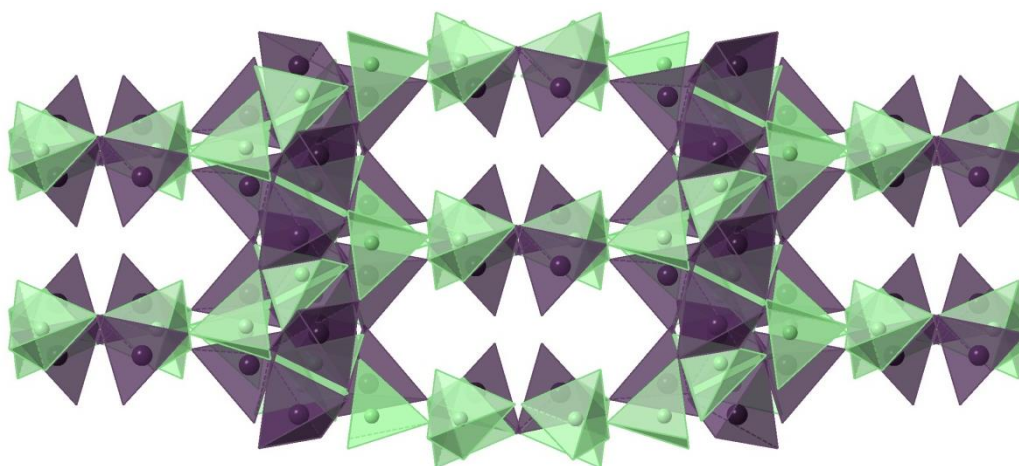


Figure 47: $[(\text{H-pyridine})_2][(\text{AsO}_4)_2(\text{AsO}_3\text{OH})\text{Be}_2(\text{BeOH}_2)]$ viewed along c , elliptical 10R channels can be seen running parallel to c . Pyridine and H atoms have been removed for clarity.

Comparison with AFI type material

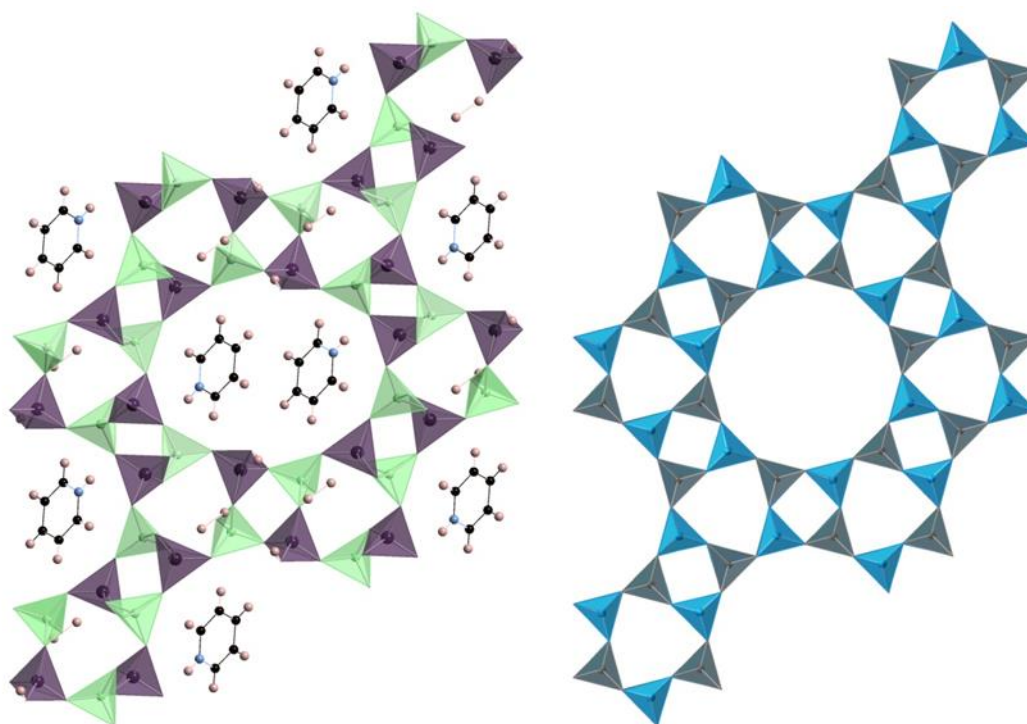


Figure 48: Comparison between $[(\text{H-pyridine})_2][(\text{AsO}_4)_2(\text{AsO}_3\text{OH})\text{Be}_2(\text{BeOH}_2)]$ (left) and AFI-type topology (right). Blue and teal tetrahedra are Al and P centred respectively

From first glance the resemblance and differences between AFI and 3.11 are clear, the basic overall structure is the same, especially when considered from a network perspective both topologies having 4-, 6- and 12Rs, however in 3.11 the ring shapes are all very distorted, leading to folding of the 6Rs which in turn causes the termination and difference in stacking as opposed to AFI. Where the AFI network is cross-linked by stacks of 4- and 6Rs made possible by the alternation of Al and P centred

tetrahedra. The berylloarsenate version has the two different types of stacks mentioned previously [Fig. 49], this is caused by the incorporation of the berylloarsenate distorted 4R which has internal T – O – T angles of 121.4 ° - 135.1° as opposed to the regular 150.4° encountered in AFI. This accounts for the folding of the 6Rs and therefore the termination of this structure.

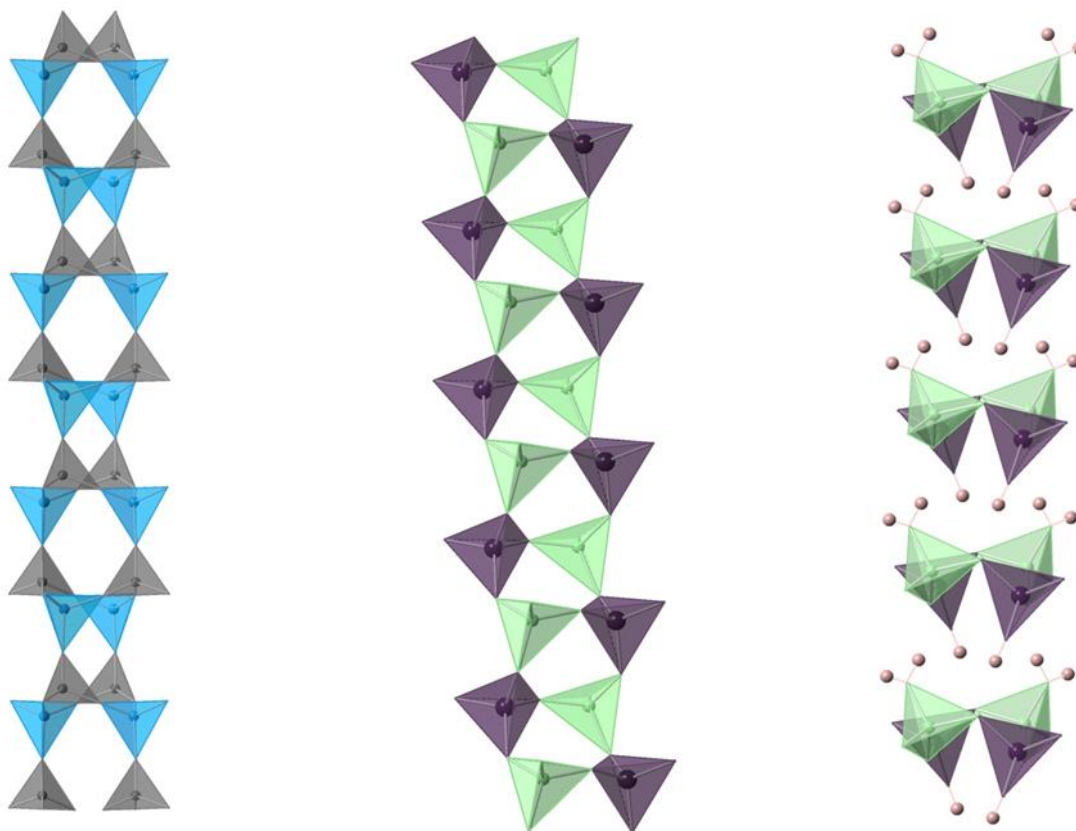


Figure 49: Comparison between stacking types between AFI and 3.12, left is the uniform 4R and 6R stacking between layers encountered in AFI, centre and right represents the two forms of stacking seen in 3.12.

Table 28: Selected bond lengths and angles for [(H-pyridine)₂][(AsO₄)₂(AsO₃OH)Be₂(BeOH₂)] including angles of AFI for comparison.

Bond	Bond length (Å)	Bond	Bond angle (°)
Average As – O	1.678(3)	Average O – T – O angle in 3.12 4Rs	128.3
Average Be – O	1.635(7)	Average O – T – O angle in AFI 4Rs	150.4
As– OH	1.705(3)		
Be – OH ₂	1.631(7)		

EDS measurements and an SEM image was taken of one of the crystals [Fig. 50]. EDS confirms the presence of both As and O and the SEM exhibits the morphology previously described.

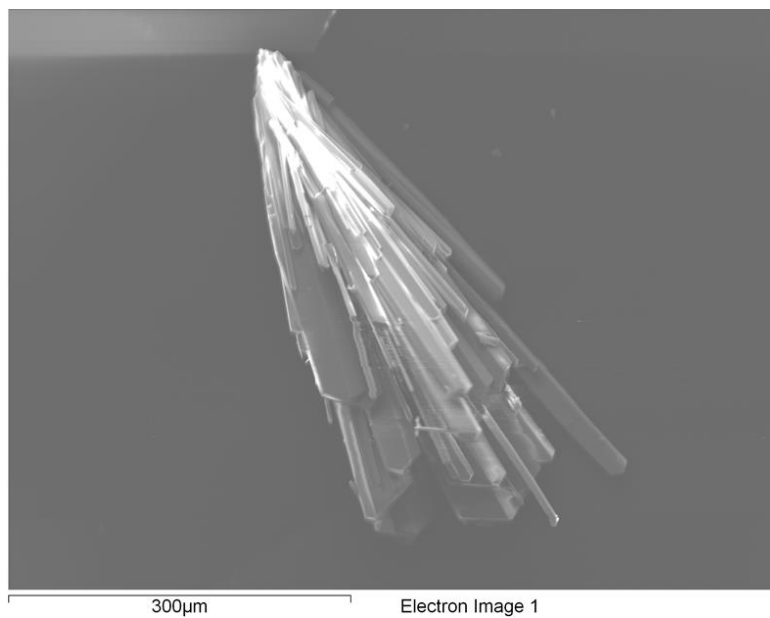


Figure 50: SEM image of $[(\text{H-pyridine})_2][(\text{AsO}_4)_2(\text{AsO}_3\text{OH})\text{Be}_2(\text{BeOH}_2)]$

3.12a: [H-bis(2-ethylhexyl)amine, NH₄]₄[(AsO₄)₃(AsO₃OH)Be₃(BeOH)]

The title compound crystallises as large rods with structural defects a common occurrence, it is a minor phase found in the bulk powder. A single crystal was selected and analysed by single crystal X-ray diffraction. The resulting structure exhibits monoclinic symmetry and occupies the C2/*c* space group. [H-bis(2-ethylhexyl)amine, NH₄]₄[(AsO₄)₃(AsO₃OH)Be₃(BeOH)] has an interrupted three dimensional structure, with the major distinguishing feature being large 10R aperture channels running parallel to the *a* crystallographic axis. Within these pores lie heavily disordered H-bis(2-ethylhexyl)amine and NH₄⁺ which are responsible for charge balancing the overall structure as well as exhibiting a structure directing effect. This structure, however can also be formed with Rb cations present (section 3.12b) so these extra-framework species can be seen has having a structure directing effect rather than acting as true ‘templates’. The 10R apertures form a network in the *bc* plane connected by helical ribbons of heavily folded 4Rs running parallel to *c* and *ac* similar to the topology encountered in UCSB-7.^[17] In UCSB-7 the ribbons are perpendicular to one another and form 12R apertures, in [H-bis(2-ethylhexyl)amine, NH₄]₄[(AsO₄)₃(AsO₃OH)Be₃(BeOH)] the ribbons cross at a 45 ° angle, leading to the network of 10Rs encountered. These networks are in turn cross-linked via 4Rs which connect to the helical backbone. Crystallographic parameters can be found in table 29.

Table 29: Table of crystallographic parameters for [H-bis(2-ethylhexyl)amine, NH₄]₄[(AsO₄)₃(AsO₃OH)Be₃(BeOH)]

Empirical formula	[H-bis(2-ethylhexyl)amine, NH ₄] ₄ [(AsO ₄) ₃ (AsO ₃ OH)Be ₃ (BeOH)]
Formula weight	674.2
Appearance	Clusters of deformed rods
Temperature	120 K
Wavelength	0.71073 Å
Crystal system	Monoclinic
Space group	C2/ <i>c</i>
<i>a</i>	12.9639(6) Å
<i>b</i>	14.0423(6) Å
<i>c</i>	18.6966(9) Å
<i>β</i>	90.160(4) °
Volume	3403.57(3) Å ³
<i>Z</i>	8
<i>D_c</i>	2.64 g cm ⁻³

R index	0.0566
Weighted R index	0.1430

[H-bis(2-ethylhexyl)amine, NH_4]₄[(AsO₄)₃(AsO₃OH)Be₃(BeOH)] was formed *via* standard solvothermal synthesis in an excess of water and Bis(2-ethylhexyl)amine. The bulk powder phase is likely made up of an mixture of unreacted starting materials and decomposition products from the amine.

The structure of [H-bis(2-ethylhexyl)amine, NH_4]₄[(AsO₄)₃(AsO₃OH)Be₃(BeOH)] was quite challenging to resolve; having β so close to 90 ° causes the dichotomy between solution as orthorhombic or monoclinic symmetry. A slight decrease in R factor was observed when solving in the lower symmetry setting, however on comparison with the Rb analogue it is likely that the true nature of the system is orthorhombic. The reduction of symmetry is due to the highly disordered nature of the extra-framework species, which in this case is an unresolvable mixture of bis(2-ethylhexyl)amine and its various decomposition products, including ammonia. It can be envisaged that if the extra-framework species was better defined the symmetry of the overall structure would be increased. For the purposes of accurate structure elucidation however, it was decided to solve the structure as a SQUEEZED monoclinic crystal system due to the more favourable fit between model and data.

[H-bis(2-ethylhexyl)amine, NH_4]₄[(AsO₄)₃(AsO₃OH)Be₃(BeOH)] has eight unique T atom sites, alternating between arsenic and beryllium centred. Three of each type are fully connected *via* oxygen bridging to their neighbours and are all involved in the 4R backbone [Fig. 53] and its crosslinking. The final two T sites are hydroxyl terminated which is suggested by a lengthening of the relevant T – O bond and confirmed by bond valence calculations [table 30]. This leaves the tetrahedra slightly distorted when compared to the fully connected tetrahedra. These terminated tetrahedra are part of the 4R backbone but where other T sites are also involved in crosslinking the network, the apical hydroxyl group is orientated into the centre of the 10R aperture where the hydroxyl group participates in strong intra-framework structure stabilisation *via* hydrogen bonding (1.756 (2) Å). The site alternates between networks, with AsO₃OH above BeO₃OH parallel to *a*. When considered from the *b* and *c* directions [H-bis(2-ethylhexyl)amine, NH_4]₄[(AsO₄)₃(AsO₃OH)Be₃(BeOH)] is relatively dense. The extra-framework species are too disordered to accurately solve but there is enough electron density to infer the presence of several organic species within the 10R channels which likely charge balance the negative framework [Fig. 54].

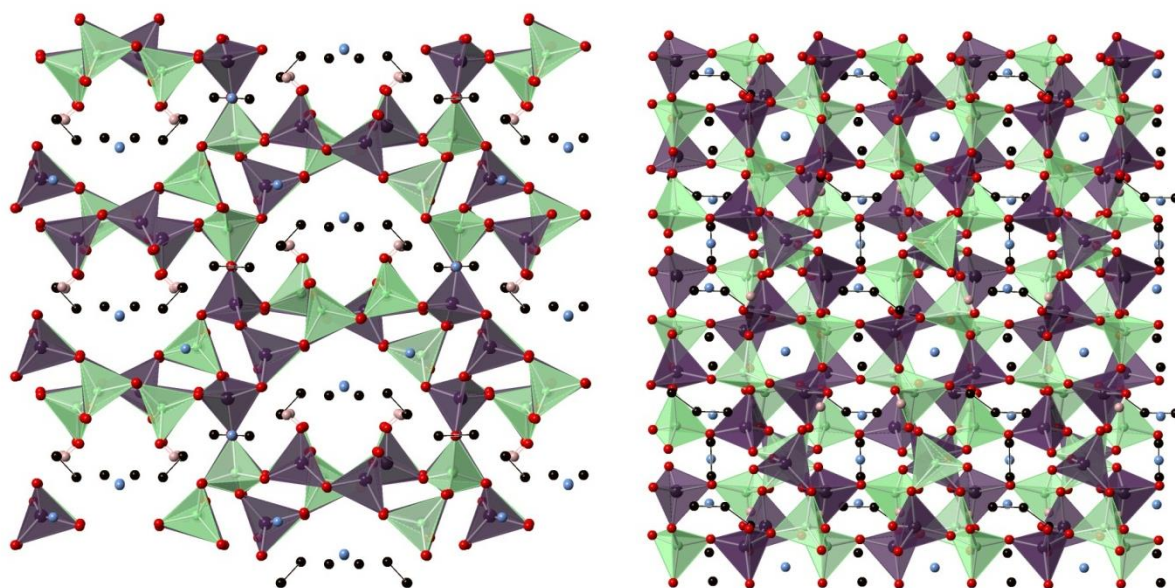


Figure 51: [H-bis(2-ethylhexyl)amine, NH_4]₄[(AsO_4)₃(AsO_3OH) Be_3 (BeOH)] viewed along *a* and *b* (left and right respectively). Green and purple tetrahedra are beryllium and arsenic. Red, black, blue and pink spheres are oxygen, carbon, nitrogen and hydrogen respectively.

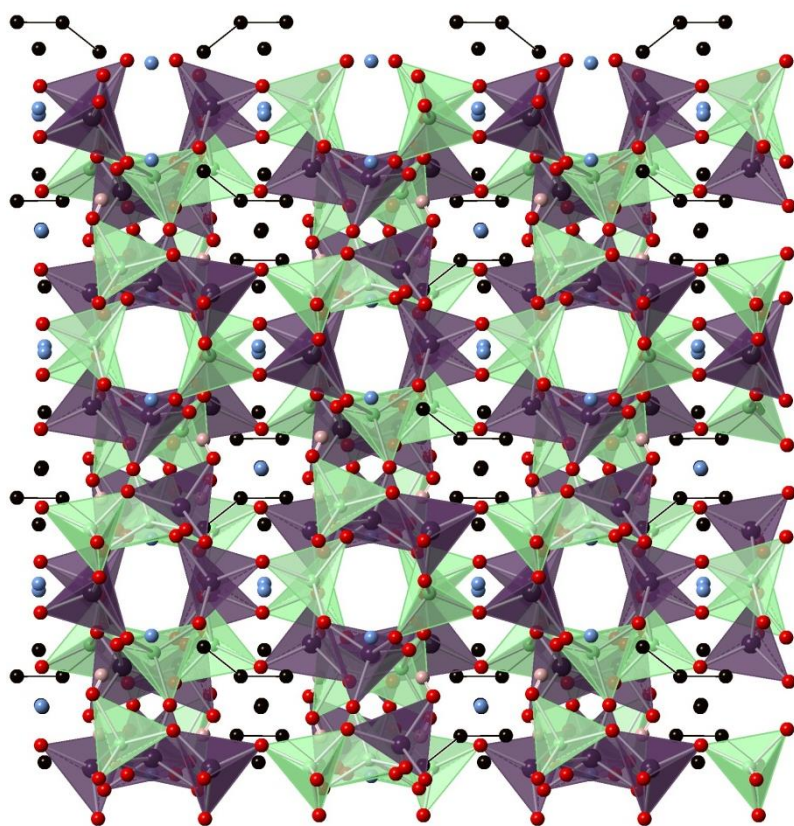


Figure 52: [H-bis(2-ethylhexyl)amine, NH_4]₄[(AsO_4)₃(AsO_3OH) Be_3 (BeOH)] viewed along *c*. Red, black, blue and pink spheres are oxygen, carbon, nitrogen and hydrogen respectively.

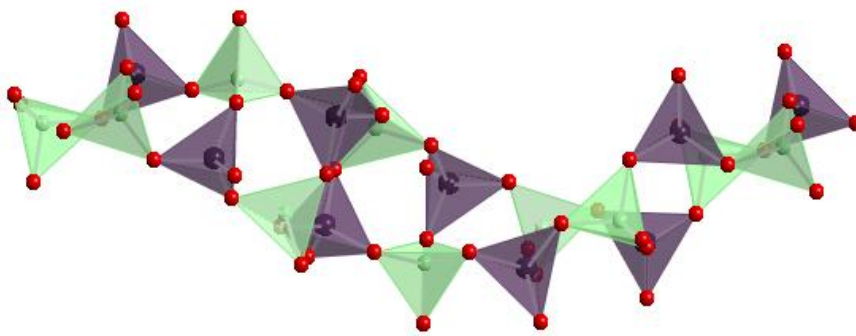


Figure 53: Helical ribbon backbone of 4Rs which form the overall network in [H-bis(2-ethylhexyl)amine, NH_4] $_4$ [(AsO_4) $_3$ (AsO_3OH) Be_3 (BeOH)]

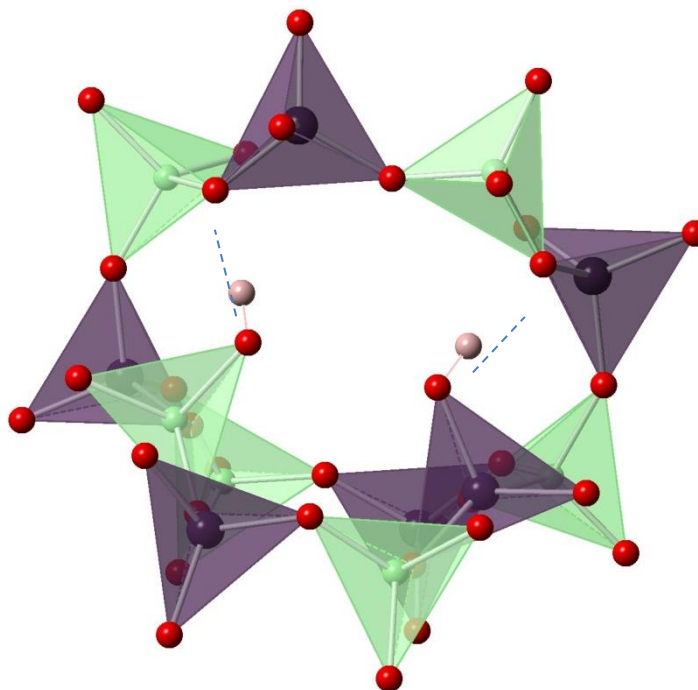


Figure 54: Intra-framework hydrogen bonding encountered in [H-bis(2-ethylhexyl)amine, NH_4] $_4$ [(AsO_4) $_3$ (AsO_3OH) Be_3 (BeOH)] it is likely that it contributes to the folded nature of the 10Rs

Table 30: Selected bond distances and angles in [H-bis(2-ethylhexyl)amine, NH_4] $_4$ [(AsO_4) $_3$ (AsO_3OH) Be_3 (BeOH)]

Bond	Bond length (Å)	Bond	Bond angle (°)
Average As – O	1.677(4)	Average O – As – OH	106.11(2)
Average Be – O	1.633(9)	Average O – Be – OH	106.19(5)
As– OH	1.733(4)		
Be – OH	1.688(9)		
(As)OH --- O	1.756 (2)		

(Be)OH --- O		1.781 (2)		
--------------	--	-----------	--	--

EDS measurements and an SEM image was taken of one of the crystals [Fig. 54]. EDS confirms the presence of both As and O and the SEM exhibits the morphology previously described. Unfortunately due to [H-bis(2-ethylhexyl)amine, NH_4] $_4$ [(AsO_4) $_3$ (AsO_3OH) Be_3 (BeOH)] being a minor phase no further characterisation was possible.

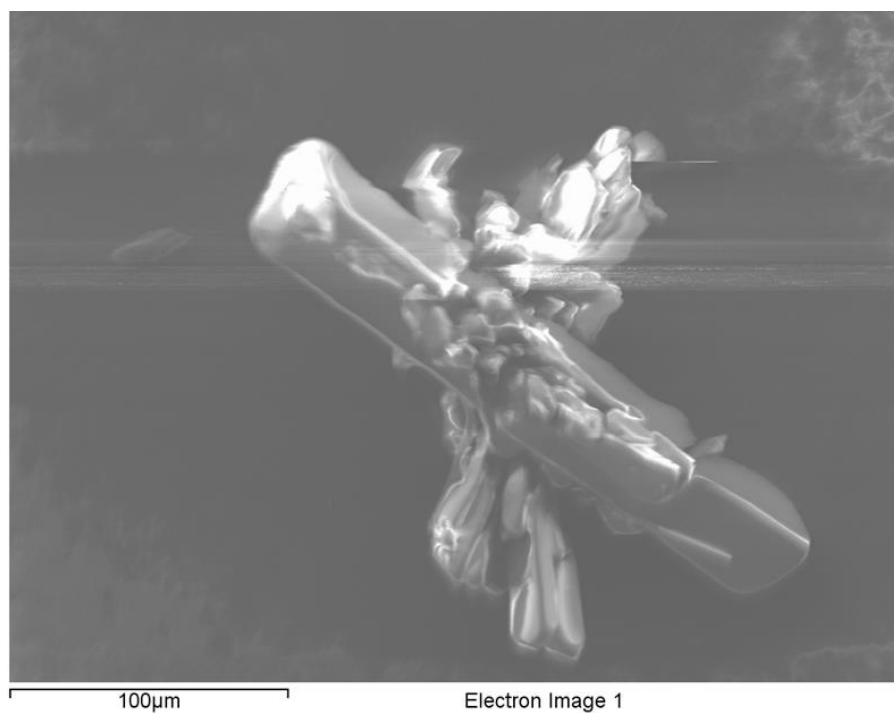


Figure 55: SEM image of [H-bis(2-ethylhexyl)amine, NH_4] $_4$ [(AsO_4) $_3$ (AsO_3OH) Be_3 (BeOH)]

3.12b: $\text{Rb}_3[(\text{AsO}_4)_3(\text{AsO}_3\text{OH})\text{Be}_3(\text{BeOH}_2)] \cdot \text{H}_2\text{O}$

Small colourless rods were discovered as a minor phase with a bulk mixed powder phase of starting materials. A single rod was selected and analysed by single crystal X-ray diffraction and the resulting interrupted three dimensional structure has orthorhombic symmetry and occupies the $C2/c$ space group. The structure of $\text{Rb}_3[(\text{AsO}_4)_3(\text{AsO}_3\text{OH})\text{Be}_3(\text{BeOH}_2)] \cdot \text{H}_2\text{O}$ is analogous to [H-bis(2-ethylhexyl)amine, $\text{NH}_4]_4[(\text{AsO}_4)_3(\text{AsO}_3\text{OH})\text{Be}_3(\text{BeOH})]$ (section 3.12a) and is formed of helical ribbons of 4Rs which in turn produce networks of 10R apertures cross linked by 4Rs. Unlike structure 3.12a, $\text{Rb}_3[(\text{AsO}_4)_3(\text{AsO}_3\text{OH})\text{Be}_3(\text{BeOH}_2)] \cdot \text{H}_2\text{O}$ has well defined extra-framework species in the form of five Rb cation sites, with variable occupancies, and one water site. This allows for structure solution in higher symmetry than encountered for 3.12a. Crystallographic parameters can be found in Table 31.

Table 31: Crystallographic parameters for $\text{Rb}_3[(\text{AsO}_4)_3(\text{AsO}_3\text{OH})\text{Be}_3(\text{BeOH}_2)] \cdot \text{H}_2\text{O}$

Empirical formula	$\text{Rb}_3[(\text{AsO}_4)_3(\text{AsO}_3\text{OH})\text{Be}_3(\text{BeOH}_2)] \cdot \text{H}_2\text{O}$
Formula weight	312.6
Appearance	Small rods
Temperature	120 K
Wavelength	0.71073 Å
Crystal system	Monoclinic
Space group	$C2/c$
<i>a</i>	13.0147(4) Å
<i>b</i>	14.0655(4) Å
<i>c</i>	18.7077(5) Å
Volume	3442.60(2) Å ³
<i>Z</i>	8
<i>D_c</i>	3.33 g cm ⁻³
R index	0.0815
Weighted R index	0.1989

On comparison to 3.12a a slight increase in all directions accompanied by an increase in cell volume is observed, this is due to the incorporation of the eight coordinated Rb cation expanding the structure out slightly.

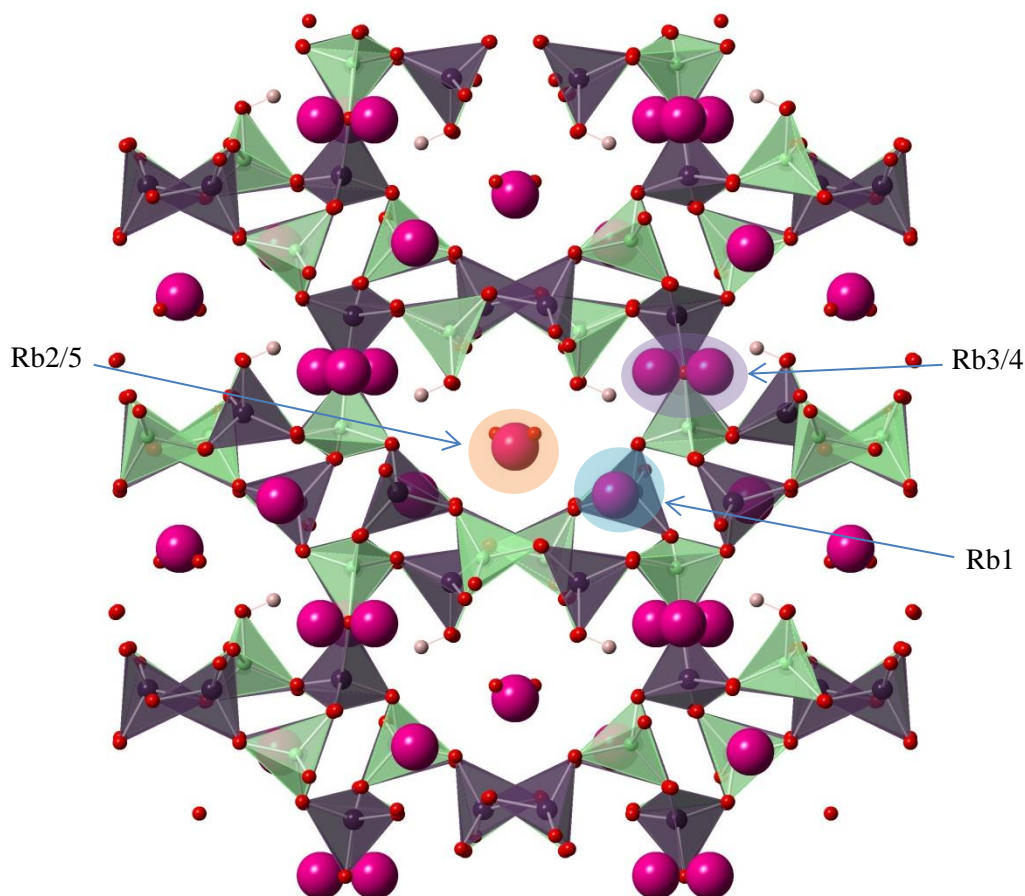


Figure 56: $\text{Rb}_3[(\text{AsO}_4)_3(\text{AsO}_3\text{OH})\text{Be}_3(\text{BeOH}_2)] \cdot \text{H}_2\text{O}$ viewed down a . Rb cations are represented as pink spheres and the sites are labelled. Green and purple tetrahedra are beryllium and arsenic. Red, and pale pink spheres are oxygen and hydrogen.

There are five crystallographic sites for Rb^+ present in the structure, each is eight coordinate with framework O or the extra-framework H_2O . Two of the sites are present as columns of alternating Rb^+ and H_2O running down the 10R channels parallel to a with each site being almost 50 % occupied (Table 35). The next two sites are either side of a 10R window formed between the networks, each site is again 50 % occupied. It is likely that these two sites actually alternate between layers as if both sites were occupied there would be a large degree of steric hindrance due to the proximity of each cation. The final site is nearly 100 % occupied and is situated in the centre of a large irregular cavity formed by 10R windows and the interaction between the 4R ribbons [Fig. 57]

Table 32: Table detailing Rb site occupancy

Rb site	Occupancy
Rb1	0.92
Rb2	0.42
Rb3	0.47
Rb4	0.47

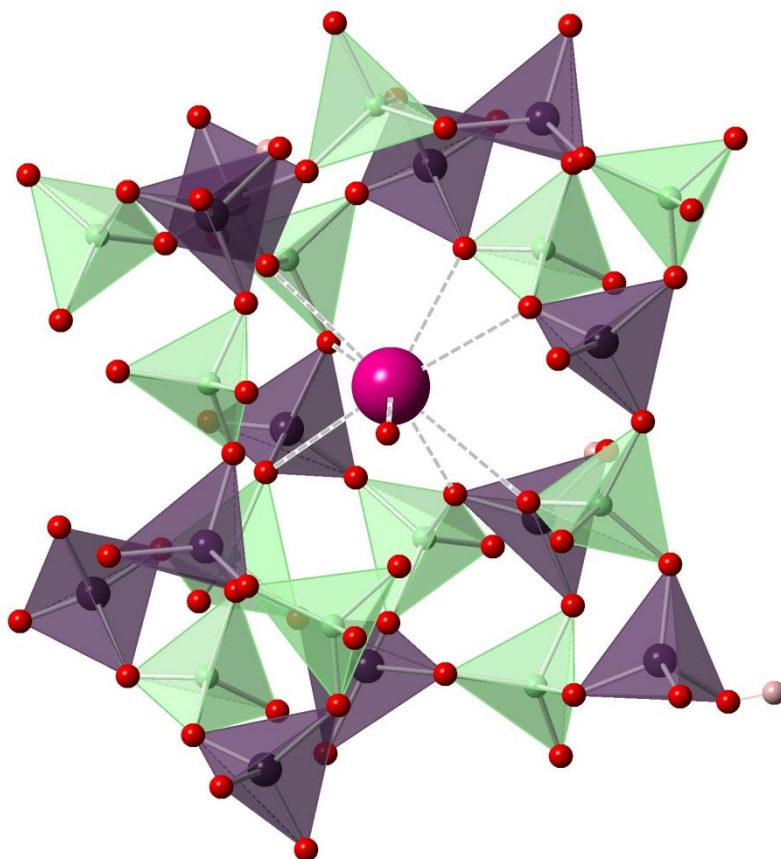


Figure 57: Coordination environment of Rb1 in $\text{Rb}_3[(\text{AsO}_4)_3(\text{AsO}_3\text{OH})\text{Be}_3(\text{BeOH}_2)] \cdot \text{H}_2\text{O}$

In comparison with structure 3.12a the framework hydroxyl groups are less well defined due to their proximity to Rb cations and have had to be elucidated by appreciating the extended bond distance on terminated tetrahedra and bond valence calculations. Selected bond distances can be found in Table 33.

Table 33: Selected bond distances and angles for $\text{Rb}_3[(\text{AsO}_4)_3(\text{AsO}_3\text{OH})\text{Be}_3(\text{BeOH}_2)] \cdot \text{H}_2\text{O}$

Bond	Bond length (Å)	Bond	Bond angle (°)
Average As – O	1.681(10)	Average O – As – OH	106.92(5)

Average Be – O	1.638(2)	Average O – Be – OH	107.65(13)
As– OH	1.734(10)		
Be – OH	1.664(2)		
(As)OH --- O	1.794 (4)		
(Be)OH --- O	1.873 (4)		
Average Rb – O	2.947(11)		

The presence of water molecules in this structure was confirmed by TGA. A gradual weight loss of 5.39 % was observed between RT and approximately 400 °C, corresponding to a calculated 5.7 % loss for dehydration of the structure [Fig. 58]. The high temperature of water loss testifies to the strength of coordination between the Rb cations and the extra-framework water. EDS measurements and an SEM image was taken of one of the crystals [Fig. 59]. EDS confirms the presence of Rb, As and O and the SEM exhibits the morphology previously described.

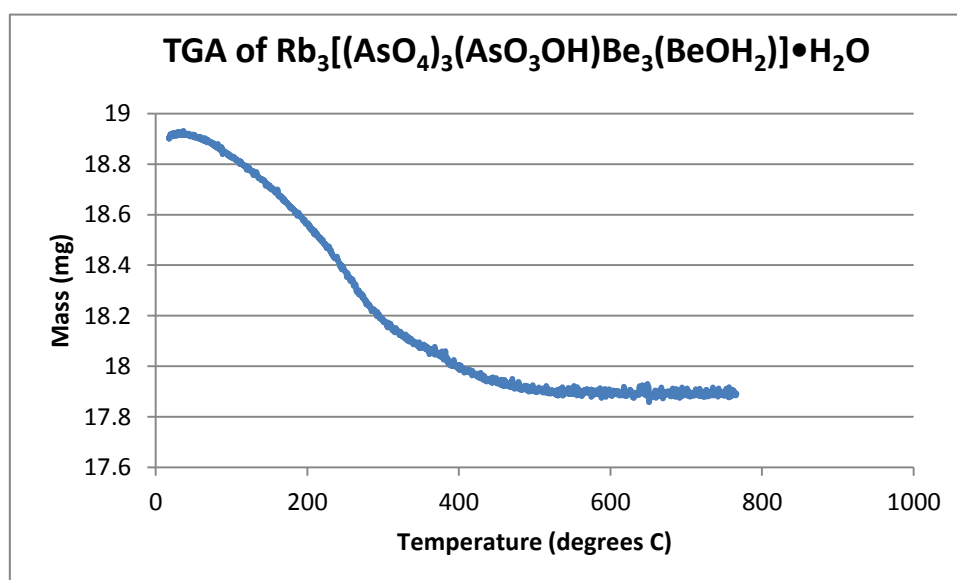


Figure 588: TGA of $\text{Rb}_3[(\text{AsO}_4)_3(\text{AsO}_3\text{OH})\text{Be}_3(\text{BeOH}_2)] \cdot \text{H}_2\text{O}$

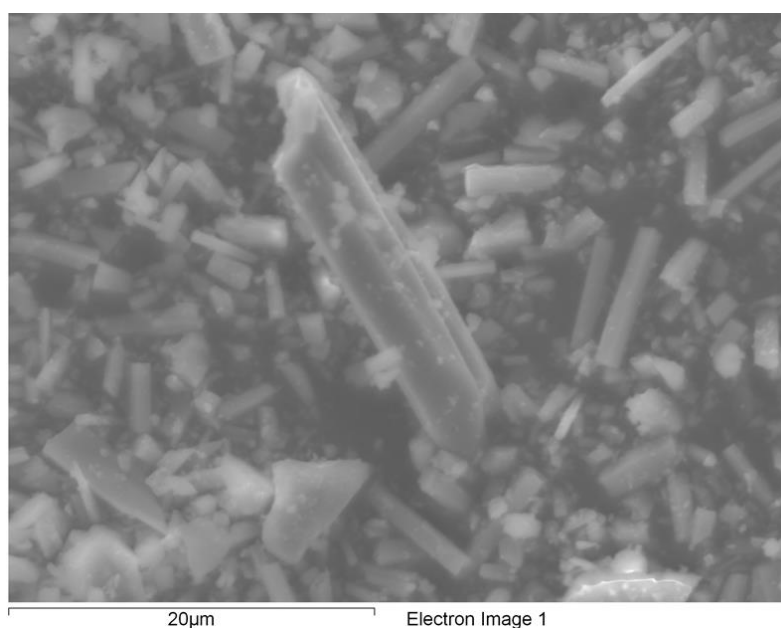


Figure 59: SEM image of $\text{Rb}_3[(\text{AsO}_4)_3(\text{AsO}_3\text{OH})\text{Be}_3(\text{BeOH}_2)] \cdot \text{H}_2\text{O}$

3.13: $\text{Rb}_2[(\text{AsO}_4)_2\text{Be}_2(\text{Be}(\text{OH})_2)] \cdot 1.5\text{H}_2\text{O}$

$\text{Rb}_2[(\text{AsO}_4)_2\text{Be}_2(\text{Be}(\text{OH})_2)]$ was originally formed as a minor phase present as clear fragments amongst an unidentifiable bulk powder phase, a fragment was selected and analysed *via* single crystal X-ray diffraction which produced an unsatisfactory model with an R factor in excess of 0.2. Further experimentation led to attempting the reaction at higher temperatures which led to the production of a phase pure sample of large chunky plate-like crystals. One of the plates was selected and analysed by single crystal diffraction and the resulting structure was found to exhibit the WEI topology, known only as a naturally occurring beryllophosphates. ^[15] $\text{Rb}_2[(\text{AsO}_4)_2\text{Be}_2(\text{Be}(\text{OH})_2)] \cdot 1.5\text{H}_2\text{O}$ represents the first synthetic route to this topology as well as being a beryllioarsenate analogue.

$\text{Rb}_2[(\text{AsO}_4)_2\text{Be}_2(\text{Be}(\text{OH})_2)] \cdot 1.5\text{H}_2\text{O}$ crystallises in the monoclinic crystal system and $\text{P2}_1/\text{n}$ space group. It is a highly unusual structure formed entirely of 3- and 4Rs which link to produce the spiro-5 ring and the νsv composite building units, as defined in chapter one. These building units form a fully connected three dimensional structure with a three dimensional channel system, comprising of 10R channels running parallel to a , 6Rs running parallel to b and 4Rs running parallel to c . The main network of 3- and 10Rs is formed entirely of spiro-5 units and each network is connected via 4Rs. Both water and Rb^+ are present as extra-framework species and are situated within the 10R channels. Crystallographic parameters can be found in Table 34.

Table 34: Crystallographic parameters of $\text{Rb}_2[(\text{AsO}_4)_2\text{Be}_2(\text{Be}(\text{OH})_2)] \cdot 1.5\text{H}_2\text{O}$

Empirical formula	$\text{Rb}_2[(\text{AsO}_4)_2\text{Be}_2(\text{Be}(\text{OH})_2)] \cdot 1.5\text{H}_2\text{O}$
Formula weight	534.5
Appearance	Chunky plates
Temperature	120 K
Wavelength	0.71073 Å
Crystal system	Monoclinic
Space group	$\text{P2}_1/\text{n}$
a	9.6117(3) Å
b	10.1725(4) Å
c	11.7152(4) Å
β	95.101(2) °
Volume	1140.92(2) Å ³

Z	4
D _c	3.11 g cm ⁻³
R index	0.0462
Weighted R index	0.1045

Rb₂[(AsO₄)₂Be₂(Be(OH)₂)]•1.5H₂O is formed at a relatively high pH (12.63) in the presence of two competitive structure directing agents, N-(3-aminopropyl)-1,3-propanediamine and RbOH. At the synthesis temperature N-(3-aminopropyl)-1,3-propanediamine has been shown to decompose into ammonium and other organic species which have a mineralising effect on some of the structures presented here. However, in the formation of Rb₂[(AsO₄)₂Be₂(Be(OH)₂)]•1.5H₂O no organic extra-framework species are observed and so it is likely that N-(3-aminopropyl)-1,3-propanediamine is present in a pH controlling role. The presence of RbOH seems vital as when the reaction is attempted with other alkali metal hydroxides or organic species no discernible product is formed, it is likely that Rb⁺ is playing a structure directing role in the synthesis.

Structurally Rb₂[(AsO₄)₂Be₂(Be(OH)₂)]•1.5H₂O has five crystallographic T sites, with two As centred and three Be. Both As centred tetrahedra are connected to four oxygen atoms at their vertices, which bridge to Be centred tetrahedra. The As centred tetrahedra are always found at the extremities of the spiro-5 units [Fig. 60] and are responsible for forming the cross-linking four rings. Of the Be centred tetrahedra, two are also situated at the extremities of the spiro-5 unit and are involved in the cross-linking 4Rs. The third beryllium site is in the centre of the spiro-5 unit and leads to formation of a consecutive chain of linked beryllium tetrahedra. Unlike in previous structures encountered in this chapter with this feature, the oxygen site is not triply bonded to T sites, instead it is left charge imbalanced (confirmed by bond valence calculations) between just the two Be centred tetrahedra, this leads to the permanent protonation of the site and therefore can be considered as a hydroxyl bridging unit rather than the much more common oxygen bridge. This hydroxyl bridge, as well producing a catalytically active framework, also stabilises the structure through weak intra-framework hydrogen bonding. The spiro-5 units alternate in layers on top of one another, with each spiro-5 twisted to connect to the one below and above to form 4- and 6R channels, orientated along *c* and *b* respectively. The resulting unbonded apices are connected to the next spiro-5 unit in the plane and result in the channels of 10Rs parallel to *a* [Fig. 61].

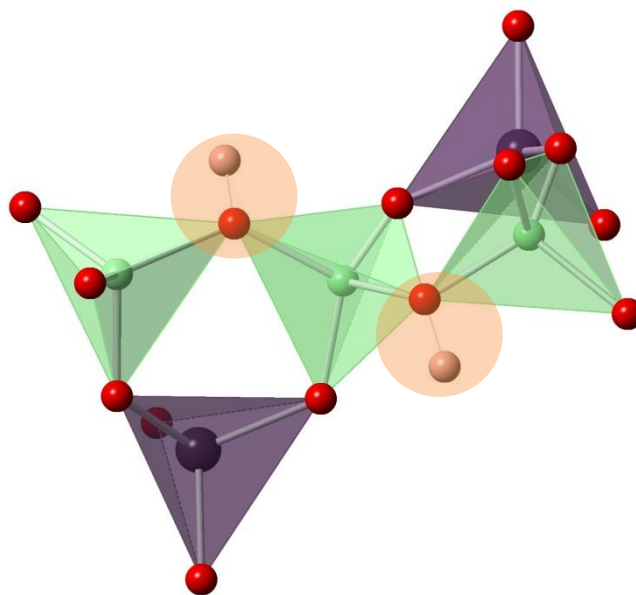


Figure 60: Spiro-5 building unit encountered in $\text{Rb}_2[(\text{AsO}_4)_2\text{Be}_2(\text{Be}(\text{OH})_2)] \cdot 1.5\text{H}_2\text{O}$ with hydroxyl bridging units highlighted. Green and purple tetrahedra are beryllium and arsenic. Red and pink spheres are oxygen and hydrogen.

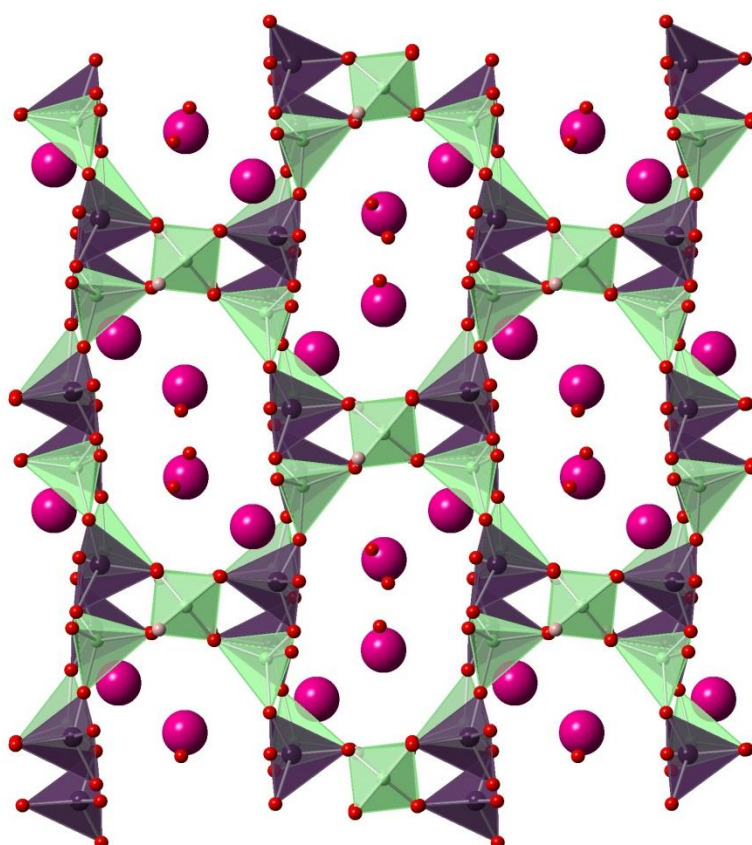


Figure 61: $\text{Rb}_2[(\text{AsO}_4)_2\text{Be}_2(\text{Be}(\text{OH})_2)] \cdot 1.5\text{H}_2\text{O}$ viewed along a . Green and purple tetrahedra are beryllium and arsenic. Red, pink and pale pink spheres are oxygen, rubidium and hydrogen respectively.

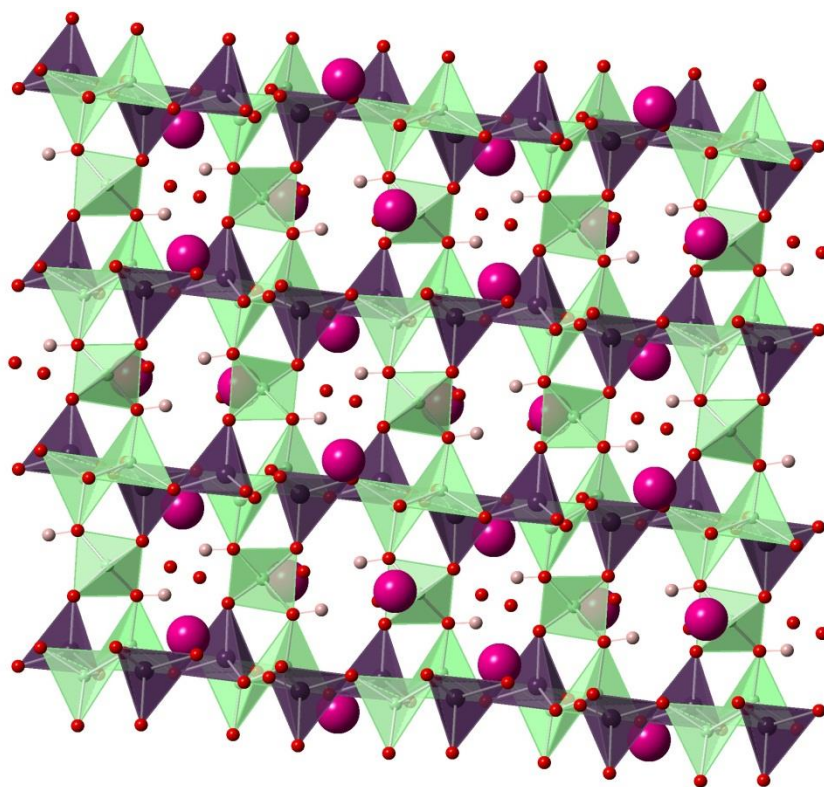


Figure 62: $\text{Rb}_2[(\text{AsO}_4)_2\text{Be}_2(\text{Be}(\text{OH})_2)] \cdot 1.5\text{H}_2\text{O}$ viewed along *b*. Green and purple tetrahedra are beryllium and arsenic. Red, pink and pale pink spheres are oxygen, rubidium and hydrogen respectively.

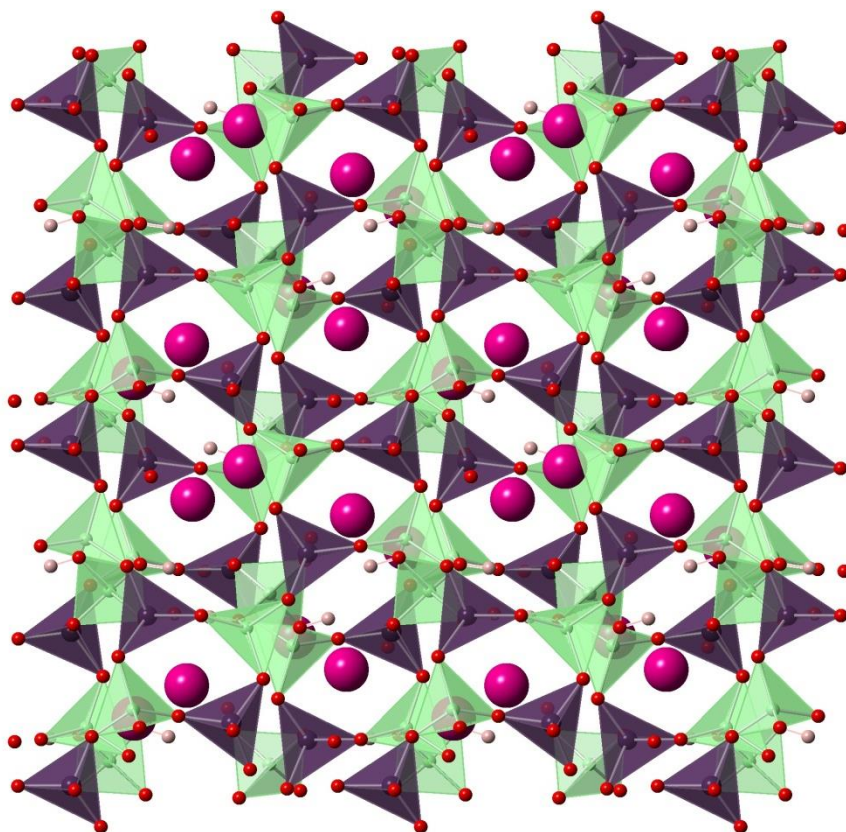


Figure 63: $\text{Rb}_2[(\text{AsO}_4)_2\text{Be}_2(\text{Be}(\text{OH})_2)] \cdot 1.5\text{H}_2\text{O}$ viewed along *c*. Green and purple tetrahedra are beryllium and arsenic. Red, pink and pale pink spheres are oxygen, rubidium and hydrogen respectively.

The large internal surface area allows for the incorporation of several extra-framework species, namely Rb^+ and H_2O . The fully occupied Rb cation sites provide both charge balancing and structure stabilisation by being 6 coordinate to both framework oxygen and the extra-framework water [Fig. 64]. There are two extra-framework water sites, one of which is fully occupied. The other is 50 % occupied and shares its site with a symmetry related oxygen site 1.585 Å away.

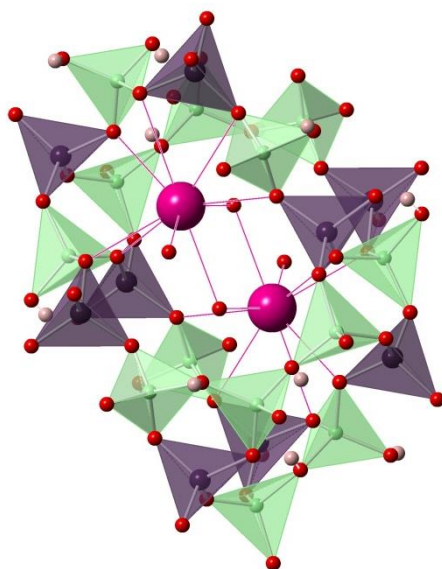


Figure 64: Rb coordination environment

Table 35: Selected bond lengths for $\text{Rb}_2[(\text{AsO}_4)_2\text{Be}_2(\text{Be}(\text{OH})_2)] \cdot 1.5\text{H}_2\text{O}$

Bond	Bond length (Å)
Average As – O	1.679(4)
Average Be – O	1.636(10)
Be – OH1	1.626(10)
Be – OH2	1.641(10)
OH1 – O	1.9742 (5)
OH2 – O	2.0051 (4)
Average Rb – O	2.970(5)

A VTPXD was carried out on $\text{Rb}_2[(\text{AsO}_4)_2\text{Be}_2(\text{Be}(\text{OH})_2)] \cdot 1.5\text{H}_2\text{O}$ and shows structure stability up to 450 °C. EDS measurements and an SEM image was taken of one of the crystals [Fig. 65]. EDS confirms the presence of Rb, As and O and the SEM exhibits the morphology previously described.

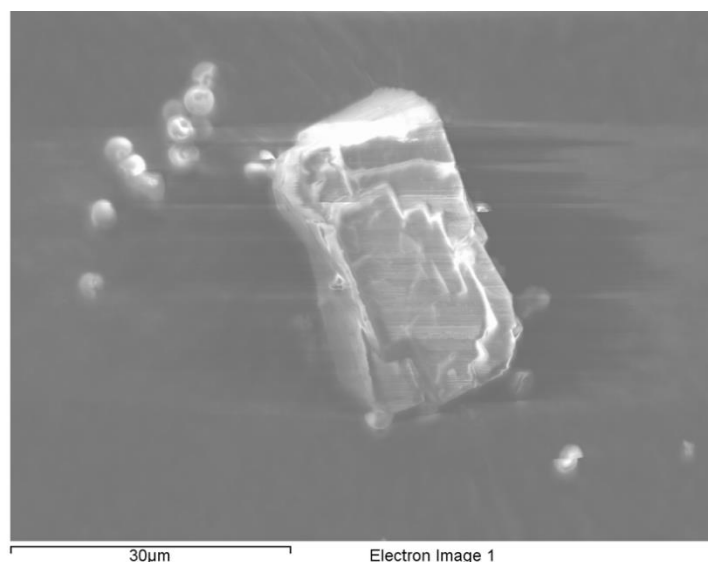


Figure 65: SEM image of $\text{Rb}_2[(\text{AsO}_4)_2\text{Be}_2(\text{Be}(\text{OH})_2)] \cdot 1.5\text{H}_2\text{O}$

Comparison with naturally occurring weinebeneite

The unit cell of the synthetic beryllarsenate WEI described here is slightly contracted by between 0.1 to 0.3 Å in comparison to naturally occurring beryllphosphate WEI (Table 36). This can be ascribed to the distortion caused by the imbalance of atomic radii between As and Be, which also leads to the more condensed, elliptical form of the 10Rs present in synthetic WEI as opposed to natural WEI [Fig. 66]. As with previously discussed MER BeAS and BeP analogues, the FD for the synthetic beryllarsenate WEI is slightly less than that of the naturally occurring analogue. The extra-framework species are also different with Rb present in synthetic WEI and Ca in natural. Otherwise the structures are analogous.

Table 36: Comparison between synthetic and natural WEI analogues

Empirical formula	$\text{Rb}_2[(\text{AsO}_4)_2\text{Be}_2(\text{Be}(\text{OH})_2)] \cdot 1.5\text{H}_2\text{O}$	$\text{Ca}_4\text{Be}_{12}\text{P}_8\text{O}_{32}(\text{OH})_8 \cdot 16\text{H}_2\text{O}$ ^[15]
Crystal system	Monoclinic	Monoclinic
Space group	$\text{P2}_1/\text{n}$	Cc
<i>a</i>	9.6117(3) Å	11.897 Å
<i>b</i>	10.1725(4) Å	9.707 Å
<i>c</i>	11.7152(4) Å	9.633 Å
β	95.101(2) °	95.76 °
Volume	1140.92(2) Å ³	1121.78 Å ³
FD (T/1000 Å ³)	17.5	18.1

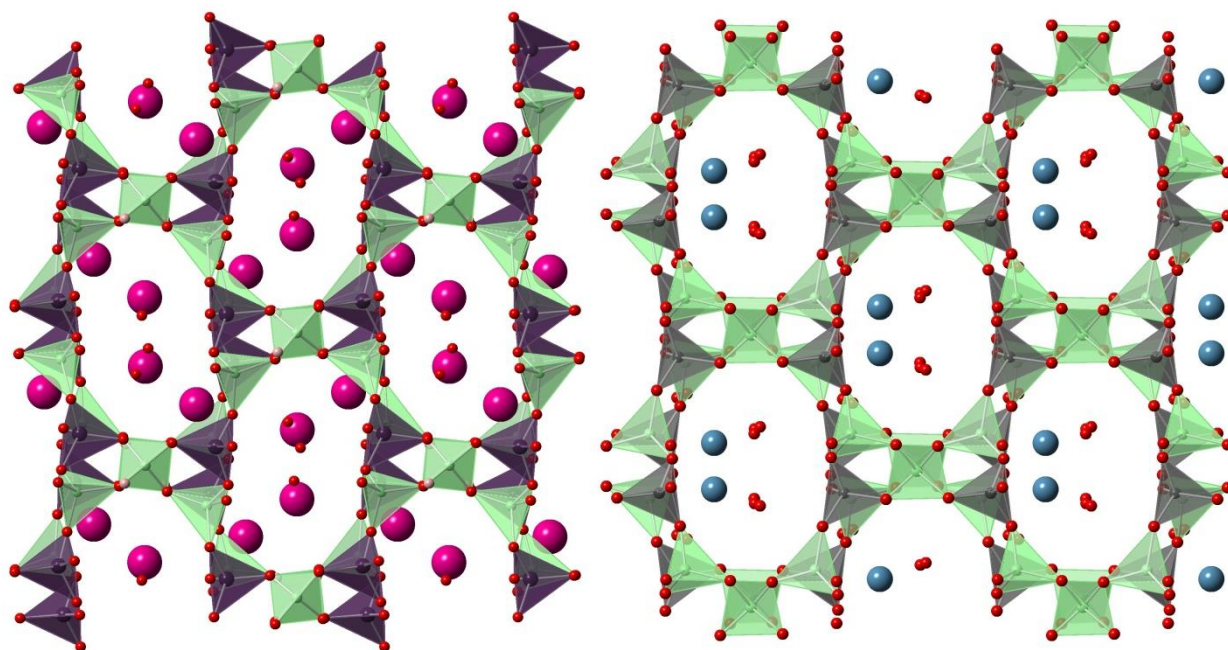


Figure 66: Synthetic WEI (left) and natural WEI (right) viewed along *a* and *c* respectively. Green and purple tetrahedra are beryllium and arsenic. Red, blue, pink and pale pink spheres are oxygen, calcium, rubidium and hydrogen respectively.

3.14: Na[AsO₄Be]

At relatively low pH (5.95 – 6.10) and high temperature (220 °C) large truncated polyhedral crystals are formed in the presence of a variety of organic structure directing agents and sodium species. A single crystal was isolated and model a for the structure obtained from single crystal X-ray diffraction. The resulting structure exhibits trigonal symmetry and crystallises in the P6₃ space group resembling the well-known quartz polymorph, β -tridymite. ^[20] Na[AsO₄Be] has a fully connected three dimensional structure formed of 6Rs of alternating Be and As centred tetrahedra which in turn form channels occupied by Na⁺ along *c*. The tetrahedra are orientated with their apices pointing along *c* or – *c* allowing for crosslinking between layers which form channels of distorted 6Rs along $\frac{1}{2}a$ $\frac{1}{2}b$ $\frac{1}{2}c$. Crystallographic parameters are displayed in Table 37.

Table 37: Crystallographic parameters of Na[AsO₄Be]

Empirical formula	Na[AsO ₄ Be]
Formula weight	170.9
Appearance	Colourless truncated polyhedra
Temperature	120 K
Wavelength	0.71073 Å
Crystal system	Trigonal
Space group	P6 ₃
<i>a</i>	8.3753(3) Å
<i>c</i>	7.9815(8) Å
Volume	484.86(1) Å ³
<i>Z</i>	6
<i>D_c</i>	2.34 g cm ⁻³
R index	0.0717
Weighted R index	0.2646

Na[AsO₄Be] has been formed in the presence of a variety of OSDAs, however none have been incorporated in to the structure so can be viewed as having a pH controlling role only. The pH of the system seem to be an important consideration as Na[AsO₄Be] only forms between pH 5.90 and 6.15 and in the presence of Na cation producing species such as NaOH and NaF. The addition of fluoride based mineraliser (NaF) has no discernible effect on the size of crystals produced. Phase pure Na[AsO₄Be] has been produced via pH control, relatively high reaction temperatures (220 °C) and the presence of NaOH.

Na[AsO₄Be] has two crystallographically unique vertex sharing [TO₂] sites, which are alternating oxygen bridged As and Be centred tetrahedra. Both sites are fully connected and are involved in sinusoidal chains which connect to form the 6Rs and each tetrahedra alternate in their apex orientation. All Be centred tetrahedra are oriented to $-c$ and crosslink to the layer of 6Rs below, the As *vice versa*. The 6Rs themselves are highly irregular, owing to the distortion in bond angles commonly observed in the berylloarsenates. The structure is templated by the presence of octahedrally coordinated Na⁺ cations, which stabilise the structure as well as provide charge balancing. The sodium cations are present in *afi* cages formed between layers of the 6R network. [Fig. 69]

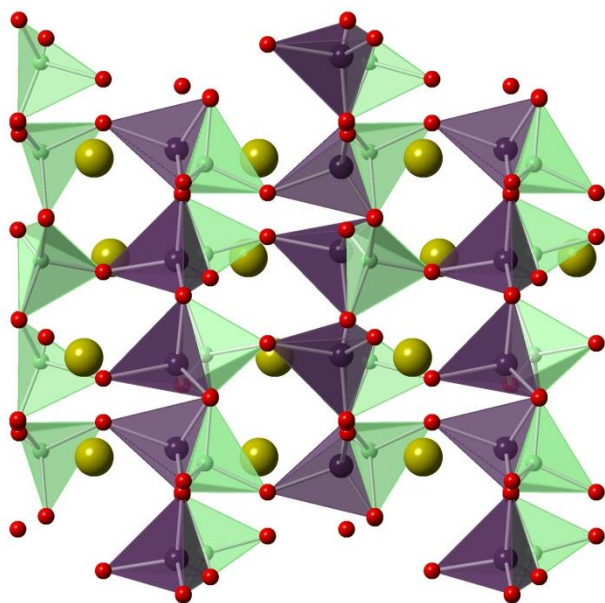


Figure 67: Na[AsO₄Be] viewed along both *a/b*. Green and purple tetrahedra are beryllium and arsenic. Red and yellow spheres are oxygen and sodium.

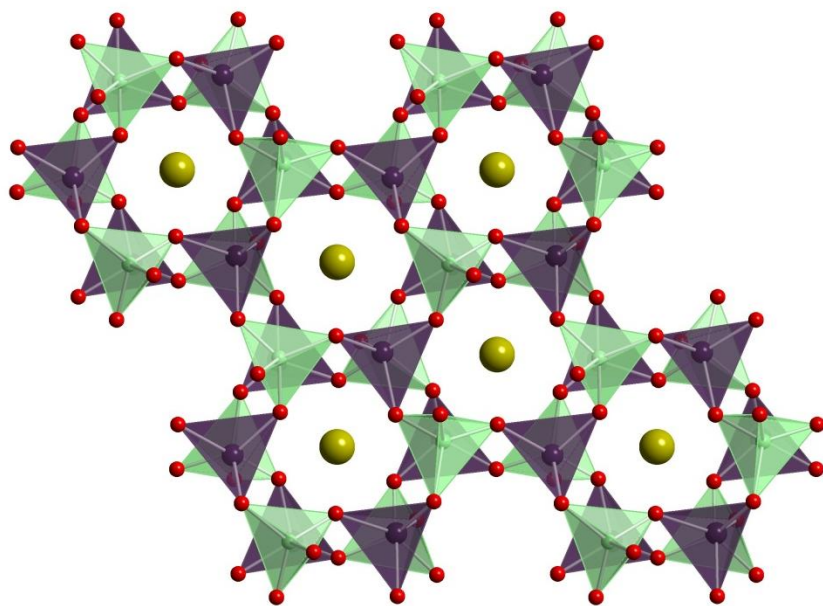


Figure 68: Na[AsO₄Be] viewed along *c*. Green and purple tetrahedra are beryllium and arsenic. Red and yellow spheres are oxygen and sodium.

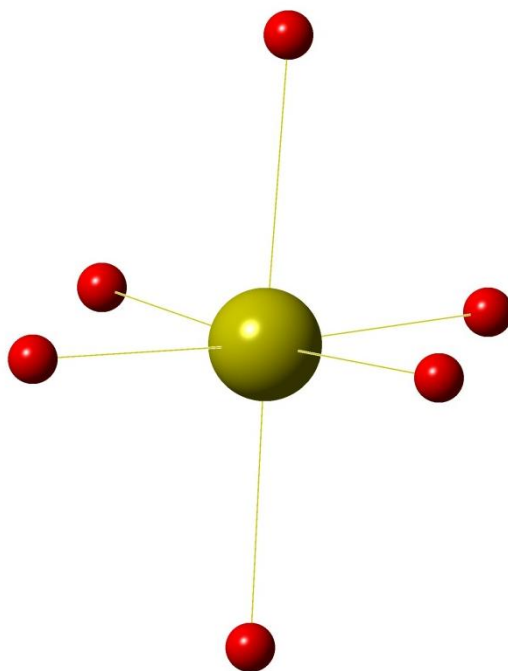


Figure 69: Octahedral coordination of Na sites present in Na[AsO₄Be]. Yellow and red spheres represent sodium and oxygen respectively.

Comparison with silicate tridymite

Na[AsO₄Be] resembles β -tridymite in that they are both formed of layers of 6Rs which are cross-linked to form *afī* cages, however, the stacking between layers in Na[AsO₄Be] is anti-parallel with respect to the triad axis of the tetrahedra, similar to the stacking found in another quartz polymorph, cristobalite. This difference in stacking, along with the distortion in ring shape encountered in berylloarsenates leads to the differences in crystallographic parameters, $a = 5.03$ and $c = 8.22$ Å for β -tridymite^[18] as opposed to 8.375(3) and 7.981(8) Å in Na[AsO₄Be].

3.15: $[\text{NH}_4]_2[(\text{AsO}_4)_2\text{Be}_2(\text{Be}(\text{OH})_2)]$

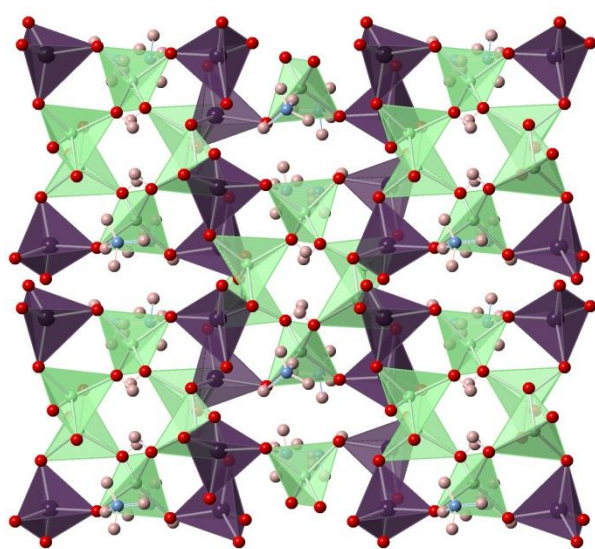
$[\text{NH}_4]_2[(\text{AsO}_4)_2\text{Be}_2(\text{Be}(\text{OH})_2)]$ was originally formed as a minor phase present as clear shards nucleating from balls of unidentifiable bulk material. A fragment was selected and analysed *via* single crystal X-ray diffraction which produced an unsatisfactory model with an R factor in excess of 0.17. Further experimentation led to attempting the reaction at higher temperatures and pH (11.89 – 12.81) which led to the production of a phase pure samples of large blocky crystals. One of the blocks was selected and analysed by single crystal diffraction and the resulting structure was found to exhibit a new fully connected zeotype topology, with no known analogues present in the IZA database. This was confirmed through modelling by Mark Weller utilising the TOTOPOL software suite.^[19] $[\text{NH}_4]_2[(\text{AsO}_4)_2\text{Be}_2(\text{Be}(\text{OH})_2)]$ is the first novel fully connected framework produced by this study and has been assigned the provisional three letter code BEN (BEryllium Nine) pending IZA structure commission approval, it has also been published as BAF1125.^[14]

$[\text{NH}_4]_2[(\text{AsO}_4)_2\text{Be}_2(\text{Be}(\text{OH})_2)]$ crystallises in the monoclinic crystal system and occupies the $\text{P2}_1/n$ space group, it has five crystallographically unique T atom sites distributed as two arsenic and three beryllium. Each site is fully connected via oxygen and hydroxyl bridging to further T atom sites. The linking of these tetrahedra leads to the formation of spiro-five rings (as seen in WEI) formed from three BeO_4 and two AsO_4 units and 4Rs connected into chains. The connectivity of these SBUs leads to the formation of cavities with elliptical 8R apertures containing ammonium cations as extra-framework species. Owing to the short average T-O distance (1.654 Å) and small mean T-O-T angle (122.6°) $[\text{NH}_4]_2[(\text{AsO}_4)_2\text{Be}_2(\text{Be}(\text{OH})_2)]$ has an almost feldsparthic framework density of 21.4 tetrahedra / 1000 Å³, however, can still be considered zeolitic due to the existence of compositionally analogous zeotypes such as $\text{NH}_4\text{-ANA}$ and $\text{NH}_4\text{-ABW}$. The zeolitic character of $[\text{NH}_4]_2[(\text{AsO}_4)_2\text{Be}_2(\text{Be}(\text{OH})_2)]$ is further reinforced by TGA and VTPXD measurements showing that the ammonium can be partially removed on heating without structural destruction. Crystallographic parameters can be found in Table 41 and $[\text{NH}_4]_2[(\text{AsO}_4)_2\text{Be}_2(\text{Be}(\text{OH})_2)]$ is considered from *a*, *b* and *c* in figure 70.

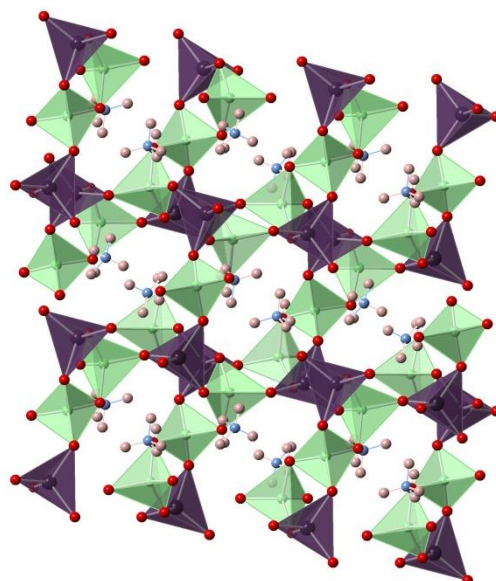
Table 38: Crystallographic parameters for $[\text{NH}_4]_2[(\text{AsO}_4)_2\text{Be}_2(\text{Be}(\text{OH})_2)]$

Empirical formula	$[\text{NH}_4]_2[(\text{AsO}_4)_2\text{Be}_2(\text{Be}(\text{OH})_2)]$
Formula weight	374.9
Appearance	Chunky blocks
Temperature	120 K
Wavelength	0.71073 Å
Crystal system	Monoclinic

Space group	$P2_1/n$
a	9.9140(3) Å
b	8.5660(3) Å
c	11.1562(4) Å
β	100.050(2) °
Volume	932.88(3) Å ³
Z	4
D_c	2.11 g cm ⁻³
R index	0.0377
Weighted R index	0.0776



(i)



(ii)

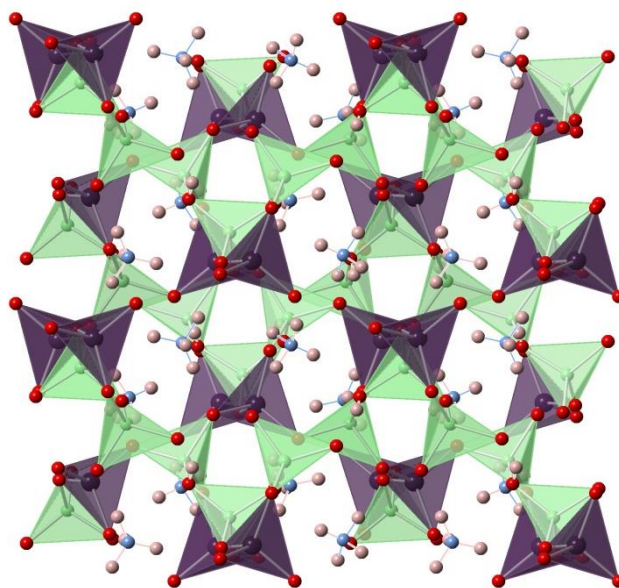


Figure 70: $[\text{NH}_4]_2[(\text{AsO}_4)_2\text{Be}_2(\text{Be}(\text{OH})_2)]$ viewed along a (i), b (ii) and c (iii). Green and purple tetrahedra are beryllium and arsenic. Red, blue and pink spheres are oxygen, nitrogen and hydrogen respectively.

$[\text{NH}_4]_2[(\text{AsO}_4)_2\text{Be}_2(\text{Be}(\text{OH})_2)]$ was originally synthesised from a hydrothermal mixture containing N-(3-aminopropyl)-1,3-propanediamine and an excess of water. The bulky amine decomposed into ammonium, which in turn acts as a structure directing agent allowing the nucleation of the dense elliptical 8Rs around it. In the original synthesis $[\text{NH}_4]_2[(\text{AsO}_4)_2\text{Be}_2(\text{Be}(\text{OH})_2)]$ was formed as an extremely minor phase, further reactions at higher temperatures (220 °C as opposed to 160°C) and high pH (11.89 – 12.81) led to the formation of much larger crystals and $[\text{NH}_4]_2[(\text{AsO}_4)_2\text{Be}_2(\text{Be}(\text{OH})_2)]$ forming as the major phase. $[\text{NH}_4]_2[(\text{AsO}_4)_2\text{Be}_2(\text{Be}(\text{OH})_2)]$ has also been formed in the presence of 1,3-diaminopropane, ethylamine and 2-aminomethylpyridine, where the original starting material has decomposed into ammonium and other organics.

Structure refinement of the original dataset was challenging due to the poor availability of crystals of sufficiently high quality, however the basic topology could be modelled with an R factor of 0.17. After further experimentation had produced larger and more regular crystals, modelling of the extra-framework species and even the hydroxyl bridging became possible.

In a similar fashion to that encountered in WEI, $[\text{NH}_4]_2[(\text{AsO}_4)_2\text{Be}_2(\text{Be}(\text{OH})_2)]$ is primarily formed of spiro-5 rings with the first beryllium site situated in the centre of the spiro-5 unit which leads to formation of a consecutive chain of linked beryllium tetrahedra. Unlike in previous structures encountered in this chapter with this feature, the oxygen site is bonded to $\text{T}^{2+}/\text{T}^{5+}$ sites, instead it is left charge imbalanced (confirmed by bond valence calculations) between just the two Be centred tetrahedra, this leads to the permanent protonation of the site and therefore can be considered as a hydroxyl bridging unit rather than the much more common oxygen bridge. This hydroxyl bridge, as well producing Brønsted sites, also potentially stabilises the structure through very weak intra-framework hydrogen bonding (2.939 (5) Å). The overall structure is also charge balanced and stabilised by strong hydrogen bonding (average: 2.051 (7) Å) with the two crystallographically unique tetrahedral ammonium sites present in the cavities [Fig. 71]

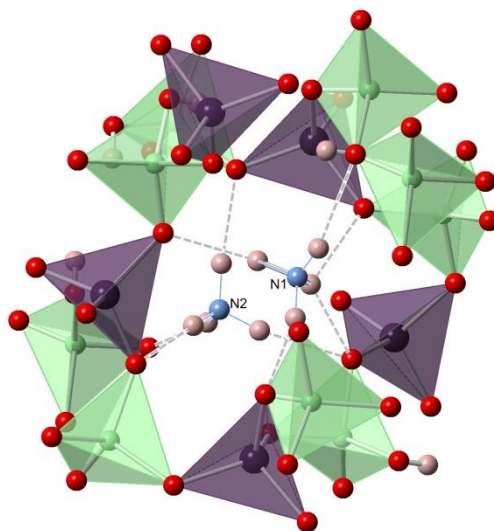


Figure 71: Extra-framework ammonium sites present in $[\text{NH}_4]_2[(\text{AsO}_4)_2\text{Be}_2(\text{Be}(\text{OH})_2)]$

Table 39: Selected bond lengths and angles in $[\text{NH}_4]_2[(\text{AsO}_4)_2\text{Be}_2(\text{Be}(\text{OH})_2)]$

Bond	Bond length (Å)	Bond	Bond angle (°)
Average As – O	1.682(3)	Average O – As – O	109.46(15)
Average Be1 – O	1.624(7)	Average O – Be – O	109.44(4)
Average Be2/3 – O	1.642(7)		
Average (Be)O – H	1.629 (9)		
Average N – H	0.897 (8)		
Average (N)H – O(framework)	2.051 (7)		

^9Be MASNMR, VTPXD and TGA analysis were carried out on $[\text{NH}_4]_2[(\text{AsO}_4)_2\text{Be}_2(\text{Be}(\text{OH})_2)]$. Analysis of the ^9Be data exhibits a singlet which suggests a single beryllium environment, there is theoretically two different beryllium environments, however, they are very similar and as such are not discernible in MASNMR. VTPXD [Fig. 72] shows a loss of ammonium at $\sim 250^\circ\text{C}$ and a complete destruction of crystallinity by 400°C . TGA [Fig. 73] measurements show a gradual decrease in mass between room temperature and 303.61°C followed by an steeper incline to 365°C , which represents a 14.5 % decrease in mass, this is in relatively good agreement with the 14.9 % mass loss expected from the loss of both extra-framework ammonium cations and the condensation of one H_2O from the structure.

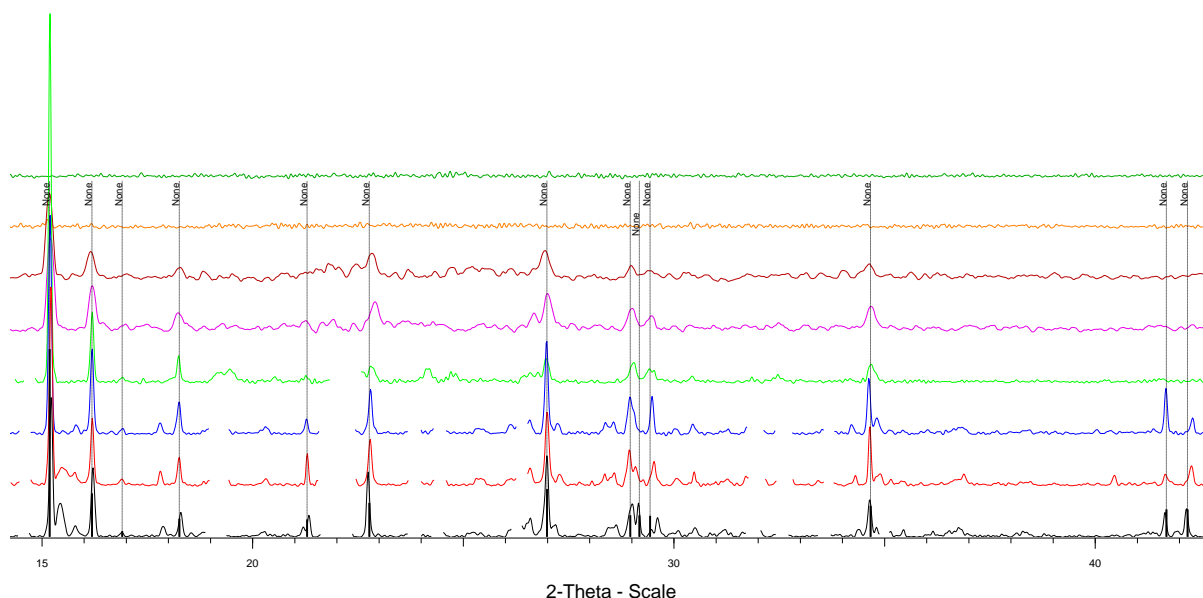


Figure 72: VTPXD of $[\text{NH}_4]_2[(\text{AsO}_4)_2\text{Be}_2(\text{Be}(\text{OH})_2)]$ between 100 and 450°C , topology peaks positions are represented by dashed lines. Loss of ammonium is seen between 200 and 250°C and total destruction of crystallinity is observed by 400°C . Bulk phase peaks have been omitted

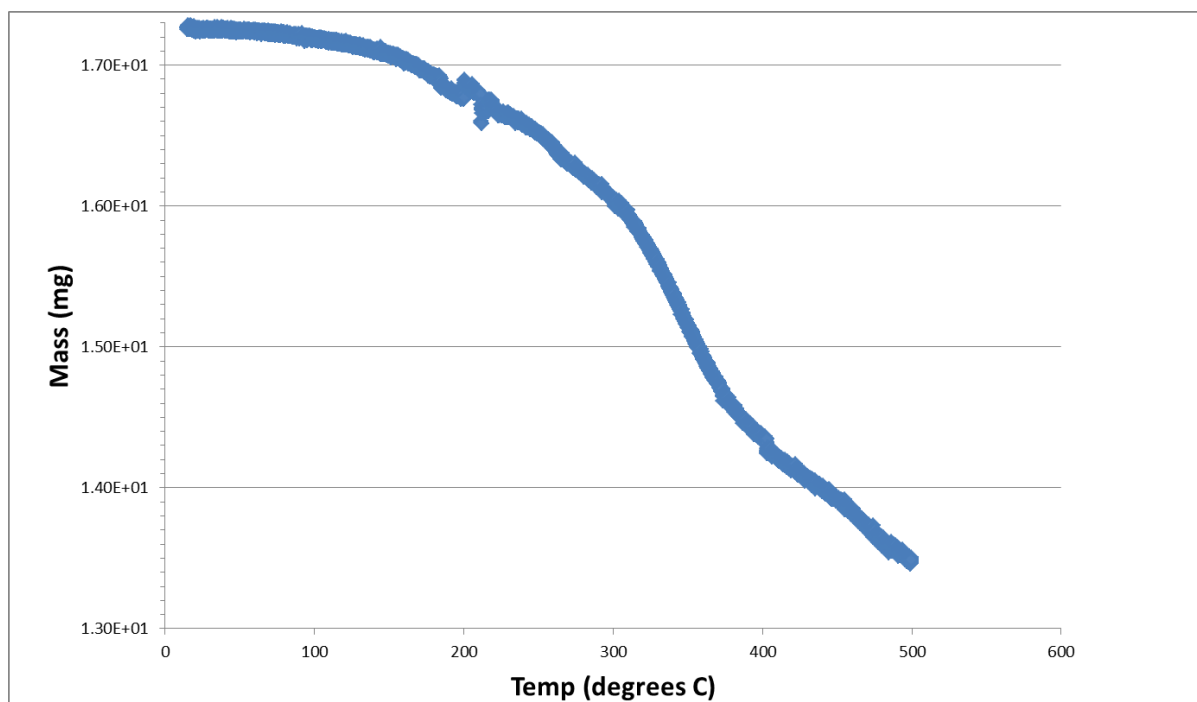


Figure 73: TGA of $[\text{NH}_4]_2[(\text{AsO}_4)_2\text{Be}_2(\text{BeOH})_2]$ showing ammonium and water loss. Anomaly at around 200 °C is likely due to disturbance of the instrument.

3.16: $[\text{C}_2\text{H}_5\text{NH}_2, \text{H}_2\text{O}]_x[\text{Be}_{66.7}\text{As}_{25.3}(\text{O})_{80.5}(\text{OH})_{103.5}]$

$[\text{C}_2\text{H}_5\text{NH}_2, \text{H}_2\text{O}]_x[\text{Be}_{66.7}\text{As}_{25.3}(\text{O})_{80.5}(\text{OH})_{103.5}]$ was originally synthesised by Natalie Seaton (while studying as a project student for the author) and is found as tiny (10 x 10 x 10 μm) transparent platelets surrounded by white powdery BeO bulk phase. A regular plate was selected and analysed *via* single crystal X-ray diffraction which scattered extremely weakly owing to the high proportion of light elements and small crystal size. Repeating the synthesis and further manual investigation led to the discovery of much larger (200 x 200 x 20 μm) crystals and on analysis by single crystal X-ray diffraction the resulting structure was found to exhibit a new fully connected zeotype topology, with no known analogues present in the IZA database. This was confirmed through modelling by Mark Weller utilising the TOTOPOL software suite.^[21] $[\text{C}_2\text{H}_5\text{NH}_2, \text{H}_2\text{O}]_x[\text{Be}_{66.7}\text{As}_{25.3}(\text{O})_{80.5}(\text{OH})_{103.5}]$ is the second novel fully connected framework produced by this study and has been assigned the provisional three letter code BOZ pending IZA structure commission approval; it has also been accepted for publication as BET.^[22]

BOZ crystallises in the monoclinic crystal system and was solved in the $\text{P2}_1/c$ space group and has 23 crystallographic unique T atom sites, each site is mixed between arsenic and beryllium with an overall Be:As ratio of 2.5(\pm 1.5):1. The resulting large charge imbalance is rectified by the bridging unit being a mixture of oxygen and predominately hydroxide. Like BEN (section 3.15) the major SBU is the spiro-5 ring, with the central site being near to fully occupied by Be. The only other simple SBU present in the asymmetric unit cell is a single 4R. The overall structure is formed of sinusoidal chains of spiro-5 rings along *a* which are further connected to form a network containing two large and unusual composite building units. The first is a pentagonal drum shaped cage formed by two 10Rs connected via spiro-5 rings [Fig. 76] hereafter termed *ben*. The second cage (*bet*) is asymmetric and is formed by four 8Rs, two 6Rs, one 4R and six 3Rs, these two cages form columns running through the structure along *c* and lead to formation of channels of 10Rs along *a* and 8Rs along *c* [Fig.76]. The crosslinking of the *ac* network layers leads to the formation of 10R channels along 101. Crystallographic parameters can be found in Table 40.

Table 40: Crystallographic parameters for BOZ

Empirical formula	$[\text{C}_2\text{H}_5\text{NH}_2, \text{H}_2\text{O}]_x[\text{Be}_{66.7}\text{As}_{25.3}(\text{O})_{80.5}(\text{OH})_{103.5}]$
Formula weight	5542.47
Appearance	Transparent platelets
Temperature	120 K
Wavelength	0.71073 Å

Crystal system	Monoclinic
Space group	$P2_1/c$
a	14.1779(3) Å
b	34.8915(7) Å
c	13.9360(2) Å
β	90.0150(2) °
Volume	6894.02(2) Å ³
Z	1
R index	0.0789
Weighted R index	0.1947

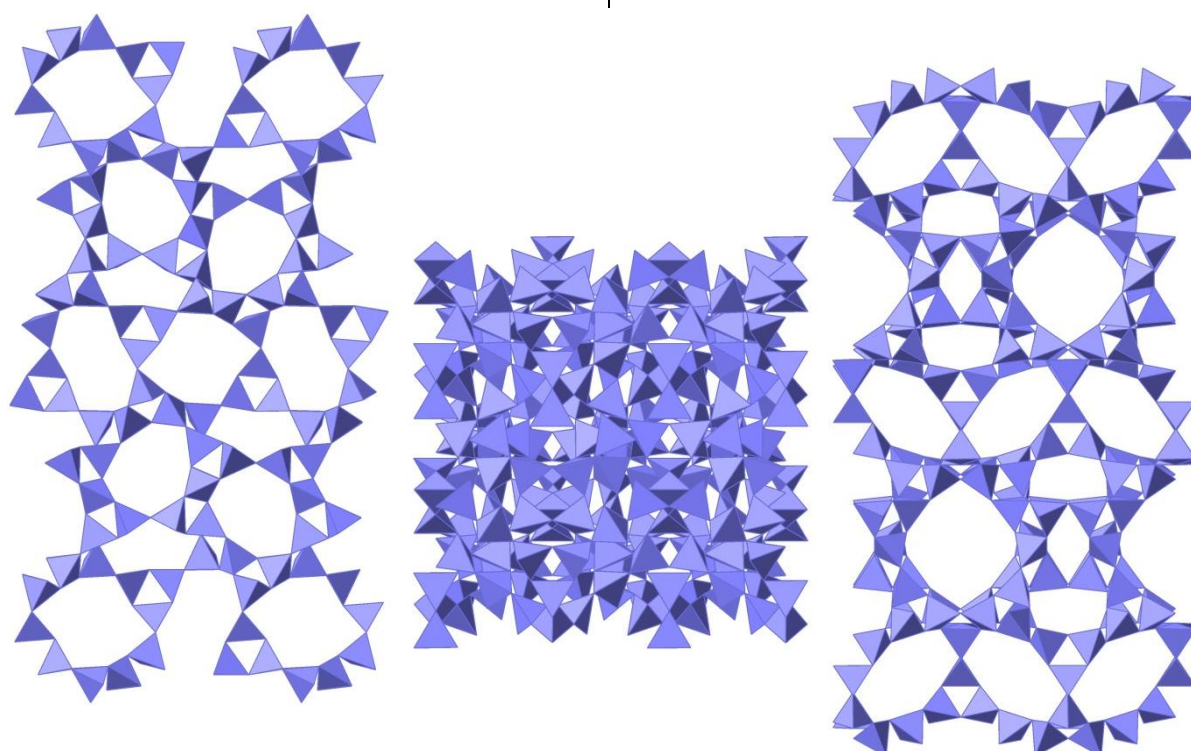


Figure 74: BOZ viewed along a , b and c (i, ii and iii respectively), magenta tetrahedra represent disordered character of T atom sites.

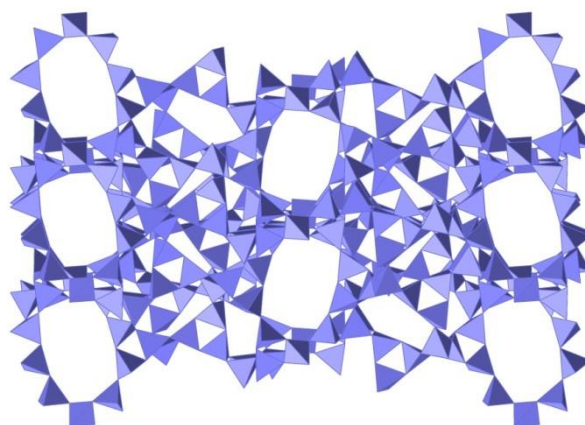


Figure 75: BOZ viewed along 101 , magenta tetrahedra represent disordered character of T atom sites.

BOZ is formed exclusively in the presence of ethylamine and at relatively mild temperatures (160 °C) and high pH (12.5 – 12.75). Its formation seems to be relatively independent of the concentration of Be, as long as it is above Be:As 1.4:1.7. Where the amount of As was varied, as soon as it is in great excess, BOZ is no longer formed. An increase in crystal size and phase purity was also noted with increasing concentrations of Be. This coincides with the high beryllium content of the structure.

The structure solution of BOZ was extremely complicated and as such was solved by Mark Weller. The first complication arose in the comparatively close to 90 ° β angle which led to attempts in solving the structure in orthorhombic Pnma which gave substantially worse fits to the experimental data. The structure was solved in monoclinic P2₁/m, direct methods found the majority of the T-atom sites, with the remainder located by Fourier maps. Initially all T-sites were refined as mixed As/Be although as the refinement progressed sites such as the centres of spiro-5 rings were close to unity for Be and therefore set as fully occupied by Be. By considering the framework atoms alone, the model converged rapidly although producing relatively high R factors; 15 – 20 %. The SQUEEZE^[23] function was used to allocate electron density to possible extra-framework species which had a further positive effect on the R factor. High anisotropy in the ADPs was observed with the majority of framework oxygen atoms, implying local positional disorder in adjacent T-sites and raising the possibility that the oxygen site may be O²⁻ or OH⁻. Attempts were made to model the structure where the oxygen atoms with the highest anisotropy were placed over split sites, however for the relatively small improvement in R factor, significantly higher numbers of parameters were introduced into the refinement. The structure reported here has full site occupancies of bridging atoms with a few remaining large ADPs.

As discussed previously the structure of BOZ is extremely complex, with 23 unique T-sites, each mixed in varying quantities between As and Be. BOZ is formed of complicated networks along the *ac* plane which are connected *via* spiro-5 rings. The other SBU and CBU present in the structure are 4Rs and *ben/bet* cages [FIG. 76]. The connectivity of these cages leads to the three-dimensional channel system mentioned above with a largest cavity parameter of 8.7 Å. Unfortunately due to the necessary use of the SQUEEZE^[23] function and the low scattering profile of the structure, the coordinates of extra-framework species or framework hydrogen have not been elucidated. It is likely however that the pores have ethylamine, its decomposition products and water present within them in structure stabilising and charge balancing roles. Due to the large amount of 3Rs present within the structure the framework density and calculated density are extremely low; 13.3 /1000 Å³ and 1.38 gcm⁻³ respectively.

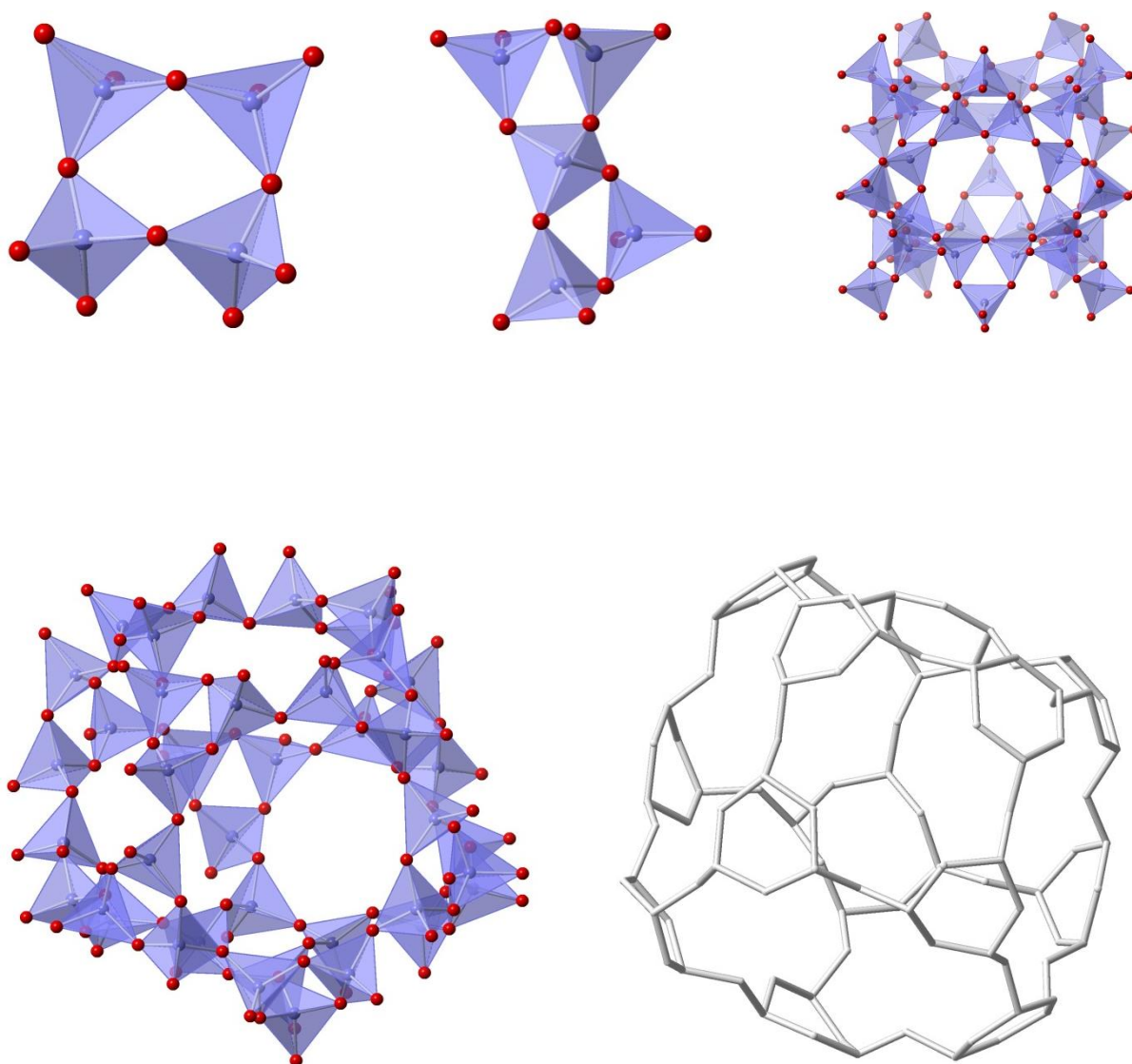


Figure 76: Secondary building units present in BOZ, from top left; 4R, spiro-5 ring (*lov*), *ben* cage. From bottom left; *bet* cage, *bet* cage in stick form for clarity. Magenta tetrahedra represent mixed TO_4 sites, red spheres represent bridging anions (O^{2-} or OH^-).

Further characterisation was carried out by Mark Weller and investigated the porosity and structural stability of BOZ. Theoretical porosities were calculated using the ZEOMICS package ^[24] and the structure theoretically displays a total pore volume of $0.670 \text{ cm}^3 \text{ g}^{-1}$ when considered as a solely $\text{Be}(\text{OH})_2$ framework, which compares to $0.508 \text{ cm}^3 \text{ g}^{-1}$ for siliceous LTA. Leading to a predicted internal surface area of $1828 \text{ m}^2 \text{ g}^{-1}$ when considering a molecular diameter of 2 \AA . This would likely be greater if the structure lacked sterically hindering OH^- groups present within the pores. BET pore volume measurements were carried out and found an experimental total pore volume of $0.36 \text{ cm}^3 \text{ g}^{-1}$. This deviation between theoretical and observed is likely due to incomplete removal of water and organic templating molecules. VTPXD shows a degradation of crystallinity above 250°C however TGA measurements show that $\sim 80\%$ of extra-framework material can be removed before structure

collapse and the mass loss combined with extra-framework electron density from SQUEEZE suggests a synthetic composition of $[\text{C}_2\text{H}_5\text{NH}_2, \text{H}_2\text{O}]_{120}[\text{Be}_{66.7}\text{As}_{25.3}(\text{O})_{80.5}(\text{OH})_{103.5}]$ with similar hydration levels to those found in FAU type frameworks. The acidity of BOZ was probed *via* IR spectroscopy and pyridine adsorption. The framework OH-stretch is located at 3479 cm^{-1} , similar to that found for $\text{Be}(\text{OH})_2$ and this indicates more acidic protons in comparison with Brønsted acid forms of aluminosilicate zeolites which generally absorb around 3600 cm^{-1} .^[25]

3.17: $[R^+]_{1.5}[As_{6.17}Be_{13.83}O_{\sim 20}OH_{\sim 20}].nH_2O$

$[R^+]_{1.5}[As_{6.17}Be_{13.83}O_{\sim 20}OH_{\sim 20}].nH_2O$ is found as large (100 x 50 x 20 μm) transparent tablets associated with lamellar needles of BTL (section 3.18) and polyphasic with large quantities of starting material. A regular tablet was selected and analysed *via* single crystal X-ray diffraction which scattered extremely weakly owing to the high proportion of light elements, small crystal size and large volume of the monoclinic unit cell. The resulting structure was found to exhibit a new fully connected zeotype topology, with no known analogues present in the IZA database. This was confirmed through modelling by Mark Weller utilising the TOTOPOL software suite.^[21] $[R^+]_{1.5}[As_{6.17}Be_{13.83}O_{\sim 20}OH_{\sim 20}].nH_2O$ is the third novel fully connected framework produced by this study and has been assigned the provisional three letter code BEL pending IZA structure commission approval, it has also been accepted for publication as BEE.^[22]

BEL crystallises from hydrothermal conditions into the monoclinic crystal system and $P2_1/n$ space group, its huge cell volume (9031.2(7) \AA^3) contains 30 crystallographically unique T-atom sites, leading BEL to be the most complicated zeotype currently known. Like BOZ (section 3.16) each site varies dramatically between As/Be with the majority predominantly beryllium centred. Unlike BOZ, BEL is formed entirely of spiro-5 (*lov*) rings, and the connectivity of these SBUs leads to the formation of *ben* cages as seen in BOZ. The *ben* cages are further connected and aligned to produce slightly sinusoidal 10R and 8R channels along *b* and *a*. The channels form a three-dimensional system through further interconnection *via* distorted 8Rs along 101 [Fig. 78]. Crystallographic parameters can be found in Table 41.

Table 41: Selected crystallographic parameters for BEL

Empirical formula	$[R^+]_{1.5}[As_{6.17}Be_{13.83}O_{\sim 20}OH_{\sim 20}].nH_2O$
Formula weight	7349.85
Appearance	Transparent tablets
Temperature	120 K
Wavelength	0.71073 \AA
Crystal system	Monoclinic
Space group	$P2_1/n$
<i>a</i>	18.3570(5) \AA
<i>b</i>	13.8239(10) \AA
<i>c</i>	36.7532(10) \AA
β	104.46(2) $^\circ$

Volume	9031.2(7) Å ³
Z	6
R index	0.118
Weighted R index	0.333

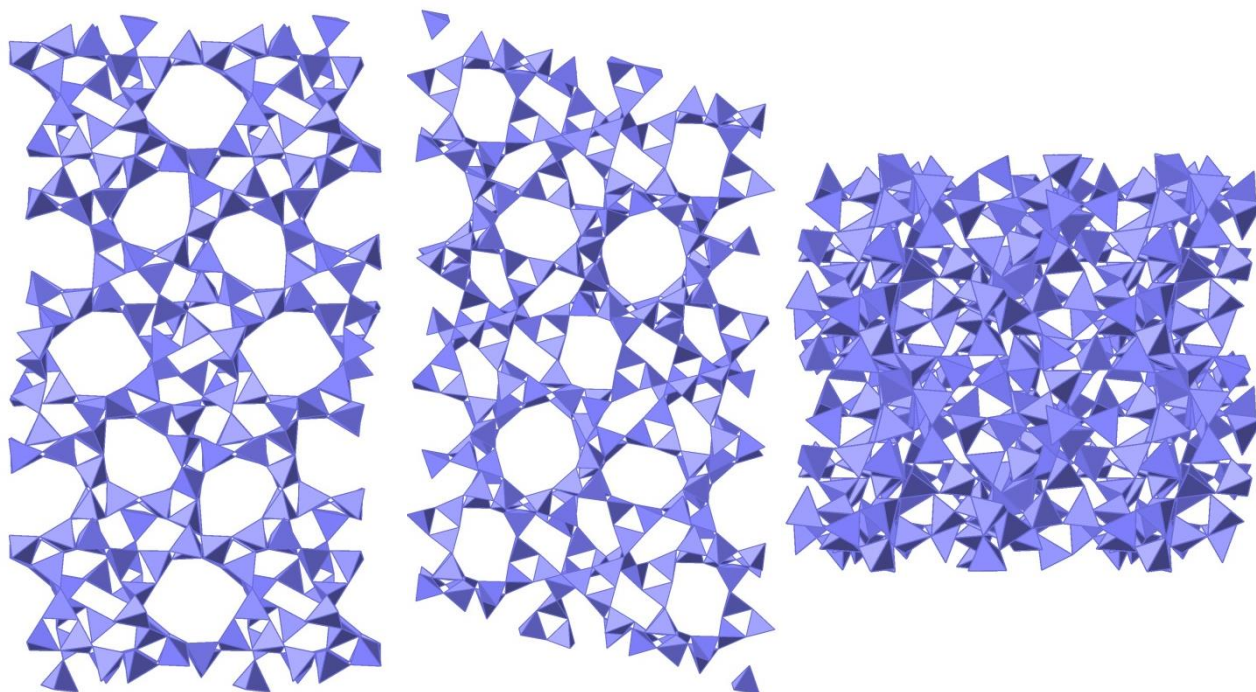


Figure 77: BEL viewed along *a*, *b* and *c* (i, ii and iii respectively), magenta tetrahedra represent disordered character of T atom sites.

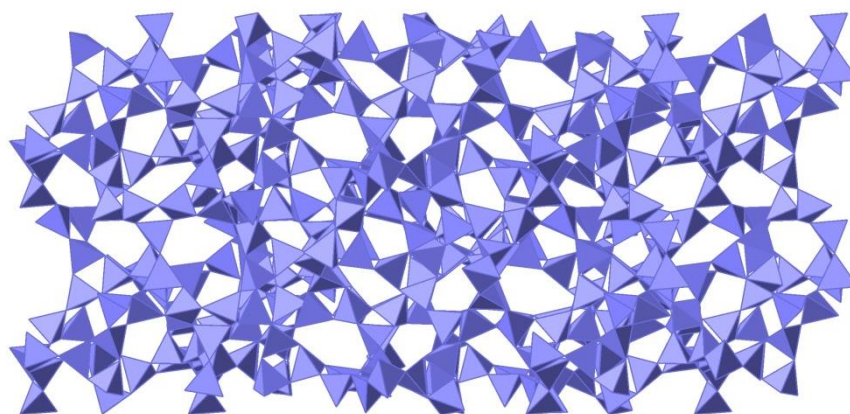


Figure 78: BEL viewed along 101, magenta tetrahedra represent disordered character of T atom sites.

BEL has only been found to crystallise under the specific conditions outlined in Table 2, with no deviation of any nature resulting in its successful formation. Full structure solution was carried out as outlined for BOZ (section 3.16), hence the high R factors. Attempts were made with BEL to collect data from synchrotron sources; however, they were unsuccessful as the crystals decomposed in the intense beam during data collection.

As discussed previously the structure of BEL is complex, with 30 unique T-sites, each mixed in varying quantities between As and Be. Like BOZ the framework is predominantly beryllium based, the under bonding of the bridging anion therefore results in its character being predominantly OH^- rather than O^{2-} . BEL is formed of complicated networks along the *ab* plane which are connected *via* angled spiro-5 rings. These networks are formed of sinusoidal chains of vertex sharing *ben* cages running parallel to *b*. The crosslinking of these layers lead to further 10R channels along *a* and *b* with a largest cavity parameter of 8 Å. Unfortunately due to the necessary use of the SQUEEZE function and the low scattering profile of the structure, the coordinates of extra-framework species or framework hydrogen have not been elucidated. It can be inferred however that the pores have ethylamine, its decomposition products and water present within them in structure stabilising and charge balancing roles. Due to the large amounts of 3Rs present within the structure the framework density and calculated density are extremely low; 13.3 /1000 Å³ and 1.37 gcm⁻³ respectively.

Due to the polyphasic and minor occurrence of BEL further experimental characterisation has been impossible, however, theoretical porosity calculations were carried out using the ZEOMIC^[24] package by Mark Weller. Theoretically BEL has a total pore volume of 0.647 cm³g⁻¹ when considered as a solely Be(OH)₂ framework, which compares to 0.508 cm³g⁻¹ for siliceous LTA and 0.670 cm³g⁻¹ for Be(OH)₂ BOZ. This leads to a predicted internal surface area of 1875 m²g⁻¹ when considering a molecular diameter of 2 Å. This would likely be greater if the structure lacked sterically hindering OH^- groups present within the pores. EDS measurements and an SEM image was taken of one of the groups of crystals [Fig. 79]. EDS confirms the presence of As and O and the SEM exhibits the morphology previously described.

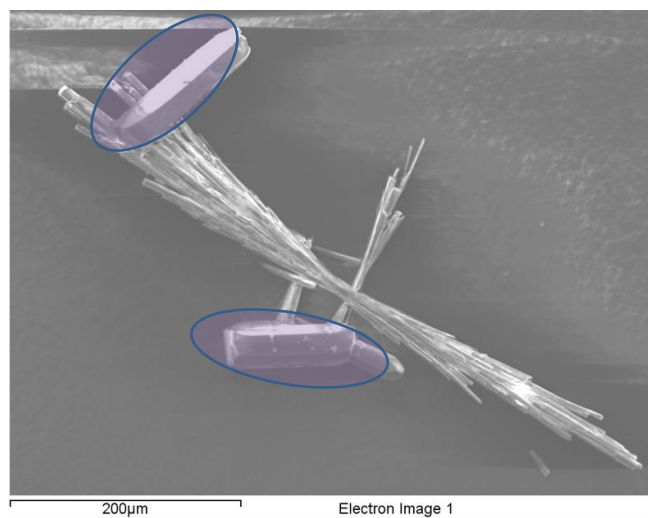


Figure 79: SEM of BEL, tabular crystals of BEL are highlighted by purple shading, needle crystals are of BTL.

3.18: [C₂H₅NH₂][Be_{42.7}As_{17.3}(O)_{~55}(OH)_{~65}]

[C₂H₅NH₂][Be_{42.7}As_{17.3}(O)_{~55}(OH)_{~65}] is found as thin (200 x 10 x 10 μm) transparent needles associated with tabular crystals of BEL (3.17) and polyphasic with large quantities of starting material. A needle was broken off a spray and selected and analysed *via* single crystal X-ray diffraction which scattered extremely weakly owing to the high proportion of light elements and small crystal size. The resulting structure was found to exhibit a new fully connected zeotype topology, with no known analogues present in the IZA database. This was confirmed through modelling by Mark Weller utilising the TOTOPOL software suite. ^[21] [C₂H₅NH₂][Be_{42.7}As_{17.3}(O)_{~55}(OH)_{~65}] is the fourth novel fully connected framework produced by this study and has been assigned the provisional three letter code BTL pending IZA structure commission approval, it has also been accepted for publication as BOT. ^[22]

BTL was solved in the orthorhombic crystal system occupying the *Cmcm* space group. As with BOZ (3.16) and BEL (3.17) the six crystallographically unique T sites are highly disordered between Be and As. It is likely that the distribution of Be and As is actually locally ordered and this would lead to the ordering of the adjacent anion (O²⁻ and OH⁻) bridging unit which would result in an overall lowering of the symmetry. The structure of BTL is similar to BEL (3.17) in that it is entirely formed of spiro-5 rings (*lov*) which in turn form sinusoidal chains of rectangular 10Rs running parallel to *c*, these chains are connected in *ac* *via* spiro-5 rings to form a network of chains and unusual 8³-6² cages along *ac*. The layers are then cross-linked *via* more spiro-5 rings running parallel to *b*, this results in the formation of a large cage with 10⁴-8²-4²-3¹⁰ rings hereafter known as *btl* [Fig. 81]. Crystallographic parameters can be found in Table 42.

Table 42: Selected crystallographic parameters for BTL

Empirical formula	[C ₂ H ₅ NH ₂][Be _{42.7} As _{17.3} (O) _{~55} (OH) _{~65}]
Formula weight	3601.63
Appearance	Transparent needles
Temperature	120 K
Wavelength	0.71073 Å
Crystal system	Orthorhombic
Space group	<i>Cmcm</i>
<i>a</i>	13.612(13) Å
<i>b</i>	25.690(2) Å
<i>c</i>	13.645(13) Å

Volume	4772(8) Å ³
Z	1
R index	0.0991
Weighted R index	0.2683

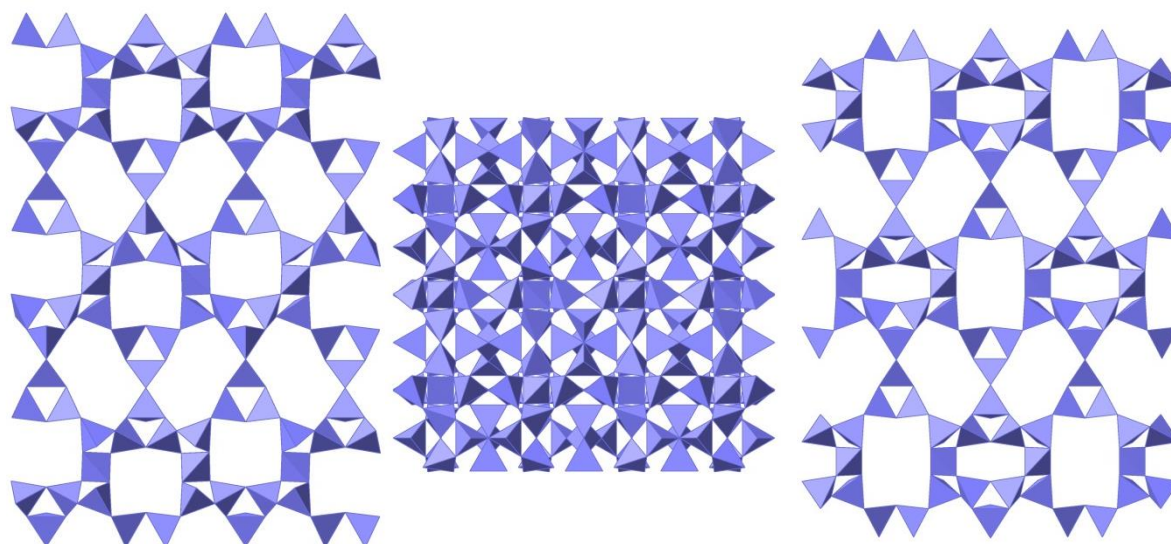


Figure 80: BTL viewed along a , b and c (i, ii and iii respectively), magenta tetrahedra represent disordered character of T atom sites.

BTL has only been found to crystallise under the specific conditions outlined in Table 2, with no deviation of any nature resulting in its successful formation. Full structure solution was carried out as outlined for BOZ/BEL (section 3.16/17), hence the high R factors. Attempts were made with BTL to collect data from synchrotron sources; however, they were unsuccessful as the crystals decomposed in the intense beam during data collection.

As discussed previously the structure of BTL is formed of networks of sinusoidal chains of 10Rs, crosslinked *via* spiro-5 rings to form *btl* cages [Fig. 81] with the largest cavity parameter of 10.2 Å. Unfortunately due to the necessary use of the SQUEEZE function and the low scattering profile of the structure, the coordinates of extra-framework species or framework hydrogen have not been elucidated. It can be inferred however that the pores contain ethylamine, its decomposition products and water present within them in structure stabilising and charge balancing roles. Due to the large amounts of 3Rs present within the structure the framework density and calculated density are extremely low; 12.6 /1000 Å³ and 1.27 gcm⁻³ respectively.

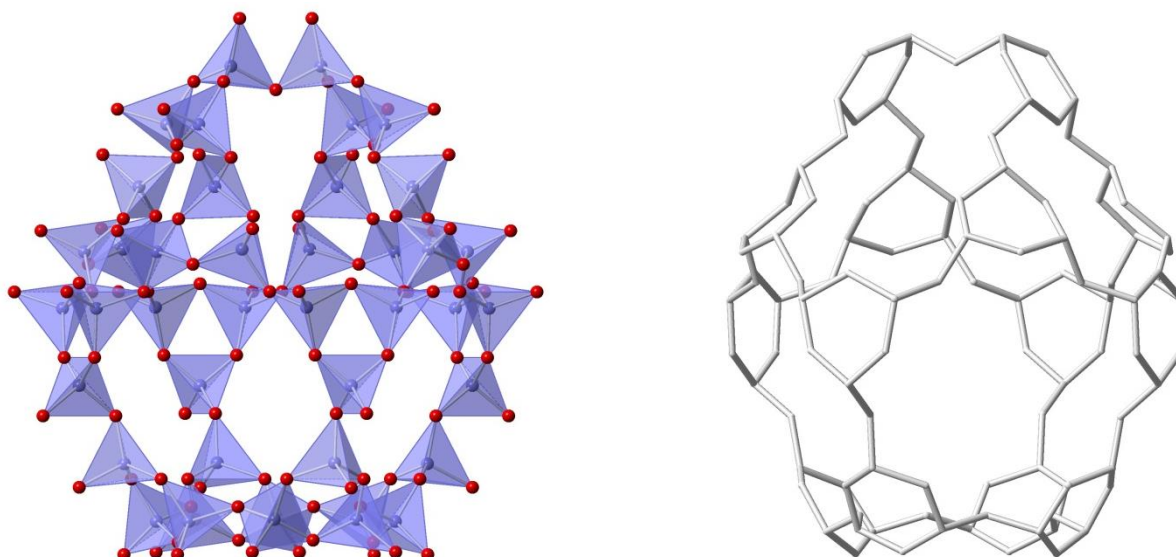


Figure 81: *btl* cages present in BTL, left is a polyhedral representation, mixed site T-atoms are represented by magenta tetrahedra, anion sites by red spheres. Right is a skeletal representation.

As with BEL (3.17) due to the polyphasic and minor occurrence of BTL further experimental characterisation has been impossible, however, theoretical porosity calculations using the ZEOMIC^[22] package by Mark Weller. Theoretically BTL has a total pore volume of $0.763 \text{ cm}^3\text{g}^{-1}$ when considered as a solely $\text{Be}(\text{OH})_2$ framework, which compares to $0.508 \text{ cm}^3\text{g}^{-1}$ for siliceous LTA and $0.670 \text{ cm}^3\text{g}^{-1}$ for $\text{Be}(\text{OH})_2$ BOZ. This leads to a predicted internal surface area of $2247 \text{ m}^2\text{g}^{-1}$ when considering a molecular diameter of 2 \AA . This would likely be greater if the structure lacked sterically hindering OH^- groups present within the pores. EDS measurements and an SEM image was taken of one of the groups of crystals [Fig. 82]. EDS confirms the presence of As and O and the SEM exhibits the morphology previously described.

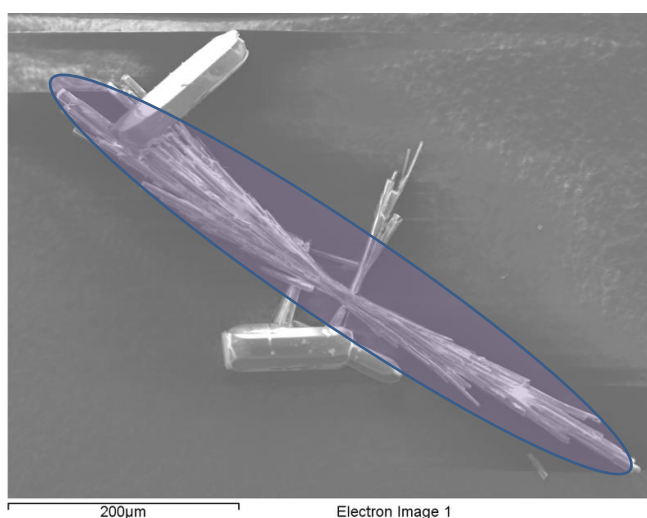


Figure 82: SEM of BTL, needle crystals of BTL are highlighted by purple shading, tabular crystals are of BEL.

3.19: Trends encountered in the beryllioarsenate frameworks

Synthetic

The initial reactions attempting to produce beryllioarsenates emulated the formation of the berylliophosphates GME, ABW ^[8] and GIS ^[9] in an attempt to produce beryllioarsenate analogues. Over the course of this research every possible variation of that starting point has been investigated, with an overall focus on varying the organic structure directing agent in an attempt to produce new and different architectures.

Although the reactions successfully producing new structures are generally very different from each other a couple of trends have been observed. When considering the relationship between $\text{Be}(\text{OH})_2$, H_3AsO_4 and organic template concentration, a successful synthesis tends to have the organic template in excess, with low (but roughly equal) concentrations of both Be and As sources [Fig. 83]. Several structures have been produced with lower organic template concentrations, however, the Be:As is still close to 1:1, when either Be or As is present in large excesses, simple unreactive species such as BeO or As_2O_5 tend to form (shaded areas in Fig. 83).

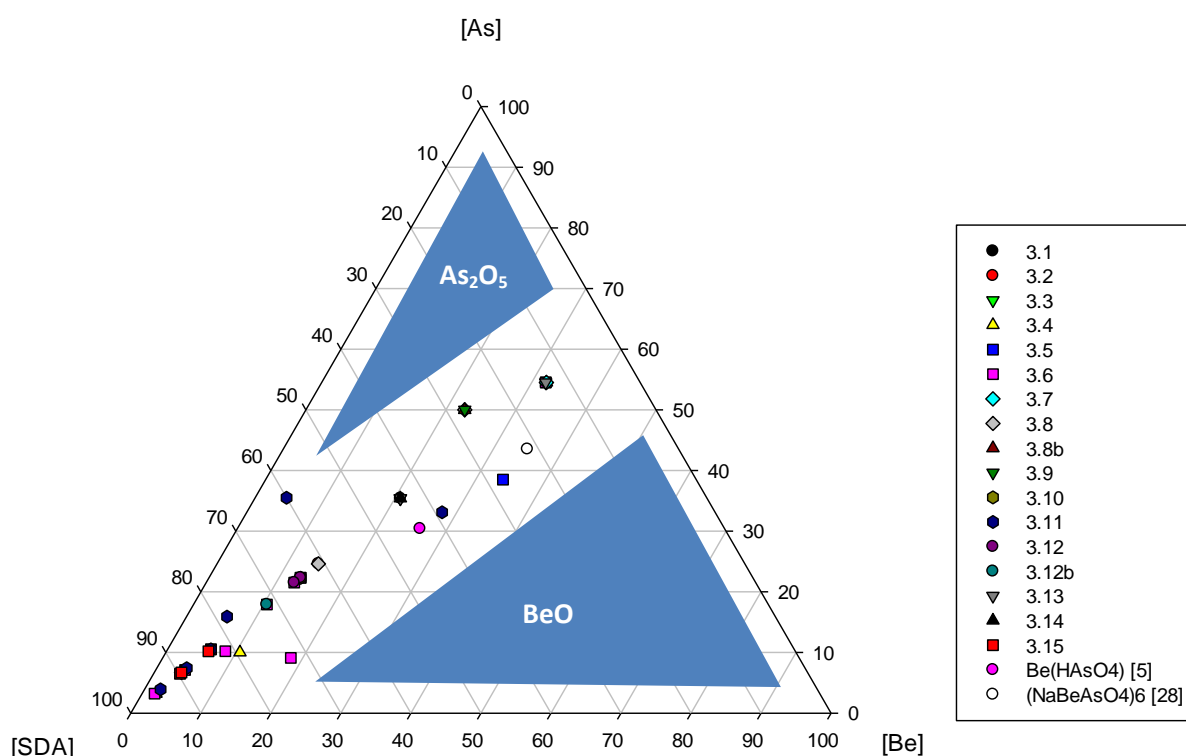


Figure 83: Ternary plot showing relationship between molar ratios of Be:As:organic template (SDA), data has been normalised and each structure is presented as a unique data point, more than one data point exists for several structures where there is more than one route to synthesis. Overlapping points are due to the use of different SDAs

Another trend observed is that the pH of reaction mixtures that produce novel structures tends to fall within two well defined sections of the pH scale, either mildly acidic (pH 4.5 – 6.25) or strongly basic (pH 10.25 – 12.8) [Fig. 84]. Strongly acidic, neutral or weakly basic reaction mixtures tend to produce unidentifiable mixed powders or unreacted starting materials. Although there is no real structural difference between products formed at the two different pH regions, the structures formed in mildly acidic conditions tend to exhibit more -OH_2 termination. Traditionally zeolitic materials are prepared at high pHs since it is through the action of hydroxide that the primary amorphous phase is broken up into the reactive monomers before they can interact with the templating cation, however at lower pH the lack of OH^- related units leads to reduced nucleation and growth and an increase of dimers and polymeric chains.

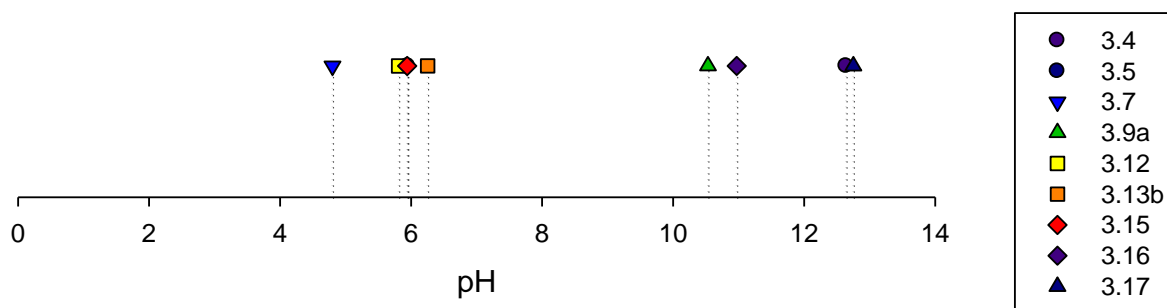


Figure 84: Graph showing pH of reaction mixture prior to heating.

Structural

As discussed at the beginning of the chapter, the primary interest in studying Be and As containing frameworks is the potential for new structures. The larger non-bonding radius of pentavalent As as opposed to Si leads to the formation of smaller O – T – O angles, which in turn stabilise three and four membered rings. When the frequency of occurrence of simple SBUs for the berylloarsenates presented in this chapter is compared to the atlas of known zeolite topologies [Fig. 87] it immediately becomes apparent that there is a much higher occurrence of 3Rs and subsequently spiro-5 rings (*lov*) in the berylloarsenates than the norm (15.2 % of all SBUs berylloarsenate vs 2.97 % for all zeolites). These small rings are known to stabilise the formation of larger ring sizes, and this is reflected in the higher occurrence of 10Rs encountered as a function of total SBUs (13.5 % of all SBUs in berylloarsenates vs 8.42 % in all zeolites). When considered by dimensionality the SBUs increase with complexity and size with dimensionality, with the greatest ring size being 4R in the 0D structure, 8R, 10R and 12R in 1D, 2D and 3D respectively. Interestingly despite 3Rs being prevalent in both 1D and 2D structures, the *lov* CBU [Fig. 86] is only present in 3D structures; this is due to its three-dimensions of tetrahedral apices which are open to further bonding. The shorter O – T – O angles also

favour the formation of irregular ring shapes [Fig. 86], leading to the elliptical or distorted nature of all larger (6, 8, 10 and 12) rings when compared to aluminosilicates/phosphates.

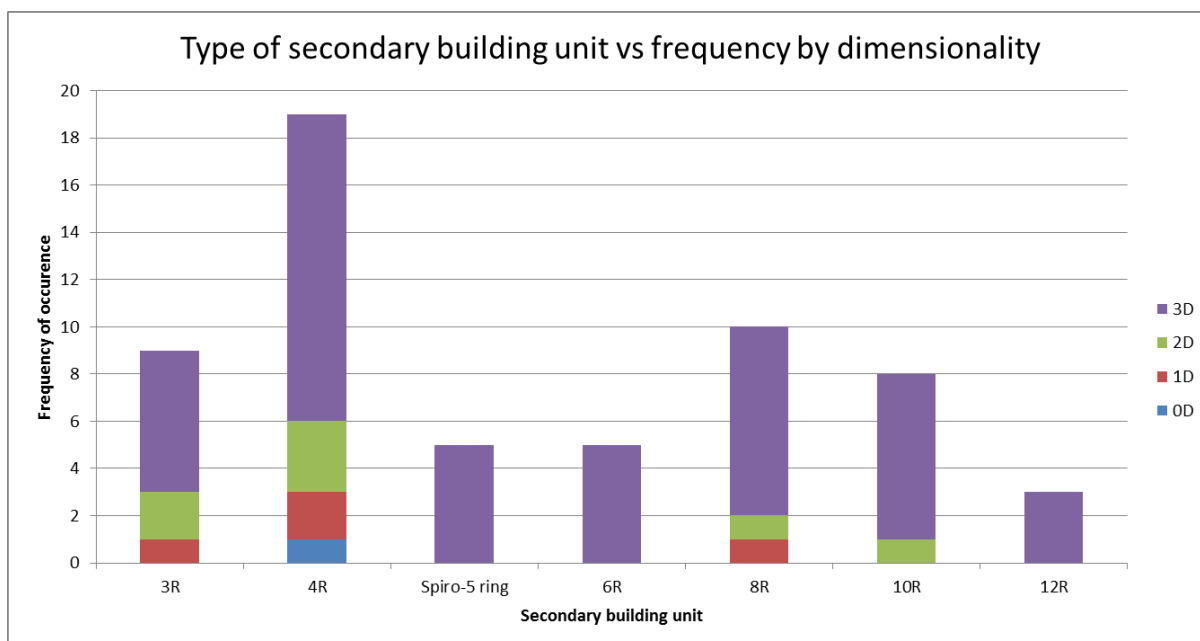


Figure 86: Distribution of common SBUs in the beryllarsenates presented in this chapter, separated by dimensionality

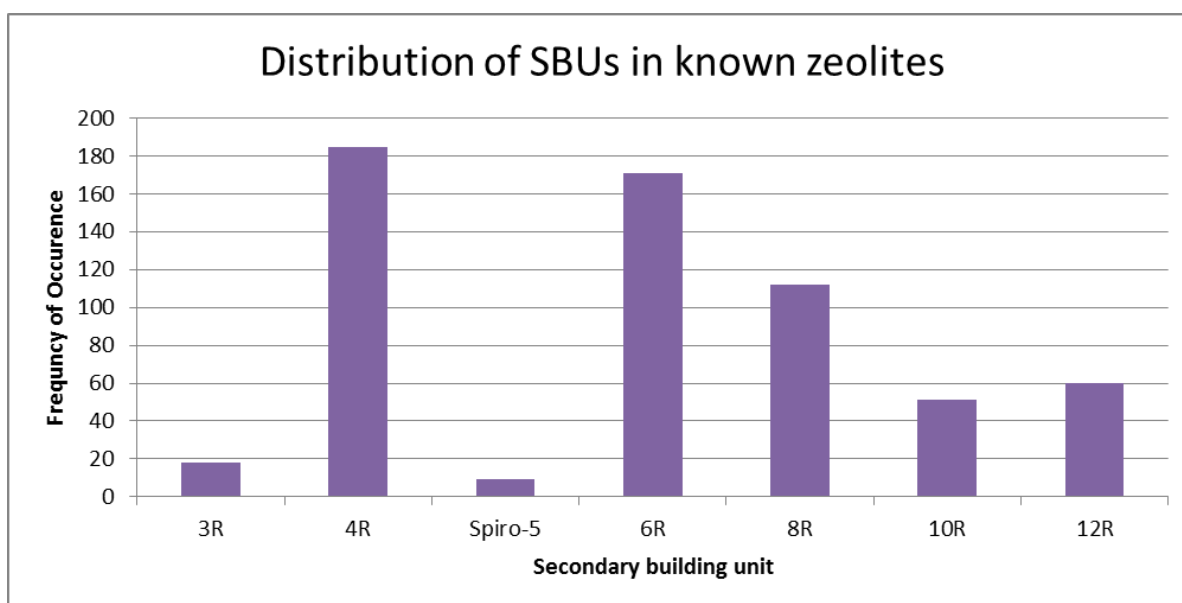


Figure 87: Distribution of common SBUs in known zeolite topologies^[25]

The use of beryllium and arsenic leads to increased termination (47 % of structures produced in this research are OH terminated, 14 % -OH₂), when compared to aluminosilicates, present in their structures,^[3,10,24] as both hydroxyl and ‘dangling’ terminal Be – OH₂, which reduces the overall connectivity of the structure but provides structural stabilisation in the form of intra-framework hydrogen bonding. Further hydrogen bonding occurs from the unusual OH⁻ bridging anion also

frequently (33 % of structures produced in this research) encountered in berylloroarsenate frameworks.^[12] This is due to the under bonding encountered by the bridging anion between two or more consecutive vertex sharing Be centred tetrahedra and exists on the majority of three rings present within the berylloroarsenates discussed here. The high degree of termination and OH⁻ bridging encountered in these structures suggest that these structures possess strong Brønsted character [Fig. 88].

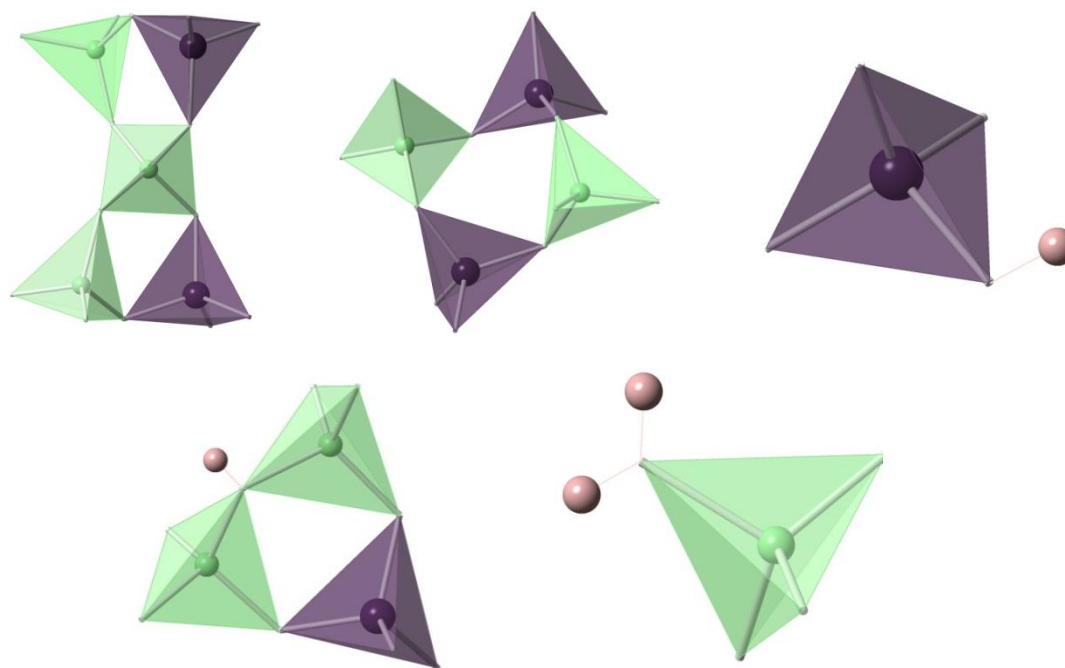


Figure 88: Selection of common structural features encountered in berylloroarsenate structures: (i) the spiro-5 ring (*lov*), (ii) distorted secondary building units (4R), (iii) hydroxyl termination present on both As and Be centred tetrahedra, (iv) hydroxyl bridging and (v) OH₂ termination on Be centred tetrahedra. Green and purple tetrahedra are Be and As centred respectively, pink spheres represent hydrogen.

The short O – T – O angle encountered in berylloroarsenates also produces more condensed structures, leading to higher framework densities (FD) observed when compared to their aluminosilicate or beryllasilicate analogues [Fig.89], with an average increase in FD of 3.14 T atoms /1000 Å³. Conversely for berylloroarsenate frameworks that currently do not have a aluminosilicate analogue (for the novel frameworks BTL, BOZ, BEL and BEN), a decrease in framework density of a similar magnitude would be expected, leading to a predicted FD for aluminosilicate BTL of 9.46, akin to values encountered for MOFs.

Framework density vs framework type

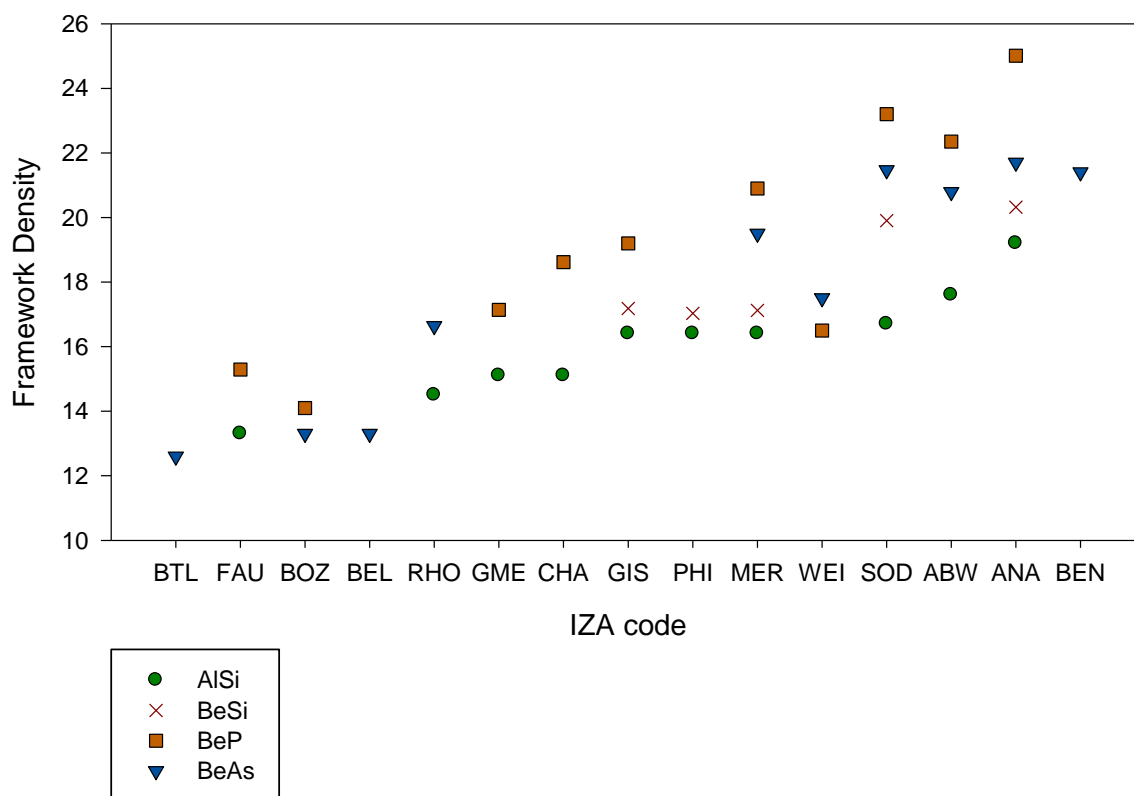


Figure 89: Graph comparing framework density (T atoms/1000 Å³) for berylloarsenate, beryllophosphate and berylsilicate zeotypes, with their aluminosilicate analogues where known

3.20: Conclusions for the berylloarsenate frameworks

After a comprehensive investigation into 33 potential organic structure directing agents, 22 new berylloarsenate frameworks of varying dimensionality have been solvothermally synthesised and where possible, characterised primarily by single crystal X-ray diffraction. This represents a significant contribution to a previously sparsely populated field and as such there are few comparative structures in the literature (Chapter 1). The lack of historic interest in this field is likely due to the toxicity and subsequent synthetic challenges, rather than a perceived lack of potential results. The work presented in this chapter represents the first major study into this field.

Structures presented here were all synthesised under mild solvothermal conditions (160 – 220 °C) with water being the predominate solvent. The major variables between reactions were the identity of extra-framework cations (both nitrogen-rich organics and alkali/alkali earth metal hydroxides) and relative concentrations of both arsenic and beryllium sources (section 3.19). It was found that generally synthesis was successful (i.e. producing a viable structure) at pHs between 4.5 – 6.25 and 10.25 – 12.8 and where the extra-framework cation was thermally stable and provided an adequate site for nucleation, without excessive steric complexity. Successful reaction periods ranged between 48 and 192 h. with some products apparently unaffected by reaction time while others saw changes in crystal size and morphology. Mineralisers in the form of fluoride media were investigated, however, led to increased structural termination which was counterproductive for the project aims. Decomposition of some of the organic species present also provided a mineralising role, leading to some of the more successful and complicated structures produced by this research.

$\text{Na}_4[\text{AsO}_4(\text{BeF}_3)(\text{BeF}_2)] \cdot \text{H}_2\text{O}$ was the sole result of investigating the effect of fluoride based mineralisers and represents the only zero-dimensional cluster structure produced in this research. Despite this it still exhibits some of the structural features common to structures of higher dimensionality, such as the 4R.

Three new one-dimensional structures were produced: $[\text{AsO}_3(\text{OH})\text{Be}(\text{C}_3\text{H}_4\text{N}_2)]$ is formed of sinusoidal chains of 4Rs with hydroxyl termination on the As-centred tetrahedra and an unusual Be – N bond to the organic cation and inter-chain stabilisation through hydrogen bonding. $\text{Na}_2[\text{AsO}_4\text{Be}(\text{OH})] \cdot \frac{1}{2} \text{H}_2\text{O}$ is formed of a ‘backbone’ of consecutive vertex sharing Be-centred tetrahedra, which form a sinusoidal chain of 3Rs when bridged to hydroxyl terminated As-centred tetrahedra. The beryllium backbone shows the first example of the OH⁻ bridging unit which is present in a third of the berylloarsenate structures presented here. $\text{Na}_2[\text{AsO}_4\text{Be}(\text{OH})] \cdot \frac{1}{2} \text{H}_2\text{O}$ is stabilised through interaction with the octahedrally coordinated Na⁺ cation and through hydrogen bonding. [{H-

pyridine_{0.5} [(As_{0.785}Be_{0.215})₂(As_{0.17}Be_{0.83})₂O₇(OH)₂]•(H₂O)_{0.65} is formed of tubes of 8Rs with a sinusoidal 4R backbone, stabilised by poorly defined extra-framework pyridine positions. The elliptical character of the 8Rs is the first example of the distorting effect of the short O – As – O angles caused by the increased ionic radii of pentavalent arsenic in comparison to silicon.

Three novel two-dimensional clay-like structures were produced during this research, the first of which is Sr[AsO₄Be(OH)]•H₂O which is formed of layers of 4 and 8Rs cross-linked and charge balanced by extra-framework octahedral Sr²⁺ cations. The other two layer structures are both hydrogen rich, with structure stabilisation and charge balancing provided by OH/OH₂ termination and in the case of AsO₄Be(OH₂)Be(OH)(OH₂) OH⁻ anion bridging. AsO₄Be(OH₂)Be(OH)(OH₂) is formed of distorted networks of 10, 4 and 3Rs whereas AsO₃(OH)Be has dense networks formed exclusively of 4 and 3Rs. The layers in both structures are cross-linked via hydrogen bonding and therefore inaccessible to any extra-framework species.

Despite the propensity of beryllioarsenates to exhibit termination, the majority of new structures produced in this study are three-dimensional. The most commonly produced structure is [NH₄]₂[(AsO₄)₂Be₂]•2H₂O and its analogue [H₂-diaminoethane][AsO₄Be], which both exhibit the MER zeolitic topology and are formed of distorted *pau* cages made from D8Rs and double crankshaft chains. [(H₂-diaminopropane)_{1.5}][(AsO₄)₂(AsO₃OH)₂(AsO₂(OH)₂)Be₄]•H₂O is an interrupted three-dimensional framework, formed of networks of distorted 8 and 12Rs cross-linked by sinusoidal chains of 4 and 8Rs, the high degree of hydroxyl termination on the arsenate tetrahedra helps stabilise the structure through hydrogen bonding. The trend of hydrated frameworks continues for the interrupted three-dimensional structure AsO₄Be(BeOH) which is formed of networks of 4 and 10Rs cross-linked by chains of hydroxyl bridged 3Rs. The hydroxyl bridges stabilise the structure through hydrogen bonding and due to the resulting short inter network distances, result in a dense structure inaccessible to extra-framework species. [H-bis(2-ethylhexyl)amine, NH₄]₄[(AsO₄)₃(AsO₃OH)Be₃(BeOH)] and its analogue Rb₃[(AsO₄)₃(AsO₃OH)Be₃(BeOH₂)]•H₂O both exhibit high degrees of termination in their porous structure and have networks formed of heavily distorted 4 and 10Rs, cross-linked by 4Rs. The extra-framework species provide charge balancing and structure stabilisation through interaction with framework anions. The final interrupted structure produced in this study is the beryllioarsenate semi- analogue of AFI, [(H-pyridine)₂][(AsO₄)₂(AsO₃OH)Be₂(BeOH₂)], which is a porous framework formed from networks of 12, 6 and 4Rs cross-linked by chains of 4Rs and hydrogen bonding from OH₂ terminated beryllium centred tetrahedra.

The greatest success of this research has been the production of several fully connected three-dimensional zeotypes, including the first synthetic route to the WEI topology which naturally occurs as the berylliophosphate weinebeneite. Rb₂[(AsO₄)₂Be₂(Be(OH)₂)]•2H₂O consists of spiro-5 rings

(*lov*) and 4Rs which form networks of 10, 8 and 6Rs, which have the octahedral Rb^+ sites within the resulting three-dimensional channel system. Structure stabilisation is in the form of the extra-framework cation and hydrogen bonding from the OH^- bridging of the Be-centred tetrahedra.

$[\text{NH}_4]_2[(\text{AsO}_4)_2\text{Be}_2(\text{Be}(\text{OH})_2)]$ represents the first novel zeolitic topology produced by this research, its fully connected three-dimensional framework is predominantly made up of *lov* units and 4Rs which forms a relatively dense porous structure with extra-framework ammonium present within 8R channels and OH^- bridging on consecutively linked beryllium tetrahedra. $[\text{NH}_4]_2[(\text{AsO}_4)_2\text{Be}_2(\text{Be}(\text{OH})_2)]$ has a high framework density ($\text{FD} = 21.4$) however if a aluminosilicate analogue was produced it would have a zeolitic FD of ~ 18.26 , this combined with the ability to partially remove the extra-framework species imply the zeolitic character of $[\text{NH}_4]_2[(\text{AsO}_4)_2\text{Be}_2(\text{Be}(\text{OH})_2)]$ and it has been assigned the provisional IZA framework code of 'BEN'.

$[\text{C}_2\text{H}_5\text{NH}_2, \text{H}_2\text{O}]_x[\text{Be}_{66.7}\text{As}_{25.3}(\text{O})_{80.5}(\text{OH})_{103.5}]$ is the second new zeotype produced by this study and has been assigned the provisional structure code 'BOZ'. BOZ has a highly complex structure formed from 23 unique T sites, each mixed between Be:As in a $2.5(\pm 1.5):1$ ratio. The entire structure is formed from *lov* units connected to produce *ben* and *bet* cages and a three-dimensional 10R channel system. For structure solution the extra-framework species electron density was modelled using the SQUEEZE command and as such structural data is unavailable, however, based on the trends observed in previous beryllioarsenates it is extremely likely that there is a high degree of OH^- bridging present as well as extra-framework cations/water.

$[\text{R}^+]_{1.5}[\text{As}_{6.17}\text{Be}_{13.83}\text{O}_{\sim 20}\text{OH}_{\sim 20}]\cdot n\text{H}_2\text{O}$ (assigned BEL) is similar to BOZ in that it is formed of *lov* and *ben* SBUs to form a complicated, three-dimensional channel system with 10R apertures containing SQUEEZED extra-framework species. BEL has 30 unique mixed T-atom sites, meaning it is the most complicated zeotype currently known. $[\text{C}_2\text{H}_5\text{NH}_2][\text{Be}_{42.7}\text{As}_{17.3}(\text{O})_{\sim 55}(\text{OH})_{\sim 65}]$ (assigned BTL) is found associated with BEL and exhibits a very similar structure to BEL, BOZ and BEN, however, it contains the unique asymmetric *btl* cage SBU which is formed by *lov* units and leads to a three-dimensional channel system with 10R apertures.

There is tremendous scope for future work in this field, particularly consolidating the above results by probing their properties and potential applications. Further characterisation is the first area for expansion, refinement of the experimental parameters should be undertaken so that phase pure materials can be produced and have their properties investigated. Some data has been collected on thermal stability, suggesting that the majority of structures produced are stable to $\sim 500^\circ\text{C}$ and can at least have any extra-framework species partially removed before structural collapse. This coupled

with the fantastically high theoretical internal surface area and low density for the three zeotypes, immediately suggests application as gas storage media. The high levels of Brønsted sites present in the various structures also lend themselves to acid catalysis, such as the ‘cracking’ of hexane. The distortion of apertures such as 10Rs by the small O – T – O angle can also be viewed as ‘fine tuning’ of the shape selective properties of zeolitic frameworks, in this way changing the T atom to As centred will result in a small degree of structural distortion which could allow the separation of sterically similar species. The simpler structures produced in this study have potential as ion exchangers, however the denser, hydrogen rich two-dimensional structures are quite limited.

As well as investigating the properties and potential applications of the structures presented in this study, many more novel structures can still be found by utilising the synthetic trends in pH and reagent concentration presented here, but continuing to vary the nitrogen-rich organic, or investigating other potential template media such as transition metal complexes.

3.21: References

- ¹ R. D. Shannon, *Acta Cryst.*, **1976**, A32, 751 – 767
- ² V. Koteswara Rao, S. Natarajan, *Inorg. Chem. Comms.*, **2010**, 13, 163 – 166
- ³ P. Feng, T. Zhang, X. Bu, *J. Am. Chem. Soc.*, **2001**, 123, 8608 – 8609
- ⁴ T. E. Gier, X. Bu, G. D. Stucky, W. T. A. Harrison, *J. Solid State Chem.*, **1999**, 146, 394 – 398
- ⁵ W. T. A. Harrison, T. E. Gier, G. D. Stucky, *Acta Cryst. C*, **1995**, 51, 181 – 183
- ⁶ T. M. Nenoff, J. B. Parise, G. A. Jones, L. G. Galya, D. R. Corbin, G. D. Stucky, *J. Physical Chem.*, **1996**, 100(33), 14256 – 14264
- ⁷ T. E. Gier, G. D. Stucky, *Nature*, **1991**, 349, 508 – 510
- ⁸ H. Zhang, M. Q. Chen, Z. Shi, X. Bu, Y. Zhou, X. Xu, D. Zhao, *Chem. Mater.*, **2001**, 13(6), 2042 - 2048
- ⁹ W. T. A. Harrison, *Acta Cryst. C*, **2001**, 57, 891 – 892
- ¹⁰ J.C. Jansen, *Studies in Surface Science and Catalysis*, **1991**, 58, 77 - 130
- ¹¹ www.sigmaaldrich.com (accessed 15/01/2012)
- ¹² W. T. A. Harrison, T. M. Nenoff, T. E. Gier, G. D. Stucky, *Inorg. Chem.*, **1993**, 32, 2437-2441
- ¹³ J. L Atwood, G. D. Stucky, *J. Am. Chem. Soc.*, **1969**, 1, 4426
- ¹⁴ B. T. R. Littlefield, M. T. Weller, *Chem. Commun.* **2011**, 47, 4769-4771
- ¹⁵ F. Walter, *Eur. J. Mineral.*, **1992**, 4, 1275-1283
- ¹⁶ E. Passaglia, D. Pongiluppi, R. Rinaldi, *N. Jb. Miner. Mh.*, **1977**, 355-364
- ¹⁷ P. Feng, X. Bu, G. D. Stucky, *Nature*, **1997**, 388, 735-741
- ¹⁸ J. A. Armstrong, M. T. Weller, *Jnl. Am. Chem. Soc.*, **2010**, 132, 15679-15686
- ¹⁹ J. M. Bennett, J. P. Cohen, E. M. Flanigen, J. J. Pluth, J. V. Smith, *ACS Sym. Ser.*, **1983**, 218, 109-118
- ²⁰ J. E. Fleming, H. Lynton, *Physics and Chemistry of Glasses*, **1960**, 1, 148-154
- ²¹ TOTOPOL. M. D. Foster, M. M. J. Treacy, A Database of Hypothetical Zeolite Structures: <http://www.hypotheticalzeolites.net> (accessed throughout project 2008 – 2012)
- ²² B. T. R. Littlefield, M. T. Weller, *Nature Commun.*, (accepted for publication September 2012)
- ²³ P. v.d. Sluis, A. L. Spek, *Acta Cryst. Sect A*, **1990**, 46, 194 – 201
- ²⁴ E. L First, C. E. Gounaris, J. Wei, C. A. Floudas, *Phys. Chem. Chem. Phys.*, **2011**, 13(38), 17339 – 17358
- ²⁵ K. Suzuki, T. Noda, N. Katada, M. Niwa, *J. Catal.*, **2007**, 250, 512-516
- ²⁶ X. Bu, P. Feng, T. E. Gier, G. D. Stucky, *J. Solid State Chem.*, **1998**, 136, 210 – 215
- ²⁷ <http://www.iza-online.org/> (accessed throughout project 2008 – 2012)
- ²⁸ T. E. Gier, X. Bu, P. Feng, G. D. Stucky, *Nature*, **1998**, 395, 154 - 157

Chapter 4

Beryllium frameworks containing phosphorus

Historically significantly more research has been undertaken into the formation of novel structures containing phosphate, spurred on by discovery of the first non-aluminosilicate zeolites, or zeotypes, the aluminophosphates (AlPOs). This is discussed in more detail in the introductory chapter, however it is important to empathise the extensive research carried out into the AlPO series of compounds and how the success in producing new topologies in this field has inspired investigations into a wide variety of tetrahedral pentavalent phosphorus containing systems, the first of which was the isomorphous substitution of aluminium for gallium, leading to the GaPO_{4-n} series.^[1] The discovery of the gallium phosphates and their subsequent arsenate analogues started a wide and rich field of research which over 37 years has encompassed transition metal phosphates, such as $\text{NH}_4[\text{Ti}_3(\text{PO}_4)_4(\text{H}_2\text{O})_2]$ ^[2] and the organically templated open framework $\text{H}_3\text{NCH}_2\text{CH}_2\text{NH}_3[\text{In}_2(\text{HPO}_4)_4]$ ^[3] to more unusual structures such as $\text{C}_2\text{H}_{10}\text{N}_2[\text{CoB}_2\text{P}_3\text{O}_{12}(\text{OH})]$ ^[4] which is a mixed cobalt-boron open framework containing octahedral cobalt and tetrahedral boron/phosphorus sites.

There has been considerable interest in the formation of divalent cation M^{2+} ($\text{M}^{2+} = \text{Be}/\text{Zn}$) and pentavalent phosphorus three-dimensional frameworks especially where arsenate analogues exist, since both group 15 elements are chemically similar aside from the effect of the smaller pentavalent phosphorus ion (0.17 Å compared to As^{+5} 0.335 Å). It is reasonable to expect the same structures are possible with both elements, indeed both $[(\text{CH}_3\text{NH}_3)_3][\text{Zn}_4\text{O}(\text{AsO}_4)_3]$ and $[(\text{CH}_3\text{NH}_3)_3][\text{Zn}_4\text{O}(\text{PO}_4)_3]$ ^[5] are structurally analogous open three dimensional frameworks, with the major crystallographic difference being an expected slight increase in crystallographic parameters for the arsenic analogue. Therefore this chapter deals with a concerted effort to produce beryllophosphate versions of each of the berylloarsenates presented in the previous chapter and potentially produce entirely new beryllophosphate frameworks and zeolitic topologies. Although not the primary target of this investigation, formation of new beryllophosphate structures which are not analogous to structures detailed in chapter 3 is less likely due to the relatively extensive research into beryllophosphates present in the literature, as discussed in the introduction.

The novel structures discussed within this chapter are the results of extensive fine tuning of reaction conditions, modifying the reactions successfully producing berylloarsenates. The vast majority of reactions carried out produced known materials, unreacted starting materials, unidentifiable powders or glasses. A typical reaction consisted of the starting materials being transferred into a 23 mL Parr

hydrothermal vessel, where they are allowed to ‘age’ while being stirred gently at room temperature; this facilitates the homogeneity of the primary amorphous phase or ‘gel’. The vessel is then transferred to an oven for a specified period of time and at a controlled temperature. On removal of the vessel it is allowed to cool to room temperature naturally over several hours and its contents are filtered under vacuum. The resulting bulk is washed with distilled water and ethanol to remove any unreacted organic molecules or water soluble impurities, the products of interest being chemically stable. A reaction was deemed successful when it produced crystals of sufficient quality and quantity to warrant analysis *via* X-ray single crystal diffraction. Further characterisation was carried out utilising EDS, SEM, VTPXD and TGA, however, the vast majority of structures presented here were only produced as minor phases, despite efforts to produce pure phases. Where a product was produced as the major/single phase further characterisation has been carried out in the form of VTPXD and TGA studies. Minor phases were investigated *via* PXD and commonly found to contain a mixture of starting materials, secondary amorphous phases and product. The successful reactions carried out are summarised in table 1 along with the materials produced and the relevant section if that material was novel.

EDS and SEM measurements were carried out to show semi-quantitatively the composition and morphology of crystals produced. EDS was of limited use however, as the emissions from beryllium are of too low energy to be able to pass through the detector window on the instrument used. TGA and VTPXD were carried out to investigate the thermal stability of materials produced and confirm the number of volatile extra-framework species present within structures.

Table 1: Synthesis conditions for novel beryllorphosphates produced as part of this research

Product	Relevant section	Defining Synthesis (Reaction that produced first solvable single crystals)	Temperature (°C)	Reaction time (h)
$\text{Na}_2[(\text{BeO}_2\text{OH})(\text{PO}_2)] \cdot \text{H}_2\text{O}$	4.1	BL118.3: $\text{Be}(\text{OH})_2$ (0.055 g, 1.28 mmol), H_3PO_4 (0.26 mL, 0.384 mmol) and distilled H_2O (1.5 mL) were added to a Teflon® vessel and stirred at room temperature for 30 minutes. NaOH (50 %, 0.09 mL) and pyridine (4.89 mL, 0.63 mol) were then added and the resulting ‘sol’ allowed to age while gently stirring for one hour before autoclaving.	160	48
$\{\text{BeO}_2(\text{OH})(\text{OH}_2)\} \{\text{BeO}_2\text{OH}_2\} \text{P}$	4.2	BL140.3: $\text{Be}(\text{OH})_2$ (0.0945 g, 2.2 mmol), H_3PO_4 (0.171 mL, 2.5 mmol) and distilled H_2O (10 mL) were added to a Teflon® vessel and stirred at room temperature for 30 minutes. $\text{Sr}(\text{OH})_2 \cdot 8\text{H}_2\text{O}$ (0.216 g, 0.813 mmol) and TEAOH (0.94 mL, 2.5 mmol) were then added and the resulting ‘sol’ allowed to age while gently stirring for one hour before autoclaving.	220	168
$[(\text{H-pyridine})_4][\text{Be}_6(\text{PO}_3\text{OH})_8]$	4.3	BL099.1: $\text{Be}(\text{OH})_2$ (0.055 g, 1.28 mmol), H_3AsO_4 (0.15 mL, 2.17 mmol) and distilled H_2O (1.5 mL) were added to a Teflon® vessel and stirred at room temperature for 30 minutes. Pyridine (4.89 mL, 0.63 mol) was then added and the resulting ‘sol’ allowed to age while gently stirring for one hour before autoclaving.	160	192
$[\text{H-pyridine}]$ $[(\text{BeO}_4)_2\text{BeO}_3(\text{OH}_2)\text{P}_3(\text{OH})]$	4.4	NS4.5: (first synthesised by Natalie Seaton) $\text{Be}(\text{OH})_2$ (0.11 g, 2.56 mmol), H_3PO_4 (0.5 mL, 7.31 mmol) and distilled H_2O (3 mL) were added to a Teflon® vessel and stirred at room temperature for 30 minutes. Pyridine (6.98 mL, 0.0863 mol) was then added and the resulting ‘sol’ allowed to age while gently stirring for one hour before autoclaving.	160	168
$[\text{H-dimethylamine}]$ $[\text{BeO}_4(\text{BeO}_2\text{OH})(\text{BeO}_2\text{OH}_2)\text{P}_2]$	4.5	BL113.11: $\text{Be}(\text{OH})_2$ (0.055 g, 1.28 mmol), H_3PO_4 (0.15 mL, 2.17 mmol) and distilled H_2O (10 mL) were added to a Teflon® vessel and stirred at	160	192

		room temperature for 30 minutes. DMF (4.88 mL, 0.063 mol) was then added and the resulting 'sol' allowed to age while gently stirring for one hour before autoclaving.		
$[(\text{BeO}_4)_2\text{BeO}_2(\text{BeO}_2(\text{OH}_2)_2)(\text{BeO}_2\text{OH}_2)(\text{BeOH}_2\text{BeO})\text{P}_4]$	4.6	BL126.1: $\text{Be}(\text{OH})_2$ (0.215 g, 5 mmol), H_3PO_4 (0.34 mL, 5 mmol) and distilled H_2O (8 mL) were added to a Teflon® vessel and stirred at room temperature for 30 minutes. Methyl piperzine (0.01 mL, 0.1 mmol) was then added and the resulting 'sol' allowed to age while gently stirring for one hour before autoclaving.	220	48
$[\text{BeO}_3(\text{Be}_{0.5}\text{O}_2)(\text{Be}_{0.5}\text{O}(\text{OH}_2)_2)(\text{Be}_{0.5}\text{O})\text{P}_2]$	4.7	BL126.1: $\text{Be}(\text{OH})_2$ (0.215 g, 5 mmol), H_3PO_4 (0.34 mL, 5 mmol) and distilled H_2O (8 mL) were added to a Teflon® vessel and stirred at room temperature for 30 minutes. Methyl piperzine (0.01 mL, 0.1 mmol) was then added and the resulting 'sol' allowed to age while gently stirring for one hour before autoclaving.	220	48
$[\text{C}_2\text{H}_5\text{NH}_2, \text{H}_2\text{O}]_x[\text{Be}_{\sim 0.78}\text{P}_{\sim 0.22}(\text{O}, \text{OH})_2]$	4.8	HR014.4: (first synthesised by Harriet Rosethorn) $\text{Be}(\text{OH})_2$ (0.374 g, 8.7 mmol), H_3PO_4 (0.252 mL, 4.34 mmol) and distilled H_2O (3 mL) were added to a Teflon® vessel and stirred at room temperature for 30 minutes. Ethylamine (2.83 mL, 0.0356 moles) and TMAOH (1.597 mL, 0.0178 moles) were then added and the resulting 'sol' allowed to age while gently stirring for one hour before autoclaving.	160	168

Rationale:

The following section describes the novel beryllophosphate structures produced as part of this thesis. The structures are divided into individual sections (4.1 – 4.8) and are ordered by ascending levels of dimensionality, zero-dimensional or cluster structures to fully connected three-dimensional zeolitic frameworks. Each structure section includes an introductory paragraph with selected crystallographic parameters, brief overview of the structure, commentary on synthetic conditions and structure solution, specific structural features of note, appreciation of the bonds and any bond valence deviations and any further characterisation data. The structure presentations are followed by a section on trends observed in these materials and a summary section. Further structural details such as crystallographic information files and PXD data can be found in the e-appendices.

4.1: $\text{Na}_2[(\text{BeO}_2\text{OH})(\text{PO}_2)] \cdot 0.5\text{H}_2\text{O}$

$\text{Na}_2[(\text{BeO}_2\text{OH})(\text{PO}_2)] \cdot \text{H}_2\text{O}$ crystallises as small crystals ($400 \times 10 \times 10 \text{ }\mu\text{m}$) with a plate-like morphology amongst a white powder bulk phase of unreacted starting materials. A regular plate was selected for single crystal X-ray diffraction resulting in the elucidation of a novel one dimensional chain structure of composition $\text{Na}_2[(\text{BeO}_2\text{OH})(\text{PO}_2)] \cdot 0.5\text{H}_2\text{O}$; crystallographic parameters are summarised in Table 2. The structure possesses orthorhombic symmetry and is formed of an infinite chain of consecutively bonded beryllium centred tetrahedra along c analogous to the berylloarsenate presented in section 3.3. Phosphorus tetrahedra alternate along either side of the chain in the a/c plane to form a sinusoidal chain of 3Rs as shown in figure 1. The phosphorus site is tetrahedral, sharing two oxygen positions with the beryllium chain and having two terminating oxygen positions. The tetrahedral beryllium sites are linked via a hydroxyl bridge, the hydrogen bonding with the adjacent chain stabilises the overall structure through. The space between the hydrogen bonded chains is occupied by two fully occupied crystallographically unique sodium sites and a 50 % occupied water position.

Table 2: Selected crystallographic parameters for $\text{Na}_2[(\text{BeO}_2\text{OH})(\text{PO}_2)] \cdot 0.5\text{H}_2\text{O}$

Empirical formula	$\text{Na}_2[(\text{BeO}_2\text{OH})(\text{PO}_2)] \cdot 0.5\text{H}_2\text{O}$
Formula weight	175.97
Appearance	Colourless plate
Temperature	120 K
Wavelength	$0.71073 \text{ }\text{\AA}$
Crystal system	Orthorhombic
Space group	Aba 2
a	$16.5798(8) \text{ }\text{\AA}$
b	$10.3077(5) \text{ }\text{\AA}$
c	$5.4350(3) \text{ }\text{\AA}$
Volume	$928.84(8) \text{ }\text{\AA}^3$
Z	8
D_c	2.52 g cm^{-3}
R index	0.0271
Weighted R index	0.0679

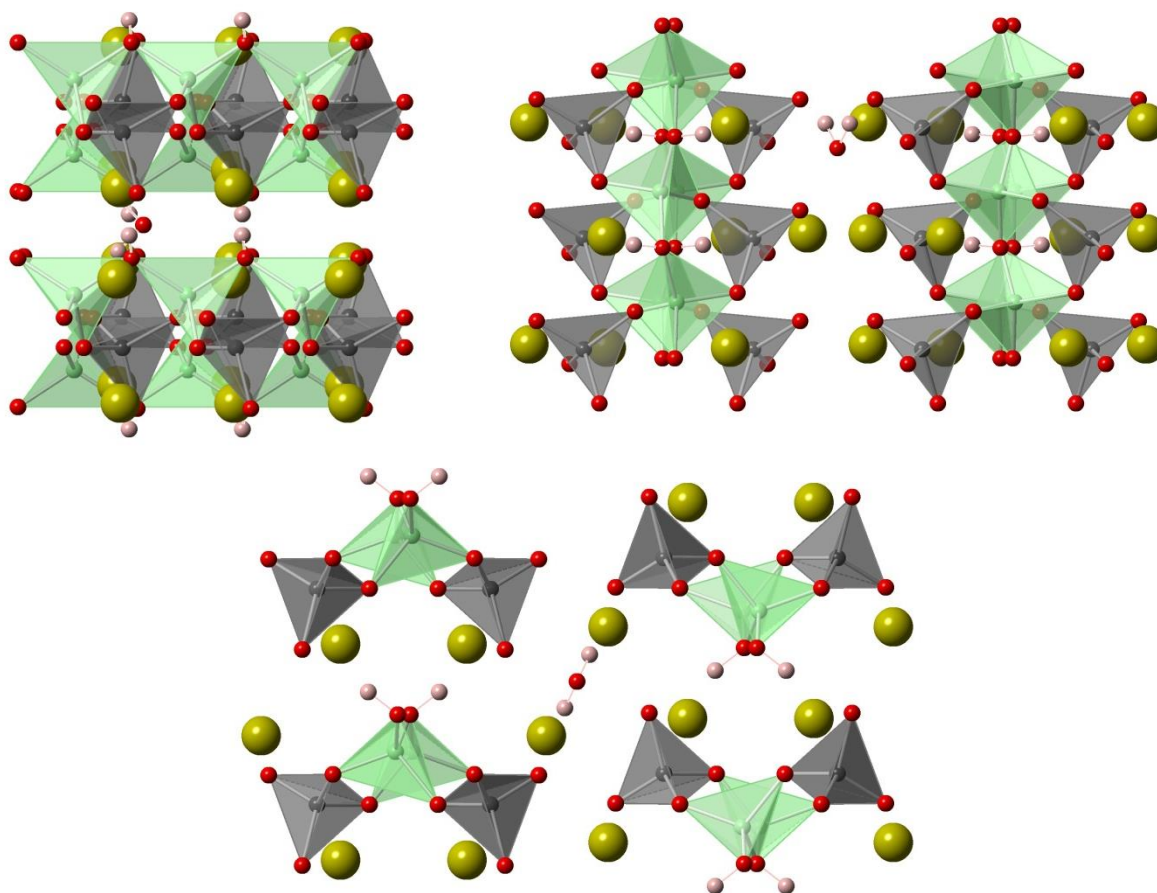


Figure 1: $\text{Na}_2[(\text{BeO}_2\text{OH})(\text{PO}_2)] \cdot 0.5\text{H}_2\text{O}$ viewed along a , b , and c (i, ii and iii respectively). Beryllium and phosphorus centred tetrahedra are light green and grey respectively, hydrogen, oxygen and sodium are represented by pink, red and yellow spheres.

$\text{Na}_2[(\text{BeO}_2\text{OH})(\text{PO}_2)] \cdot 0.5\text{H}_2\text{O}$ is formed at extremely high pHs (14.1 +) with the sodium cation providing a pH controlling and structure directing role. It is unlikely that pyridine has any major role in the synthesis, despite being present, since it is not apparent in the structure solution. Structure solution was straight-forward with the model and experimental data rapidly converging.

$\text{Na}_2[(\text{BeO}_2\text{OH})(\text{PO}_2)] \cdot 0.5\text{H}_2\text{O}$ has two crystallographically unique fully occupied T sites, one beryllium and one phosphorus centred. These are anion bridged to form an infinite sinusoidal chain of 3Rs along c formed around a chain of consecutively bonded beryllium centred tetrahedra. The phosphate apices of the 3Rs alternate in orientation along b leading to stacking of the chains as ABAB along a . The bridging anion is predominantly O^{2-} , however where the bridge is between two divalent centred tetrahedra such as in the beryllium ‘backbone’ it is underbonded as opposed to the more commonly encountered Be-O-P linkage. As such it is protonated as a OH^- group, confirmed *via* bond valence calculations, where the sum deviation is -0.75 v.u. if considered as O^{2-} rather than OH^- . The hydroxyl character also helps stabilise the overall structure via strong (1.888 (3) Å) hydrogen bonding

between chains [Fig. 2]. Two octahedrally coordinated sodium sites [Fig. 3] are present along with a single water site as extra-framework species. The octahedral character of the sodium sites is slightly distorted (average Na - O length: 2.559(3) Å, mean O - Na - O angle: 101.15(8) °) but further stabilises the structure.

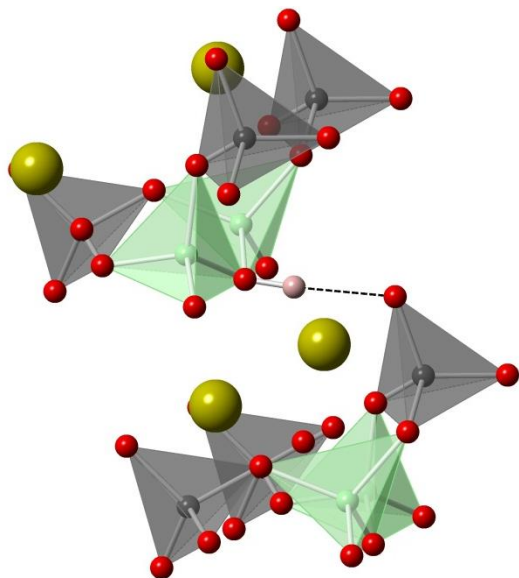


Figure 2: Inter-chain hydrogen bonding present in $\text{Na}_2[(\text{BeO}_2\text{OH})(\text{PO}_2)] \cdot 0.5\text{H}_2\text{O}$, grey, green tetrahedra, pink, red and yellow spheres are phosphorus, beryllium, hydrogen, oxygen and sodium respectively.

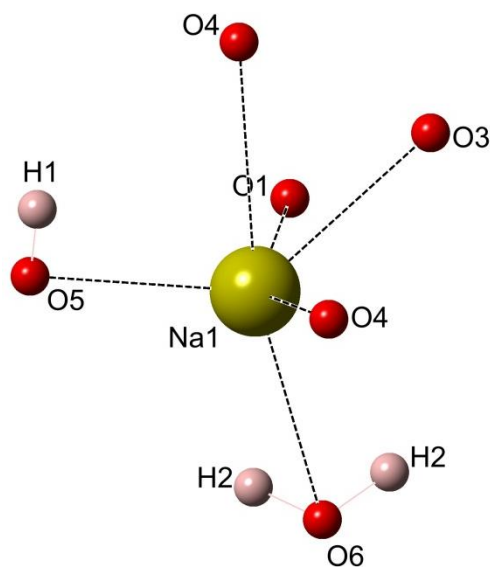


Figure 3: Sodium coordination environment present in $\text{Na}_2[(\text{BeO}_2\text{OH})(\text{PO}_2)] \cdot 0.5\text{H}_2\text{O}$.

Table 3: Selected bond lengths and angles present in $\text{Na}_2[(\text{BeO}_2\text{OH})(\text{PO}_2)] \cdot 0.5\text{H}_2\text{O}$

Bond	Bond length (Å)	Bond	Bond angle (°)
Average P – O	1.543(10)	P – O2 – Be	120.54(18)
Average Be – O	1.633(4)	O5 – H --- O1	168.62
Be – O5H	1.633(4)	Be – O5H – Be	113.88(2)
H – O5	0.883 (3)		
(O5)H --- O3	1.888 (3)		
Average Na1 – O	2.559(3)		
Average Na2 – O	2.418(3)		

Further characterisation was carried out in the form of semi-quantitative EDS measurements which confirmed the presence of phosphorus and sodium as well as producing an SEM image presented in figure 4.

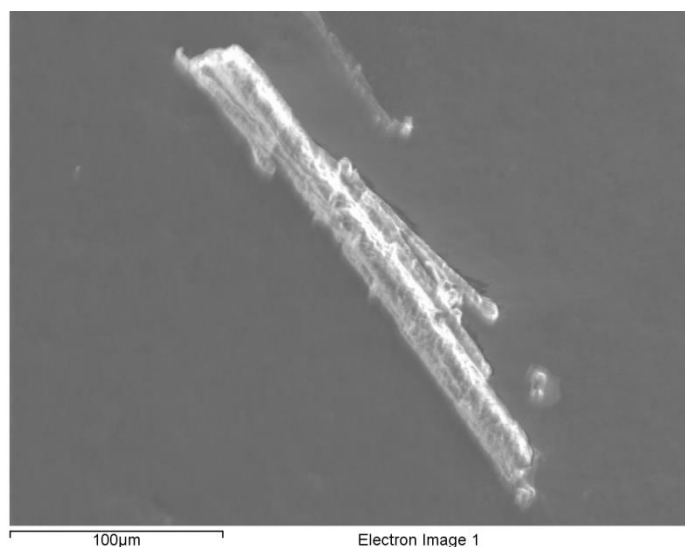


Figure 4: SEM image of Na₂[PO₄Be(OH)] • 0.5H₂O clearly showing the needle morphology

Comparison to berylloarsenate analogue

Na₂[(BeO₂OH)(PO₂)] • 0.5H₂O is a structural analogue of Na₂[AsO₄Be(OH)] • H₂O described in section 3.3. Due to the simple one-dimensional nature of the structures, there are no major differences apart from a slight contraction (7.6 %) observed in the phosphate analogue's cell volume (928.84(8) Å³) when compared to the arsenate (992.58(1) Å³). This is expected and attributed to the decreased ionic radii and T – O exhibited by pentavalent phosphate in comparison to pentavalent arsenate.

4.2: $\{\text{BeO}_2(\text{OH})(\text{OH}_2)\}\{\text{BeO}_2\text{OH}_2\}\text{P}$

A single rod shaped colourless crystal (60 x 15 x 15 μm) of $\{\text{BeO}_2(\text{OH})(\text{OH}_2)\}\{\text{BeO}_2\text{OH}_2\}\text{P}$ was selected and analysed via single crystal X-ray diffraction, the resulting two-dimensional monoclinic structure is an analogue of $\text{AsO}_4\text{Be}(\text{OH}_2)\text{Be}(\text{OH})(\text{OH}_2)$ (section 3.6) and exhibits some extremely interesting features which are observed frequently in the more complicated beryllophosphate and berylloarsenate structures. The layers of $\{\text{BeO}_2(\text{OH})(\text{OH}_2)\}\{\text{BeO}_2\text{OH}_2\}\text{P}$ are aligned along the *ac* plane and are formed exclusively of the 3-4-3 secondary building unit which is a zig-zag of two 3Rs in the same orientation connected by a 4R. The 3Rs are formed of two beryllium and one phosphorus centred tetrahedra and the apical beryllium tetrahedra is oxygen bridged to the 4R of the next 3-4-3 SBU, thus forming the network of 8R, 4R and 3Rs [Fig. 5]. The layers are cross-linked via extensive hydrogen bond interaction between terminating and bridging hydroxyl and water groups. Crystallographic parameters can be found in Table 4.

Table 4: Selected crystallographic parameters for $\{\text{BeO}_2(\text{OH})(\text{OH}_2)\}\{\text{BeO}_2\text{OH}_2\}\text{P}$

Empirical formula	$\{\text{BeO}_2(\text{OH})(\text{OH}_2)\}\{\text{BeO}_2\text{OH}_2\}\text{P}$
Formula weight	166
Appearance	Colourless rod
Temperature	120 K
Wavelength	0.71073 Å
Crystal system	Monoclinic
Space group	$\text{P2}_1/\text{n}$
<i>a</i>	6.3177(3) Å
<i>b</i>	11.0588(4) Å
<i>c</i>	8.1046(3) Å
β	105.910(2) °
Volume	544.55(3) Å ³
<i>Z</i>	4
<i>D_c</i>	2.02 g cm ⁻³
R index	0.0350
Weighted R index	0.0752

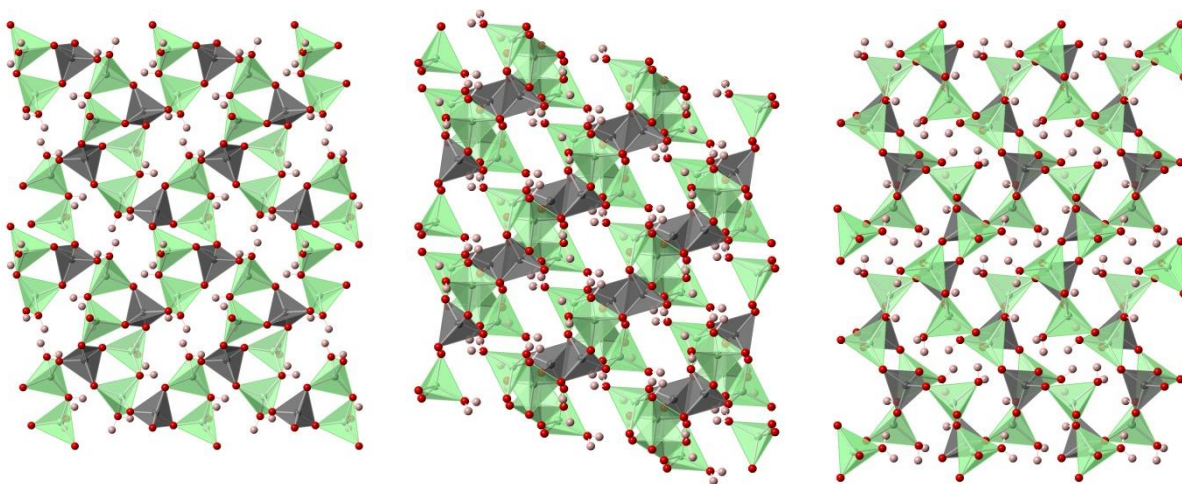


Figure 5: $\{\text{BeO}_2(\text{OH})(\text{OH}_2)\}\{\text{BeO}_2\text{OH}_2\}\text{P}$ viewed from the three major crystallographic axis, a , b and c . (i, ii and iii respectively). Green and grey tetrahedra are Be/P respectively. Pink and red spheres are hydrogen and oxygen respectively.

$\{\text{BeO}_2(\text{OH})(\text{OH}_2)\}\{\text{BeO}_2\text{OH}_2\}\text{P}$ solves easily in $\text{P}2_1/n$ and has three crystallographically unique T-atom sites, two beryllium and one phosphorus, which form a 3R as the simplest SBU [Fig. 6]. The P centred tetrahedra has two anion apices involved in the three ring whilst the third apex forms a 4R with another 3R leading to the formation of the 3-4-4 SBU. The final apex connects to the adjacent 3-4-3 SBU along c to form the two-dimensional network. As in $\text{AsO}_4\text{Be}(\text{OH}_2)\text{Be}(\text{OH})(\text{OH}_2)$ (section 3.6) the connectivity of the 3-4-3 SBU leads to the formation of rhombic shaped 10R channels running through the network along the a axis. Where most zeolitic T-atom sites are anion bridged via O^{2-} , this structure contains an OH^- bridge between the two unique beryllium sites. Although uncommon this form of bridging has been encountered before in the naturally occurring beryllophosphate zeotype weinebeneite (WEI).^[6] If the structure did not contain these permanent sites of protonation then the oxygen atoms would be underbonded due to the proximity to two divalent T-sites, leading to a highly negative overall framework charge, confirmed by a sum bond valence deviation of -0.94 v. u. Protonation of the framework is also present in the form of water termination of the apical beryllium sites (confirmed by bond valence calculations with a deviation of -1.51 v.u.), extensive hydrogen bonding between these sites and the adjoining layer provides structural stabilisation as well as charge balancing [Fig. 7]. There are no extra-framework species present within the pores, owing to the high degree of steric hindrance that would be encountered from the hydroxyl groups, therefore where TMAOH and Sr^{2+} are present in the reaction medium, they can be envisaged to have a pH controlling role. Selected bond lengths and angles can be found in Table 5.

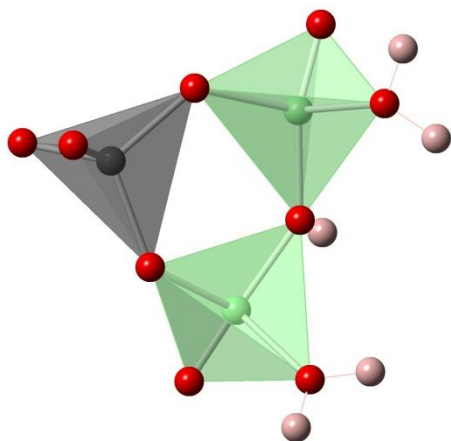


Figure 6: The entire structure of $\{\text{BeO}_2(\text{OH})(\text{OH}_2)\}\{\text{BeO}_2\text{OH}_2\}\text{P}$ is formed of this basic 3R SBU. Green/grey tetrahedra: Be/P, pink/red spheres: Hydrogen/oxygen

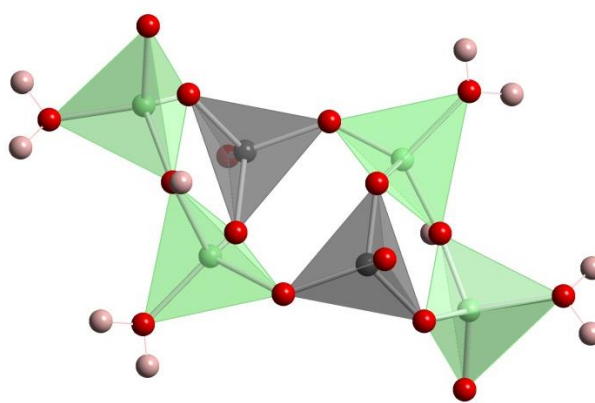


Figure 7: The 3-4-3 SBU present in $\{\text{BeO}_2(\text{OH})(\text{OH}_2)\}\{\text{BeO}_2\text{OH}_2\}\text{P}$. Green/grey tetrahedra: Be/P, pink/red spheres: Hydrogen/oxygen

Table 5: Selected bond lengths and distances for $\{\text{BeO}_2(\text{OH})(\text{OH}_2)\}\{\text{BeO}_2\text{OH}_2\}\text{P}$

Bond	Bond length (Å)	Bond	Bond angle (°)
Average P – O	1.536(12)	Average O – P – O	109.46(7)
Average Be1 – O	1.634(3)	Average O – Be1 – O	109.28(14)
Average Be2 – O	1.621(3)	Average O – Be2 – O	109.44(15)
Be1 – (OH ₂)	1.697(3)		
Be1 – OH	1.592(3)		
Be2 – (OH ₂)	1.642(3)		
Be2 – OH	1.599(3)		
Bridging O – H	0.8883(7)		
WEI bridging O – H	0.8897(6)		

Bond lengths and angles involved in both OH[−] and OH₂ termination are substantially different from the values found normally with bridging Be-O-P distance, water termination leads to Be – O bond lengths of up to 0.033 Å longer, attributed to electronic and steric hindrance, mirrored by an increase in O – Be – O angle in the opposite triad. The H – O distance in the bridging anion OH[−] is comparable to the distances observed in natural WEI.

Further characterisation was hampered by the polyphasic character of the bulk material. Semi-quantitative EDS measurements were carried out on a rod which confirmed the presence of phosphorus and oxygen. A SEM image was also acquired [Fig. 8] which shows the morphology and form of crystal growth of $\{\text{BeO}_2(\text{OH})(\text{OH}_2)\}\{\text{BeO}_2\text{OH}_2\}\text{P}$.

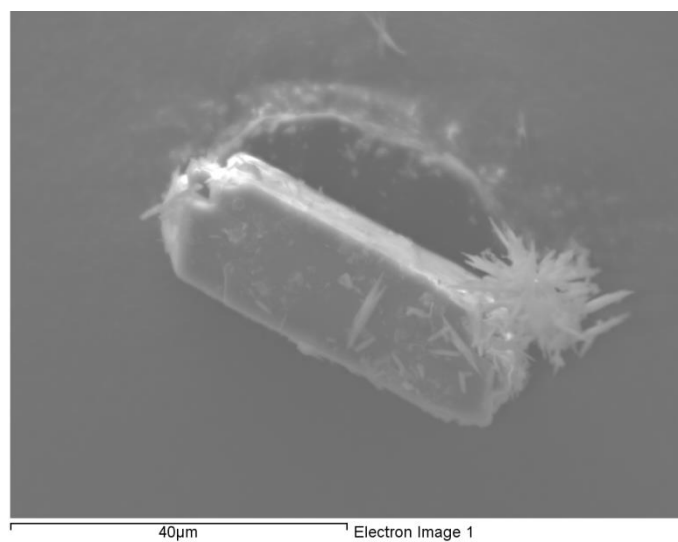


Figure 8: SEM image of $\{\text{BeO}_2(\text{OH})(\text{OH}_2)\}\{\text{BeO}_2\text{OH}_2\}\text{P}$ clearly showing rod morphology with a side cluster of unreacted $\text{Be}(\text{OH})_2$

4.3: [(H-pyridine)₄][Be₆(PO₃OH)₈]

[(H-pyridine)₄][Be₆(PO₃OH)₈] is found as large (160 x 90 x 75 μm) prismatic blocks, though polyphasic, with large quantities of starting material. A regular prism was selected and analysed *via* single crystal X-ray diffraction. The resulting structure was found to exhibit a new interrupted three-dimensional topology, with no known beryllarsenate analogue.

[(H-pyridine)₄][Be₆(PO₃OH)₈] crystallises from hydrothermal conditions into the orthorhombic crystal system and *Pbca* space group; it's large unit cell of volume (8343.15(14) Å³) contains 14 crystallographically unique T-atom sites [Fig. 9]. [(H-pyridine)₄][Be₆(PO₃OH)₈] has an extremely complicated structure built around truncated helical 'S' chains of elongated 8Rs and 4Rs arranged as 4⁴-8¹-4⁴ [Fig. 12] which spiral along the (111) direction and via connections to six other roughly perpendicular 'S' chains form a complicated network in the *ac* plane. The connectivity of these chains leads to the formation of channels with 10R apertures down (111). The networks are cross-linked by two edge sharing 4Rs connected to the 8Rs involved in the helical 'S' chain motifs. This leads to the formation of distorted 10R and 8R channels running parallel to *a* between networks, The 10Rs are heavily sterically hindered by the orientation of hydroxyl terminated phosphate centred tetrahedra. Extra-framework species are present as four crystallographically unique pyridine positions. Crystallographic parameters can be found in Table 6.

Table 6: Selected crystallographic parameters for [(H-pyridine)₄][Be₆(PO₃OH)₈]

Empirical formula	[(H-pyridine) ₄][Be ₆ (PO ₃ OH) ₈]
Formula weight	1142.3
Appearance	Colourless prism
Temperature	120 K
Wavelength	0.71073 Å
Crystal system	Orthorhombic
Space group	<i>Pbca</i>
<i>a</i>	19.9473(3) Å
<i>b</i>	20.2763(2) Å
<i>c</i>	20.6280(2) Å
Volume	8343.15(14) Å ³
<i>Z</i>	8
<i>D_c</i>	1.61 g cm ⁻³
R index	0.0426
Weighted R index	0.1043

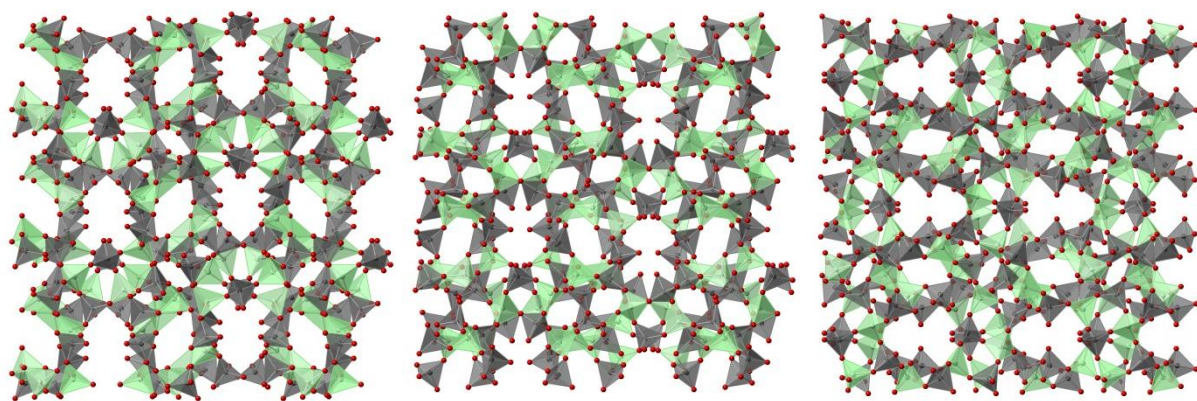


Figure 9: $[(\text{H-pyridine})_4][\text{Be}_6(\text{PO}_3\text{OH})_8]$ viewed along a , b and c . Extra-framework cations have been removed for clarity. Green/Grey tetrahedra are Be/P respectively, red spheres are oxygen.

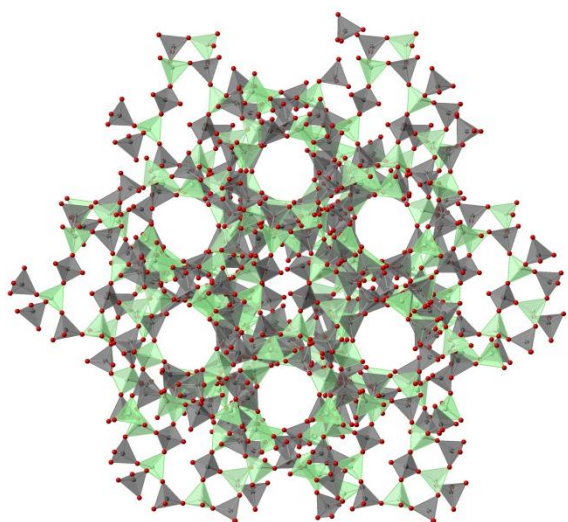


Figure 10: $[(\text{H-pyridine})_4][\text{Be}_6(\text{PO}_3\text{OH})_8]$ viewed along (111) . Extra-framework cations have been removed for clarity. Green/Grey tetrahedra are Be/P respectively, red spheres are oxygen.

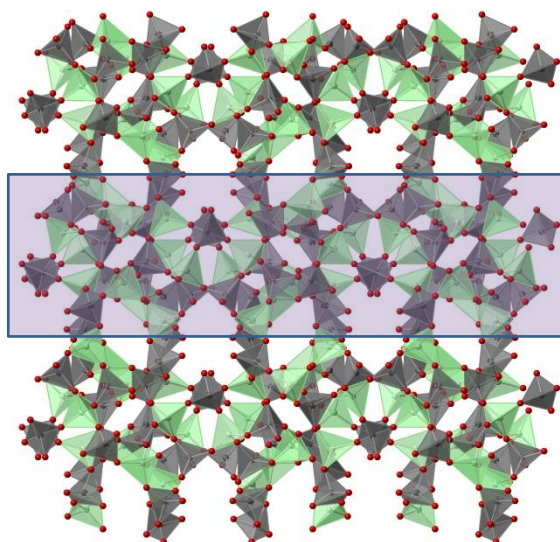


Figure 11: $[(\text{H-pyridine})_4][\text{Be}_6(\text{PO}_3\text{OH})_8]$ viewed along a with network in ac plane highlighted by purple shading. Extra-framework cations have been removed for clarity. Green/Grey tetrahedra are Be/P respectively, red spheres are oxygen.

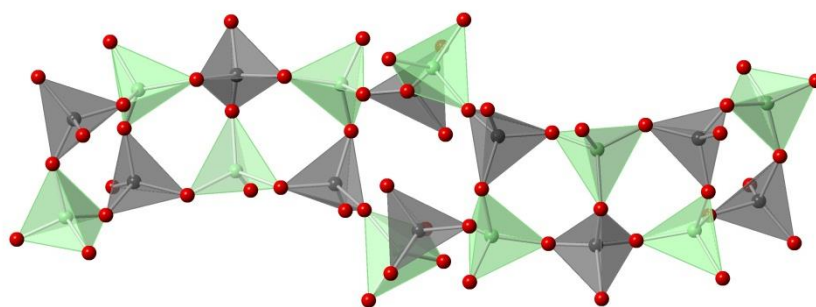


Figure 12: 'S' curve formed of $4^4-8^1-4^4$ rings present in $[(\text{H-pyridine})_4][\text{Be}_6(\text{PO}_3\text{OH})_8]$. Green/Grey tetrahedra are Be/P respectively, red spheres are oxygen

$[(\text{H-pyridine})_4][\text{Be}_6(\text{PO}_3\text{OH})_8]$ forms at low temperatures (100 – 160 °C) and relatively acidic pH (~ 6). Pyridine exhibits a clear templating role and reactions using the same reagent ratios but with different or no organic structure directing agent present proving unsuccessful. Variations of phosphate concentration (source H_3PO_4) seem to have no major effect on the synthesis, as long as the pH is kept mildly acidic by control of the pyridine. Due to the very large crystals encountered (~ 1 mm in some cases) structure solution was straightforward and convergence was quickly achieved, sensible ADPs were produced even for hydrogen positions from X-ray data.

$[(\text{H-pyridine})_4][\text{Be}_6(\text{PO}_3\text{OH})_8]$ exhibits a complicated structure with many interesting features, based around networks in the *ac* plane. The connectivity of the ‘S’ curve composite building units leads to the formation of 8R and two types of 10R channels. The 8R channels are sterically hindered by OH^- termination of the apices of phosphorus centred tetrahedra which are orientated with the hydroxyl directed out into the channel [Fig. 13] and stabilise the structure through strong intra-framework hydrogen bonding (1.968 (5) Å). The first type of 10R encountered is similarly sterically hindered [Fig. 14], with a circular arrangement of moderately strong intra-framework hydrogen bonding (average length: 2.314 (4) Å). Whereas the second 10R style encountered in this structure is much more accessible and contains the four well defined pyridine positions. The extra-framework pyridine molecules provide both charge balancing and structure stabilisation through hydrogen bonding [Fig. 15]. Selected bond lengths, angles and bond valence deviations are presented in Table 7.

Table 7: Selected bond distances, angles and bond valence deviations for $[(\text{H-pyridine})_4][\text{Be}_6(\text{PO}_3\text{OH})_8]$.

Bond	Bond length (Å)	Bond	Bond angle (°)
Average P – O	1.536(13)	Average O – P – O	109.41(7)
Average Be – O	1.621(2)	Average O – Be – O	109.45(14)
Average P – O(H)	1.594(12)		
	Selected bond valence sum deviations in v. u. for oxygen in terminating hydroxyl groups		
O10	0.15	O11	0.08
O13	0.14	O23	0.30
O24	0.02	O27	0.08
O31	0.16	O32	0.15

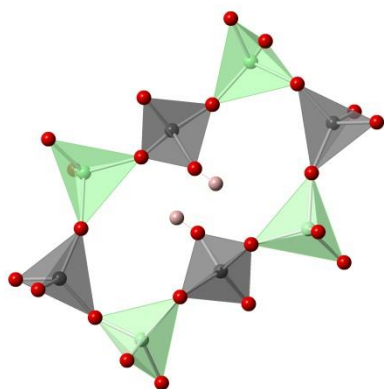


Figure 13: Sterically hindered 8R exhibiting intra-framework H-bonding

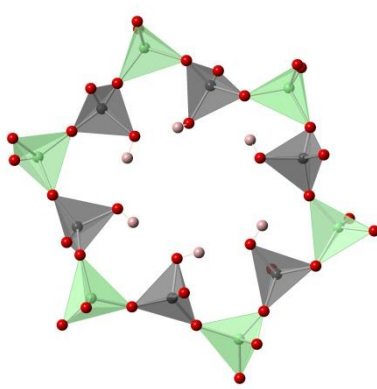


Figure 14: Sterically hindered 10R exhibiting intra-framework H-bonding

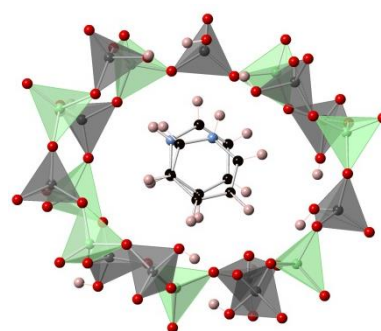


Figure 15: Well defined pyridine positions in 10R apertures.

Further characterisation (apart from electron microscopy based techniques) was not possible due to polyphasic nature of samples produced. Semi-quantitative EDS measurements were carried out on a spray of crystals which confirmed the presence of phosphorus and oxygen. A SEM image was also acquired [Fig. 16] which shows the morphology and form of crystal growth of $[(\text{H-pyridine})_4][\text{Be}_6(\text{PO}_3\text{OH})_8]$.

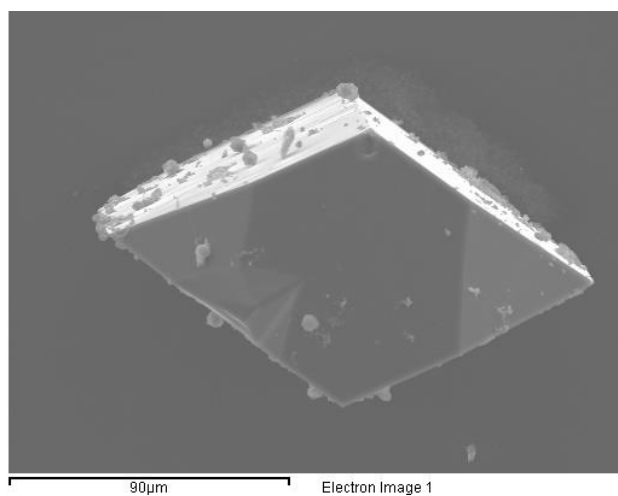


Figure 16: SEM image of $[(\text{H-pyridine})_4][\text{Be}_6(\text{PO}_3\text{OH})_8]$ exhibiting its rhombohedra prism morphology

4.4: [H-pyridine][(BeO₄)₂BeO₃(OH₂)P₃(OH)]

[H-pyridine][(BeO₄)₂BeO₃(OH₂)P₃(OH)] crystallises as relatively large flat-needles, a fragment was broken off a plate and analysed by single crystal X-ray diffraction. The resulting monoclinic structure occupies the C2/c space group and is an interrupted three-dimensional beryllophosphate framework analogue of the berylloarsenate exhibiting AFI-like topology (section 3.11).^[7] Structure 4.4 is loosely formed of a network of 4-, 6- and 12Rs in the *ac* plane cross linked by double zig-zag chains of 4Rs running parallel to *b* which gives rise to distorted *afi* type CBUs. The topology is templated by well-defined pyridine molecules. Crystallographic parameters are summarised in Table 8.

Table 8: Selected crystallographic parameters for [H-pyridine][(BeO₄)₂BeO₃(OH₂)P₃(OH)]

Empirical formula	[H-pyridine][(BeO ₄) ₂ BeO ₃ (OH ₂)P ₃ (OH)]
Formula weight	415.9
Appearance	Sprays of flat needles/rods
Temperature	120 K
Wavelength	0.71073 Å
Crystal system	Monoclinic
Space group	C2/c
<i>a</i>	25.3755(7) Å
<i>b</i>	4.8777(1) Å
<i>c</i>	24.2076(6) Å
β	118.600(2) °
Volume	2630.68(33) Å ³
<i>Z</i>	8
<i>D</i> _c	2.10 g cm ⁻³
R index	0.0706
Weighted R index	0.1610

[H-pyridine][(BeO₄)₂BeO₃(OH₂)P₃(OH)] was formed under mild alkaline conditions (pH 10 – 11) and is produced as a single minor phase with bulk unreacted starting material. On variation of the pyridine content of the reaction, it was found as long as pyridine is present above a ratio of 10:1 pyridine:Be, [H-pyridine][(BeO₄)₂BeO₃(OH₂)P₃(OH)] is formed, with the only discernible effect of increasing pyridine concentration being a slight change in crystal morphology and size; from thin plate needles (100 x 30 x 10 μm), to much larger blocky plates (300 x 100 x 100 μm). [H-

pyridine][$(\text{BeO}_4)_2\text{BeO}_3(\text{OH}_2)\text{P}_3(\text{OH})$] has been synthesised as phase pure when a pyridine:beryllium ratio of 20:1 is utilised.

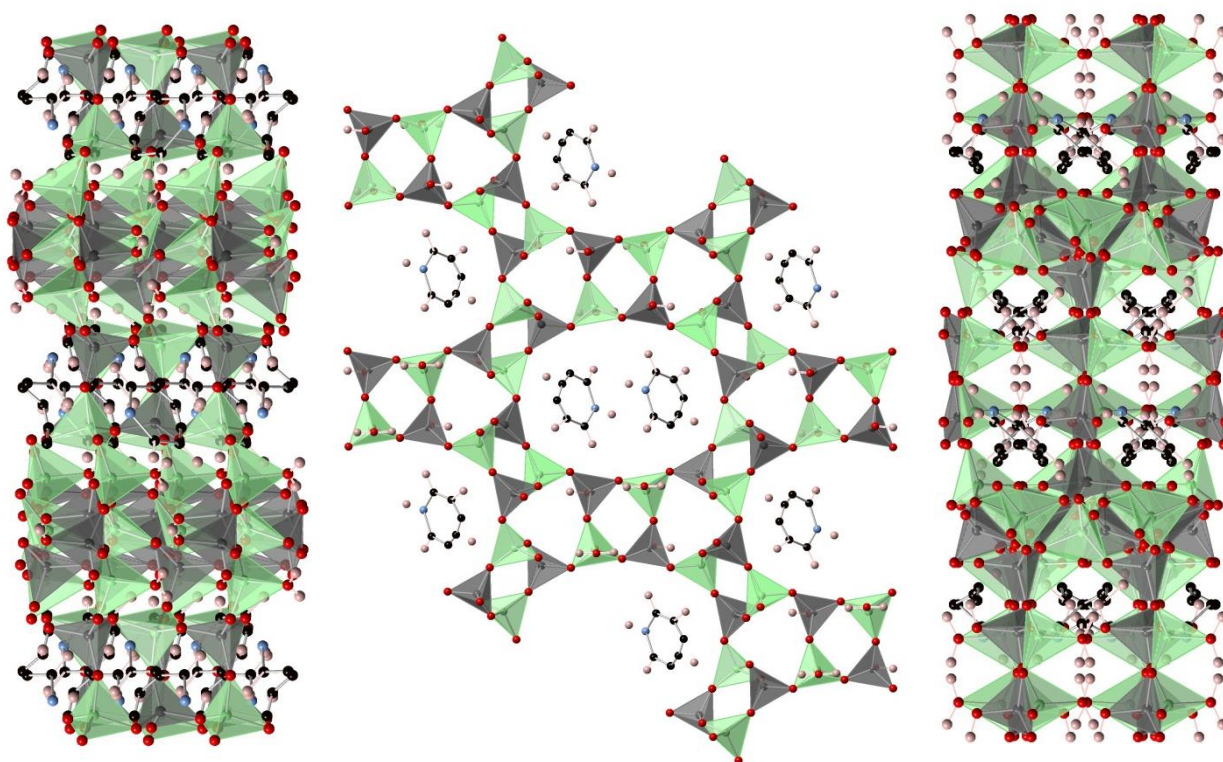


Figure 17: [H-pyridine][$(\text{BeO}_4)_2\text{BeO}_3(\text{OH}_2)\text{P}_3(\text{OH})$] viewed along a , b and c (i, ii and iii respectively). Green and grey tetrahedra are Be/P respectively. Black, pink, blue and red spheres are carbon, hydrogen, nitrogen and oxygen respectively.

The structure solution of [H-pyridine][$(\text{BeO}_4)_2\text{BeO}_3(\text{OH}_2)\text{P}_3(\text{OH})$] progressed relatively smoothly with areas of electron density pertaining to framework T-sites and bridging anions converging with the model quickly. A small amount of disorder is present on the extra-framework protonated pyridine positions, leading to higher than usual ADPs for N/C and H positions, this is likely due to a slightly below unity occupancy of extra-framework cation and is responsible for the slightly high R factor encountered. Constraints on bond distance (0.95 \AA) were applied on the terminal hydroxyl groups as although unassigned electron density was present and bond valence calculations implied hydroxyl termination, when assigned without constraints the hydrogen position tended to shift closer than possible to the oxygen site.

Structurally [H-pyridine][$(\text{BeO}_4)_2\text{BeO}_3(\text{OH}_2)\text{P}_3(\text{OH})$] has 6 crystallographically unique T sites, leading to a FD of 18.2. The first two P tetrahedra are fully vertex oxygen sharing with neighbouring Be tetrahedra and are both part of the double sinusoidal chain of 4Rs running parallel with b . These double zig-zags form the main mode of crosslinking between the ac networks and form 6Rs leading to distorted afi composite building units. The final P centred tetrahedron is hydroxyl

terminated (confirmed by bond valence calculations) which disconnects a third of the 4R zig-zags. The three alternating Be centred tetrahedra have analogous character to the P, with two sites being fully coordinated and involved with the connected 4R zig-zags and the third being terminated. This is confirmed by ^{31}P MASNMR exhibiting a doublet with an intensity ratio of 2:1 [Fig. 18]. The former peak relates to the two fully connected P environments, the latter weaker peak represents the single hydroxyl terminated P environment.



Figure 18: ^{31}P MASNMR of [H-pyridine][$(\text{BeO}_4)_2\text{BeO}_3(\text{OH}_2)\text{P}_3(\text{OH})$]

The stacks of 4Rs link to produce pillars of strongly distorted 6Rs which in turn link to form the 12Rs where the pyridine rings are sited. The pyridine molecules are protonated and have a structure stabilising role through charge balancing as well as structure directing in the formation of [H-pyridine][$(\text{BeO}_4)_2\text{BeO}_3(\text{OH}_2)\text{P}_3(\text{OH})$].

Table 9: Selected bond lengths and angles for [H-pyridine][(BeO₄)₂BeO₃(OH)₂P₃(OH)], including T – O – T angles in 4R for AFI and berylloarsenate analogue.

Bond	Bond length (Å)	Bond	Bond angle (°)
Average P – O	1.526(3)	Average T – O – T in 4.4 (beryllophosphate)	146.4
Average Be – O	1.623(8)	Average T – O – T angle in 3.12 4Rs	128.3
P– OH	1.574(4)	Average T – O – T angle in AFI 4Rs	150.4
Be – OH ₂	1.642(9)		
	Selected bond valence sum deviations in v. u. for oxygen in terminating hydroxyl groups		
O13 (H ₂ terminated)	0.25	O8 (H terminated)	0.19

The terminated tetrahedra exhibit distortion in their axis. The longer than average bond distance to the terminating species results in slightly condensed angles and bond distances for the other three bridging anions, which in turn leads to further distortion of the structure. On consideration of the T – O – T angles present in the 4Rs it is apparent that the beryllophosphate is much closer to that expected for AFI-type topologies, and therefore exhibits less distortion in structural features when compared to the berylloarsenate analogue.

TGA measurements were carried out and show a two stage decrease in mass, the first is a gradual slope between RT and 271.8 °C and represents a 3.5 % loss in mass and equates roughly to the 4.4 % loss expected for the condensation of the terminating hydroxyl [Fig. 19]. The second step represents a 16.19 % loss in mass and is a rapid drop between 271.86 °C and 426.74 °C, which strongly suggests the incomplete removal of 83 % of the extra-framework pyridine, however, it is difficult to be sure of this explanation with this as the exact occupancy of the pyridine is uncertain as previously discussed. VTPXD suggests that crystallinity is lost after 400 °C.

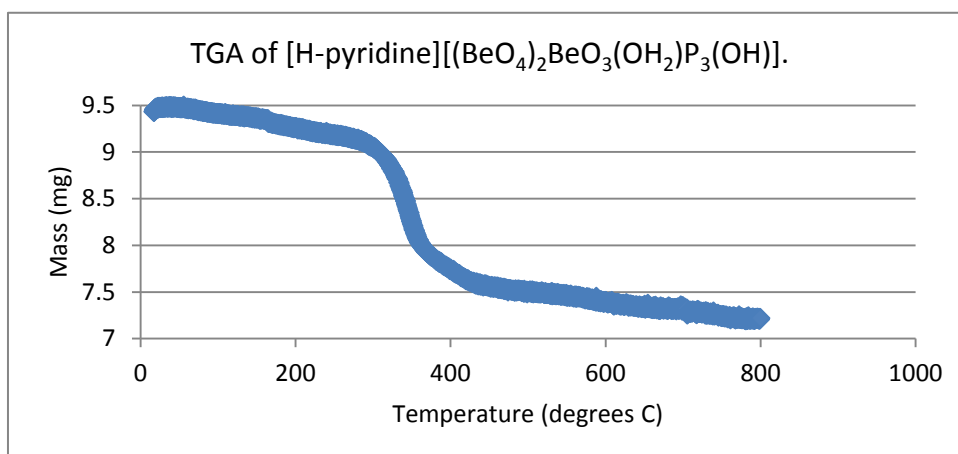


Figure 19: TGA of [H-pyridine][(BeO₄)₂BeO₃(OH₂)P₃(OH)]

EDS measurements and an SEM image was taken of one of the crystals [Fig. 20]. EDS confirms the presence of both P and O and the SEM exhibits the morphology previously described.

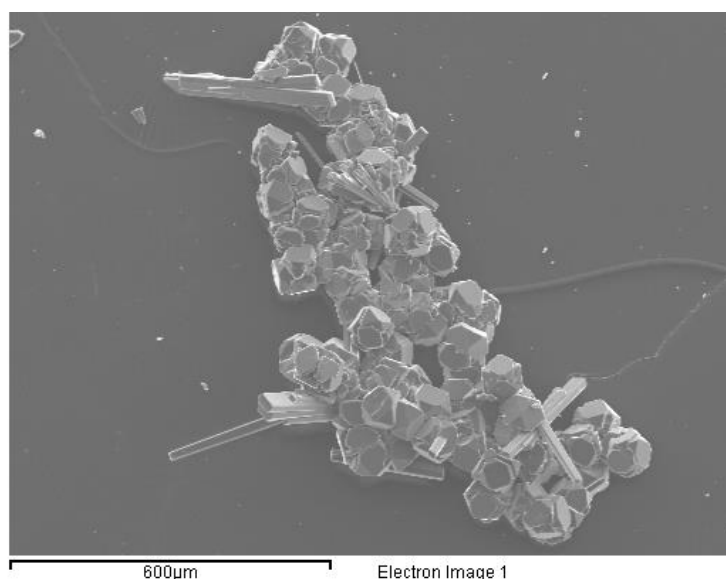


Figure 20: SEM image of [H-pyridine][(BeO₄)₂BeO₃(OH₂)P₃(OH)] showing plate-like morphology and growing associated with an unidentifiable polycrystalline material.

Comparison to beryllarsenate analogue

[H-pyridine][(BeO₄)₂BeO₃(OH₂)P₃(OH)] is a structural analogue of [(H-pyridine)₂][(AsO₄)₂(AsO₃OH)Be₂(BeOH₂)] described in section 3.11. The major structural difference between the two analogues is the lower level of SBU distortion (when compared to AFI) encountered in the berylllophosphate, this can be attributed to the reduced disparity between compositions and therefore similar bond distances and ionic radii between the berylllophosphate and

aluminophosphate AFI structures. There is also a 5.4 % reduction in unit cell volume in the beryllophosphate analogue as opposed to the berylloarsenate; this is due to the increased ionic radii of pentavalent arsenic and the resulting increase in bond distance.

4.5: [H-dimethylamine][BeO₄(BeO₂OH)(BeO₂OH₂)P₂]

[H-dimethylamine][BeO₄(BeO₂OH)(BeO₂OH₂)P₂] crystallises as balls of extremely fine needles (100 x 4 x 4 μm). A fragment of a single needle was selected for single crystal X-ray diffraction, resulting in the novel (no beryllioarsenate analogue) interrupted three-dimensional structure [H-dimethylamine][BeO₄(BeO₂OH)(BeO₂OH₂)P₂]. Its crystallographic parameters are summarised in Table 10. The framework possesses monoclinic symmetry and is formed of a network of rectangular 14Rs, 4Rs and 3Rs in the *bc* plane. The networks are cross-linked by a sinusoidal chain of 4Rs running parallel to *a*. Structure stabilisation is provided by both intra-framework hydrogen bonding from –OH₂ termination and OH[–] bridging units, and a single well-defined protonated dimethylamine site.

Table 10: Selected crystallographic parameters for [H-dimethylamine][BeO₄(BeO₂OH)(BeO₂OH₂)P₂]

Empirical formula	[H-dimethylamine] [BeO ₄ (BeO ₂ OH)(BeO ₂ OH ₂)P ₂]
Formula weight	297.7
Appearance	Balls of fine needles
Temperature	120 K
Wavelength	0.71073 Å
Crystal system	Monoclinic
Space group	P2 ₁ /c
<i>a</i>	4.8962(2) Å
<i>b</i>	12.6366(7) Å
<i>c</i>	16.3034(10) Å
<i>β</i>	93.676(3) °
Volume	1006.64(2) Å ³
<i>Z</i>	4
<i>D_c</i>	1.96 g cm ^{–3}
R index	0.0714
Weighted R index	0.1404

[H-dimethylamine][BeO₄(BeO₂OH)(BeO₂OH₂)P₂] is formed from mild hydrothermal conditions (160 °C, 8 days) in a mixed solvent, DMF:H₂O 49.2:217. The DMF decomposes to dimethylamine which is resolved within the structure. This also plays a mineralising role within the synthesis since [H-

dimethylamine][BeO₄(BeO₂OH)(BeO₂OH₂)P₂] cannot form until enough local DMF decomposes, reducing the amount of potential nucleation sites but leading to larger crystallites.

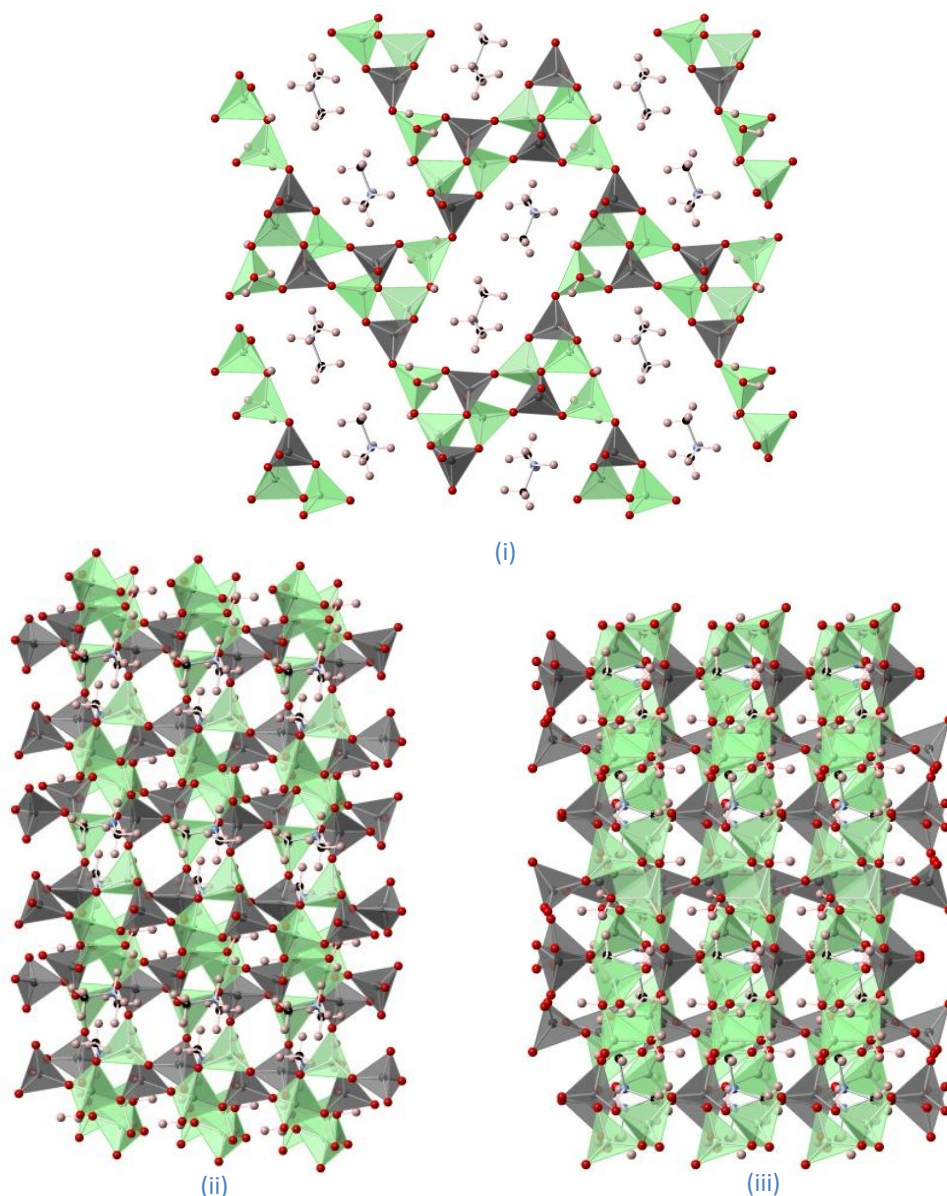


Figure 21: [H-dimethylamine][BeO₄(BeO₂OH)(BeO₂OH₂)P₂] viewed along *a*, *b* and *c* (i, ii and iii respectively). Green and grey tetrahedra are Be/P respectively. Black, pink, blue and red spheres are carbon, hydrogen, nitrogen and oxygen respectively.

The fine needle morphology of [H-dimethylamine][BeO₄(BeO₂OH)(BeO₂OH₂)P₂] caused complications in structure solution as a result of poor scattering. The framework positions converged rapidly, however the low remaining electron density led to the heavily constrained assignment of extra-framework species and framework hydrogen sites. Each H – X (X = C or O) bond has been constrained to 1.10 Å with a standard deviation (s.d.) of 0.02, the H – N distances have been constrained to 1 Å with s.d. = 0.02. This was necessary to produce a sensible model and the assignments have been confirmed *via* bond valence calculations and observed tetrahedra deformation.

[H-dimethylamine][BeO₄(BeO₂OH)(BeO₂OH₂)P₂] has five fully occupied crystallographically unique T-atom sites, with a 3:2 distribution of Be:P. The first beryllium centred tetrahedron is fully connected via oxygen bridging to four symmetry P centred tetrahedra and one Be centred, leading to a triply bonded oxygen site [Fig. 22] confirmed by bond valence calculations. This connectivity leads to the formation of the 4R ‘backbone’. The consecutive Be – O(P) – Be bridge leads to the formation of a 3R on either side of the 4R ‘backbone’. The second Be site is involved in the aforementioned 3R and is connected to the third Be site, leading to an OH⁻ bridge between the two Be sites and a chain of three consecutively bridged Be tetrahedra. The apical O²⁻ on the third Be tetrahedra is unbonded and to compensate exists as a terminal water. The third Be site and second P site complete the basic unit by forming another 3R.

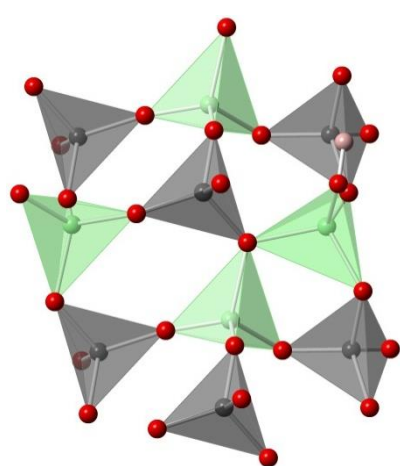


Figure 22: Triply bonded O site present in [H-dimethylamine][BeO₄(BeO₂OH)(BeO₂OH₂)P₂]. Green and grey tetrahedra are beryllium and phosphorus. Red and pink spheres are oxygen and hydrogen.

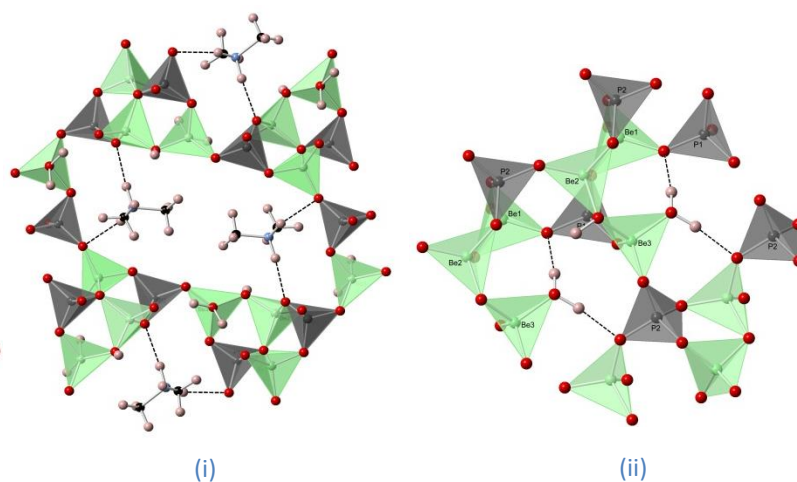


Figure 23: Framework structure stabilisation *via* H-bonding in [H-dimethylamine][BeO₄(BeO₂OH)(BeO₂OH₂)P₂]. Extra-framework (i), intra-framework (ii). Green and grey tetrahedra are Be/P respectively. Black, pink, blue and red spheres are carbon, hydrogen, nitrogen and oxygen respectively.

The resulting columns of 3R bordered 4R chains connect to form rectangular 14R channels running parallel to *a* where the well-defined dimethylamine extra-framework cations are positioned. The protonated dimethylamine cations provide structure stabilisation *via* charge balancing and hydrogen bonding ((N)H---O distance 2.008 (4) Å) as well as templating the overall structure [Fig. 23]. Further structural stabilisation is present in the form of strong (average 1.849 (3) Å) intra-framework hydrogen bonding [Fig. 23] however this has the adverse effect of condensing the structure, leading to its one-dimensional channel system.

Table 11: Selected bond lengths and angles for [H-dimethylamine][BeO₄(BeO₂OH)(BeO₂OH₂P₂)], including T–O–T angles in 4R for AFI and beryloarsenate analogue.

Bond	Bond length (Å)	Bond	Bond angle (°)
Average P – O	1.535(3)	Average O – P – O	109.48(19)
Average Be – O	1.639(7)	Average O – Be – O	109.41(4)
Be – OH ₂	1.679(8)		
	Selected bond valence sum deviations in v. u. for oxygen in terminating hydroxyl groups		
O10 (H ₂ terminated)	0.28	O9 (OH [−] bridging)	-0.08

As observed in other water terminated structures, the OH₂ causes electronic and steric hindrance, lengthening the Be – O(H₂) bond and shortening the triad of uninvolved O^{2−} O – T – O angles.

Further characterisation was carried out in the form of VTPXD which showed structure stability up to 250 °C.

EDS measurements and an SEM image was taken of one of the crystals [Fig. 24]. EDS confirms the presence of both P and O and the SEM exhibits the morphology previously described.

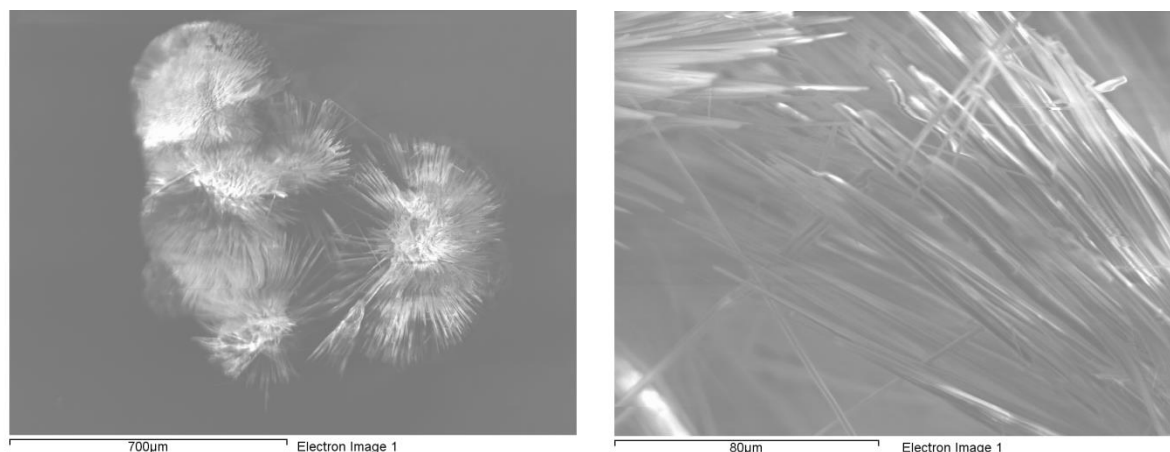


Figure 24: SEM images of [H-dimethylamine][BeO₄(BeO₂OH)(BeO₂OH₂P₂)]. Left shows nucleation environment as balls of fine needles, right shows a close up of the needle morphology exhibited by this structure.

4.6: $[(\text{BeO}_4)_2\text{BeO}_2(\text{BeO}_2(\text{OH}_2)_2)(\text{BeO}_2\text{OH}_2)(\text{BeOH}_2\text{BeO}_2)\text{P}_4]$

$[(\text{BeO}_4)_2\text{BeO}_2(\text{BeO}_2(\text{OH}_2)_2)(\text{BeO}_2\text{OH}_2)(\text{BeOH}_2\text{BeO}_2)\text{P}_4]$ crystallises as large (800 x 200 x 200 μm) irregular blocks, polyphasic with $[\text{BeO}_3(\text{Be}_{0.5}\text{O}_2)(\text{Be}_{0.5}\text{O}(\text{OH}_2))_2(\text{Be}_{0.5}\text{O})\text{P}_2]$ (section 4.7). A fragment of a block was selected for single crystal X-ray diffraction. $[(\text{BeO}_4)_2\text{BeO}_2(\text{BeO}_2(\text{OH}_2)_2)(\text{BeO}_2\text{OH}_2)(\text{BeOH}_2\text{BeO}_2)\text{P}_4]$ is an interrupted three-dimensional structure with crystallographic parameters presented in Table 12. The framework possesses monoclinic symmetry and is formed of a network of 10Rs and 4Rs in the *ac* plane. The networks are cross-linked by chains of sinusoidal 3Rs running parallel to *b*. Structure stabilisation is provided by intra-framework hydrogen bonding from a high degree of OH_2 termination.

Table 12: Selected crystallographic parameters for $[(\text{BeO}_4)_2\text{BeO}_2(\text{BeO}_2(\text{OH}_2)_2)(\text{BeO}_2\text{OH}_2)(\text{BeOH}_2\text{BeO}_2)\text{P}_4]$

Empirical formula	$[(\text{BeO}_4)_2\text{BeO}_2(\text{BeO}_2(\text{OH}_2)_2)(\text{BeO}_2\text{OH}_2)(\text{BeOH}_2\text{BeO}_2)\text{P}_4]$
Formula weight	154.5
Appearance	Irregular blocks
Temperature	120 K
Wavelength	0.71073 Å
Crystal system	Monoclinic
Space group	<i>C2/c</i>
<i>a</i>	31.8815(78) Å
<i>b</i>	9.1510(20) Å
<i>c</i>	9.5148(23) Å
β	94.219(5) °
Volume	2768.40(15) Å ³
<i>Z</i>	8
<i>D_c</i>	2.41 g cm ⁻³
R index	0.0414
Weighted R index	0.1670

$[(\text{BeO}_4)_2\text{BeO}_2(\text{BeO}_2(\text{OH}_2)_2)(\text{BeO}_2\text{OH}_2)(\text{BeOH}_2\text{BeO}_2)\text{P}_4]$ is formed exclusively in the presence of methyl piperzine and at high (220 °C) temperatures and short time spans (48 h.); attempts to form the product by variation of these reaction conditions were unsuccessful. Since the methyl piperzine is not present in the extra-framework space, it can be envisaged to only have a pH or minor mineralising role in the formation of the target structure.

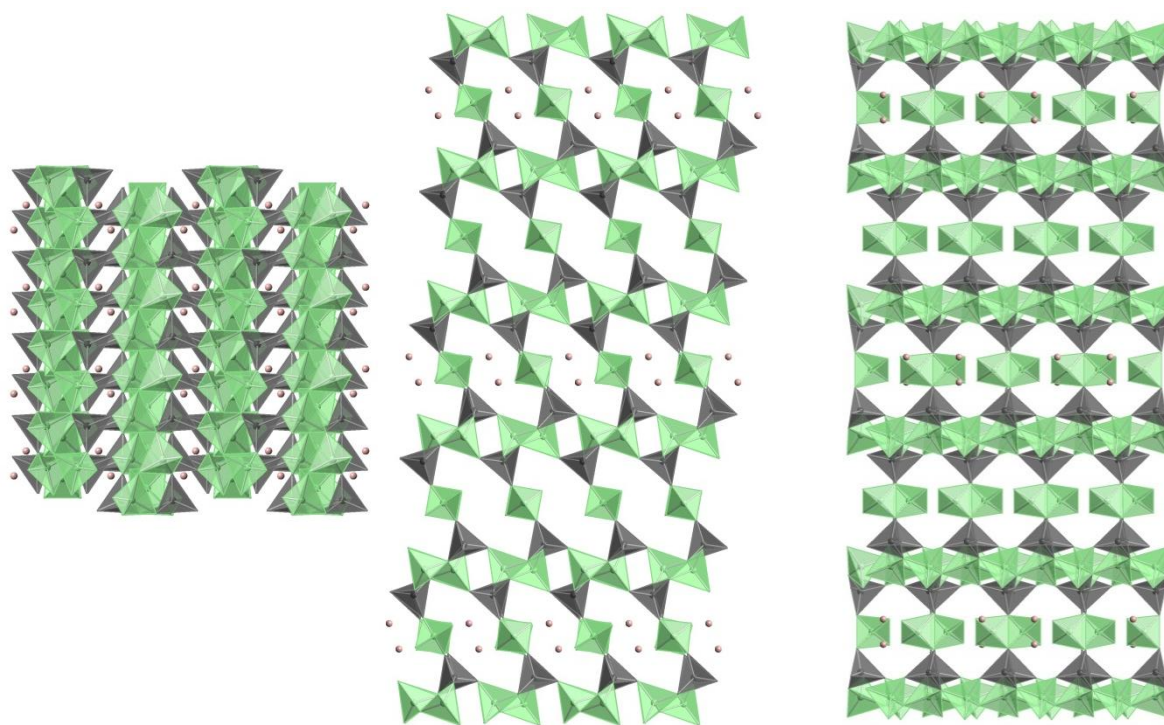


Figure 25: $[(\text{BeO}_4)_2\text{BeO}_2(\text{BeO}_2(\text{OH}_2)_2)(\text{BeO}_2\text{OH}_2)(\text{BeOH}_2\text{BeO}_2)\text{P}_4]$ viewed along a , b and c (i, ii and iii respectively). Green and grey tetrahedra are Be/P respectively. Pink spheres are hydrogen.

During the structure solution of $[(\text{BeO}_4)_2\text{BeO}_2(\text{BeO}_2(\text{OH}_2)_2)(\text{BeO}_2\text{OH}_2)(\text{BeOH}_2\text{BeO}_2)\text{P}_4]$ the electron density assigned to the framework sites converged with the model rapidly, however the hydrogen assignment proved problematic and all attempts to assign hydrogen sites to free electron density resulted in nonsensical coordinates and ADPs. This has resulted in artificially increased cell parameters, with the a and b lengths being approximately double what should have been found with correct hydrogen positioning. The presence of hydrogen is implied by under-bonded oxygen sites supported by bond valence calculations.

There are 11 fully occupied unique T-sites present in $[(\text{BeO}_4)_2\text{BeO}_2(\text{BeO}_2(\text{OH}_2)_2)(\text{BeO}_2\text{OH}_2)(\text{BeOH}_2\text{BeO}_2)\text{P}_4]$. The P centred sites are fully connected to a zig-zag chain of consecutive vertex sharing symmetry related beryllium centred tetrahedra running parallel to the b crystallographic axis. Each chain is linked to the next by the P centred tetrahedra orientated in a and a in relation to the centre of the chain, leading to two of the PO_4 vertices forming a 3R and a third connecting to the next Be-chain along c via 4Rs. The first P vertex is a triply bonded oxygen site shared between two Be and the P, as seen in $[\text{H-dimethylamine}][\text{BeO}_4(\text{BeO}_3\text{OH})(\text{BeO}_2\text{OH}_2)\text{P}_2]$ (section 4.5) which leads to a lengthening of the P – O bond distance (1.574 (13) Å). The final vertex of the P tetrahedra alternates in orientation between $-a$ and a and is connected to the second Be site, forming the network of elliptical 10Rs introduced above. The Be sites involved in the beryllium ‘backbone’ are fully connected whereas the second group of

Be sites are likely doubly terminated with $-\text{OH}_2$ groups (as seen in the beryllioarsenate analogue and confirmed by BV calculations). This is reflected by longer than usual bond lengths ($\text{Be} - \text{OH}_2$, 1.685(3) Å) leading to a slightly distorted tetrahedra (selected bond lengths and angles can be found in table 13). The $-\text{OH}_2$ groups would be orientated directly into the centre of the 10Rs sterically hindering any potential extra-framework species and stabilise the structure via hydrogen bonding, causing the elliptical character of the 10Rs. The complete lack of incorporation of the OSDA (in this case methyl piperzine) suggests that the potential template is too bulky and under reaction conditions had no templating decomposition products. The beryllium backbone and subsequent sinusoidal chain of 3Rs present in this structure can be considered as a common CBU as it is present in several structures (3.3, 3.9 and 4.1)

Table 13: Selected bond lengths, angles and bond valence deviations for $[(\text{BeO}_4)_2\text{BeO}_2(\text{BeO}_2(\text{OH}_2)_2)(\text{BeO}_2\text{OH}_2)(\text{BeOH}_2\text{BeO}_2)\text{P}_4]$

Bond	Bond length (Å)	Bond	Bond angle (°)
Average P – O	1.535(13)	Average O – P – O	109.48(7)
Average Be – O	1.636(3)	Average O – Be – O	109.41(14)
Be – O(predicted H)	1.681(3)		
	Selected bond valence sum deviations in v. u. for oxygen involved in water termination.		
O18	-1.50	O17	-1.49
O19	-1.48	O20	-1.46

Due to the polyphasic nature of the sample, aside from SEM based techniques, further characterisation has not been possible. EDS measurements and an SEM image was taken of one of the crystals [Fig. 26]. EDS confirms the presence of both P and O and the SEM exhibits the morphology previously described.

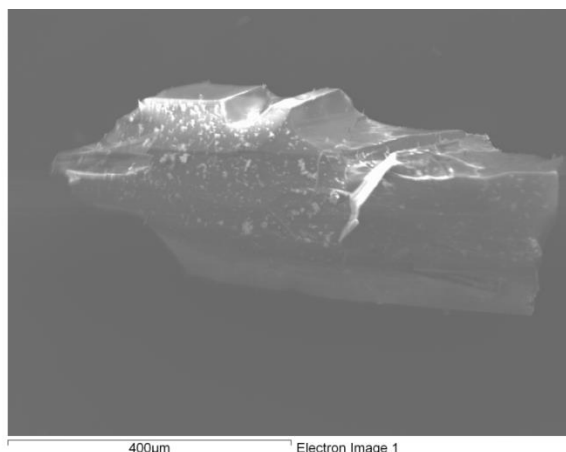


Figure 26: SEM image of $[(\text{BeO}_4)_2\text{BeO}_2(\text{BeO}_2(\text{OH}_2)_2)(\text{BeO}_2\text{OH}_2)(\text{BeOH}_2\text{BeO}_2)\text{P}_4]$, exhibiting its irregular morphology.

4.7: $[\text{BeO}_3(\text{Be}_{0.5}\text{O}_2)(\text{Be}_{0.5}\text{O}(\text{OH}_2))_2(\text{Be}_{0.5}\text{O})\text{P}_2]$

$[\text{BeO}_3(\text{Be}_{0.5}\text{O}_2)(\text{Be}_{0.5}\text{O}(\text{OH}_2))_2(\text{Be}_{0.5}\text{O})\text{P}_2]$ is found as quite large (100 x 10 x 10 μm) tablets polyphasic with $[(\text{BeO}_4)_2\text{BeO}_2(\text{BeO}_2(\text{OH}_2)_2)(\text{BeO}_2\text{OH}_2)(\text{BeOH}_2\text{BeO}_2)\text{P}_4]$ (section 4.6). A regular tablet was selected and analysed *via* single crystal X-ray diffraction. The resulting structure was found to exhibit a new interrupted three-dimensional topology, with no known beryllioarsenate analogue.

$[\text{BeO}_3(\text{Be}_{0.5}\text{O}_2)(\text{Be}_{0.5}\text{O}(\text{OH}_2))_2(\text{Be}_{0.5}\text{O})\text{P}_2]$ crystallises from hydrothermal conditions into the orthorhombic crystal system and *Cmca* space group, it contains 8 fully occupied crystallographically unique T-atom sites [Fig. 27] in a 5:3 Be:P ratio. $[\text{BeO}_3(\text{Be}_{0.5}\text{O}_2)(\text{Be}_{0.5}\text{O}(\text{OH}_2))_2(\text{Be}_{0.5}\text{O})\text{P}_2]$ has a condensed structure built around networks of ‘horse-shoe’ shaped 8Rs and 4Rs in the *bc* plane. The networks are cross-linked by very unusual 7Rs which are formed from the connectivity of $(\text{BeO}_3)_2(\text{PO}_3)_6$ composite building units [Fig. 28] where the two beryllium centred tetrahedra are edge sharing leading to the triply bonded O^{2-} bridge which is a common occurrence in the beryllophosphates/arsenates.^[8] Each $(\text{BeO}_3)_2(\text{PO}_3)_6$ is connected to the next via an arrangement of 4Rs which is seen as a helical chain down *b*. Crystallographic parameters can be found in Table 14.

Table 14: Selected crystallographic parameters for $[\text{BeO}_3(\text{Be}_{0.5}\text{O}_2)(\text{Be}_{0.5}\text{O}(\text{OH}_2))_2(\text{Be}_{0.5}\text{O})\text{P}_2]$

Empirical formula	$[\text{BeO}_3(\text{Be}_{0.5}\text{O}_2)(\text{Be}_{0.5}\text{O}(\text{OH}_2))_2(\text{Be}_{0.5}\text{O})\text{P}_2]$
Formula weight	253
Appearance	Colourless tablet
Temperature	120 K
Wavelength	0.71073 Å
Crystal system	Orthorhombic
Space group	<i>Cmca</i>
<i>a</i>	13.0922(8) Å
<i>b</i>	14.6169(8) Å
<i>c</i>	16.5541(12) Å
Volume	3167.91(3) Å ³
<i>Z</i>	16
<i>D_c</i>	2.12 g cm ⁻³
R index	0.0359
Weighted R index	0.0931

$[\text{BeO}_3(\text{Be}_{0.5}\text{O}_2)(\text{Be}_{0.5}\text{O}(\text{OH}_2))_2(\text{Be}_{0.5}\text{O})\text{P}_2]$ forms both as a minor phase in the presence of 2,2-bipyridyl or polyphasic with $[(\text{BeO}_4)_2\text{BeO}_2(\text{BeO}_2(\text{OH}_2)_2)(\text{BeO}_2\text{OH}_2)(\text{BeOH}_2\text{BeO}_2)\text{P}_4]$ in the presence of methyl piperzine (section 4.6). The reaction conditions are very different in both instances, the former is at low (160 °C) temperature and for a long (8 days) reaction period, the latter is at high temperature (220 °C) for a short period of time (48 h.), which suggests that external reaction conditions are not the driving synthetic factor. The beryllium and phosphorus ratios utilised in both reactions are relatively similar but have been used in multiple reactions without producing either product. The key synthetic parameter is therefore the addition of large bulky, decomposition resistant, organic agents which direct the structure into the condensed phases observed for both 4.6/7 by providing no architecture on which to nucleate around and forcing the structures to form from their monomeric primary amorphous phases.

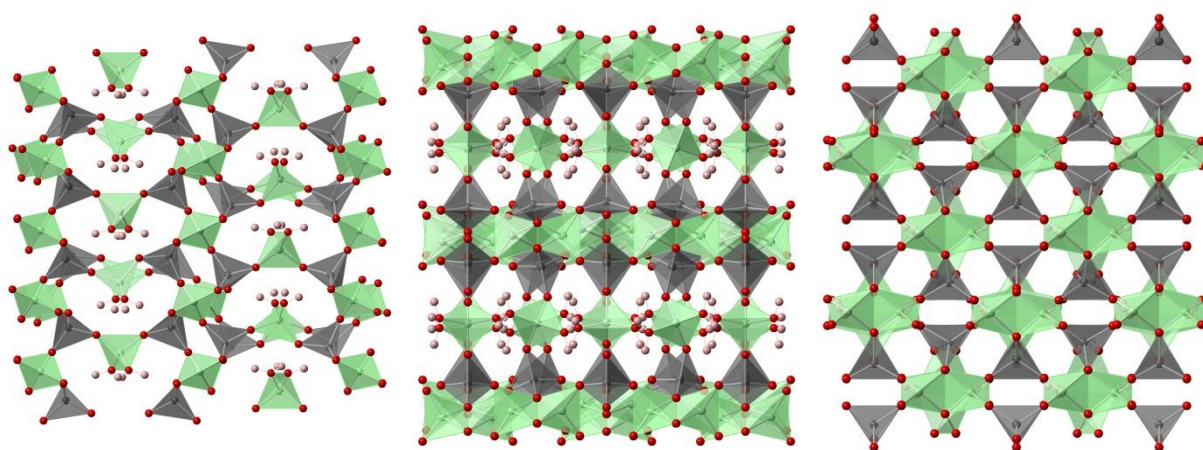


Figure 27: $[\text{BeO}_3(\text{Be}_{0.5}\text{O}_2)(\text{Be}_{0.5}\text{O}(\text{OH}_2))_2(\text{Be}_{0.5}\text{O})\text{P}_2]$ considered from the three major crystallographic axis, *a*, *b* and *c*. (i, ii and iii respectively). Green and grey tetrahedra are Be/P respectively. Pink and red spheres are hydrogen and oxygen respectively.

Structure solution progressed rapidly with quick assignment of framework atomic sites, due to the high quality of the crystal selected; the hydrogen positions were well defined and did not require restraints. As mentioned previously $[\text{BeO}_3(\text{Be}_{0.5}\text{O}_2)(\text{Be}_{0.5}\text{O}(\text{OH}_2))_2(\text{Be}_{0.5}\text{O})\text{P}_2]$ has eight crystallographically unique T sites, five of which are Be-centred and the remainder are P-centred. Of the Be-centred T-sites there are two different environments occupied, the first being involved in the edge sharing unit [Fig. 28] and the second a doubly water terminated bridge (confirmed *via* bond valence calculations, Table 15) [Fig. 29] between *ab* networks of $(\text{BeO}_3)_2(\text{PO}_3)_6$ composite building units. The Be-centred tetrahedra involved in edge sharing are heavily distorted, with a greatly extended Be – O distance (average 1.679(3) Å) for the anion bridges involved in the edge sharing. The linking of *ab* leads to the 1 dimensional channel system of distorted 8Rs running parallel to *a*. The distortion is due to the high degree of strong (average 1.95 Å) intra-framework hydrogen bonding

present [Fig. 30]. The water termination stabilises the structure through hydrogen bonding, however it also sterically hinders the one accessible channel present in the structure.

Table 15: Selected bond distances, angles and bond valence deviations for $[\text{BeO}_3(\text{Be}_{0.5}\text{O}_2)(\text{Be}_{0.5}\text{O}(\text{OH}_2))_2(\text{Be}_{0.5}\text{O})\text{P}_2]$

Bond	Bond length (Å)	Bond	Bond angle (°)
Average P – O	1.527(16)	Average O – P – O	109.47(9)
Average Be – O	1.620(3)	Average O – Be – O	109.49(9)
Edge sharing Be – O	1.679(3)		
Average Be – O(H ₂)	1.632(3)		
Selected bond valence sum deviations in v. u. for oxygen in terminating water groups and edge sharing			
O11 (H ₂)	0.33	O1 (edge sharing)	0.11
O12 (H ₂)	0.32	O6 (edge sharing)	0.09
		O9 (edge sharing)	0.08

Bond valence deviation for the two –OH₂ terminating groups are slightly high due to the polarisation of the electron density towards the electronegative O atom.

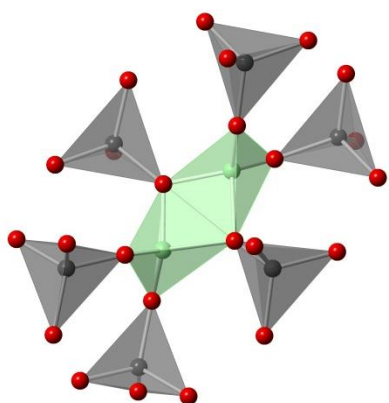


Figure 28: $(\text{BeO}_3)_2(\text{PO}_3)_6$ CBU in $[\text{BeO}_3(\text{Be}_{0.5}\text{O}_2)(\text{Be}_{0.5}\text{O}(\text{OH}_2))_2(\text{Be}_{0.5}\text{O})\text{P}_2]$

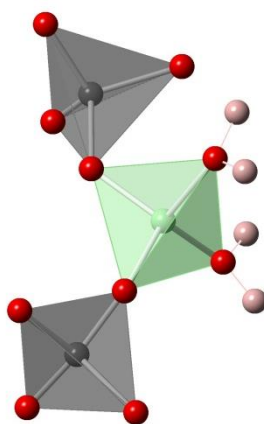


Figure 29: $\text{BeO}_2(\text{OH}_2)_2$ bridging units

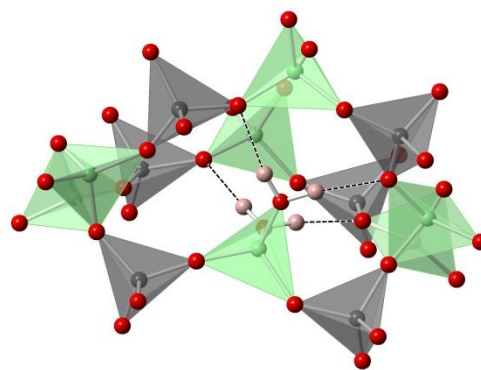


Figure 30: H-bonding present in $[\text{BeO}_3(\text{Be}_{0.5}\text{O}_2)(\text{Be}_{0.5}\text{O}(\text{OH}_2))_2(\text{Be}_{0.5}\text{O})\text{P}_2]$

Unfortunately as $[\text{BeO}_3(\text{Be}_{0.5}\text{O}_2)(\text{Be}_{0.5}\text{O}(\text{OH}_2))_2(\text{Be}_{0.5}\text{O})\text{P}_2]$ only forms as a minor phase or polyphasic, no further characterisation has been carried out.

4.8: [C₂H₅NH₂, H₂O]_x[Be_{~0.78}P_{~0.22}(O,OH)₂] (BOZ-P)

The above compound was synthesised by Harriet Rosethorn while working as a project student for the author and characterised by Mark Weller. The author declares that he had no direct part of the production/characterisation of this material, only supervised the research. Since it is a topographical analogue of the fully connected berylloarsenate [C₂H₅NH₂, H₂O]_x[Be_{66.7}As_{25.3}(O)_{80.5}(OH)_{103.5}] or BOZ (section 3.16) it is worth mentioning for comparison. The BOZ framework represents a new zeolite topology (confirmed by Mark Weller utilising the TOTOPOL software ^[9]) with both berylloarsenate and beryllophosphate forms being produced as part of this work and has recently been accepted for publication. ^[10]

BOZ-P crystallises as large colourless flat needles (150 x 25 x 5 µm) as a minor phase associated with bulk white unidentifiable powder. A regular crystal was selected for single crystal X-ray diffraction and the resulting model exhibited a monoclinic crystal system and was solved in the P2₁/c space group. As with BOZ-As, BOZ-P has 23 crystallographic unique T atom sites, each site is mixed between phosphorus and beryllium with an overall Be:P ratio of 3(±0.3):1, significantly more Be than encountered in BOZ-As. The resulting large charge imbalance is rectified by the bridging unit being a mixture of oxygen and predominately hydroxide. Like BEN and WEI-type frameworks (section 3.14/15 respectively) the major SBU is the spiro-5 ring, with the central site being near to fully occupied by Be. The only other simple SBU present in the asymmetric unit cell is a single 4R. The overall structure is formed of sinusoidal chains of spiro-5 rings along *a* which are further connected to form a network containing two large and unusual composite building units. The first is a pentagonal drum shaped cage formed by two 10Rs connected via spiro-5 rings termed *ben*. The second cage (*bet*) is asymmetric and is formed by four 8Rs, two 6Rs, one 4R and six 3Rs, these two cages form columns running through the structure along *c* and lead to formation of channels of 10Rs along *a* and 8Rs along *c*. The crosslinking of the *ac* network layers leads to the formation of 10R channels along 101 [Fig. 31]. Crystallographic parameters can be found in Table 16.

Table 16: Selected crystallographic parameters for BOZ-P

Empirical formula	[C ₂ H ₅ NH ₂ , H ₂ O] _x [Be _{~0.78} P _{~0.22} (O,OH) ₂]
Formula weight	45.08x + ~4225.25
Appearance	Transparent flat needles
Temperature	120 K
Wavelength	0.71073 Å
Crystal system	Monoclinic
Space group	P2 ₁ /c

<i>a</i>	13.620(3) Å
<i>b</i>	13.8290(7) Å
<i>c</i>	34.6378(2) Å
β	90.0150(2) °
Volume	6524(2) Å ³
<i>Z</i>	1
Weighted R index	0.3057

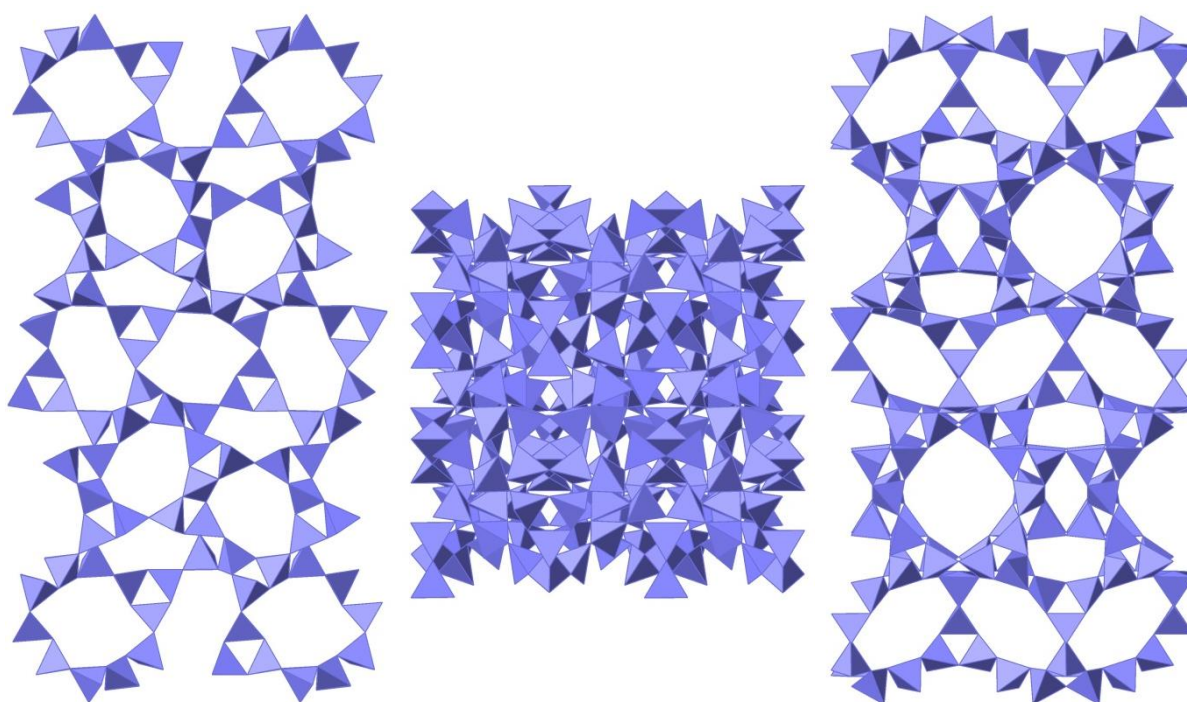


Figure 31: BOZ-type topology viewed down *a*, *b* and *c* (i, ii and iii respectively), magenta tetrahedra represent disordered character of T atom sites.

The structure of BOZ-P was refined by Mark Weller using the same methods as described for BOZ-As (section 3.16), which resulted in the very high R factor encountered and absence of extra-framework species in the structure.

Comparison with BOZ-As

Despite being topologically the same as the arsenate version of the BOZ framework, there are still some differences encountered due to the change of composition. The unit cell of BOZ-P is 5.37 % smaller than encountered in BOZ-As, due to the smaller ionic radii and T – O distances encountered for P centred tetrahedra. The Be:pnictogen differs substantially between As and P containing frameworks; 3:1 and 2.5:1 for Be:P and Be:As respectively. This leads to a slightly less condensed

structure for BOZ-P and due to the increase in low density beryllium, the already low Dc is further reduced (1.12 gcm^{-3} as opposed to 1.37 gcm^{-3}).

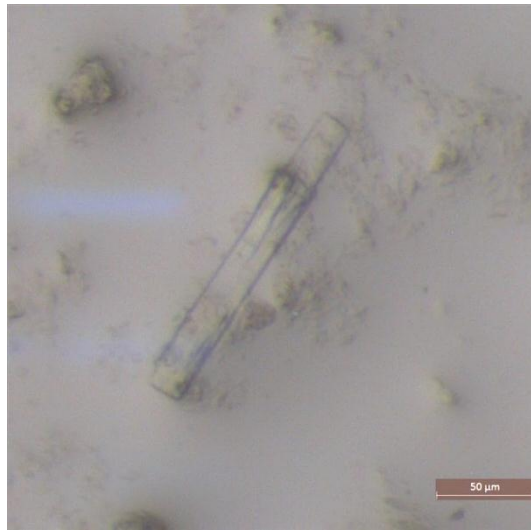


Figure 32: Microscope image of BOZ-P, confirming morphology

4.9: Trends encountered in the beryllophosphate frameworks

Synthetic

The synthetic objective for the beryllophosphates was to emulate the conditions successfully producing novel berylloarsenate frameworks, however since arsenates tend to form in slightly milder conditions than phosphates some synthetic pathway modification was required. As a whole the beryllophosphates were prepared over similar reaction lengths (48 – 192 h.), temperatures (160 – 220 °C) and pH (5 – 6.5 and ~ 14) to the arsenates. Consideration of the interplay between the concentrations of the main reagents; template, P source and Be source, shows a very similar trend to the arsenates. The majority of structures form in excess template with relatively equal concentrations of beryllium and phosphorus [Fig. 33], however in comparison with the formation of the berylloarsenates the beryllophosphates seem to form at slightly higher phosphorus concentrations.

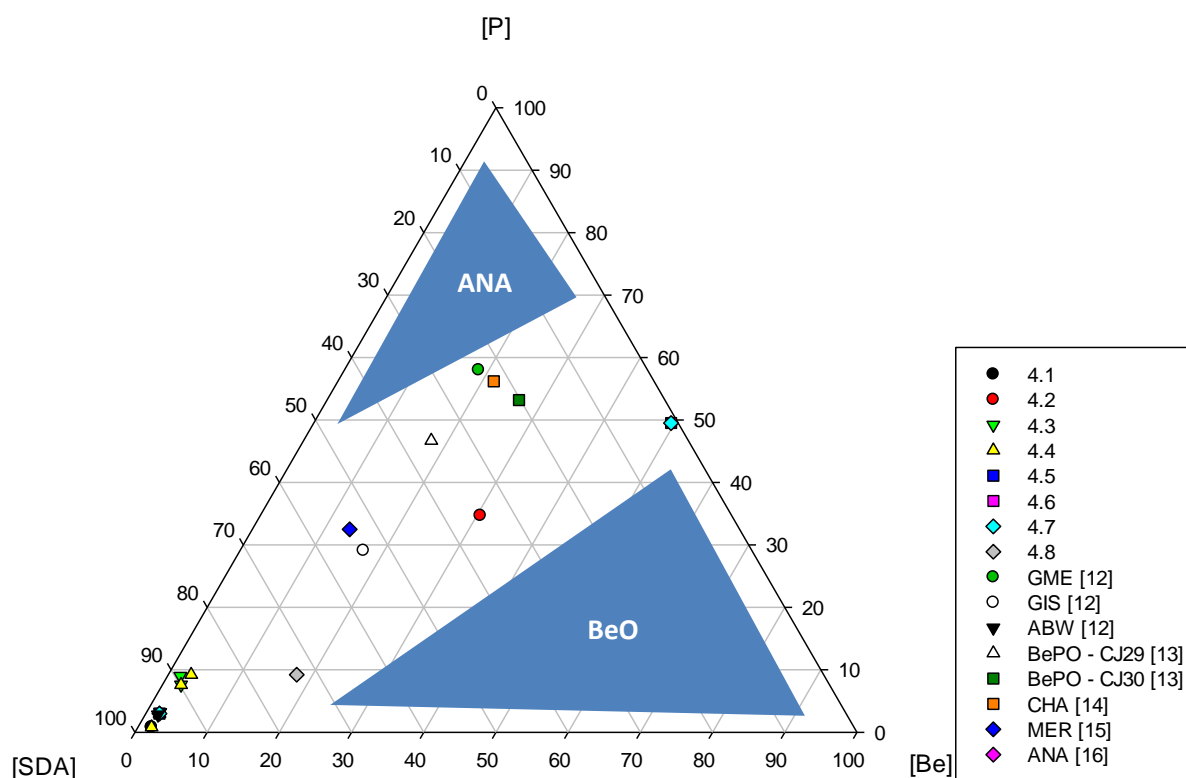


Figure 33: Ternary plot showing relationship between molar ratios of Be:P:organic template (SDA), data has been normalised and each structure is presented as a unique data point, more than one data point exists for several structures where there is more than one route to synthesis. Overlapping points are due to the use of different SDAs

One major difference between the berylloarsenates and beryllophosphates is, where at high arsenic concentrations the predominate phases encountered are simple arsenates, in the beryllophosphates at

high phosphorus concentrations the most common product is the well-known beryllophosphate analogue of the ANA topology.^[16]

Structural

Since the majority of the structures produced are analogues of the berylloarsenates discussed in the previous chapter, the structural trends are similar, with a high degree of termination as both –OH and –OH₂ present. Bridging anions in the form of OH[–] are also prevalent, providing much need structure stabilisation via hydrogen bonding. One key difference to the berylloarsenates is the less distorted character of the larger ring structures, due to a closer to observed for aluminosilicate O – T – O angle for the phosphorus-centred tetrahedra.

4.10: Conclusions for the beryllophosphate frameworks

After repeating the reactions which successfully produced novel beryloarsenates with phosphorus as the pentavalent species, eight new beryllophosphate frameworks of varying dimensionality have been solvothermally synthesised and characterised primarily by single crystal X-ray diffraction. Five of these structures fulfil this chapter's objective of being analogues of beryloarsenate structures, whereas the other three structures are all previously unknown topologies. This represents a significant contribution to an expanding field of research and contributes to the already well-populated family of beryllophosphate frameworks (Chapter 1

Structures presented here were all synthesised under mild solvothermal conditions (160 – 220 °C) with water being the predominate solvent. The major variables between reactions were the identity of extra-framework cations (both nitrogen-rich organic molecules and alkali/alkali earth metal hydroxides) and relative concentrations of both phosphorus and beryllium sources (section 4.9). It was found that generally synthesis was successful (i.e. producing a viable structure) at pHs between 5 – 6.25 and ~ 14 and where the extra-framework cation was thermally stable and provided an adequate site for nucleation, without excessive steric complexity. Successful reaction periods ranged between 48 and 192 h, with some products apparently unaffected by reaction time while others saw changes in crystal size and morphology.

$\text{Na}_2[(\text{BeO}_2\text{OH})(\text{PO}_2)]\cdot\text{H}_2\text{O}$ is a structural analogue of $\text{Na}_2[\text{AsO}_4\text{Be}(\text{OH})]\cdot\text{H}_2\text{O}$ and represents the only one-dimensional beryllophosphate formed by this research. It is formed of a chain of consecutive anion sharing beryllium-centred tetrahedra, which leads to the under bonding of the bridging O^{2-} causing it to be permanently protonated. Phosphorus centred tetrahedra alternate either side of the beryllium 'backbone' leading to a chain of 3Rs, with extra framework structure stabilisation in the form of octahedrally coordinated Na^+ cations and hydrogen bonding.

$[\{\text{BeO}_2(\text{OH})(\text{OH}_2)\}\{\text{BeO}_2\text{OH}_2\}\text{P}]$ is a structural analogue of $\text{AsO}_4\text{Be}(\text{OH})_2\text{BeOH}(\text{OH}_2)$ and represents the only two-dimensional beryllophosphate formed by this research. $\{\text{BeO}_2(\text{OH})(\text{OH}_2)\}\{\text{BeO}_2\text{OH}_2\}\text{P}$ has a hydrogen rich layer structure with a network formed of 3, 4 and distorted 8Rs in the *b/c* plane. A high degree of Be tetrahedra termination is present as either hydroxyl or water groups, this stabilises the layers by hydrogen bonding.

The majority of beryllophosphate structures produced in this study have been three-dimensional, three of which $([\text{C}_2\text{H}_5\text{NH}_2, \text{H}_2\text{O}]_x[\text{Be}_{\sim 0.78}\text{P}_{\sim 0.22}(\text{O},\text{OH})_2], [(\text{BeO}_4)_2\text{BeO}_2(\text{BeO}_2(\text{OH}_2)_2)(\text{BeO}_2\text{OH}_2)(\text{BeOH}_2\text{BeO}_2)\text{P}_4]$ and $[\text{H}-$

pyridine][$(\text{BeO}_4)_2\text{BeO}_3(\text{OH}_2)\text{P}_3(\text{OH})$] are structural analogues of previously reported berylloarsenates, however the remaining three are all novel structures with no known structural analogues. $[\text{H-pyridine}]_4[\text{Be}_6(\text{PO}_3\text{OH})_8]$ is a novel porous interrupted three-dimensional framework with well-defined extra framework pyridine positions. BeO_4 and PO_3OH tetrahedra alternate to form 12, 8 and 4Rs. $[\text{H-dimethylamine}][\text{BeO}_4(\text{BeO}_3\text{OH})(\text{BeO}_2\text{OH}_2)\text{P}_2]$ is a porous interrupted three-dimensional framework formed of a network of 3, 4 and heavily distorted 14R channels running down *a*. The networks are cross-linked by distorted 8Rs, 3Rs and zig-zag chains of 4Rs. Dimethylamine provides a charge balancing and structure stabilising role and is situated in the 14R channels. $\text{BeO}_3(\text{Be}_{0.5}\text{O}_2)(\text{Be}_{0.5}\text{O}(\text{OH}_2))_2(\text{Be}_{0.5}\text{O})\text{P}_2$ exhibits a novel highly disordered three-dimensional framework formed of a network of ‘horse shoe’ shaped 8Rs and 4Rs in the *b/c* plane. In the *a/b* plane there is a lattice of $(\text{BeO}_3)_2(\text{PO}_3)_6$ units where the Be centred tetrahedra are edge sharing leading to triply bonded O sites (Be-O(P)-Be); each unit is connected to the next via an arrangement of 4Rs which is seen as a helical chain down *b*. The *a/b* layers are cross-linked by $\text{BeO}_2(\text{OH})_2$ tetrahedra to form the network in the *b/c* plane.

As with the berylloarsenates there is huge scope for further work with this research. The first objective would be the further characterisation of the structures produced as part of this study. Further investigations of increased phosphorus concentration reactions would be the next logical step, since on consideration of the ternary phase diagram [Fig. 33] there are still wide areas of reaction compositions which would likely lead to more novel structures. Investigating the properties and potential applications of the beryll phosphates would also be a major objective for any future work carried out, since the beryll phosphates exhibit fewer toxicity issues than their arsenic analogues and are more likely to find real-world applications in anything from gas sorption to catalysis.

4.11: References:

- ¹ J. B. Parise, *J. Chem. Soc. Chem. Comm.*, **1985**, 22, 606-607
- ² D. M. Poojary, A. I. Bortun, L. N. Bortun, A. Clearfield, *J. Solid State Chem.*, **1997**, 132, 213-223
- ³ S. S. Dhingra, R. C. Haushalter, *J. Chem. Soc. Chem. Comm.*, **1993**, 1665
- ⁴ S. C. Sevov, *Angew. Chem. Int. Ed. Engl.*, **1996**, 35, 2630
- ⁵ W. T. A. Harrison, M. L. F. Philips, A. V. Chavez, T. M. Nenoff, *J. Mater. Chem.*, **1999**, 9, 3087 – 3092
- ⁶ F. Walter, *Eur. J. Mineral.*, **1992**, 4, 1275-1283
- ⁷ J. M. Bennett, J. P. Cohen, E. M. Flanigen, J. J. Pluth, J. V. Smith, *ACS Sym. Ser.*, **1983**, 218, 109-118
- ⁸ V. V. Bakakin, Y. V. Seretkin, S. P. Demin, *J. Struc. Chem.* **2009**, 2, 356 - 360
- ⁹ TOTOPOL. M. D. Foster, M. M. J. Treacy, A Database of Hypothetical Zeolite Structures: <http://www.hypotheticalzeolites.net> (accessed throughout project 2008 – 2012)
- ¹⁰ B. T. R. Littlefield, M. T. Weller, *Nature Commun.*, (accepted for publication September 2012)
- ¹¹ X. Bu, G. D. Stucky, *Zeolites*, **1997**, 19, 200 – 208
- ¹² H. Zhang, M. Chen, Z. Shi, X. Bu, Y. Zhou, X. Xu, D. Zhao, *Chem. Mater.*, **2001**, 13, 2042 – 2048
- ¹³ M. Guo, J. Yu, J. Li, Y. Li, R. Xu, *Inorg. Chem.*, **2006**, 45, 3281 – 3286
- ¹⁴ H. Zhang, L. Weng, Y. Zhou, Z. Chen, J. Sun, D. Zhao, *J. Mater. Chem.*, **2002**, 12, 658 – 662
- ¹⁵ X. Bu, T. E. Gier, G. D. Stucky, *Micro. Meso.*, **1998**, 26, 61 – 66
- ¹⁶ H. Zhang, Z. Chen, L. Weng, Y. Zhou, D. Zhou, *Micro. Meso.*, **2003**, 57, 309 - 316

Chapter 5

Other beryllate chemistry

The following chapter describes the synthesis of several new structures produced during the investigation into light atom frameworks and are collected together owing to their different chemistry in regards to previous chapters. Two new beryllogermanate layer structures have been produced, $\text{Na}[\text{BeGeO}_3(\text{OH})]$ and $\text{Ba}[\text{BeGeO}_3(\text{OH})]$ as well as the first definitive synthesis and characterisation of the tetrahydroxyberyllate anion, $\text{Be}(\text{OH})_4^{2-}$ and a selection of transition metal hexaqua complex templated beryllioarsenate frameworks.

Beryllogermantes and germanium in framework structures.

Germanium is an ideal candidate for substituting for silicon or arsenic within a zeolitic framework. Being both part of group 14 and therefore isoelectronic, silicon and germanium generally present similar properties and reactivity, for example their isostructural Si/Ge-O_2 quartz forms^[1] and elemental bond distances^[2]. In germanate frameworks however, germanium has been known to coordinate four, five and even six fold whereas Si based zeotypes are generally tetracoordinated. Also, the Ge-O distance is 1.74Å compared to a Si-O distance of 1.60Å^[3] which stabilises certain zeolite topologies and building units such as double four rings (D4R)^[4]. Several known zeolite structures have been produced with Ge substituted Si sites, such as Ge-ZSM-5^[3], analcime (ANA)^[5] natrolite (NAT)^[6], cancrinite (CAN)^[7], gismondine (GIS)^[6], faujasite (FAU)^[6] and rho (RHO)^[6].

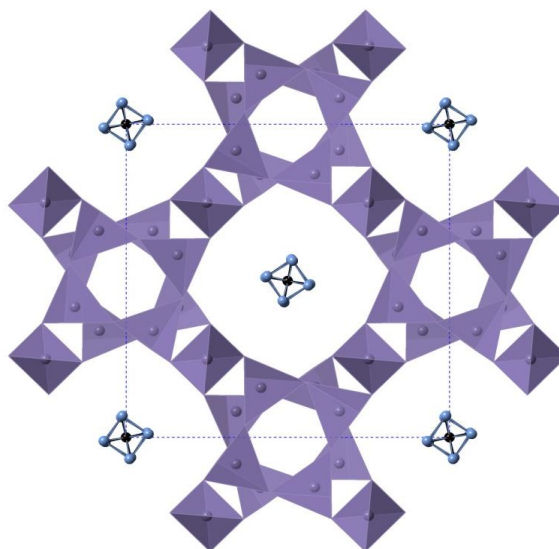


Figure 1: Zeotype ASU-7 viewed along c. A framework solely formed from Ge T sites, templated by dimethylamine.^[8]

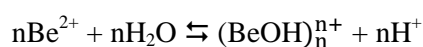
The first novel porous silicogermanate was synthesised in 1991^[9] using an aqueous medium with an amine as a SDA, however, this framework proved to be unstable when calcined. Following this a multitude of novel germanium containing structures have been synthesised including the ASU-n (Arizona State University-n) family^[10] [Figure 1] which contains four, five and six coordinated Ge atoms as well as frameworks containing all-tetrahedral Ge. Another important silicogermanate family is represented by the ITQ-n^[11,12] series, which presents new topologies which cannot be obtained by germanium-free mixtures, owing to their reliance of their stability on the smaller angles of the Ge-O-Ge units in comparison to the strained Si-O-Si angle that would have to exist. This reduced angle is due to the larger atomic radii of germanium when compared to silicon.

In contrast, work on beryllium and germanium containing frameworks is extremely sparse, perhaps owing to the hazards in using beryllium. There were only two beryllogermanate structures known in the literature prior to this research, rare earth containing melilite structured beryllogermanates, $\text{Ln}_2\text{Be}_2\text{GeO}_7$ ^[13] (where X = Y, Er, Dy, Gd, Pr, Sm, and La) and a beryllogermanate adopting the sodalite structure, $\text{Mn}_8[\text{Be}_6\text{Ge}_6\text{O}_{24}]\text{Se}_2$. ^[14]

$\text{Ln}_2\text{Be}_2\text{GeO}_7$ exhibits the tetragonal melilite structure which adopts a two dimensional network composed of 5 membered rings formed of two germanium tetrahedra and three beryllium tetrahedra, where two of the beryllium centred tetrahedra are vertex sharing. The rare earth ions connect the network along the *c* axis, which changes dependant on the identity of Ln. $\text{Mn}_8[\text{Be}_6\text{Ge}_6\text{O}_{24}]\text{Se}_2$ adopts the classic sodalite β cage, with Se and Mn present as extra-framework ions. Crucially both materials are formed at relatively high temperatures, the melilite analogue is synthesised by solid state means at 1100 °C and the sodalite analogue is formed by high temperature hydrothermal methods at 750 °C. Therefore the structures described in this chapter represent the first examples of beryllogermanates formed by low temperature hydrothermal synthesis.

Solution/alkaline chemistry of Be

The solution chemistry of divalent beryllium is primarily influenced by its high charge to radius ratio, thus it polarises any surrounding water molecules and causes them to orient with the negative end of their dipoles attracted to the Be^{2+} ion. ^[15] The extent of repulsion encountered by the protons attached to the affected water molecules is sufficient that they can be transferred to a more distant water molecule, leaving OH^- with the Be^{2+} ion. This process increases with pH and is represented as:



At high pH the oligated polymer $\text{Be}_3(\text{OH})_3^{3+}$ is the most important beryllium species, formed of beryllium atoms linked by hydroxyl bridges. ^[16] On further increase of the alkali concentration it is

theorised that the hydroxyl bridges are broken down, leading to a reduction in the degree of polymerisation until the mononuclear beryllate anion $[\text{Be}(\text{OH})_4]^{2-}$ is reached.

Aside from theoretical studies and IR data, $[\text{Be}(\text{OH})_4]^{2-}$ has never been confirmed or isolated as a crystal structure. Indeed the existence of $\text{Be}(\text{OH})_4$ vertex sharing units has only been indicated by infrared studies of the $\text{BeO-H}_2\text{O}$ system. ^[17] Scholder *et al.* claimed the synthesis of a series of compounds; $\text{M}[\text{Be}(\text{OH})_4]$ ($\text{M} = \text{Na}_2, \text{K}_2, \text{Cs}_2, \text{Ca}$ and Ba) ^[18] and report the growth of large crystals, however, this report was not backed up by any structural determination. Despite extensive efforts to reproduce their findings in this research, no crystalline material has been produced and it is possible that their reactions were contaminated by atmospheric carbon dioxide. As such research presented here represents the first definitive synthesis and characterisation of the discrete $[\text{Be}(\text{OH})_4]^{2-}$ anion in the form of $\text{Sr}[\text{Be}(\text{OH})_4]$. ^[19]

Transition metal complexes as templates

Alkali metal hydroxides and nitrogen rich organic compounds are not the only potential templates investigated in the formation of microporous framework materials, transition metal complexes have been used to successfully form new topologies for the past 20 years. The use of compounds such as the chiral metal complex $\text{Co}(\text{en})_3\text{Cl}_3$ in solvothermal synthesis, allows for even greater structural and compositional diversity, especially since the chiral nature of the template can be ‘imprinted’ into the resulting templated framework. ^[20] Chiral nanoporous materials would enable enantioselective catalysis, a key objective for the pharmaceutical industries. ^[21]

Despite the potential of transition metal complex templated structures, the research is relatively limited, restricted mainly to the formation of gallium, ^[22] aluminium, ^[23, 24, 25] and zinc phosphates templated with Co, Cu, Ni, Cd and Zn complexes. ^[20, 26] $[\text{Co}^{\text{III}}(\text{en})_3][\text{Zn}_8\text{P}_6\text{O}_{24}\text{Cl}]\bullet 2\text{H}_2\text{O}$ is a connected three-dimensional framework structure formed built up of ZnO_4 , ZnO_3Cl and PO_4 tetrahedra which connect to form layers along *c* which are cross-linked by Cl to form intersecting tunnels with 12R apertures. ^[20] As far as the author is aware there are no examples of transition metal complex templated beryllium containing structures and so this field represents a potential rich source of structures with interesting functionalities.

Table 1: Reaction conditions for successful beryllogermante and tetrahydroxyberyllate structures

Product	Relevant section	Defining Synthesis (Reaction that produced solvable single crystals)	Temperature (°C)	Reaction time (h)
Na[BeGeO ₃ (OH)]	5.1	BL026.4: Molecular ratios adapted from the synthesis of OSB-1 ^[12] . Be(OH) ₂ (0.378 g, 8.8 mmol), Na ₂ GeO ₃ (0.833 g, 5 mmol) and distilled H ₂ O (1.43 mL) was added to a Teflon vessel and stirred at room temperature for five minutes. KOH (0.28 mL, 3.24 mmol, 45 wt. % in H ₂ O) and tetraethylammonium hydroxide (0.2 mL, 0.486 mmol, 40 wt. % in H ₂ O) were then added and the resulting ‘sol’ allowed to age while gently stirring for 1 hour before autoclaving.	200	48
Ba[BeGeO ₃ (OH)]	5.2	BL045.1: Be(OH) ₂ (0.378 g, 8.8 mmol, BaGeO ₃ (1.29 g, 5 mmol) and distilled H ₂ O (0.54 mL) was added to a Teflon vessel and stirred at room temperature for five minutes. KOH (1.38 mL, 0.0162 moles, 45 wt. % in H ₂ O) and tetraethylammonium hydroxide (0.2 mL, 0.486 mmol, 40 wt. % in H ₂ O) were then added and the resulting ‘sol’ allowed to age while gently stirring for 1 hour before autoclaving.	200	48
Sr[Be(OH) ₄]	5.3	PR06.1b: First synthesised by Christopher Hinde. Sr(OH) ₂ •8H ₂ O (0.527 g, 1.98 mmol), Be(OH) ₂ (5.5 mg, 0.13 mmol) and distilled H ₂ O (10 mL) was added to a Teflon vessel and stirred gently for 1 hour before autoclaving.	200	48
[Co ^{II}] _{0.11} [(AsO ₄ (H) _{0.66}) ₂ Be ₂ (BeOH ₂) _{0.33}]• 2H ₂ O	5.4	BL0129.2: Be(OH) ₂ (0.54 g, 0.0126 moles, H ₃ AsO ₄ (2.1 mL, 0.0276 moles) and distilled H ₂ O (10 mL) was added to a Teflon vessel and stirred at room temperature for 30 minutes. CoCl ₂ •6H ₂ O (0.75 g, 3.15 mmol) and 1,3-diaminopropane (1.126 mL, 0.0152 moles) were then added and the	220	168

		resulting 'sol' allowed to age while gently stirring for 1 hour before autoclaving.		
--	--	---	--	--

Solvothermal synthesis methods were applied for all of the reactions pertaining to the formation of $\text{Na}_2[\text{BeGeO}_3(\text{OH})]$ and $\text{Ba}[\text{BeGeO}_3(\text{OH})_2]$. To combat the comparatively low solubility of germanium compounds, the germanium sources investigated were the alkali/alkali earth metal germanates, MGeO_3 (where $\text{M} = \text{Li}_2, \text{Na}_2, \text{K}_2$ and Ba) which were produced via solid state methods.^[27] The initial molar ratios were based upon those used in the synthesis of the beryllosilicate Oslo Santa Barbera-1 (OSB-1),^[28] but heavily modified with every possible parameter undergoing some variation in an attempt to produce a beryllogermanate version of the very large pored OSB-1.

Reactions initially focused on varying the amount of structure directing species present (either organic or alkali metal hydroxide) with Na_2GeO_3 as the starting material. When the pH was raised to above 12 from the addition of alkali metal hydroxides the only identifiable solid products were BeO and occasionally various carbonates. When the pH was controlled using NaOH , between 8.5 and 11.5 $\text{Na}[\text{BeGeO}_3(\text{OH})]$ was formed. Varying the amount and type of organic structure directing agent seemed to have little effect on products other than assisting pH control. Temperature and pressure (the latter controlled by fill volume) had little effect if the pH was in range, other than a slight impact on the size of crystals grown, which in turn could be balanced by modifying the time of reaction. The concentration of the reagents, $\text{Be}(\text{OH})_2$ and Na_2GeO_3 played a crucial role, where an excess of either produced only their most thermodynamically stable products. Mineraliser in the form of NaF was added but had no effect on the structure other than facilitating large crystal growth. The role of the three major reagents for the formation of $\text{Na}[\text{BeGeO}_3(\text{OH})]$ is summarised in Figure 2.

Unsurprisingly a similar trend is observed for the structural analogue $\text{Ba}[\text{BeGeO}_3(\text{OH})]$, which was first isolated from a reaction containing high concentrations of BaGeO_3 and using KOH for pH control. Further reactions applying $\text{Ba}(\text{OH})_2$ to produce a similar pH range (8.5-11.5) routinely produced $\text{Ba}[\text{BeGeO}_3(\text{OH})]$, when varying any of the other synthetic parameters, the same effects were observed as seen in the synthesis of $\text{Na}[\text{BeGeO}_3(\text{OH})]$. Several attempts were made to form structures with higher dimensionality, focusing mainly on the addition of various acids to further modify the pH, however these were all unsuccessful. The role of the three major reagents for the formation of $\text{Ba}[\text{BeGeO}_3(\text{OH})]$ is summarised in Figure 3.

The use of LiOH and/or Li_2GeO_3 produced only unreacted starting materials or LiCO_3 , suggesting that the structure needs a cation of a larger ionic radii to stabilise the layers. Use of KOH and K_2GeO_3 produces the layer structure $\text{K}_2[\text{BeGeO}_3(\text{OH})]$ which had been previously produced by another member of the Weller group.^[29]

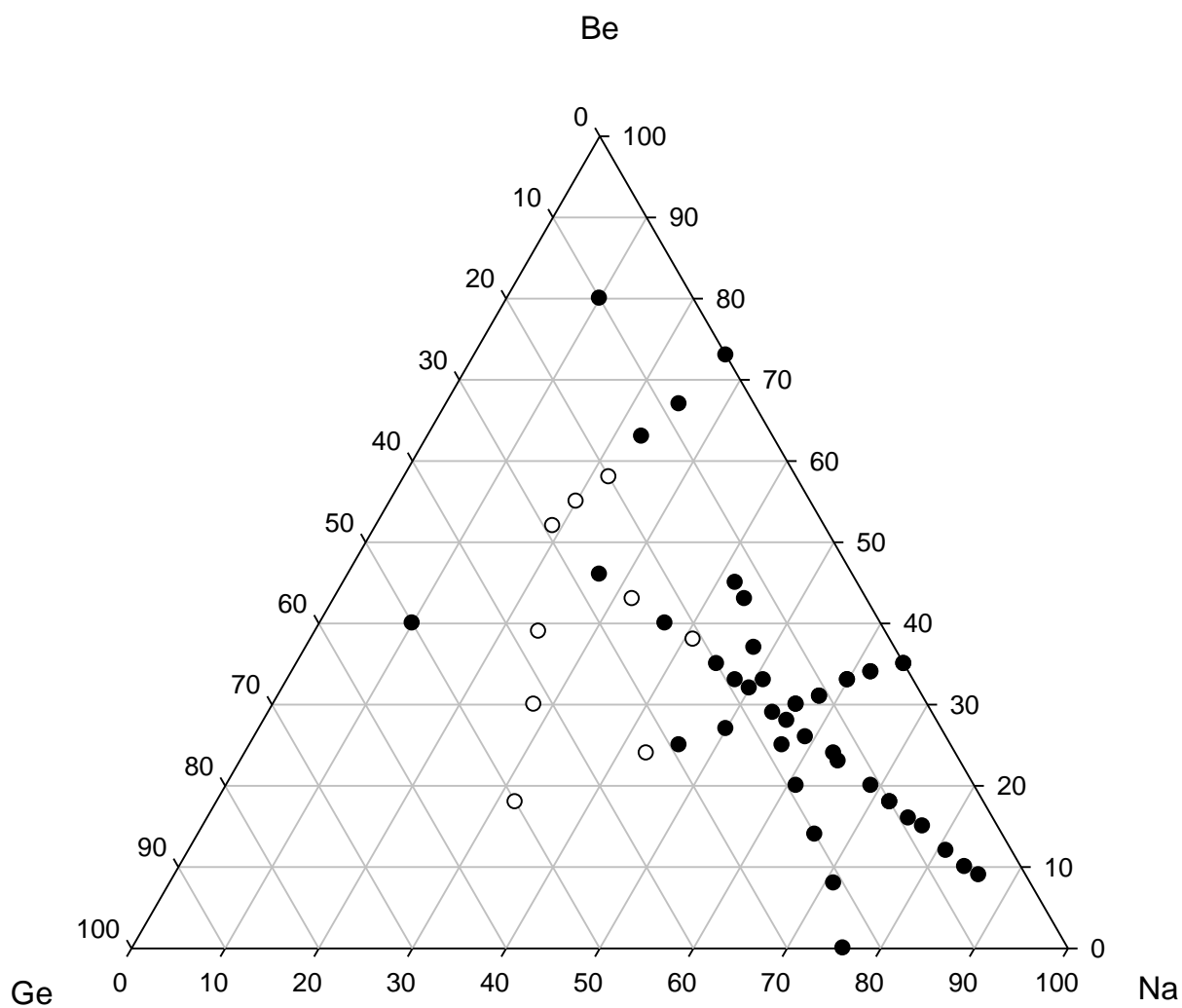


Figure 2: Phase diagram showing the impact of varying concentration of the major reagents in the formation of Na[BeGeO₃(OH)]. White and black spots are Na[BeGeO₃(OH)] and BeO/starting materials respectively.

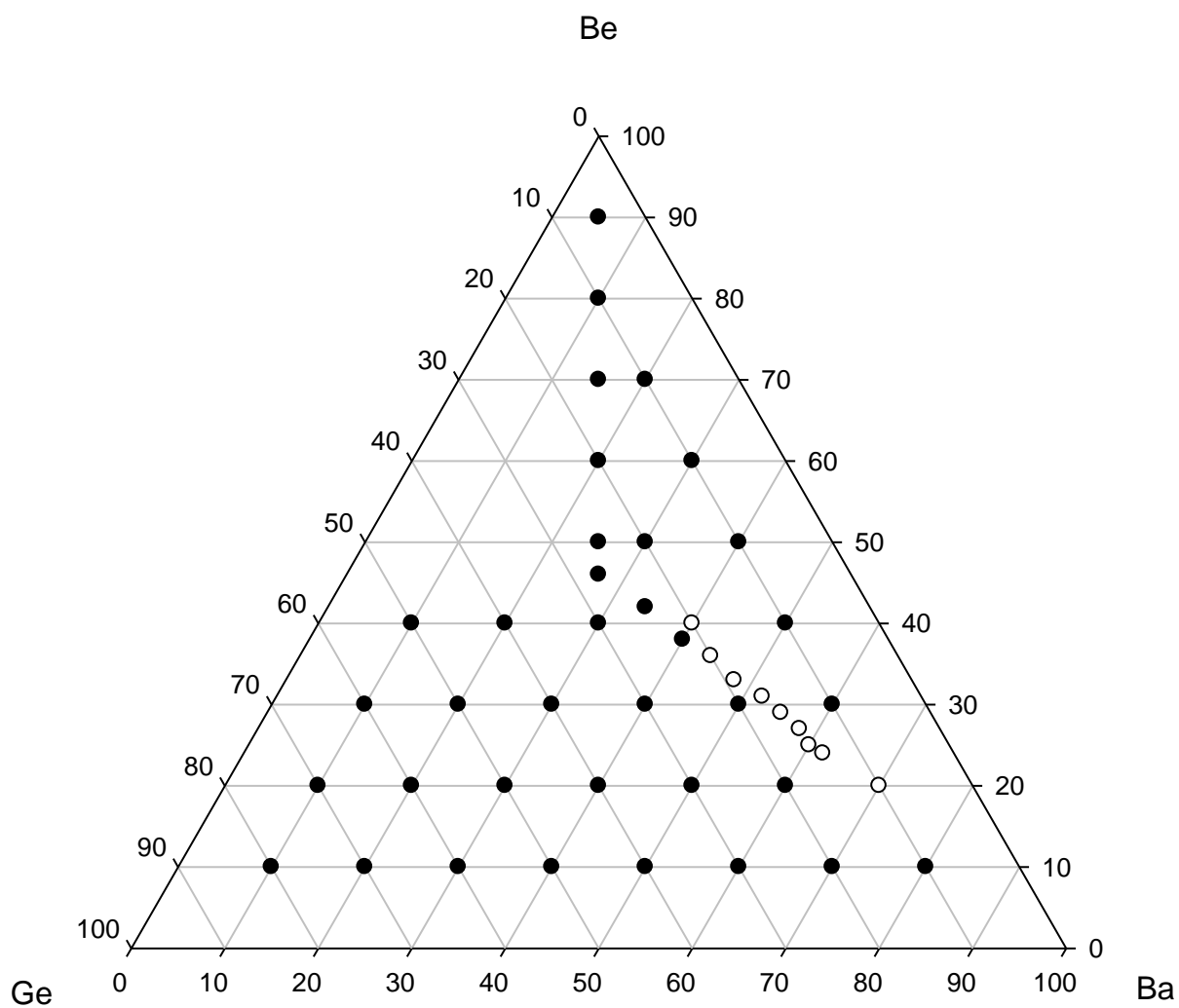


Figure 3 Phase diagram showing the impact of varying concentration of the major reagents in the formation of Ba[BeGeO₃(OH)]. White and black spots are Ba[BeGeO₃(OH)] and BeO/starting materials respectively.

5.1 Na[BeGeO₃(OH)]

Na[BeGeO₃(OH)] crystallises as large (~ 500 µm) colourless sheet crystals which grow from an obvious site of nucleation to form attractive sprays of sheets. A large regular sheet which had a single sharp angle of extinction was selected and analysed by single crystal X-ray diffraction, the full crystallographic data is summarised in table 2. Na[BeGeO₃(OH)] crystallises in the monoclinic crystal system, with a space group of P 2₁ and has a dense two dimensional network formed of 3- and 4-membered rings which lies in the *a/b* plane [Fig. 4]. The layers are cross-linked by a fully occupied Na⁺ site. The secondary building units are formed of vertex sharing Be and tetravalent Ge centred tetrahedra alternating in a 1:1 ratio, selected bond lengths and angles are presented in Table 3.

Table 2: Crystallographic information for Na[BeGeO₃(OH)]

Empirical formula	Na[BeGeO ₃ (OH)]
Formula weight	169.6
Appearance	Large colourless sheets
Temperature	120 K
Wavelength	0.71073 Å
Crystal system	Monoclinic
Space group	P 2 ₁
<i>a</i>	5.1246(5) Å
<i>b</i>	4.6634(5) Å
<i>c</i>	7.2208(6) Å
β	92.145(6) °
Volume	172.44(3) Å ³
<i>Z</i>	2
D _c	3.27 g cm ⁻³
Reflections collected/unique	2987/751
R index	0.0333
Weighted R index	0.0869

The beryllium tetrahedra are consecutively vertex sharing, forming an infinite sinusoidal chain running parallel with b . The germanium tetrahedra alternate orientation in c , between being above or below the chains in forming chains of three rings. Each germanium tetrahedra is bonded to two beryllium tetrahedra in its ‘parent’ chain and a third beryllium tetrahedra in the next chain along, forming 4-membered rings in the crosslinking of the chains. The fourth corner of the germanium tetrahedra is terminated by a structure stabilising and charge balancing hydroxyl group. The single hydrogen position is confirmed by bond valence calculations (Table 4) and due to its high degree of thermal motion has been fixed at a distance of 0.95 Å.

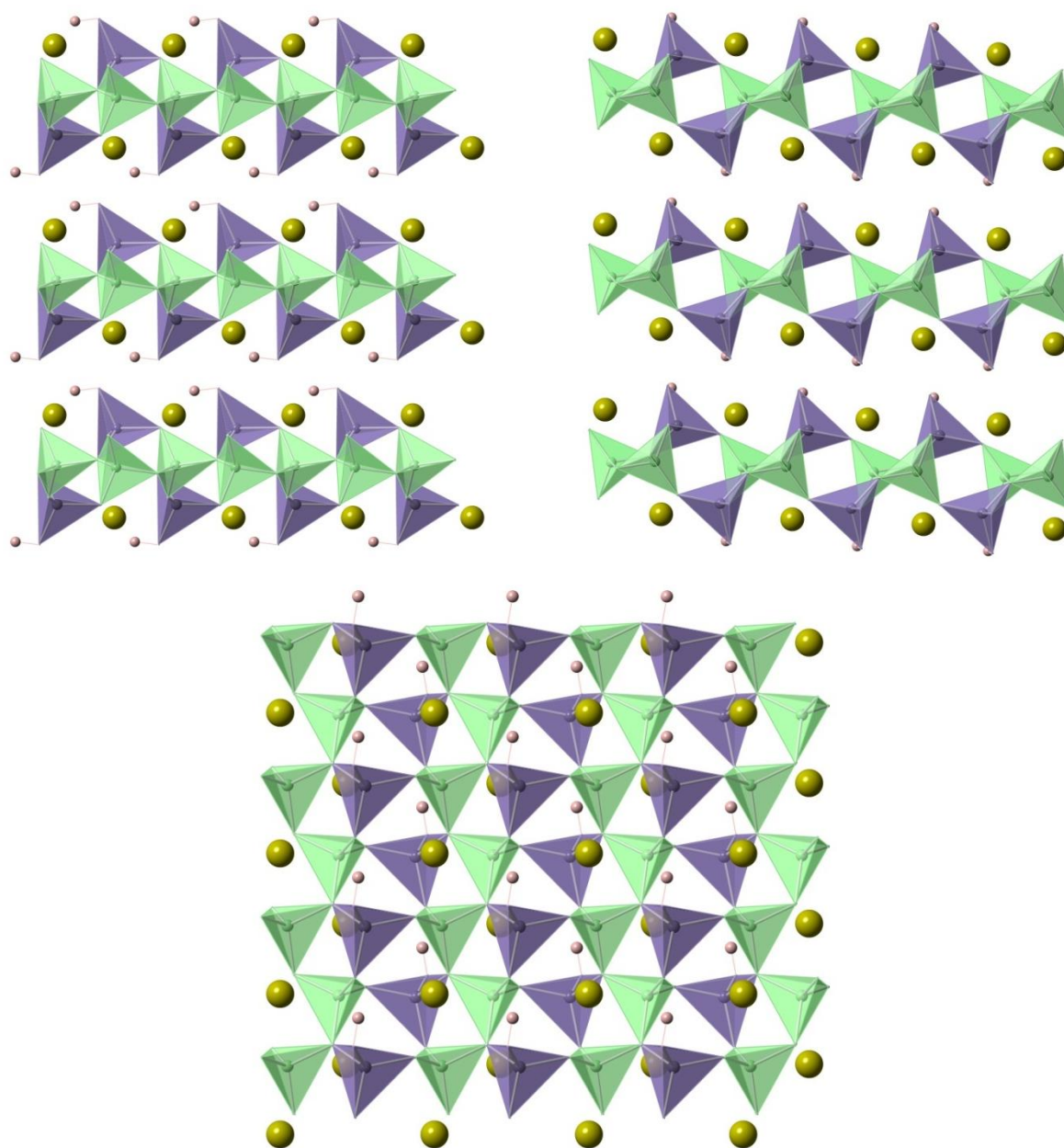


Figure 4: Structure of $\text{Na}[\text{BeGeO}_3(\text{OH})]$, with a , b and c directions represented by top left, right and bottom respectively. Green and purple tetrahedra are Be and Ge, yellow and pink spheres are Na and H respectively.

Table 3: Selected bond lengths/angles for Na[BeGeO₃(OH)]

Bond	Bond length (Å)	Bond	Bond angle (°)
Be – O1	1.594(9)	Average O-Be-O	109.40(7)
Be – O2	1.673(10)	Average O-Ge-O	109.45(2)
Be – O2	1.646(10)		
Be – O4	1.650(17)		
Ge – O1	1.733(5)		
Ge – O2	1.768(6)		
Ge – O3(H)	1.782(6)		
Ge – O4	1.736(6)		
Na – O1	2.317(6)		
Na – O2	2.418(6)		
Na – O3	2.264(6)		
O3H --- O4	1.965 (4)		

Table 4: Selected bond valences for Na[BeGeO₃(OH)]

Bond	Bond valence (v.u.)	Bond	Bond valence (v.u.)
O3 – H	0.86	O4 – Be	0.44
O3 – Ge	0.90	O4 --- H	0.09
O3 – Na	0.23	O4 – Ge	1.01/0.04
	$\Sigma = 2.13$	O4 – Na	0.12/0.09
			$\Sigma = 1.87$

The slight discrepancy in the bond valences calculated for O3 and O4 is likely due to the requirement of fixing the hydrogen bond distance, based on the v.u. values it is likely that the true position is slightly closer to O4. Interestingly the hydrogen atom is not involved in layer crosslinking as it is hydrogen bonded to the nearby network O4 site; this is facilitated by the proximity of the sodium cation [Fig. 5]. The sodium cation is octahedrally coordinated to two sets of three symmetry related oxygen sites. The main role of hydrogen in this structure is therefore to charge balance the negative network, the extra-framework sodium cation also charge balances but also stabilises the overall structure through coordination to the network oxygen. An SEM image of Na[BeGeO₃(OH)]

has also been acquired and is shown in [Fig 6], the sheet morphology is clearly exhibited along with the nucleation centre.

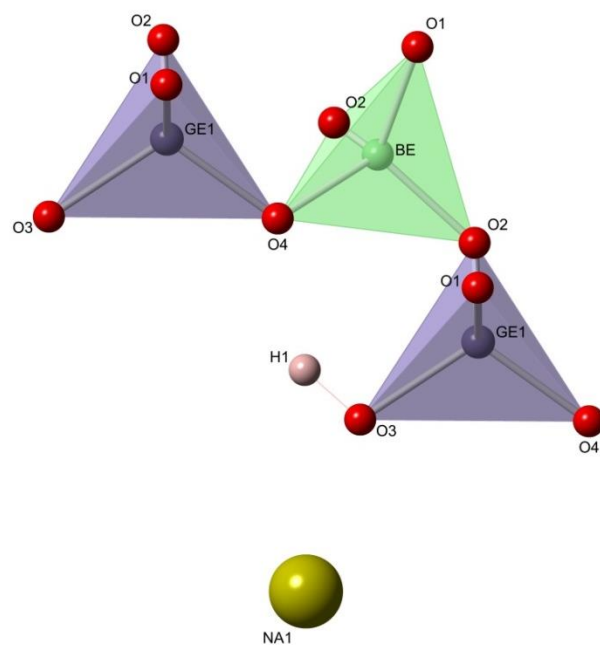


Figure 5: Hydrogen bonding environment for Na[BeGeO₃(OH)], Green and purple tetrahedra are Be and Ge, yellow and pink spheres are Na and H respectively.

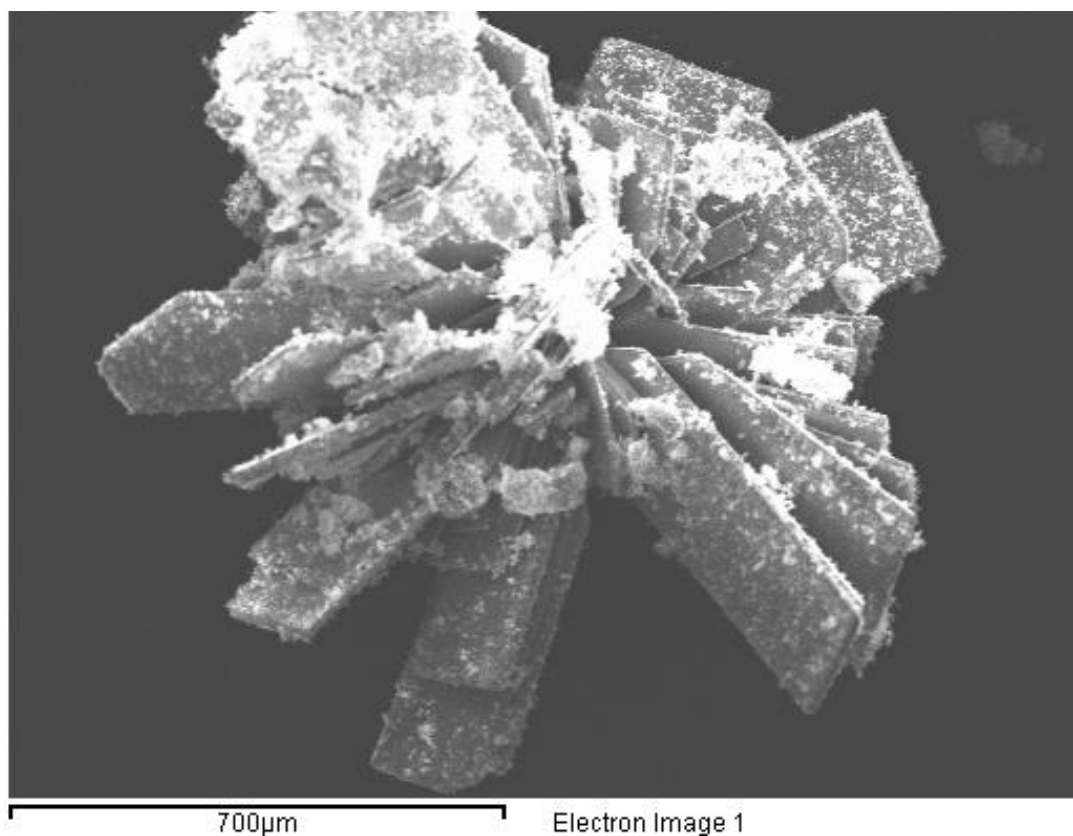


Figure 6: SEM image of Na[BeGeO₃(OH)]

5.2 Ba[Be(OH)GeO₃(OH)]

Ba[Be(OH)GeO₃(OH)] crystallises as long (800 μm) colourless needle crystals and is often found as a mixed phase with BaCO₃ which is an impurity from the starting material. A suitable crystal was collected by single crystal X-ray diffraction, crystallographic parameters are summarised in table 5. Ba[Be(OH)GeO₃(OH)] is a two dimensional layered structure akin to Na[BeGeO₃(OH)] with some subtle but crucial differences. The structure exhibits the monoclinic crystal system with a space group of P 2₁/c where infinite networks of distorted 4- and 8-membered rings are aligned along the *b/c* plane. The networks can be considered to be formed by sinusoidal chains of alternating 4- and 8Rs where each chain is connected to its neighbour by alternating Be-O-Ge bridging via the 4Rs. The layers are cross-linked by a combination of weak hydrogen bonding and extra-framework Ba²⁺ cations. Since there is an absence of OSDA in the structure it is likely that in the synthesis TEAOH has a pH control and mineralising role.

Table 5: Crystallographic information for Ba[Be(OH)GeO₃(OH)]

Empirical formula	Ba[Be(OH)GeO ₃ (OH)]
Formula weight	300.9
Appearance	Large colourless needles
Temperature	120 K
Wavelength	0.71073 Å
Crystal system	Monoclinic
Space group	P 2 ₁ /c
<i>a</i>	5.8651(2) Å
<i>b</i>	9.8839(2) Å
<i>c</i>	7.7115(2) Å
β	95.551(2) °
Volume	444.94(1) Å ³
<i>Z</i>	4
D _c	4.49 g cm ⁻³
Reflections collected/unique	6320/1080
R index	0.0227
Weighted R index	0.0660

The beryllium environment is found to be tetrahedral with three vertices oxygen bridged to germanium tetrahedra and one terminated by one of the two hydrogen sites within the structure. The germanium site is likewise situated and through the bonding of these two sites leads to the formation of the sole secondary building unit in this structure, the 4R. The 4Rs are arranged in a cross shape, forming the 8R in its centre and leading to the sinusoidal ‘crank shaft’ chains previously mentioned [Fig. 8]. The barium cation site is octahedrally coordinated to four network oxygen in the layers above and below its position, leading its coordination sphere to be aligned with half of the 8R. The presence of the barium cation distorts the orientation of the two hydrogen sites in the structure so that the germanium terminating hydroxyl is involved in overall structure stabilisation by crosslinking the layers [Fig. 9a], whereas the beryllium terminating hydroxyl, due to its proximity to the cation (2.913 Å) is present only in a charge balancing and intra-network stabilising role [Fig. 9b]. The two hydrogen positions are confirmed by bond valence calculations and have had their distances fixed to 0.95 Å to aid refinement. Selected bond distances and angles can be found in table 6 along with pertinent bond valence calculations in table 7.

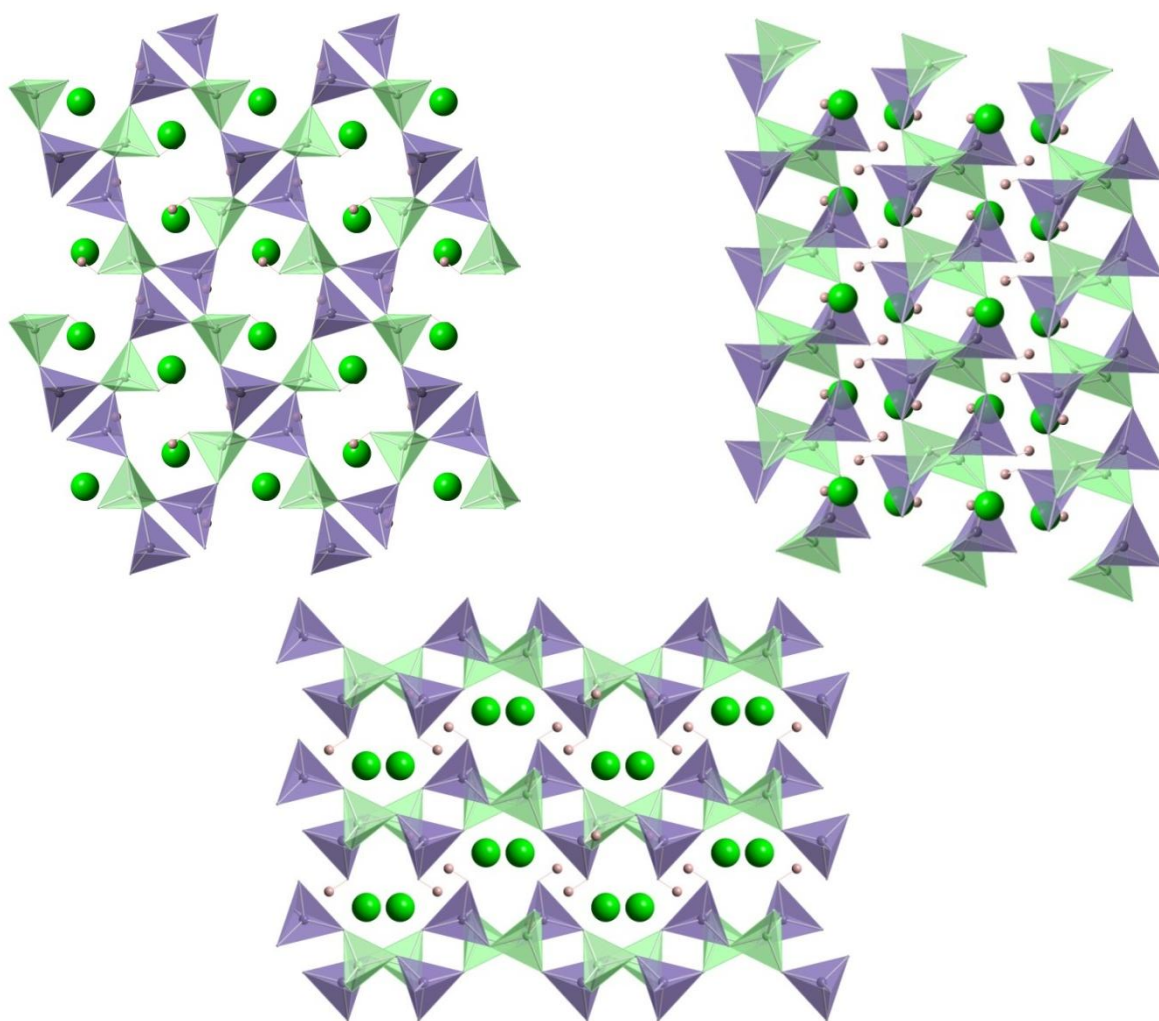


Figure 7: Structure of $\text{Ba}[\text{Be}(\text{OH})\text{GeO}_3(\text{OH})]$, with a , b , and c directions represented by top left, right and centre respectively. Green and purple tetrahedra are beryllium and germanium, lime green and pink spheres are barium and hydrogen respectively.

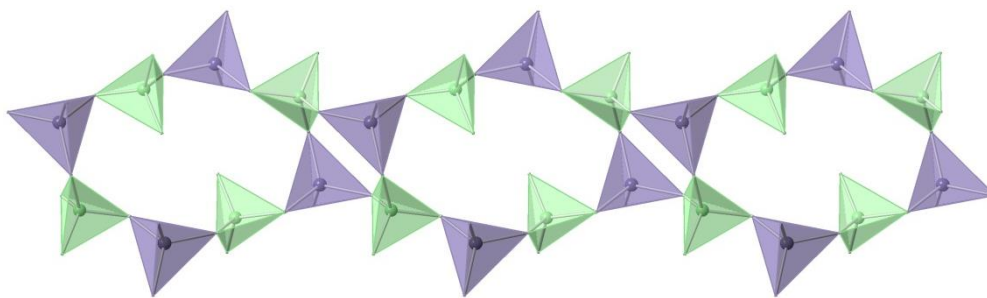


Figure 6: Crankshaft arrangement of 4- and 8Rs, key as above

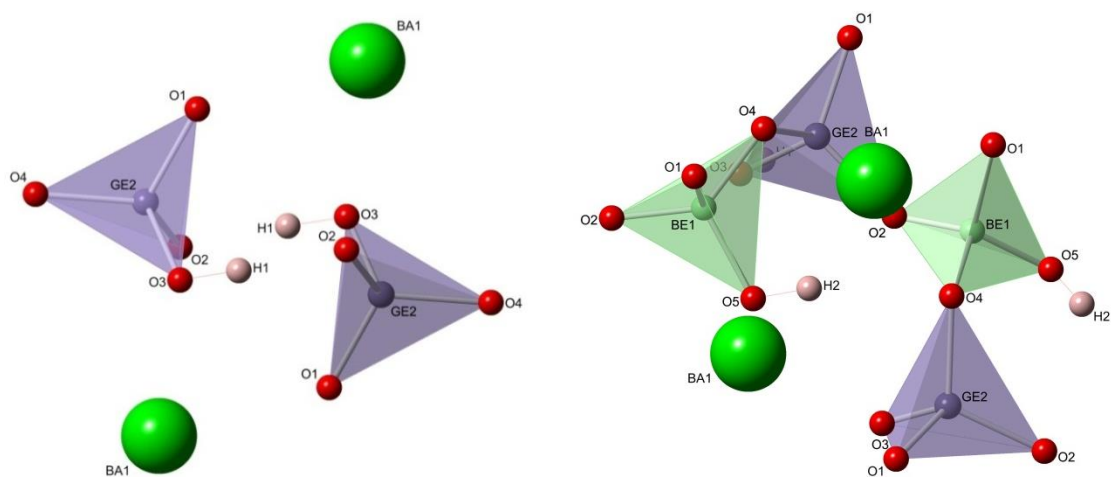


Figure 9: a/b positions of H1 and H2 relative to rest of structure, key as above

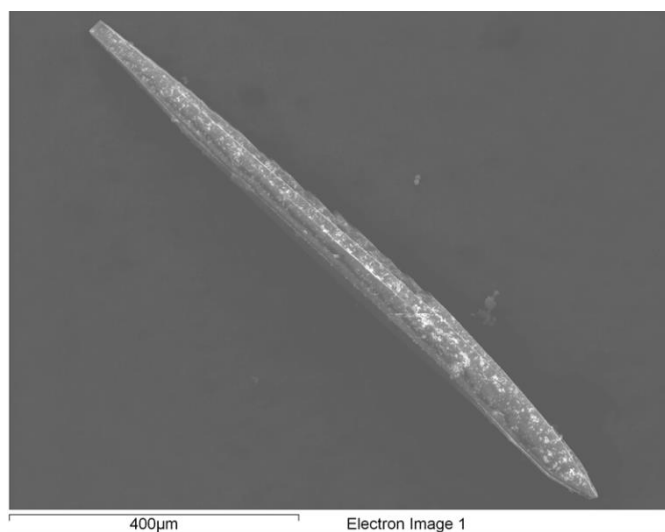
Table 6: Selected bond lengths/angles for Ba[Be(OH)GeO₃(OH)]

Bond	Bond length (Å)	Bond	Bond angle (°)
Be – O1	1.644(7)	Average O-Be-O	109.53(4)
Be – O2	1.630(7)	Average O-Ge-O	109.23(15)
Be – O4	1.646(7)	O3 – H --- O2	169.38
Be – O5(H)	1.639(7)		
Ge – O1	1.736(3)		
Ge – O2	1.742(3)		
Ge – O3(H)	1.806(3)		
Ge – O4	1.739(3)		
H1 --- O2	1.725 (3)		

Table 7: Selected bond valences for Ba[Be(OH)GeO₃(OH)]

Bond	Bond valence (v.u.)	Bond	Bond valence (v.u.)
O3 – H1	0.85	O5 – H2	0.95
O3 – Ge	0.84	O5 – Be	0.45
O3 – Ba	0.21/0.25	O5 – Ba	0.25/0.21/0.06
	$\Sigma = 2.27$		$\Sigma = 2.02$

An SEM image of Ba[Be(OH)GeO₃(OH)] has also been acquired and is shown in figure 10, the needle-like morphology is clearly exhibited. EDS also confirms the presence of germanium, barium and oxygen.

**Figure 10:** SEM image of Ba[Be(OH)GeO₃(OH)]

Interestingly on comparison to other known structures $\text{Ba}[\text{Be}(\text{OH})\text{GeO}_3(\text{OH})]$ is found to be isorecticular to the dense naturally occurring three-dimensional barium containing aluminosilicate paracelsian, $\text{BaAl}_2\text{Si}_2\text{O}_8$.^[30] The most obvious differences being the lack of framework cross linking in $\text{Ba}[\text{Be}(\text{OH})\text{GeO}_3(\text{OH})]$ and the complete lack of distortion in the SBUs observed in paracelsian. The ‘crank shaft’ of 4- and 8Rs observed in $\text{Ba}[\text{Be}(\text{OH})\text{GeO}_3(\text{OH})]$ is not observed nor possible in paracelsian due to the 4Rs crosslinking to the layer below, therefore causing the network to be closer to planar rather than sinusoidal.

It can be envisaged that heating $\text{Ba}[\text{Be}(\text{OH})\text{GeO}_3(\text{OH})]$ to cause condensation of the hydroxyl groups may cause the layers to crosslink and therefore form a beryllogermanate analogue of paracelsian. Indeed when studied *in situ* via VTPXD a change in structure is noted at 400 °C which coincides with a loss of 4.6 % of mass observed in TGA studies [Fig. 11] which represents the loss of one molecule of H_2O from the structure. Therefore since the crystallinity has not been destroyed at 500 °C and both beryllium and germanium sites are now under bonded from the condensation it is likely that cross-linking has occurred to stabilise the structure.

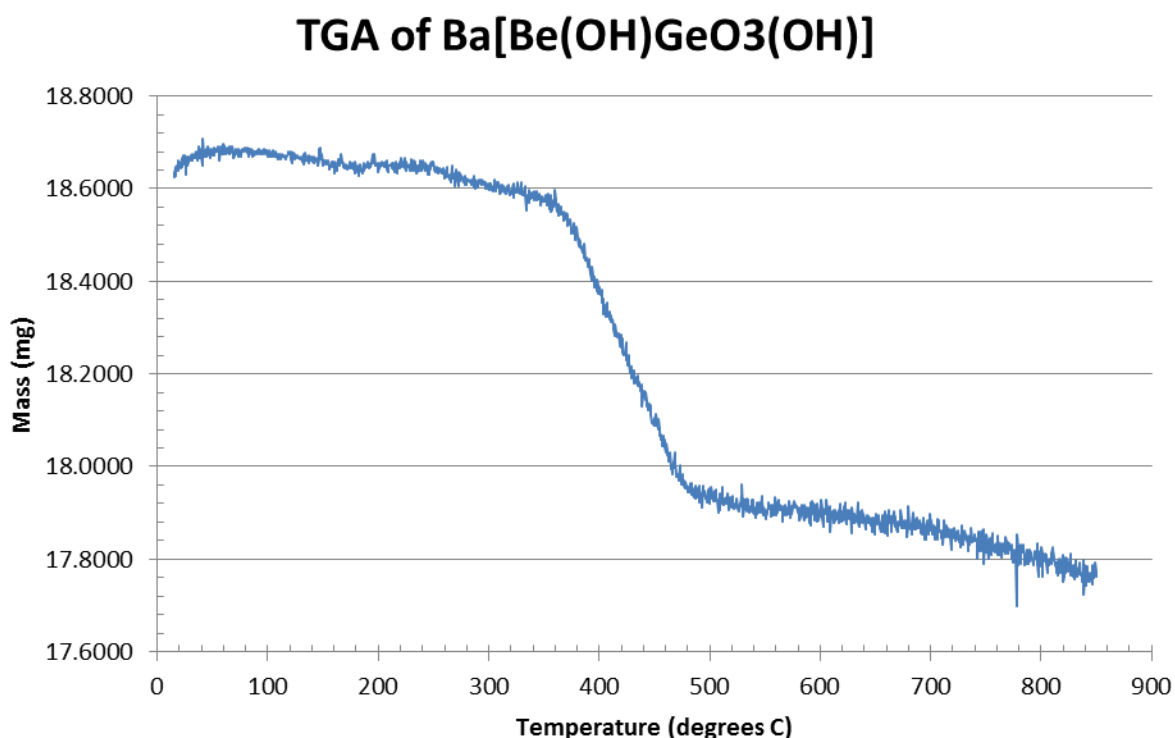


Figure 11: TGA of $\text{Ba}[\text{Be}(\text{OH})\text{GeO}_3(\text{OH})]$ showing 4.3 % loss in mass

$\text{Ba}[\text{Be}(\text{OH})\text{GeO}_3(\text{OH})]$ is also structurally analogous to the berylloarsenate $\text{Sr}[\text{AsO}_4\text{Be}(\text{OH})]\cdot\text{H}_2\text{O}$ which is discussed previously in Chapter 3. Differences in crystallographic parameters are summarised in table 8. $\text{Sr}[\text{AsO}_4\text{Be}(\text{OH})]\cdot\text{H}_2\text{O}$ exhibits a slight expansion in b and c (0.409 and 0.274 Å respectively) and a large contraction in both a (0.782 Å) and β (4.913 °) and an overall reduction in volume of 28.04 Å. The overall decrease encountered is due to the smaller ionic

radii of Sr^{2+} in comparison to Ba^{2+} , however this allows for less distortion in the secondary building units and therefore the network is slightly more planar, providing the small expansion observed in *b* and *c*. Since quadravalent germanium has been replaced by pentavalent arsenic there is no need for Ge-O-H termination as exhibited in $\text{Ba}[\text{Be}(\text{OH})\text{GeO}_3(\text{OH})]$.

The hydrogen bonding related structural stabilisation is significantly different, where in the beryllogermanate version it is via strong inter network $-\text{O}-\text{H}\cdots\text{O}$ bonds (1.75 (3) Å) the berylloarsenate version is via interaction with an extra-framework water molecule (2×1.349 Å). This difference is also culpable when considering why $\text{Sr}[\text{AsO}_4\text{Be}(\text{OH})]$ is more planar as it can be seen that the shorter hydrogen bonding in $\text{Ba}[\text{Be}(\text{OH})\text{GeO}_3(\text{OH})]$ causes the structure to be ‘pinched’ around the cations, leading to the sinusoidal character of the networks.

Table 8: Comparing key parameters between $\text{Ba}[\text{Be}(\text{OH})\text{GeO}_3(\text{OH})]$ and $\text{Sr}[\text{AsO}_4\text{Be}(\text{OH})]\cdot\text{H}_2\text{O}$

$\text{Ba}[\text{Be}(\text{OH})\text{GeO}_3(\text{OH})]$		$\text{Sr}[\text{AsO}_4\text{Be}(\text{OH})]\cdot\text{H}_2\text{O}$	
<i>a</i>	5.8651(2) Å	<i>a</i>	5.0833(2) Å
<i>b</i>	9.8839(2) Å	<i>b</i>	7.9685(3) Å
<i>c</i>	7.7115(2) Å	<i>c</i>	10.2929 Å
β	95.551(2) °	β	90.638(2) °
V	444.94(1) Å ³	V	416.90(3) Å ³
Average Be-O-Ge angle	124.906 °	Average Be-O-As angle	121.110 °

5.3: Sr[Be(OH)₄]

Isolated initially as a minor phase in beryllogermanate reactions, further refinement of experimental parameters produced phase pure Sr[Be(OH)₄]. The tetrahydroxyberyllate crystallises as large (10 - 15 mm) rod crystals which commonly include a rivulet/fault running down the middle, an SEM image is shown in [Fig 14]. Sr[Be(OH)₄] exists in the tetragonal system at room temperature, space group I4₁/acd. When cooled below 210 K structural distortion, potentially due to a change in the hydrogen bonding, destroys the crystal integrity and makes structure elucidation impossible. Full structure refinement was undertaken on single crystal X-ray diffraction data collected at room temperature. Crystallographic information is detailed in Table 9.

Table 9: Crystallographic Information for Sr[Be(OH)₄]

Empirical formula	Sr[Be(OH) ₄]
Formula weight	164.7
Appearance	Colourless rods
Temperature	293 K
Wavelength	0.71073 Å
Crystal system	Tetragonal
Space group	I 4 ₁ /acd
<i>a</i>	9.5536(4) Å
<i>c</i>	17.1539(18) Å
Volume	1565.66(19) Å ³
<i>Z</i>	16
<i>D_c</i>	2.79 g cm ⁻³
Reflections collected/unique	8455/464
R index	0.030
Weighted R index	0.060

The structure of $\text{Sr}[\text{Be}(\text{OH})_4]$ [Fig. 12] is very simple and consists of layers of $\text{Be}(\text{OH})_4^{2-}$ tetrahedra separated by charge balancing Sr^{2+} ions perpendicular to the tetragonal unit cell c -axis. The tetrahydroxyberyllate layers are stabilised by pincer-like weak hydrogen bonding, with OH-O distances in the range of 2.69 – 2.85 Å [Fig. 13]. If you exclude the Sr^{2+} ions the sheets of tetrahydroxyberyllate adopt an ABA'B'AB configuration, where layers A and A' are the same but adopt the opposite orientation with their hydroxyl 'pincers'. Selected bond lengths and angles can be found in Table 10. The tetrahydroxyberyllate exhibits regular tetrahedral geometry for the BeO_4 primary building unit, with Be-O distances of 1.625 x 2 and 1.642 x 2 Å and O-Be-O angles between 106 – 110 °. The hydroxyl groups are angled away from the high charge/low radius Be centre and engage in hydrogen bonding with the adjacent hydroxyberyllate.

The Be-O bond distances present in $\text{Be}(\text{OH})_4^{2-}$ are similar to those encountered in polymeric $\text{Be}(\text{OH})_2$ (1.59 – 1.65 Å), where the vertex is shared to form $\text{Be}(\text{OH})_4$ units. When compared to other known $\text{M}(\text{OH})_4^{n-}$ structures, $\text{B}(\text{OH})_4^-$ and $\text{Zn}(\text{OH})_4^{2-}$, the M-O distances (average M-O, $\text{B}^{3+} = 1.476$ Å, $\text{Be}^{2+} = 1.634$ Å and $\text{Zn}^{2+} = 1.966$ Å) increase as charge decreases, as would be expected. [31,32]

Table 10: Selected bond lengths and angles for $\text{Sr}[\text{Be}(\text{OH})_4]$ from SXD.

Bond	Bond length (Å)	Bond	Bond angle (°)
Be-O1	1.625(5) x2	Be-O1-H1	117.5(4)
Be-O2	1.642(5) x2	Be-O2-H2	114.7(4)
O2-H2	0.80(3)	O1-Be-O1	116.0(5)
H1-O1	0.80(3)	O1-Be-O2	106.4(2) x2
Sr1-O2	2.557(3) x4	O1-Be-O2	108.7(2) x2
Sr1-O1	2.708(3) x4	O2-Be-O2	110.8(5)

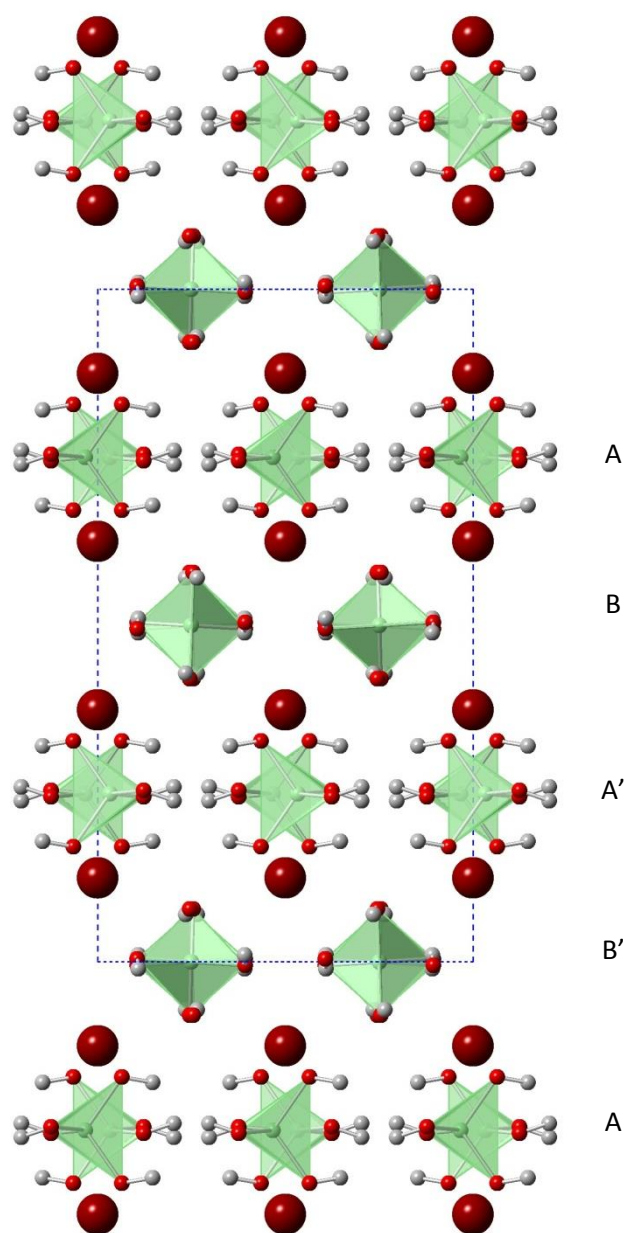


Figure 12: Structure of $\text{Sr}[\text{Be}(\text{OH})_4]$ viewed along b , with labelled ABA'B'AB sequence.

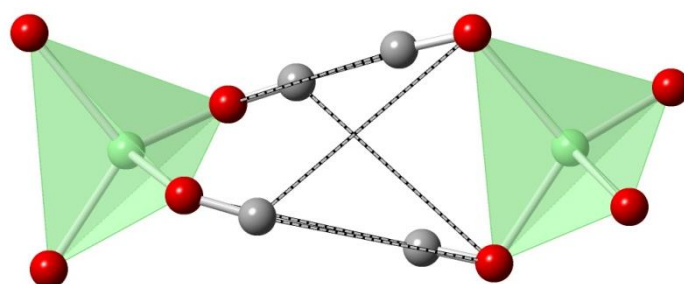


Figure 13: 'Pincer' hydrogen bonding between tetrahedra in same layer.

Further characterisation was carried out in the form of bond valence calculations, SEM/EDS and neutron powder diffraction data. Bond valence calculations were carried out and confirms the structural assignment presented. Semi-quantitative EDS measurements show the presence of Sr and O in levels consistent with the formula. Structure was solved by Mark Weller from neutron diffraction data and provides accurate internuclear O-H distances: O1-H1, 0.948(9) Å and O2-H2, 0.969(8) Å.

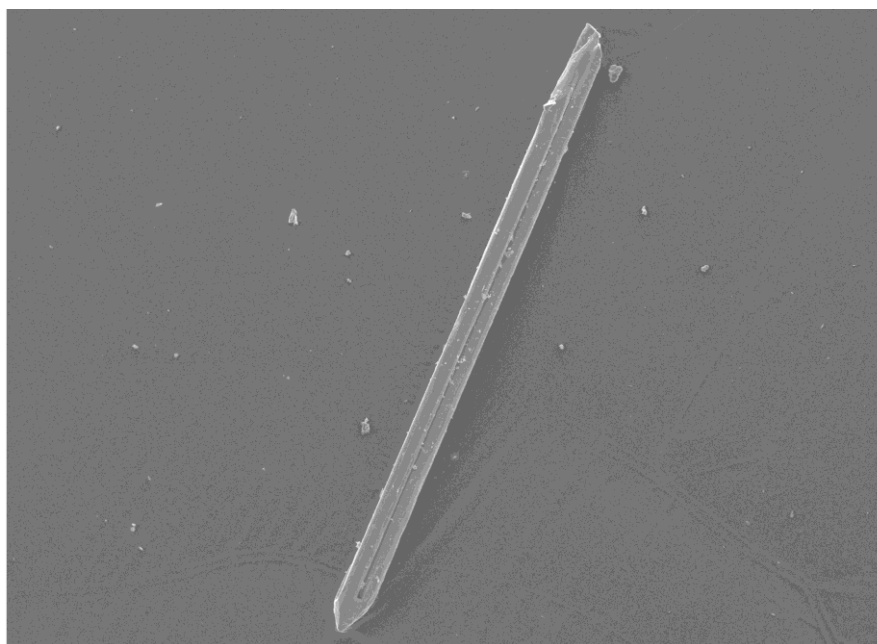


Figure 14: SEM image of Sr[Be(OH)₄]

5.4: $[\text{Co}^{\text{II}}]_{0.11}[(\text{AsO}_4(\text{H})_{0.66})_2\text{Be}_2(\text{BeOH}_2)_{0.33}]\cdot 2\text{H}_2\text{O}$

$[\text{Co}^{\text{II}}]_{0.11}[(\text{AsO}_4(\text{H})_{0.66})_2\text{Be}_2(\text{BeOH}_2)_{0.33}]\cdot 2\text{H}_2\text{O}$ is formed polyphasically with BeAs-MER (section 3.8a) and crystallises as large (250 x 250 x 250 μm) purple tetrahedra. A single regular tetrahedra was selected and analysed by single crystal X-ray diffraction. The resulting structure is in the trigonal crystal system and occupies the P6_3 space group. $[\text{Co}^{\text{II}}]_{0.11}[(\text{AsO}_4(\text{H})_{0.66})_2\text{Be}_2(\text{BeOH}_2)_{0.33}]\cdot 2\text{H}_2\text{O}$ has five crystallographically unique oxo-anion bridged T atom sites, distributed over two arsenic sites, two fully occupied beryllium sites and one 33 % occupied beryllium site. The disorder present on the third beryllium site has ramifications for the porosity and connectivity of the overall structure, since it is involved in the formation of a 12, 6 and 4R based network along the *ab* plane which is connected via a sinusoidal backbone of consecutive beryllium centred tetrahedra which form 3Rs with the arsenate tetrahedra. The overall structure is therefore a novel interrupted three-dimensional framework with a one dimensional channel system with termination present as a $-\text{OH}_2$ group on the 33 % occupied beryllium centred tetrahedra. However, this site is also shared with an absence of the beryllium centre and $-\text{OH}_2$ termination, and instead is 66 % occupied by two terminating hydroxyl groups on arsenate centred tetrahedra which leads to a second 12R channel running parallel to *c*. Extra-framework species are present as water and a 10 % occupied hexaqua cobalt complex. Crystallographic parameters can be found in Table 11.

Table 11: Selected crystallographic parameters for $[\text{Co}^{\text{II}}]_{0.11}[(\text{AsO}_4(\text{H})_{0.66})_2\text{Be}_2(\text{BeOH}_2)_{0.33}]\cdot 2\text{H}_2\text{O}$

Empirical formula	$[\text{Co}^{\text{II}}]_{0.11}[(\text{AsO}_4(\text{H})_{0.66})_2\text{Be}_2(\text{BeOH}_2)_{0.33}]\cdot 2\text{H}_2\text{O}$
Formula weight	348.7
Appearance	Purple tetrahedra
Temperature	120 K
Wavelength	0.71073 Å
Crystal system	Trigonal
Space group	$\text{P } 6_3$
<i>a</i>	16.5333(7) Å
<i>c</i>	4.7821(3) Å
Volume	1132.06(1) Å ³
<i>Z</i>	6
<i>D_c</i>	2.17 g cm ⁻³
R index	0.0895
Weighted R index	0.1474

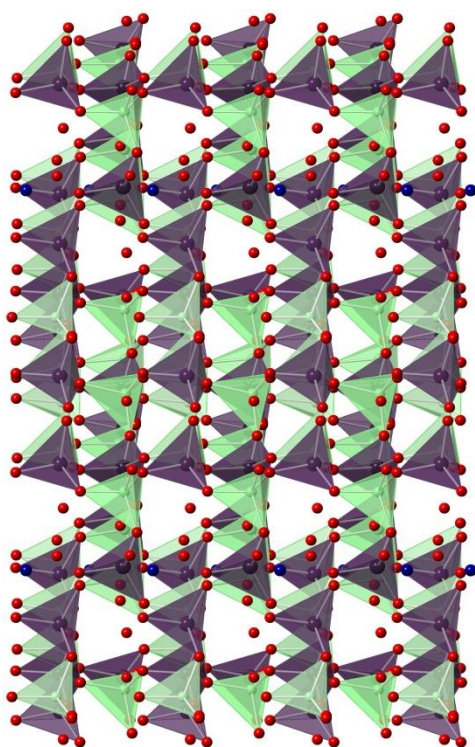


Figure 15:

$[\text{Co}^{\text{II}}]_{0.11}[(\text{AsO}_4(\text{H})_{0.66})_2\text{Be}_2(\text{BeOH}_2)_{0.33}] \cdot 2\text{H}_2\text{O}$ viewed along a and b . Purple and green tetrahedra are arsenic and beryllium centred respectively. Blue and red spheres represent cobalt and oxygen respectively.

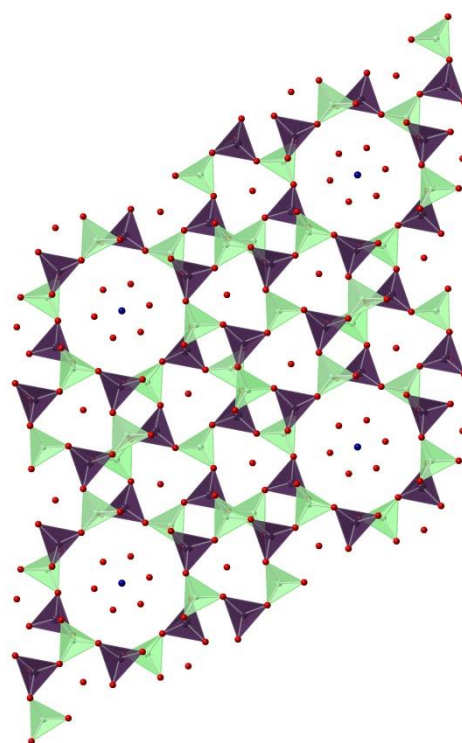


Figure 16:

$[\text{Co}^{\text{II}}]_{0.11}[(\text{AsO}_4(\text{H})_{0.66})_2\text{Be}_2(\text{BeOH}_2)_{0.33}] \cdot 2\text{H}_2\text{O}$ viewed along c . Purple and green tetrahedra are arsenic and beryllium centred respectively. Blue and red spheres represent cobalt and oxygen respectively.

$[\text{Co}^{\text{II}}]_{0.11}[(\text{AsO}_4(\text{H})_{0.66})_2\text{Be}_2(\text{BeOH}_2)_{0.33}] \cdot 2\text{H}_2\text{O}$ was originally synthesised from a hydrothermal reaction mixture containing 1,3-diaminopropane, $\text{CoCl}_2 \cdot 6\text{H}_2\text{O}$ and an excess of water. The reactive beryllate and arsenate monomers readily nucleated around the hydration sphere of the cobalt complex. At the high synthesis temperature it is likely that 1,3-diaminopropane decomposes and only plays a pH influencing role.

Structure solution was challenging with convergence achieved at a relatively high R factor (0.0895), this is due to the relatively large amount of disorder present in the structure in both extra-framework and topological species. The hydrogen assignments are purely theoretical, however it is likely that they are correct for the structure to fully charge balance.

$[\text{Co}^{\text{II}}]_{0.11}[(\text{AsO}_4(\text{H})_{0.66})_2\text{Be}_2(\text{BeOH}_2)_{0.33}] \cdot 2\text{H}_2\text{O}$ exhibits a one-dimensional channel structure and is formed of networks of 12, 6 and 4Rs in the ab plane cross linked by sinusoidal chains of 3 and 4Rs which link to form unusual asymmetric $8^1-6^4-4^4-3^2$ cages [Fig. 17/18]. These cages contain the 33 % occupied beryllium site, which shares a site with 66 % occupied hydroxyl termination on the arsenate centred tetrahedra, the location is highlighted on Fig. 18. This mixed site has implications on the overall porosity of the structure, which is represented in Fig. 19 with two possible channel systems

down *c*. The first incorporating the --OH_2 terminated site and resulting in the previously presented network of 12, 6 and 4Rs, the second represents the site when in its --OH terminated arsenate form and exhibits a network of regular 12Rs, irregular ‘clover leaf’ 12Rs and 4Rs. In the absence of the central beryllium tetrahedra, the irregular 12R is condensed by hydrogen bonding which is implied by the $\text{O}(\text{H})\cdots\text{O}$ average distance of 2.629 (8) Å. Both water and hexa-aqua cobalt are present as extra-framework species, with the 10 % occupied cobalt present in the centre of the regular 12Rs. The extra-framework water position is sited within the previously described asymmetric cages. Selected bond lengths and angles are presented in Table 12.

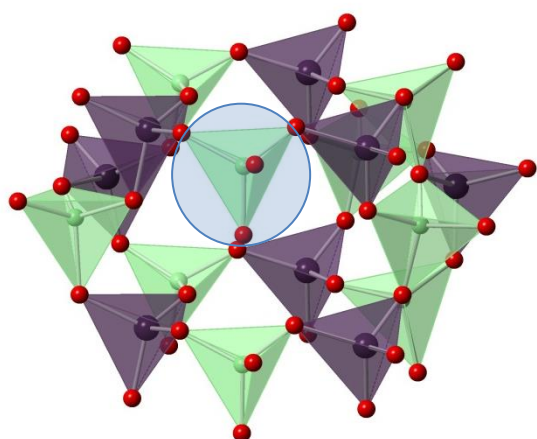


Figure 17: Polyhedral representation of asymmetric cage in $[\text{Co}^{\text{II}}]_{0.11}[(\text{AsO}_4(\text{H})_{0.66})_2\text{Be}_2(\text{BeOH}_2)_{0.33}] \cdot 2\text{H}_2\text{O}$, mixed site is highlighted by blue shading. Purple and green tetrahedra are As and Be centred respectively, red spheres represent oxygen.

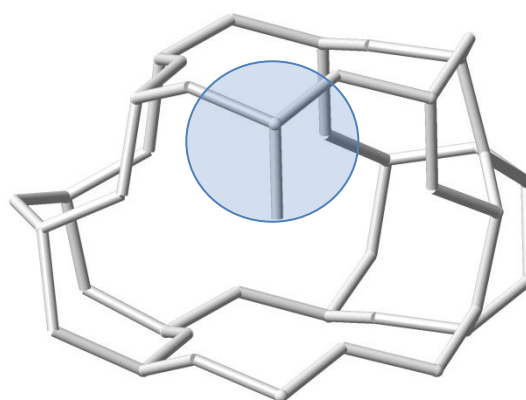


Figure 18: Skeletal representation of asymmetric cage in $[\text{Co}^{\text{II}}]_{0.11}[(\text{AsO}_4(\text{H})_{0.66})_2\text{Be}_2(\text{BeOH}_2)_{0.33}] \cdot 2\text{H}_2\text{O}$, mixed site is highlighted by blue shading.

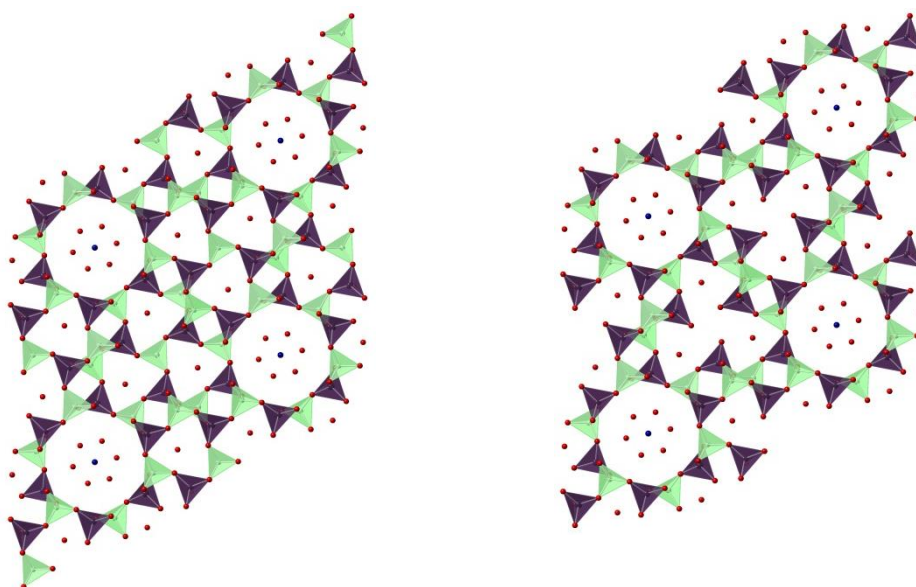


Figure 19: $[\text{Co}^{\text{II}}]_{0.11}[(\text{AsO}_4(\text{H})_{0.66})_2\text{Be}_2(\text{BeOH}_2)_{0.33}] \cdot 2\text{H}_2\text{O}$ viewed along *c* with 33 % occupied Be-centred tetrahedral site (left) and with 66 % occupied terminated arsenate-centred tetrahedra (right)

Table 12: Selected bond lengths and angles in $[\text{Co}^{\text{II}}]_{0.11}[(\text{AsO}_4(\text{H})_{0.66})_2\text{Be}_2(\text{BeOH}_2)_{0.33}]\cdot 2\text{H}_2\text{O}$

Bond	Bond length (Å)	Bond	Bond angle (°)
Average As – O	1.676(9)	Average O – As – O	109.41(4)
Average Be – O	1.625(8)	Average O – Be – O	109.49(10)
Average Co – O	2.0910(14)		
Be3 – OH ₂	1.7125(8)		

The longer than average bond distance between Be3 and its terminating oxygen help strengthen the hypothesis that it is water terminated, as this is a trend observed throughout the beryllioarsenates presented in Chapter 3.

Unfortunately due to the mixed nature of the product further characterisation other than SEM based measurements were impossible. EDS measurements and an SEM image was taken of one of the groups of crystals [Fig. 20]. EDS confirms the presence of As, Co and O and the SEM exhibits the morphology previously described.

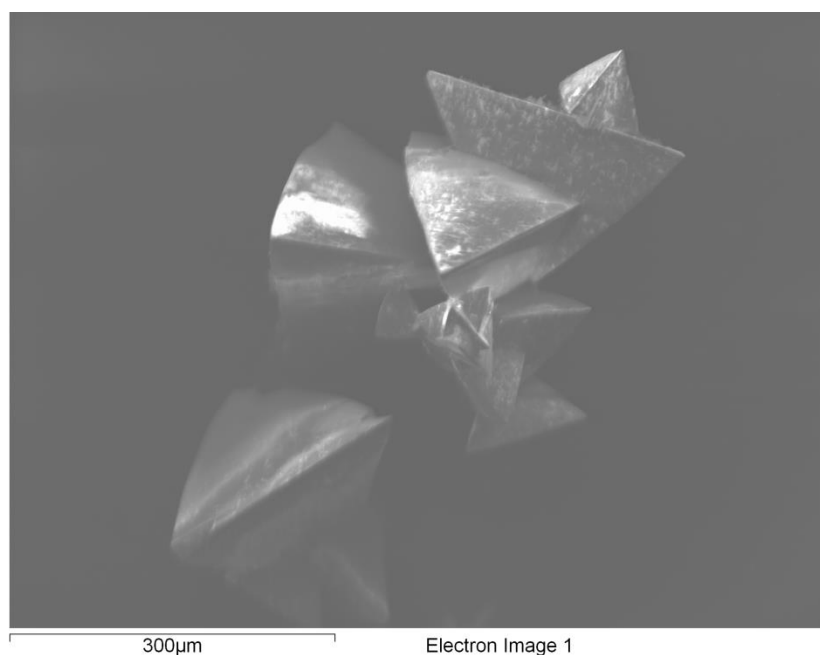


Figure 20: SEM image of $[\text{Co}^{\text{II}}]_{0.11}[(\text{AsO}_4(\text{H})_{0.66})_2\text{Be}_2(\text{BeOH}_2)_{0.33}]\cdot 2\text{H}_2\text{O}$ clearly exhibiting the tetrahedral morphology of the crystals

Ni containing analogues

Following the successful templating of $[\text{Co}^{\text{II}}]_{0.11}[(\text{AsO}_4(\text{H})_{0.66})_2\text{Be}_2(\text{BeOH}_2)_{0.33}]\cdot 2\text{H}_2\text{O}$ using a transition metal complex, a small amount of further work was initiated to investigate other elements and complexes, however, this was at the very end of the time allocated for this research and so only produced a hexa-aqua Ni templated structural analogue of $[\text{Co}^{\text{II}}]_{0.11}[(\text{AsO}_4(\text{H})_{0.66})_2\text{Be}_2(\text{BeOH}_2)_{0.33}]\cdot 2\text{H}_2\text{O}$, with very little structural impact aside from a slight change in unit cell volume attributed to the different ionic radii of octahedrally co-ordinated divalent Co (0.8 Å) and Ni (0.69 Å).^[33] Comparison of selected crystallographic parameters is in Table 13.

Table 13: Comparison between selected crystallographic parameters of the transition metal analogues of $[\text{Co}^{\text{II}}]_{0.11}[(\text{AsO}_4(\text{H})_{0.66})_2\text{Be}_2(\text{BeOH}_2)_{0.33}]\cdot 2\text{H}_2\text{O}$

Transition metal	Co^{2+}	Ni^{2+}
Appearance	Purple tetrahedra	Pale green thin plates
Temperature	120 K	120 K
Wavelength	0.71073 Å	0.71073 Å
Crystal system	Trigonal	Trigonal
Space group	P 6 ₃	P 6 ₃
<i>a</i>	16.5333(7) Å	16.5119(6) Å
<i>c</i>	4.7821(3) Å	4.7799(2) Å
Volume	1132.06(1) Å ³	1128.61(1) Å ³
Z	8	8
D _c	2.17 g cm ⁻³	2.43 g cm ⁻³
R index	0.0895	0.0726
Weighted R index	0.1474	0.2028

5.5 Conclusions and further work

Two new beryllogermanate layer structures are presented here and they represent the first hydrothermally synthesised materials containing oxygen bridged beryllium and germanium tetrahedra. $\text{Na}[\text{BeGeO}_3(\text{OH})]$ and $\text{Ba}[\text{Be}(\text{OH})\text{GeO}_3(\text{OH})]$ are both formed of BeO_4 and GeO_4 tetrahedra which are bridged via vertex sharing to produce infinite layers, cross linked through coordination with either an alkali or alkali earth cation and hydrogen bonding. Systematic investigation into all possible controllable synthetic parameters leads to the conclusion that very specific reaction conditions are required to produce crystals of sufficient size and quality to allow for structure elucidation. Both syntheses rely on pH management as a crucial parameter, only crystallising in mild alkaline conditions. Other parameters such as temperature or amounts of certain reagents seem to have little effect on the formation of either compound, other than on crystallite size where temperature is varied and experimental success where there is an extreme deficit/excess in one of the starting materials. Organic structure directing agents were investigated along with fluorides with little discernible effect, this may be due to competition with solvated alkali/alkali earth metals. Further synthetic investigation could be carried out by using other pH controlling media than metal hydroxides.

$\text{Na}[\text{BeGeO}_3(\text{OH})]$ has a very dense network, formed of 3- and 4Rs which are both stabilised by the inclusion of beryllium and germanium within the structure. The high density and lack of larger channels is likely because of the small ionic radii of the structure directing sodium cation, it is likely that with larger cations this structure would not form. Ion exchange would be a useful tool to investigate whether larger species can be accommodated between the layers. Due to the alkaline conditions used in its synthesis there is a low level of protonation present within the structure in form of a single charge balancing hydrogen position. The difficulty in producing phase pure samples of $\text{Na}[\text{BeGeO}_3(\text{OH})]$ make further characterisation and property investigation challenging.

$\text{Ba}[\text{Be}(\text{OH})\text{GeO}_3(\text{OH})]$ has a more open network than that of the sodium beryllogermanate discussed above, being formed of 4- and 8Rs. This is likely due to the incorporation of barium as the structure directing agent, its large ionic radii requires extra-framework cavities of at least 2.9 Å to accommodate it. Bond valence calculations show the presence and involvement in hydrogen bonding of one of the hydroxyl terminating groups. $\text{Ba}[\text{Be}(\text{OH})\text{GeO}_3(\text{OH})]$ is extremely interesting owing to its similarity to the aluminosilicate paracelsian and its berylloarsenate analogue. It shows that despite the differences in chemistry the geometric similarities between germanium and arsenic allow for isorecticular structures to form.

$\text{Sr}[\text{Be}(\text{OH})_4]$, ^[19] represents the first structure solution of a much theorised crucial part of the equilibrium chemistry of beryllium in solution. The highly alkaline synthesis has been refined to a point where phase pure samples can be produced. The structure is made of clusters of tetrahydroxyberyllate involved in extensive hydrogen bonding and octahedrally coordinated divalent strontium cations. The positions of hydrogen atoms have been confirmed by neutron diffraction, although a phase change is observed at around 200 K which would benefit from further investigation to elucidate the high temperature structure of $\text{Sr}[\text{Be}(\text{OH})_4]$. Attempts were made to produce the other alkali/alkali earth versions of the tetrahydroxyberyllate ^[18] however these were unsuccessful.

$[\text{Co}^{\text{II}}]_{0.11}[(\text{AsO}_4(\text{H})_{0.66})_2\text{Be}_2(\text{BeOH}_2)_{0.33}]\cdot 2\text{H}_2\text{O}$ and its Ni analogue represents the first transition metal complex templated beryllium containing framework, and is a completely new interrupted three-dimensional framework structure exhibiting a one-dimensional channel system and with 12Rs present as the largest ring size. $[\text{Co}^{\text{II}}]_{0.11}[(\text{AsO}_4(\text{H})_{0.66})_2\text{Be}_2(\text{BeOH}_2)_{0.33}]\cdot 2\text{H}_2\text{O}$ and its structural analogues also exhibit primary building unit disordered with a 33 % occupied Be site, which has an impact on the structures overall topology and porosity. Although such templating effects do exist in other zeotypical systems, they are poorly investigated.

As with the other chapters mentioned in this thesis each structure discussed here would benefit from refinement of its synthesis and subsequent further extensive characterisation. The greatest weakness demonstrated here is the polyphasic nature of the majority of materials presented in this work. This represents a barrier between investigating the properties of these structures and therefore their potential applications. After surmounting this barrier, further work should be carried out into investigating the effect of different transition metal complexes on the formation of new three-dimensional structures as the more stable co-ordination complexes should be able to resist mild hydrothermal synthesis conditions and may produce a whole new family of templated frameworks.

5.6: References

- ⁽¹⁾ R. M. Barrer, J. W. Baynham, F. W. Bultitude, W. M. Meier, *J. Chem. Soc.* **1959**, 195
- ⁽²⁾ G. Sastre, *Phys. Chem. Chem. Phys.*, **2007**, 9, 1052-1058
- ⁽³⁾ H. Kosslick, V. A. Tuan, R. Fricke, C. Peuker, W. Pilz, W. Storek, *J. Phys. Chem.*, **1993**, 97, 5678-5684
- ⁽⁴⁾ G. Sastre, A. Pulido, R. Castaeda, A. Corma, *J. Phys. Chem.*, **2004**, 108, 8830-8835
- ⁽⁵⁾ X. Bu, P. Feng, T. E. Gier, D. Zhao, G. D. Stucky, *J. Am. Chem. Soc.*, **1998**, 120, 13389 – 13397
- ⁽⁶⁾ G. M. Johnson, A. Tripathi, J. B. Parise, *Chem. Mat.*, **1999**, 11, 10-12
- ⁽⁷⁾ E. I. Belokoneva, T. G. Uvarova, L. N. Dem'yanets, *Kristallografiya*, **1986**, 31, 874-878
- ⁽⁸⁾ M. P. Attfield, F. Al-Otaibi, Y. Al-Ebini, *Micro. and Meso. Mat.*, 2009, 118, 508-512
- ⁽⁹⁾ J. Cheng, R. Xu, *J. Chem. Soc. Chem. Commun.*, **1991**, 1, 483
- ⁽¹⁰⁾ H. Li, O. M. Yaghi, *J. Am. Chem. Soc.*, **1998**, 120, 10569
- ⁽¹¹⁾ L. A. Villaescusa, P. A. Barret, M. A. Camblor, *Angew. Chem. Int. Ed. Engl.*, **1999**, 38 (13-14), 1997
- ⁽¹²⁾ P. Caullet, J. L. Paillaud, A. Simon-Masseron, M. Soulard, J. Patarin, *C. R. Chimie*, **2005**, 8, 245-266
- ⁽¹³⁾ Y. Ochi, H. Morikawa, F. Marumo, H. Nozaki, *Yogyo Kyokai Shi*, **1983**, 91, 229-235
- ⁽¹⁴⁾ S. E. Dann, M. T. Weller, B. D. Rainford, D. T. Adroja, *Inorg. Chem.*, **1997**, 36, 5278-5283
- ⁽¹⁵⁾ D. A. Everest, *The Chemistry of Beryllium*, Elsevier Publishing, Barking, UK, 1963
- ⁽¹⁶⁾ H. Kakihana, L.G. Sillen, *Acta Chem. Scand.*, **1956**, 10, 985
- ⁽¹⁷⁾ I. J. Bear, G. M. Lukaszewski, A. G. Turnbull, *Aust. J. Chem.*, **1965**, 18, 1317
- ⁽¹⁸⁾ V. R. Scholder, H. Hund, H. Schwarz, *Z. Anorg. Allg. Chem.*, **1968**, 361, 284
- ⁽¹⁹⁾ B. T. R. Littlefield, C. Hinde, M. T. Weller, *Dalton Trans.*, **2011**, 40, 782-784
- ⁽²⁰⁾ J. Yu, Y. Wang, Z. Shi, R. Xu, *Chem. Mater.* **2001**, 13, 2972 – 2978
- ⁽²¹⁾ M. E. Davis, *Acc. Chem. Res.*, **1993**, 26, 111
- ⁽²²⁾ Y. Wang, J. Yu, Z. Shi, R. Xu, *Jnl. Solid State Chem.*, **2003**, 170, 176 – 181
- ⁽²³⁾ R. Garcia, I. J. Shannon, A. M. Z. Slawin, W. Zhou, P. A. Cox, P. A. Wright, *Micro. Meso. Mat.*, **2003**, 58, 91 – 104
- ⁽²⁴⁾ D. A. Bruce, A. P. Wilkinson, M. G. White, J. A. Bertrand, *J. Chem. So. Chem. Commun.*, **1995**, 20, 2059 – 2060
- ⁽²⁵⁾ F. Duan, J. Li, W. Sun, P. Chen, J. Yu, R. Xu, *Science China Chemistry*, **2010**, 53, 2159 – 2163
- ⁽²⁶⁾ Y. Han, Y. Li, J. Yu, Q. Pan, R. Xu, *Eur. J. Inorg. Chem.* **2012**, 1, 36 - 39
- ⁽²⁷⁾ W. Pugh, *J. Chem. Soc.*, **1926**, 2828-2832
- ⁽²⁸⁾ A. K. Cheetham, H. Fjellvag, T. E. Gier, K. O. Kongshaug, K. P. Lillerud, G. D. Stucky, *Stud. Surf. Sci. Catal.*, **2001**, 135, 158

⁽²⁹⁾ J. A. Armstrong, unpublished work

⁽³⁰⁾ Chiari, G.;Gazzoni, G.;Craig, J.R.;Gibbs, G.V.;Louisnathan, S.J. (1985)

American Mineralogist 70, 969-974

⁽³¹⁾ R. Stahl, R. Niewa, H. Jacobs, *Z. Anorg. Allg. Chem.*, **1999**, 625, 48-50

⁽³²⁾ L. J. Csetenyi, F. P. Glasser, R. A. Howie, *Acta Crystallogr., Sect. C: Cryst. Struct. Commun.*, **1993**, 49, 1039-1041

⁽³³⁾ R. D. Shannon, *Acta Cryst.* **1976**, A32, 751 – 767

Chapter 6

General Conclusions

The aim of this research was to produce new frameworks built out of beryllium based tetrahedra, with a particular emphasis on the formation of new zeolitic topologies exhibiting higher porosity and low density. This was to be achieved through isomorphous heteroatom substitution of other oxo-anion bridged tetrahedral species and by utilising the various structure influencing factors available to the zeolite chemist, temperature, pH, gel composition, starting materials, solvent, mineralisers and in particular the nature and concentration of the structure directing agent.

The tetrahedral species investigated were the phosphates, arsenates and germanates, of which previous research into beryllium containing frameworks is extremely sparse, despite the successes of other similar materials such as the aluminophosphates. The berylloarsenates in particular represent a potentially lucrative field of research owing to the very small amount of historical work carried out, and the complete lack of investigation into the formation of novel berylloarsenates with organic structure directing agents. This is despite the large amount of structural variation promised by incorporating arsenic into the structure, briefly touched on by research into such fields as the zincoarsenates.

Solvothermal techniques were employed to synthesise all of the materials reported here, with the main solvent used being water, but ethanol and ammonia were also employed. In some reactions the organic species was used in such a large amount that it could be considered as a co-solvent with the intended solvent. Temperature, time of reaction and concentration and identity of starting materials were all varied with varying levels of success or impact on the materials produced. Mineralisers were even investigated in both F^- and OH^- forms. The greatest amount of synthetic variation was in the identity of the nitrogen rich organic structure directing agent, with 33 different compounds in varying concentrations being investigated. The combined synthetic variations result in over 1000 unique reactions being carried out for this research.

Through this wide spectrum of experimental alteration a large number of novel structures have been produced by this research. Each structure presented here has been characterised by single crystal X-ray diffraction and, where possible, other analytical techniques including; SEM, TGA, IR, BET, PXD and neutron diffraction.

Chapter three represents the bulk of the work for this thesis and presents the formation of 21 novel berylloarsenates ranging from the zero-dimensional cluster structure $Na_4[AsO_4(BeF_3)(BeF_2)] \cdot H_2O$ to the entirely new zeotype framework BOZ. The structures exhibiting lower dimensionality are formed of secondary and composite building units such as 3Rs, 4Rs and sinusoidal 3R chains which are precursors for the more complicated, higher connectivity structures. Several features are common across the majority of the berylloarsenate structures produced. [{H-

pyridine_{0.5}][(As_{0.785}Be_{0.215})₂(As_{0.17}Be_{0.83})₂O₇(OH)₂]•(H₂O)_{0.65} is a one dimensional chain structure formed of tubes of elliptical 8Rs and high degrees of arsenate OH termination, the same distorted 8Rs are seen in [NH₄]₂[(AsO₄)₂Be₂]•2H₂O, a merlinoite berylloarsenate analogue and the hydroxyl termination encountered on the arsenic tetrahedra is present throughout the two and interrupted three-dimensional structures, playing a vital structural stabilising role. Other common features are the water termination of beryllium centred tetrahedra and the prevalence of OH⁻ bridging anions due to the existence of consecutive Be centred tetrahedra. There are further structural trends encountered too, such as a higher ratio of 3Rs and spiro-5 rings compared to aluminosilicates, these result in the formation of large porous, low density structures and all four of the new zeotype topologies presented in chapter three are predominantly made of this rare secondary building unit.

Chapter four outlines the efforts to produce beryllophosphates, based on the chemical similarity between these two pentavalent elements, and to an extent it was successful, with the formation of five structural analogues of varying dimensionality, as well as three entirely new beryllophosphate frameworks which was unexpected due to the higher levels of historic research into frameworks formed from beryllium and phosphorus. Similar trends in structure are encountered for the beryllophosphates, with emphases on hydroxyl and water termination of tetrahedra. The one-dimensional and two-dimensional structures Na₂[(BeO₂OH)(PO₂)]•H₂O and {BeO₂(OH)(OH₂)}{BeO₂OH₂}P are extremely interesting despite being analogues of berylloarsenates as very few beryllophosphates of low dimensionality have been prepared. The lower levels of success encountered for the beryllophosphates can be attributed to the lower pK_a value of H₃PO₄ when compared to H₃AsO₄, both routinely utilised as starting materials in this research but due to that slight difference in acid strength, straight analogous syntheses were unsuccessful. Despite this synthetic challenge a beryllophosphate analogue of one of the new topologies was formed and represents one of the lowest framework density zeolitic topologies known. BOZ-P's lower toxicity in relation to BOZ-As may result in its application as a gas storage medium, for which it is ideal due to its low calculated density and high theoretical porosity.

Chapter five presents the results of small investigations into other related chemistry. First the results of investigating the potential formation of beryllogermanate structures are detailed. Since germanium is geometrically similar to arsenic it seemed reasonable to expect that analogues could be formed. This hypothesis was proven true by the synthesis of Ba[Be(OH)GeO₃(OH)] which is isorecticular to Sr[AsO₄Be(OH)]•H₂O, however, further attempts to make beryllogermantes of higher dimensionality were unsuccessful, this is due to the high negative framework charge of any structure formed from T²⁺/T⁴⁺ which would require a very large amount of extra-framework cations to charge balance, something unachievable with organic cations due to steric hindrance. Investigations were also carried out into the use of other species to template structures, in particular transition metal complexes, resulting in the formation of the novel structure <Co containing structure> and its

hexaaqua complex templated analogues. This area would benefit immensely from further work as it was only initiated at the end of the research presented here. The solution chemistry of beryllium was also investigated, more by serendipity than by design, but while attempting the synthesis of light-weight frameworks, the discrete $\text{Be}(\text{OH})_4^{2-}$ anion was synthesised and characterised, which represented the first definitive characterisation of a fundamental part of beryllium solution chemistry.

The final chapter details a small amount of work carried out at the start of this research pertaining to the identification of hydrogen positions within known zeolites or other hydrogenous materials, although its relevance to the rest of the research carried out is limited, it is still of scientific value and so considered pertinent to present it. Presented is an *in-situ* dehydration study of the well-known zeolite thomsonite and an investigation of the water sites present within the vanadosilicate cavansite.

All of the concepts and material presented in this thesis can be built upon; the author is convinced that there remains huge scope for the synthesis of even more beryllo-arsenate and phosphate materials, as well as investigating the potential applications of the already synthesised materials. The emerging field of transition metal complex templated structures is also an ideal starting point for further work.

A large number of novel structures have been synthesised and fully characterised, extending the range of beryllophosphates and representing the first major investigation into the formation of berylloarsenate frameworks. Minor contributions have also been made to; the use of metal complexes as structure directing agents, beryllogermantes, the solution chemistry of beryllium and the field of hydrogenous materials. By investigating the incorporation of new elements and their effects on the structure of zeolitic topologies a greater understanding of fine tuning zeolitic frameworks for specific applications can be achieved. It is hoped that combined with further information on the effects of different nitrogen rich organics in framework synthesis, this work has made a meaningful contribution to the field of zeolite science.

Appendix 1

Hydrogenous materials

This final chapter details a brief investigation into two hydrogenous naturally occurring minerals, thomsonite and cavansite. Thomsonite, $4[\text{NaCa}_2\text{Al}_5\text{Si}_5\text{O}_{20} \cdot 6\text{H}_2\text{O}]$, underwent an *in situ* dehydration study with special attention paid to the occupation of water oxygen sites. Cavansite, $\text{CaVO}[\text{Si}_4\text{O}_{10}] \cdot 4\text{H}_2\text{O}$, underwent a low temperature data collection to accurately resolve the hydrogen positions in its extra-framework water. This work was carried out primarily at the D20 instrument, ILL, Grenoble, France, with the assistance of Paul Henry and Valeska Ting. Structures were modelled via Rietveld methods described in the experimental section.

A.1: Thomsonite

Zeolites of the Natrolite-Thomsonite series have been extensively studied over the years, ^[1] thomsonite (a pseudo-tetragonal orthorhombic zeolite mineral with the chemical formula $4[\text{NaCa}_2\text{Al}_5\text{Si}_5\text{O}_{20} \cdot 6\text{H}_2\text{O}]$) ^[2] itself being the subject of many conventional X-ray, ^[3,4,5] synchrotron, ^[6,7] neutron ^[8,9] powder diffraction and ¹H-NMR ^[10] investigations into its structure. As such its lattice parameters, atomic coordinates and space group are well documented.

There has been a lot of confusion in the correct assignment of the lattice parameters for thomsonite in the literature, which is due to its tendency to adopt either a disordered or ordered structure with respect to Si/Al sites. As such most pre 1990 studies are confused between the two. Initially the structure was derived in 1933 ^[3] as the disordered form; $a = 13.03$, $b = 13.03$, $c = 6.61$ Å having a space group and volume of *Pbnm* and 1122.25 Å³ respectively. This structure was further investigated in 1978 and again in 1982 using powder X-ray diffraction. ^[4,5] A re-study of the orientation and geometry of the thomsonite unit cell was conducted in 1981 ^[2] which from the systematic absences $h+1$ odd for $hk0$, $h+k$ odd for $hk0$ and l odd for $0kl$ combined with more recent x-ray and optical studies concluded the unit cell dimensions as $a = 13.05$ $b = 13.08$ $c = 13.22$ Å (from Parkgate quarry thomsonite) and the space group as *Pcnn* which is of the ordered version of the structure. This is in contradiction with a more recent study ^[5] however as Nawaz and Malone ^[2] suggest; both Amirove ^[4] and Pechar ^[5] have derived their structures from the disordered thomsonite used by Taylor. ^[3]

The first conclusive investigation into ordered thomsonite was carried out by single crystal neutron diffraction at 13 K in 1990, ^[9] and included positions of the hydrogen atoms comprising the

coordinated water molecules, as well as updated lattice parameters of $a = 13.1043$, $b = 13.0569$, $c = 13.2463$ Å. It was found that the framework was very similar to the room temperature version, just with the expected T-O bond distance reduction. The disordered version of thomsonite was most recently investigated by single crystal X-ray diffraction in 2010 ^[11] providing updated crystal lattice parameters of $a = 13.0809$, $b = 13.0597$, $c = 6.6051$ Å. It is suggested that the disordered and ordered versions are determined by their locality, for example Neapolitan thomsonite (of volcanic tuff origin) crystallises as the disordered version and the Irish Parkgate quarry locality produces the ordered version. The version is then dependant on the geological conditions of formation, rather than randomly distributed.

The dehydration of thomsonite, like all zeolites, is interesting from an application and scientific basis. There exists four independent water positions, with a total of 24 waters/unit cell ^[6]. Initially ordered thomsonite was studied by stepwise dehydration and powder X-ray diffraction. ^[12] This showed a continuous contraction of the lattice parameters to $a = 12.9725$, $b = 12.9537$, $c = 13.2288$ Å up to an initial loss of two of the waters coordinated to Ca/Na and a shift of another by 0.3 Å at 523 K. By 573 K one further water had been lost and the lattice parameters had changed to $a = 12.908$, $b = 13.039$, $c = 13.034$ Å, the final water was observed to leave above 573 K and the crystallinity decreases as the compounds become amorphous. A more recent thermogravimetric analysis (TGA) study suggests most of the zeolitic water is lost in three stages; 453 K, 613 K and 663 K. ^[13] A combined synchrotron and powder X-ray diffraction study, with stepwise dehydration at 523, 553 and 583 K confirms the initial TGA result as two water sites coordinated to the mixed Ca/Na site are lost by 523 K. ^[6] This corresponds to a reduction of 8 H₂O/unit cell. At 553 K a further 4 waters/unit cell are lost, and the Na positions are shifted to approximately occupy the former water positions. Almost full dehydration is achieved at 583 K and the crystallinity deteriorates at 620 – 650 K. Until the research presented here, there has not been an *in situ* dehydration study of thomsonite.

Neutron diffraction of thomsonite

Orthorhombic ordered thomsonite, $4[\text{NaCa}_2\text{Al}_5\text{Si}_5\text{O}_{20} \cdot 4\text{H}_2\text{O}]$, occupies the $Pncn$ space group and at room temperature has lattice parameters of; $a = 13.0968$, $b = 13.0741$, $c = 13.2054$ Å which is in relatively good agreement with previous studies.^[6] Thomsonite is a three dimensional zeolitic framework (THO) exhibiting three dimensional channels of 8-membered rings down all three crystallographic axes. The framework is made up of 4 and 8-membered rings which are in turn formed of the *nat* composite building unit and the 4=1 secondary building unit [Fig. 1].

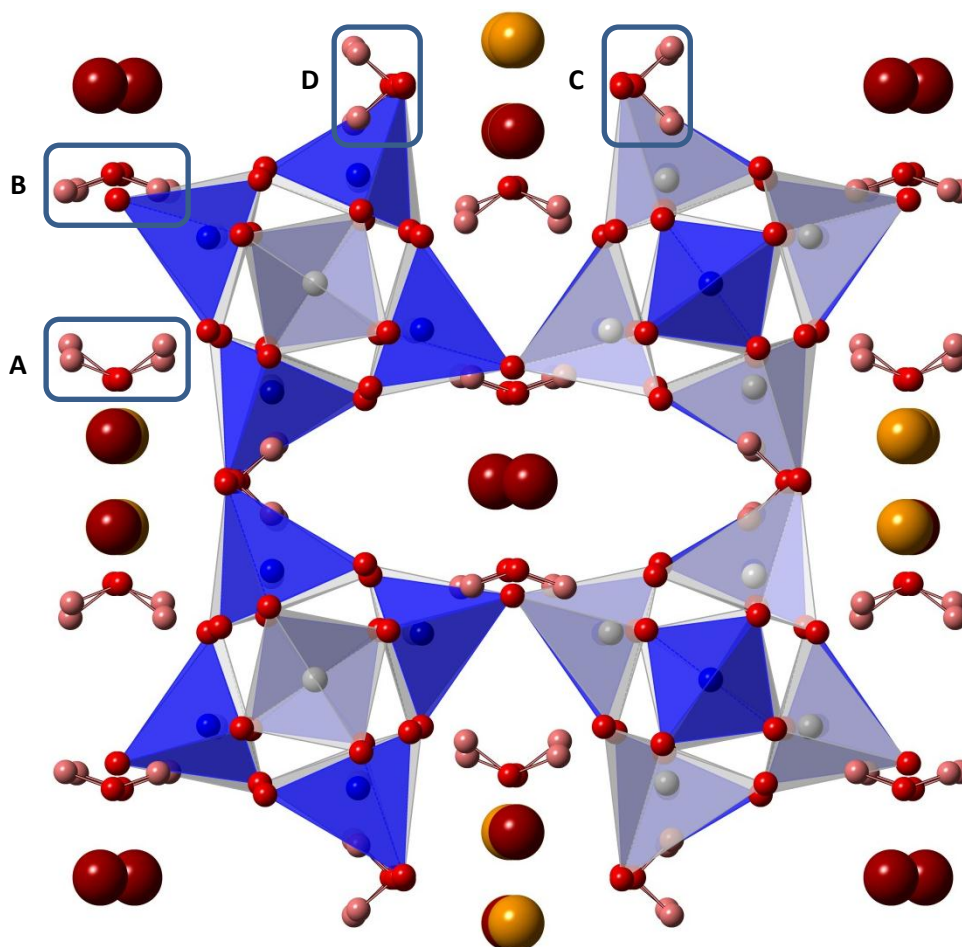
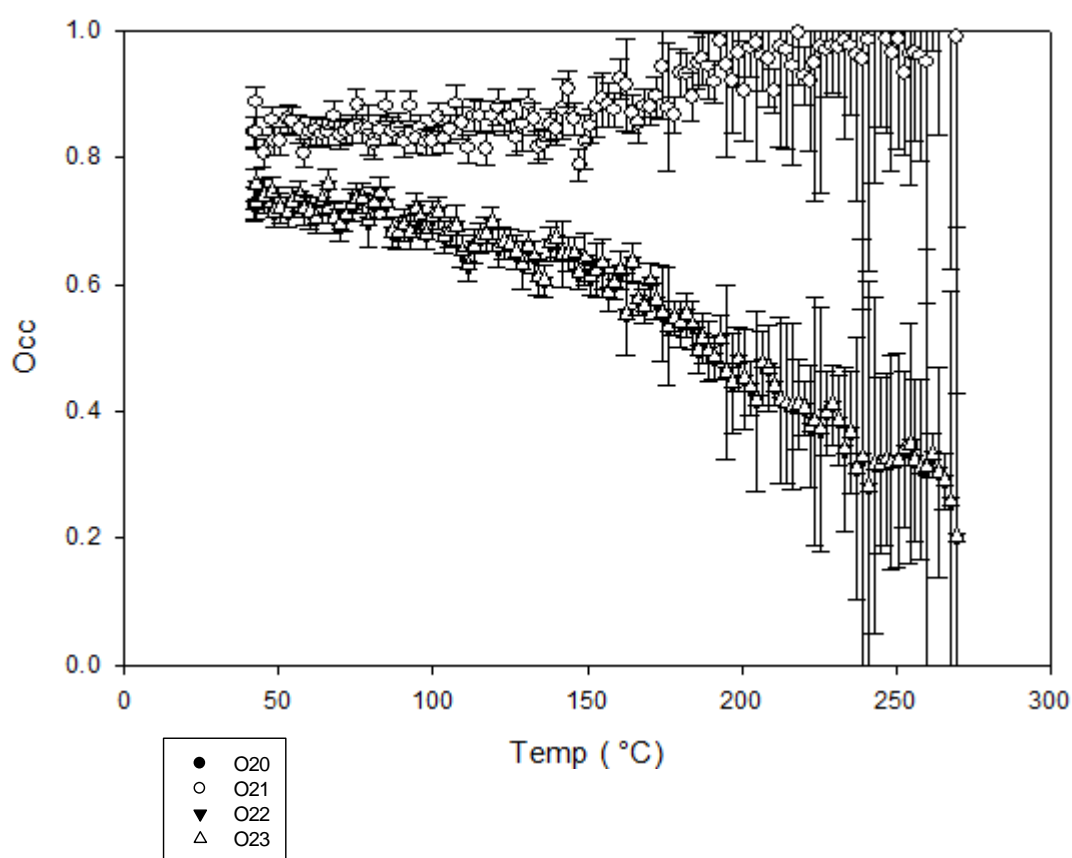


Figure 1: Thomsonite viewed along c . Si and Al centred tetrahedra are blue and grey respectively. Maroon, red, orange and pink spheres are Ca, O, Na and H respectively. Water sites are labelled as A, B, C and D which corresponds to O20, O21, O22 and O23 sites respectively

Extra-framework species occupy the channels formed by 8-membered rings with two charge balancing cation sites present, both of which exhibit disorder. The Ca site consists of two separate positions 0.565 Å apart, represented by 50 % occupancy on this site. This dual site is octahedrally coordinated to two water and 6 framework oxygen. The so-called CaNa site has a random distribution between Na and Ca.^[6] Each position is octahedrally coordinated to four water and four framework oxygen, with an average Ca-O distance of 2.552 Å.

An *in situ* neutron diffraction dehydration study of thomsonite has been carried out from room temperature to 533 K which shows a slight contraction in lattice parameters indicative of water loss and confirmed by previous dehydration studies.^[12] The initial dataset had an Rwp of 0.0150 and the final at 533 K was 0.0187, suggestive of a good model. The exact nature of the loss of the first 8 waters (two water sites) has been modelled based on sequential refinement of the four water sites coordinates, occupancy and thermal parameters. The CaNa site is coordinated to two O20s and both O22/23, whereas the Ca site is coordinated to two O21s.

Graph 1: Showing occupancy vs temperature for the O20/21/22/23 sites



When the occupancy of each water oxygen (O20, 21, 22 and 23) is plotted, a preferential shift in position is observed [Graph 1]. The occupancy for sites O20/O21 (A & B in Fig. 1) actually increases from 0.9400/0.9326 to fully occupied, whereas the occupancy for O22/23 (C & D) decreased from 0.6269 to 0.1107. This suggests that the equilibrium between the two positions differs at higher temperatures with preferential cation coordination for the O20/21 sites. This is supported by appreciation of the bond distances, at RT O20 is on average 2.521 Å away from the CaNa site unlike the O22/23 sites which are on average 2.595 Å away. The average distance between the Ca site and

O21 is even shorter, 2.371 Å which would imply this would be the most favoured water position and therefore last to be dehydrated. The difference in bond distances reflects the strength of the coordination to the cation sites and therefore the water molecules proclivity to leave.

A.2: Cavansite

The vanadium containing phyllosilicate cavansite (an orthorhombic mineral which along with pentagonite are dimorphs of $\text{CaVO}[\text{Si}_4\text{O}_{10}]\cdot 4\text{H}_2\text{O}$) is a rare blue-green mineral which crystallises as attractive sheet-like crystals commonly associated with stilbite or other aluminosilicate zeolites. Due to its comparatively recent discovery in 1960^[14] and its scarcity there exists little literature beyond the initial papers^[14,15] and two more modern X-ray studies, one of which studied the dehydrated mineral.^[16,17]

The initial structural study by Evans^[15] determined that cavansite has crystal lattice parameters of $a = 9.792$, $b = 13.644$, $c = 9.629$ Å, $Z = 4$ and is in the centrosymmetric space group $Pcmm$. This initial study provides the full atomic coordinates for all non-hydrogen elements. The structure of cavansite is a relatively simple two dimensional network, formed of sinusoidal chains of SiO_4 tetrahedra joined laterally to form 4- and 8-rings, where each 4-ring is encircled by 8-rings. The layers run parallel to the a/c plane and are cross-linked by the interaction of tetravalent square pyramidal vanadium. Charge balancing is provided by the incorporation of extra framework calcium as well as the vanadium. Interestingly if vanadium was replaced by oxygen bridging the structure would exhibit the GIS zeolitic framework.^[18]

Single crystal X-ray diffraction studies on a sample dehydrated at 220 °C shows an expected lattice contraction to $a = 9.368$, $b = 12.808$, $c = 9.550$ Å due to the removal of three H_2O between the silicate layers leading to a contraction of the b axis.^[16] The most recent study found in the literature involves the use of modern X-ray crystallography equipment and thus allows for the refinement of the atomic coordinates, and the first observations of the hydrogen positions on the water molecules present in the structure.^[17] This study suffers from the limitations of determining hydrogen positions using X-rays and as such the coordinates are likely incorrect.

Neutron diffraction of cavansite

The structure of cavansite is a two dimensional silicate layer structure, cross-linked by tetravalent square pyramidal vanadium, charge balanced by extra-framework calcium and contains four extra-framework waters between the layers and in the channels formed by the 4- and 8-membered rings [Fig. 2]. Neutron powder diffraction on the D20 instrument at the ILL, combined with the single crystal model from the literature^[17] has allowed for the accurate determination of the hydrogen positions of the extra-framework water in cavansite (Table 1), which when compared with the positions detailed in the literature show a small but marked effect. The greatest change is observed with site H3, where the

x coordinate changes from 0.422 to 0.3656. This is due to the previously discussed limitations in using X-ray techniques to resolve hydrogen positions.

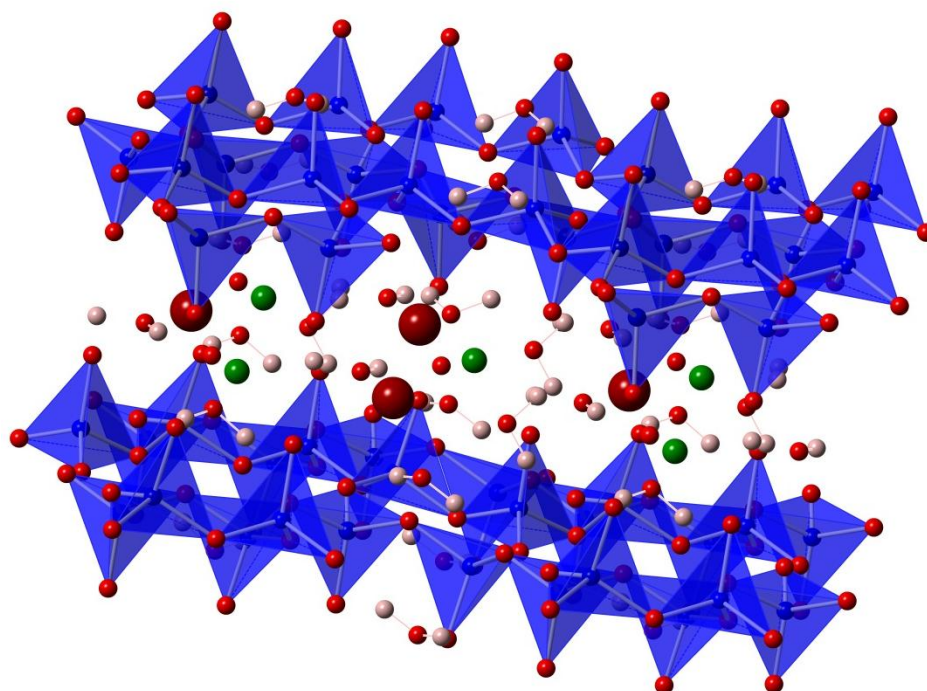


Figure 2: Cavansite viewed down *c* clearly showing extra-framework species between layers of blue Si-centred tetrahedra. Dark red, green, red and pink are Ca, V, O and H respectively

Table 1: Comparison between literature ^[15] site coordinates and observed (**bold**) coordinates

Site	x	y	z
H1/ H1	0.580/ 0.5713	0.085/ 0.0845	0.059/ 0.055
H2/ H2	0.860/ 0.8699	0.115/ 0.1038	0.430/ 0.4165
H3/ H3	0.422/ 0.3656	0.205/ 0.1981	0.159/ 0.2020
H4/ H4	0.72/ 0.7275	0.25/ 0.25	0.34/ 0.3263
H5/ H5	0.74/ 0.7860	0.25/ 0.25	0.19/ 0.1829

A.3: Conclusions and recommendations

Both thomsonite and cavansite have been successfully investigated by utilising a combination of single crystal X-ray and neutron diffraction data. Thomsonite exhibits a shift in water site occupancy on dehydration up to 533 K, with 2 water molecules being lost and a change in site preference from O22/23 to O20/21. The investigation into cavansite has produced more accurate hydrogen coordinates than those currently in the literature. Ideally further study would be carried out on the *in situ* dehydration of thomsonite, with observation of the full range of temperatures until destruction of crystallinity. Cavansite would benefit from a complimentary study of its dimorph pentagonite to allow comparisons to be made as well as further investigate the relationship between these two structures.

A.4: References

- ⁽¹⁾ T. N. Kol'tsova, *Inorganic Materials*, **2005**, 7, 750-756
- ⁽²⁾ R. Nawaz, J. F. Malone, *Mineralogical Magazine*, **1981**, 44, 231-234
- ⁽³⁾ W.H. Taylor, C. A. Meek, W. W. Jackson, The structure of the fibrous zeolites, *Z. Kristallogr*, **1993**, 24, 373-398
- ⁽⁴⁾ S. T. Amirove, I. R. Amiraslanov, B. T. Usubaliev, H. S. Mamedov, *Azerbaidzhanskii Khimicheskii Zhurnal*, **1978**, 120-127
- ⁽⁵⁾ F. Pechar, *Crys. Research and Technology*, **1982**, 17, 1141-1144
- ⁽⁶⁾ K. Stahl, *Materials Science Forum Vols. 378-381*, **2001**, 346-350
- ⁽⁷⁾ A. Y. Likhacheva, Y. V. Seryotkin, A. Y. Manakov, S. V. Goryainov, A. I. Ancharov, M. A. Sheromov, *American Mineralogist*, **2007**, 92, 1610-1615
- ⁽⁸⁾ J.J. Pluth, S.V. Smith, A. Kvick, *Zeolites*, **1985**, 5, 74-80
- ⁽⁹⁾ K. Stahl, A. Kvick, J. V. Smith, *Acta Cryst.*, **1990**, 46, 1370-1373
- ⁽¹⁰⁾ L. V. Kashkina, S. P. Gabuda, *Z. Strukturnoi Khimii*, **1972**, 13, 6, 1016-1019
- ⁽¹¹⁾ D. Gatta, V. Kahlenberg, R. Kaindl, N. Rotiroti, P. Cappelletti, M. De'Gennaro, *American Mineralogist*, **2010**, 95, 495-502
- ⁽¹²⁾ K. Stahl, R. Thomasson, *J. Appl. Cryst.*, **1992**, 25, 251-258
- ⁽¹³⁾ A. Yamazaki, Y. Inoue, M. Koike, T. Sakamoto, R. Otsuka, *J. Therm. Ana.*, **1993**, 40, 85-97
- ⁽¹⁴⁾ H. T. Evans, J. R. Lindsay, *American Mineralogist*, **1973**, 58, 405-411
- ⁽¹⁵⁾ H. T. Evans, *American Mineralogist*, **1973**, 58, 412-424
- ⁽¹⁶⁾ R. Rinaldi, J. J. Pluth, J. V. Smith, *Acta Cryst. B*, **1975**, 31, 1598
- ⁽¹⁷⁾ M. V. Solov'ev, R. K. Rastsvetaeva, D. Y. Pushcharovskii, *Krystallografiya*, **1993**, 38(2), 264 – 267
- ⁽¹⁸⁾ K. Fischer, V. Schramm, *Adv. Chem. Ser.*, **1971**, 101, 250 – 258